To the graduate council:

I am submitting herewith a dissertation written by Jae-Won Park entitled "Adhesion Mechanisms of Metallic Thin Films deposited on Surface-Modified Ceramics". I have examined the first copy of this dissertation for form and content and recommend that it be accepted in partial fulfillment of the requirements for the degree of Doctor of Philosophy with a major in Metallurgical Engineering.

Anthony J. Pedraza, Major Professor

We have read this dissertation
and recommend its acceptance:

D. H. Lowndes

R. A. Buchanan

WR Allen

Accepted for the Council:

Associate Vice Chancellor
and Dean of the Graduate School

ADHESION MECHANISMS OF METALLIC THIN FILMS DEPOSITED ON SURFACE-MODIFIED CERAMICS

A Dissertation
Presented for the
Doctor of Philosophy
Degree
The University of Tennessee, Knoxville

Jae-Won Park

December, 1995

DEDICATION

To my wife, daughter, and parents

ACKNOWLEDGMENT

I am greatly indebted to my main professor, Dr. Anthony J. Pedraza for his guidance, advisory, and support during the whole period of this thesis work. Gratitude is extended to Dr. D. H. Lowndes and Dr. W. R. Allen for being on my thesis committee and arranging the equipments used for this research. Graditude is also extended to other committee members, Dr. R. A. Buchanan and Dr. H. Weitering, for their valuable advices.

I am deeply thankful to my wife for her sanctified support and encouragement during the whole period of my graduate study and research.

I would like to acknowledge the Center for Materials Processing (CMP) at the University of Tennessee, Knoxville and National Science Foundation (NSF) for the financial supports and the maintenance of the experimental facilities during this work.

I am also indebted to Dr. S. Cao for his assistance on TEM and SEM works and Dr. M. J. DeSilva and Mr. R. Kumar for their assistance and providing the data on the pull adhesion testing.

I am also grateful to Surface Analysis group members, Dr. H. M. Meyer, Dr. J. C. Mabon, Ms. A. Lynn Glover, and Mr. S. Cristy, in Oak Ridge Centers for Manufacturing Technology (ORCMT) for their help with the surface analytical equipments such as Auger Electron Spectroscopy and X-ray Photoelectron Spectroscopy, and Secondary Ion Mass Spectroscopy used in this research.

ABSTRACT

One of the most fundamental aspects of the metal/ceramic couple applications is strong adhesion. For this reason, a substatial effort has been made in this work to establish the processing conditions that enhance the adhesion between two dissimilar materials and discover the adhesion mechanisms responsible for the strong bonding. In this work, representative systems chosen included gold and copper as the metallic films and Al_2O_3 and AlN as the ceramic substrates. These metals and ceramics are non-reactive with each other under thermodynamic equilibrium and, for this reason, the ceramic surfaces were modified to increase the reactivity between the ceramics and the metals. Laser irradiation and ion bombardment methods were used for the surface modifications and aimed at disordering and debonding the surface atomic arrangement and chemical changes of the ceramics. The surface characterizations were conducted with X-ray photoelectron spectroscopy (XPS) and Auger electron spectroscopy (AES) before and after surface modifications. The results were compared with TEM analysis. These ceramics were decomposed leaving metallic aluminum and/or substoichiometric ceramics on the surface, followed by the reoxidation of the utmost layers. The metallic films were sputter-deposited on the as-received and surface modified ceramic substrates, and the film/substrate couples were annealed to increase the atomic mobility at the interface. Pull adhesion testing was conducted next, and then the interfaces of the strongly and weakly adhered couples were analyzed with AES technique. The analysis of the interface of the metal/ceramic couples using AES is usually not easy due to the sample charging and decomposition of ceramic substrates. Hence, a new method was devised, in which the analysis is performed on the film using the Auger electron escape depth. This method can also eliminate the problems during the AES analysis of the ceramics. The analysis takes advantage of various film thickness and the variation of Auger electron kinetic energies of the elements of interest.

The interfacial reactions of the metallic films and alumina and aluminum nitride couples were greatly affected by the laser energy densities and irradiation atmospheres used for the substrate treatment and annealing temperatures of the couples. Also, the surface contaminants played a very important role for the enhanced adhesion. In the copper/Al_2O_3 couple, the strong bonding mechanisms were i) the formation of double oxides at the interface which could be achieved by the laser irradiation of the ceramics in air followed by the low temperature (300°C) annealing of the couple and ii) direct interaction between the copper film and metallic aluminum and/or substoichiometric alumina that could be obtained by the laser irradiation in Ar-4%H_2 followed by 500°C annealing of the couple. In the gold film/Al_2O_3 couple, the gold was also reacted with the substrate when the substrate was irradiated in the oxygen atmosphere at 1 J/cm^2 energy density and the couple was annealed at 300°C.

The amount of the metallic aluminum that formed by the decomposition of AlN was much more than that formed in alumina. Since the metallic aluminum is easily reoxidized, the bonding mechanism in these couples were not much different to the copper-alumina couples. In the strongly bonded couple, Cu-O-Al compound was always found at the interface. Gold reacted with laser irradiated AlN substrate in the strongly bonded Au/AlN couple.

When Ar+ ions bombardment of sapphire (single crystalline Al_2O_3) and gold film deposition were conducted simultaneously, pull adhesion testing of the couple also showed very strong bonding without a following anneal of the couple. The effects of ion beam bombardment on the sapphire substrate were investigated *in situ* with AES. Metallic aluminum was detected on the surface of sapphire substrate after irradiating for 3 min. with 7 keV Ar^+ - ions, These results were consistent with TRIM calculations that yield preferential sputtering of oxygen. An AES analysis revealed that Au-Al-O compound formed at the interface that may have caused the strong bonding. The compound must have been favored by the surface cleaning and the reduction of the sapphire due to the ion bombardment prior to the gold film deposition.

A study on the copper diffusion into SiO_2 substrate was also conducted in this work. Copper deposited on the thermally grown SiO_2 substrate drifted into the substrate upon annealing at 300°C under 1 MV /cm^2 electric field application. AES analysis showed formation of a copper oxide at the interface of this couple.

TABLE OF CONTENTS

LIST OF TABLES

LIST OF FIGURES

CHAPTER 1

INTRODUCTION

In response to the growing applications of metals bonded to insulators, such as microelectronics, electronic packaging systems, magnetic and optical devices, composites, and hybrid structural materials, extensive studies have been performed to improve the quality of metal/ceramic couples. In these couples, the interfaces are often required to resist internal/external stresses without failure or debond in a controlled way. In their electronic packaging applications, thermal expansion of the conductive path by the heat generated during the service may give arise to stresses at the interface and then result in a system failure. Therefore, strong adhesion between two dissimilar materials in these couples is of great importance among the many other aspects that affect service performance.

Good adhesion at the interface between mutually reactive materials can be easily obtained; however, reactions of metals and ceramics are very restricted because ceramics are thermodynamically so stable that most metals cannot reduce them. Thus, the near surface of ceramic substrates or metal/ceramic couples should be properly treated to facilitate interfacial reactions between metals and ceramics.

Past efforts pursued in our research group have successfully produced strongly adherent copper, gold, and nickel films to alumina substrates; However, the mechanisms leading to such a strong adhesion were not clearly understood. In this work the mechanisms were investigated and adhesion of different couples, e.g., metallic films/AlN, have also been studied. This research was motivated by the electronic packaging application of thin metallic films/ceramics. The film materials used were pure copper and gold and the substrates were alumina, sapphire, aluminum nitride, and silicon oxides.

The overall experimental scheme consisted of surface modification of ceramics, metallic film deposition, post-deposition annealing, adhesion testing, and surface and interface analyses. Additionally, dielectric loss of SiO_2 due to copper

drift under the electric field in the copper/SiO_2 couple has also been studied. A brief summary of the experimental program follows:

1) The substrate surface was modified by the laser-irradiation at various laser energy densities in oxygen and Ar-4%H_2 atmospheres. Then, copper and gold films approximately 80 nm thick were sputter-deposited onto the irradiated substrates. After deposition, metallic film/ceramic couples were annealed at 300°C or 500°C in vacuum for 1h to increase the atomic mobility in the interface and assist interfacial reactions. Pull-testing was subsequently performed to measure the adhesion strength.

Surface analytical techniques such as X-ray photoelectron spectroscopy (XPS) and Auger electron spectroscopy (AES) were employed to analyze the substrate surfaces laser-irradiated at various energy densities and atmospheres prior to film deposition. After pull-testing, the interfaces of strongly and weakly bonded couples were analyzed with AES to investigate the adhesion mechanism. In the analyses, the metallic films were sputter - etched with an Ar^+ gun till the interface was revealed and then the Auger peaks were scanned on the fresh surface at each sputtering cycle. Surface topographical changes due to the laser irradiation were observed with Secondary Electron Microscopy (SEM) as well .

2) The surface modification of sapphire substrate was also performed using ion beam bombardment. Pre-sputtering of the substrate and film deposition were conducted *in situ* and then pull adhesion tests were made. The effects of ion beam bombardment on the substrate and the film/substrate interface were analyzed with AES. Since the thickness of the interface in this couple was expected to be very thin (one or two monolayers thick), a new technique taking advantage of various film thickness at the sputter crater edge and the Auger electron escape depth was devised for the interfacial analysis.

Surface sputtering and subsurface damage produced during ion beam bombardment was evaluated using TRIM calculations.

3) Decomposition and charging effects that are two important drawbacks in AES

analysis of ceramic materials were studied. Detailed investigations were carried out to reduce and/or eliminate the sample charging and the electron beam induced decomposition on Al_2O_3 was studied *in situ*.

4) The low temperature electric field driven diffusion of copper in SiO_2 was studied using Secondary Ion Mass Spectroscopy (SIMS). Copper drifting into SiO_2 substrate under an applied electric field results in a dielectric loss of SiO_2, eventually leading to failure of electronic devices. The reaction of copper with the surface of SiO_2 substrate is also investigated with AES. The results of this study provided useful information for future studies on surface modifications and/or the application of a diffusion barrier coating on the surface to prevent the dielectric loss of insulating substrates.

CHAPTER 2

REVIEW OF THE LITERATURE

2.1 Metallization in the ultra-large-scale integration (ULSI) structure

Currently, increasing demand for high circuit speed, high packing density, and low power dissipation in the integrated circuit (IC) devices requires a miniaturization of the feature sizes in ULSI structure. As the chip size is becoming smaller, the propagation delay time decreases. However, increase of on-chip interconnect resistance capacitance (RC) delay time limits the enhancement of high circuit speeds. The reason why shrinking the chip size causes an increase in the RC delay time is due to the reduction of the wiring pitch which increases current densities and the wiring resistance. Interconnect resistance in a conductive path increases with decrease of its cross sectional area. The decrease of the aspect ratio (the metallic line height to width ratio) may produce poor step coverage of metal in deep via holes which can be another cause of the increase of interconnect resistance. Therefore, it is needed to increase the aspect ratio to reduce the resistance of the interconnect. Increasing the aspect ratio requires adding more metallization levels. However, adding more levels with the same metal may cause several adverse effects such as planarization, pattern transfer, and process yield, because it increases the wiring density.

Therefore, along with the reduction in the chip size, the development of a new device with lower resistance interconnecting materials and materials with lower dielectric constant are required. Currently, Al and its alloys as interconnect materials and SiO_2 as a dielectric material are being replaced by lower resistance metals and lower dielectric constant materials.

Copper is the main candidate to replace aluminum and aluminum alloys as interconnect material due to its lower resistivity, lower electromigration, and better mechanical properties. Possible materials for the interconnect are listed in table 2.1 [1] and their main properties for this application are compared. Gold has the best properties in electromigration and corrosion resistances: however, its

Table 2.1

Comparison of materials properties and problems in processing among possible interconnect materials.

Properties	Al	W	Au	Ag	Cu
Resistivity (μΩ cm)	2.66	5.65	2.35	1.59	1.67
Electromigration resistance (0.5μm)	low	very high	very high	very low	high
Corrosion resistance in air	high	high	very high	low	low

higher electric resistivity than copper may be a restriction in the application. Silver exhibits the best electrical conductivity, but its corrosion and electromigration resistances are very poor.

In this work, gold and copper are studied for thin film metallization.

2.2 Substrate materials in the electronic packaging applications

Heat is generated in the conductive path during power application and it must be effectively dissipated not only to decrease the resistivity, but also to prevent possible system failure. Complex cooling systems have been developed to dissipate the heat generated in the circuit [2], but the simpler and better way to dissipate the heat is to use a high thermal conductivity ceramic substrate.

Although Matthiessen's rule for the metal conductivity was formulated for the bulk materials, it may be also assumed to be valid for thin metallic films. That is, the total electric resistivity (ρ_T) is given by

$$\rho_T = \rho_{Th} + \rho_I + \rho_D, \qquad \text{eq.(2.1)}$$

where ρ_{Th}, ρ_I, and ρ_D are respectively thermal , impurity , and defect contributions. Since the thermal resistivity is caused by electron collisions with vibrating atoms displaced from their equilibrium position, it increases linearly with temperature. However, the impurity and defect contributions to the resistivity are independent of temperature, provided the concentration of impurities and defects are low.

Generally the substrates used in the electronic packaging applications require high thermal conductivity, low thermal expansion coefficient, low dielectric coefficient, and must be good insulators. Some properties of ceramics, e.g., BeO, SiC, AlN which can replace alumina are tabulated in table 2.2 [3]. Although alumina has the lowest thermal conductivity, it has been used most widely in the packaging applications due to its low processing cost and the lack of stringent requirement for thermal conductivity so far. Nowadays, however, ceramics exhibiting higher thermal conductivity and reasonable processing cost

Table 2.2

Properties of some substrate materials comparable to alumina.

Property	**AlN**	**BeO**	**SiC**	**Al_2O_3**
Crystal Structure	Hex.	Cub.	Cub.	Hex.
Density (g/cm^3)	3.3	2.9	3.3	3.9
Melting Point (°C)	2400	2530	2700	2030
Youngs Modulus (10^3 Kg/mm^2)	30-31	30-35	38	30-38
Bend Strength (Kg/mm^2)	30-50	17-25	45-50	25-30
Hardness (Knoop)	1200	1000	2000	2000
Thermal Conductivity (W/m.K)	320	250	270	20-30
CTE (10^{-6} / °C)*	4.2	7.5	3.7	8.1
Electrical Resistivity at 298 K (ohm.cm)	10^{14}	10^{14}	10^{13}	10^{13}
Dielectric Constant at 1 MHz	8.8	6.5	40	9.7
Dielectric loss at 1 MHz (10^{-4})	8	2	500	3-4
Dielectric Strength (kV/mm)	14-17	10-14	0.7	10
Problems	Easy oxidation	Toxicity	Semi-conductor	-

* CTE of silicon = 3.5 X 10^{-6} / °C , of copper = 17 X 10^{-6} / °C

are replacing alumina. It seems that aluminum nitride is the most promising material among other ceramics, because SiC may lose the dielectric property easily and BeO is toxic in its powder form thus presenting safety problems during processing.

2.3 Surface modification of the ceramics prior to thin film deposition

In many metal -ceramic systems, adhesion of the metals to the ceramic surfaces is normally weak because metals and ceramics are non-reactive with each other. For instance, in the Cu/Al_2O_3 couple, copper does not reduce Al_2O_3 chemically and the solution of Cu in Al_2O_3 is negligible, so that no chemical reaction can occur at the interface. For metals to adhere at the ceramic surface, therefore, it is required to disturb the ordering and break bonding of the surface atoms. That is, a chemical bonding between metals and ceramics might be achieved with a change of the electronic structure at the interface. In this work, excimer laser irradiation and ion beam bombardment techniques are employed to modify the ceramic surface.

2.3.1 Effects of excimer laser irradiations on ceramics

When a nearly coherent laser beam is incident on a material, a part of the energy is reflected and the remainder is absorbed by the electrons as a result of electron-photon interaction [4]. Metallic materials, which have a high density of conduction electrons, can absorb the laser light in the first few tens of nanometers [5], while the absorption of the laser light in semiconductor materials is also within a similar distance when the wave length of the laser light is in the ultravilolet range (most commonly at 193 nm, 248 nm, or 308 nm) [6]. Ceramic materials, which have usually very low absorption coefficient in the UV range, can absorb the energy when the photon energy is higher than the band gap [7]. The energy can be transferred as heat to the lattice in a very short time (10^{-11} - 10^{-12}s) [8]. At most laser fluences, pulsed laser irradiation incident on the material usually heats up the surface layers abruptly, causing an extremely high thermal gradient. Thus,

the laser can modify only the near surface region of the materials by heating as well as stresses resulted from the high thermal gradient (approx. 10^7K/cm).

Temperature gradient as a function of the distance from the surface and possible melting, decomposition, and evaporation can be predicted by process modeling problem. Excimer laser heating can be regarded as an one-dimensional heat diffusion model because the irradiated area is of the order of several millimeters, while the heat affected region is only a few micrometers thick. The appropriate Fourier equation is

$$c.\rho.\frac{\partial T}{\partial t} = \frac{\partial}{\partial X}\left(k\frac{\partial T}{\partial x}\right) + P(x,t), \qquad \text{eq.(2.2)}$$

where c,ρ and K are the material specific heat, density and thermal conductivity, respectively, P(x,t) represents the heat source term produced by a laser pulse. The boundary conditions are the initial sample temperature, the limiting temperature down in the bulk depth, and the radiative loss at the surface, i.e., respectively

$$T(x,0) = To\,;\quad T(\infty,t) = To;\quad \frac{\partial T}{\partial x}\Big|_{x=0} = 0, \qquad \text{eq.(2.3)}$$

where To is the initial temperature of the material. In the case of melting or resolidification the condition (x-axis directed toward the sample interior);

$$\rho\Delta H_m V = K_S\,\frac{\partial T_l}{\partial x}\Big|_{x^+}(s,l) \;-\; K_l\frac{\partial T}{\partial x}\Big|_{x^-}(l,s), \qquad \text{eq.(2.4)}$$

must be satisfied at the melt-solid interface. Here, ΔH_m is the heat of melting, V is rate of advance of the interface at time t, and K_l and K_S are, respectively, the thermal conductivities of liquid and solid. Moreover,

$$V = f(T_i - T_m), \qquad \text{eq.(2.5)}$$

where f is a function of the difference between the solid-liquid interface

temperature T_i and the equilibrium melting temperature Tm.

Past studies of pulsed XeCl (308nm) laser irradiation effects on polycrystalline Al_2O_3 of 99.6% purity and on single crystal Al_2O_3 [9] showed that laser etching can be achieved above a threshold laser energy density. Above this threshold, the etching is observed after a certain incubation given by a number of laser pulses. At a fluence ≥ 0.7 J/cm^2 alumina melts and flows under repeated irradiation. It is reasoned that, during such an incubation period, a certain threshold concentration of absorption centers are generated by laser. Subsequently, strong coupling of the laser pulse with the absorption center occurs in the near-surface region [10]. Melting and thermal evaporation of alumina are the effects due to this coupling. Surface smoothing of polycrystalline alumina is due to melt flowing on the surface. XPS studies of the Al_2O_3 laser-irradiated at 308nm wavelength showed that Al_2O_3 can be decomposed by irradiation under reducing atmosphere (Ar-4%H), leaving some metallic aluminum on the surface of the alumina [11,12]. Part of the results will be presented in this thesis and compared with the results obtained by other analytical techniques such as TEM and AES. Aluminum nitride (AlN), which is decomposed thermally at a temperature of 2537 K, can also be decomposed by excimer laser irradiation [13]. The decomposition products are liquid Al and gaseous N which is ejected to the atmosphere. Selective metallization was obtained on laser irradiated AlN [13]. In this work, different aspects of the laser irradiated AlN will be examined. If the temperature is further raised to 2767 °K, the liquid aluminum evaporates [14]. It was reported that the ablation rate of AlN increases linearly with the laser energy density in the range of 1 - 6 J/cm^2 [15]. Similar to Al_2O_3, the surface of as received AlN which exhibits faceted and protruded grains due to the sintering can be smoothened by the melting caused by the laser irradiation. This will also be shown in the experimental section.

2.3.2 Effects of ion beam bombardment on ceramics

Ion beam bombardment has been reported to produce several effects in

materials: 1) atomic collision induced by recoil implantation, cascade mixing, migration of species followed by trapping at defect sites and vacancies, and radiation enhanced diffusion [16,17], 2) change of the electronic structure of the materials surface [18], and 3) cleaning of surface contaminants like hydrocarbon residue [19].

Ion beam bombardment is also frequently employed for surface modification of ceramic substrates for thin film metallization. It was reported that the adhesion of copper thin films to sapphire substrate increases with increasing ion dose on the sapphire surface prior to film deposition [20]. The adhesion of Au film (approx. 500Å thick) evaporated on vitreous silica substrates was enhanced when the substrates were irradiated with ^{31}P ions [21]. Low energy (500eV) Ar^+ ion beam bombardment of Al_2O_3 greatly improved the adhesion of a copper film deposited on it by forming Cu-Al-O compounds at the interface [22]. This compound may have been formed because the Al_2O_3 surface was enriched in Al due to preferential sputtering which is caused by different secondary ion yield between O and Al in Al_2O_3. Preferential sputtering effects were studied experimentally with SIMS [23] and by calculation with a concentration-dependent surface binding energy model [24] for PtCu and PtSi mixtures, in which Pt atoms are less easily sputtered than the other species.

It was reported that N and Ni ion implantation in single crystalline α-alumina resulted in strengthening due to irradiation induced damage and formation of spinel structure at the surface [25].

In this work, ion beam bombardment effects on the adhesion of gold film to single crystalline Al_2O_3 were studied and the bonding mechanism were investigated with AES.

2.4 Thin film deposition techniques

Thin film deposition techniques used commercially and for research and development purposes include electro- and electroless-deposition, chemical vapor deposition (CVD), physical vapor deposition (evaporation and sputtering), molecular beam epitaxy (MBE), organometallic vapor phase epitaxy (OMVPE). In

general, most films prepared by those techniques are not perfect single crystals. They may contain voids, grain boundaries, short-, intermediate-, and long range orders, and they can be amorphous and exhibit clustering and compositional variations, depending on the preparation conditions. Since the functions of each process are in many aspects overlapping, an eventual selection of the processes depends on the balance of technical, scientific, and economic considerations. Some properties of copper films obtained from different deposition processes are shown and compared in the Table 2.3 [26].

2.4.1 Physical Vapor Deposition (PVD)

In general, this deposition process can be classified into three steps; production of the vapor phase, transport of vapor from the target to substrate, and film growth on the substrate surface.

In PVD technique, there are two vaporization methods, e.g., sputtering and evaporation [27]. Sputtering is a process in which atoms are ejected from the surface of a target material as a result of momentum and energy transfer by bombardment of the surface with energetic particles [28]. Evaporation is a process of thermal vaporization of the target in which heating is carried out at a low pressure [29].

During the transport of vapor from the source to the substrate the following collisional processes take place:

1) elastic scattering processes, which influence the vapor distribution in the deposition chamber and then the thickness uniformity of the film grown on the substrate surface,

2) inelastic collisions, e.g., ionization, recombination, and dissociation, which determine the concentration and flux of species (atoms, ions, radicals) bombarding the substrate surface.

Depending on the gases present in the chamber, that may have significant effects on the film properties, the deposition process can be classified into three processes [30]:

1) vacuum processes (line -of-sight movement of the sputtered particles)

Table 2.3

Properties of copper film deposited by different deposition processes.

	CVD	PVD	Laser reflow	Electroless	Electrolytic
Resistivity ($\mu\Omega$)	≥2	1.75 - 2	2.6	approx. 2	approx. 2
Impurities	C, O	Ar	---	seed layer	---
Deposition rate (nm/min.)	approx. 100	≥100		≤100	approx. 200
Process temp. (°C)	approx. 250	RT	melt	50 - 60	RT
Step coverage	good	fair		good	good
Via filling capability	good	poor	good	fair - poor	fair - poor
Environmental impact (waste)	good	good	good	poor	poor

2) inert processes (scattering of the particles)

3) reactive processes (formation of compound on the surface of the substrate surface depending on the gas species present in the chamber; oxide, nitride, carbide, boride, etc.)

The nature of the films grown on the substrate surface can be influenced not only by the substrate temperature and material but also by the fluxes and energies of all the particles bombarding the substrate surface, e.g., particles from the target, the reactive gas particles, and ions. Here, ions and energetic particles play an important role in advanced thin film deposition techniques because of their significant effects in non-equilibrium bombardment processes that accompany film growth and affect its properties. The physical effects of the energetic particles on the substrate surface and the growing film depend mainly on the energy and type of the bombarding particle. In general, the following effects have been observed [31 - 33]:

Near surface effect

a) heating

b) desorption of physically and chemically bonded species

c) enhancement of surface mobility of adatoms

d)enhancement of chemical reactions of adsorbed species

e)sticking of incident particles on the surface

f)ejection of secondary electrons

g) reflection of the incident particles as ions or neutrals

h) sputtering of surface atoms or clusters and re-deposition of sputtered species

Subsurface effect

a) heating

b)displacement of lattice atoms and creation of lattice defects in collisional cascades

c) implantation of incident particles

d) recoil implantation of surface species into the subsurface lattice
e)trapping of mobile species at lattice defects.

Sputtering is one of the main processes in particle interaction with the surface of a solid using an energy ranging from the threshold energy for sputtering (10-30 eV) [34] to energies of about 10 keV or higher. Sputtering is quantified in terms of the sputter yield. The yield depends on the target material, the bombarding species, and its energy and angle of incidence [35]. Due to the momentum transfer process, the yield depends on the relative masses of atom and ion. Also, most of the atoms are sputtered from the top layers. Typical values of the sputter yield are 0.1- 3 atoms/ion for ion energies up to 1 keV [36] .

Depending on the source, there are two sputtering systems, e.g, ion source sputtering and plasma sputtering. In the plasma system three steps have been developed: 1) conventional diode or triode sputtering, 2) magnetron sputtering. and 3) magnetron sputter ion plating. There are two ways to sputter the target (cathode) materials in a plasma system: direct current (dc) sputtering and radio frequency (rf) sputtering. The dc negative potential can be used only for the sputtering of conductive targets. It cannot be used for nonconducting targets because of charge accumulation at the target surface. In contrast, the rf sputtering can be used for both conducting and nonconducting materials.

The evaporation method is quite different from the sputtering method. In evaporation, increasing source temperature is required to produce the metallic vapor at a pressure of approximately 1 torr [36]. Several methods can be used, namely, 1) resistance- or induction- heated source, 2) electron beam heated source, 3) laser beam heating, and 4) cathodic arc discharge [29].

In the processing chamber, the gas pressure must be low enough ($\leq 10^{-4}$ torr) so that the evaporated atoms are not scattered by collisions with the residual gas [36]. The deposition rate of the vaporized species on the substrate strongly depends on the chamber vacuum pressure, since the mean free path (MFP) of the species is a function of the vacuum pressure in the chamber. MFP can be expressed as [37];

MFP(cm) = 1.5/P, where P is pressure in pascals. eq.(2.6)

2.4.2 Chemical vapor deposition (CVD) [38]

In CVD a solid material is deposited from gaseous precursors onto a substrate. The substrate is typically heated to promote the deposition reaction and/or provide sufficient mobility of adatoms to form the desired structure.

The main advantages of CVD are high deposition rate (≥ tens of microns per hour) and control over stoichiometry, morphology, crystal structure, and orientation, which is governed by the deposition parameters. The disadvantages of CVD include heating of the substrate and corrosiveness and toxicity of the process gases. Sometimes, the elevated temperature to promote film deposition and obtain the desired film properties can result in adverse effects for microelectronics applications such as phase change, grain growth, and diffusion of the dopants into the substrate. Corrosive reactant and product species in CVD can attack substrate materials, causing porosity, poor adherence, and contamination of the coating. CVD is largely a near-equilibrium process producing crystalline films although it produces amorphous films of certain materials. Thus, metastable materials which can be easily produced by sputtering may not be reproduced using CVD techniques.

2.4.3 Electroless depositions

Electroless deposition is one of the chemical plating techniques, in which the electrons required for the metal reduction are supplied by simultaneous oxidation of a reducing agent in the solution [39]. In order for this process to take place, the redox potential of the reducing agent must be more negative than that of the metal being plated, and the surface for the metallization must be energetically favorable for oxidation of the reductant and electrically conductive for the electrons to transfer. The deposition can be started in a number of ways such as substrate canalization, galvanic displacement , surface activation, using metal-mediator, etc.. In the substrate catalytic method, the deposition initiates

from a seed layer which has the catalytic properties for the anodic oxidation initiation. On the other hand, pre-deposition catalization can be produced by laser induced activation of the substrate surface for copper metallization, in alumina and aluminum nitride substrates [40, 41]. In the latter method deposition took place only on the laser irradiated areas and the deposition rate increases with increasing laser energy density, implying that the nucleation of copper islands on the irradiated surface is proportional to the degree of surface activation [41].

2.4.4 Other deposition techniques

2.4.4.1 Molecular Beam Epitaxy (MBE)

MBE is a thin film deposition process in which thermalized beams of atoms or molecules react on the clean surface of a single crystalline substrate, held at high temperature under ultrahigh vacuum conditions, to form an epitaxial film [42]. Thus, MBE is a physical film deposition technique. In MBE, temperature is the primary parameter controlling high adatom mobility, and ultraclean and ultra high vacuum conditions allow the atoms to have sufficient time to adjust their positions on the growing film surface. Also, the ultra high vacuum (better than 10^{-10} torr) prevents the undesirable impurity additions in the film and at the interface with the substrate. Several vacuum chambers for sample introduction, deposition, and analysis with attachable surface analytical devices such as Auger Electron Spectroscopy (AES), X-ray Photoelectron Spectroscopy (XPS), Secondary Ion Mass Spectroscopy (SIMS), Reflection High Energy Electron Diffraction (RHEED) allow in situ deposition and analysis to produce high quality films [43]. RHEED is generally used to monitor and control the growth process and played a major role in the development of MBE process [44].

2.4.4.2 Organometallic Vapor Phase Epitaxy (OMVPE)

Since most of the compound semiconductors decompose into their constituent components at high temperature, epitaxial growth in its simplest form

can be accomplished by transporting individual components at high temperature, where they react to form the compound semiconductor. Growth of semiconducting materials at atmospheric pressure is highly advantageous from a commercial point of view. However, if one of the components in the compound has a very low vapor pressure, transport of the components will be very difficult at atmospheric pressure. Therefore, the use of volatile organometallic compounds [45, 46] as transport mediums, especially for the Column III components (Ga, In, Al) having a very low vapor pressure, has been developed. This technique is called as OMVPE. Since the compound is required to have an electronic grade (99.999% or better) after deposition [47], the selection of the compound materials is very important.

2.5 Bonding theories of metal/ceramic couples

Various interfacial reactions can occur at metal/ceramic interfaces and equilibrium thermodynamics is useful in predicting possible reactions. Bonding can take place by either charge transfer between metal and ceramic (chemical bonding) or mass transport across the metal/ceramic interface (physical bonding). In this section we will briefly review the surface energies of metals and ceramics and then discuss the adhesion of metals and ceramics in terms of interfacial energy and work of adhesion.

2.5.1 Surface energy of metals and ceramics

A certain energy is associated with a solid or liquid surface because the bonding forces of the surface atoms or ions are unbalanced. The magnitude of the surface energy increases with the bonding strength between the atoms (the cohesive energy) and the number of broken bonds per unit area of surface. The surface energy is also related to physical properties like melting temperature, heat of vaporization, and heat of sublimation. It has been reported that the heats of vaporization and sublimation are linearly proportional to the surface energy [48]. The surface energy of ceramics is generally lower than metals as implied by their

higher melting temperature and Young's modulus [49].

2.5.2 Interfacial energy and work of adhesion of metals and ceramics

The driving force for the formation of a metal/ceramic interface is the decrease in free energy when the metal is in contact with the ceramic. The free energy change (ΔG) by forming the interface can be expressed by Dupre' equation.

$$\Delta G = \gamma_m + \gamma_c - \gamma_{mc} \qquad \text{eq.(2.7)}$$

where γ_m and γ_c are the surface energies of the metal and the ceramic, respectively, and γ_{mc} is the metal/ceramic interfacial energy. If we confine the bonding to the chemical bonding and assume no plastic deformation during debonding, the free energy change will be equal to the work of adhesion (W_{ad}). Therefore, by replacing ΔG in eq.(2.7) with W_{ad} the equation is rearranged as

$$\gamma_{mc} = \gamma_m + \gamma_c - W_{ad} \qquad \text{eq.(2.8)}$$

So, it is clear that the interfacial energy is oppositely correlated with the work of adhesion. This correlation is shown in figure 2.1 [48]. When mechanical testing is used to measure the adhesion strength, a considerable energy is usually dissipated before debonding, so that $W_{ad} \geq \Delta G$, where the work of adhesion includes the dissipative processes that occur during separation. On the other hand, the interfacial energy can be derived from the known surface energies of liquid or solid metal and ceramic substrates by measuring the contact angle (θ) (figure 2.2). At equilibrium, the balance among the interfacial energies is given by the Young - Dupre equation [49].

$$\gamma_{mc} - \gamma_c + \gamma_m \cos\theta = 0 \qquad \text{eq.(2.9)}$$

Combining eq.(2.8) with eq.(2.9)

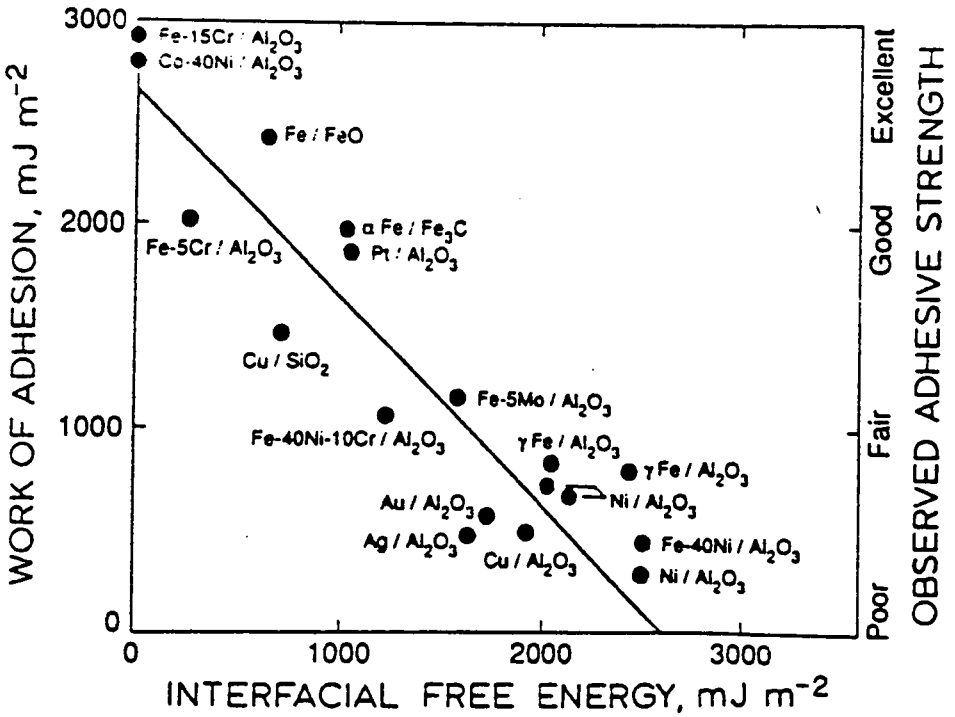

Figure 2.1 The relation between thermodynamic work of adhesion and interfacial energy between metal and non-metal

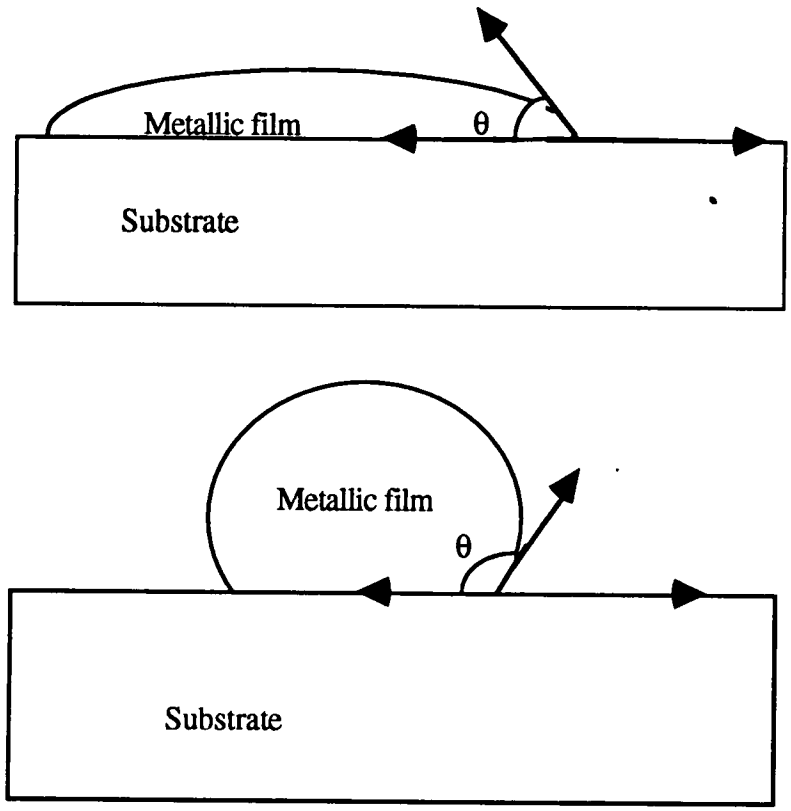

Figure. 2.2 Two types of contact angle of liquid wetted on the solid substrate

$$W_{ad} = \gamma m (1 + \cos\theta) \qquad \text{eq.(2.10)}$$

These equations show that wetting of the substrate occurs as $\theta<90^\circ$ and complete spreading occurs as θ approaches 0°. However, eq.(2.10) is not valid in many cases, because the surface structure and composition of the metals and ceramics are usually different from those of the bulk. For instance, chemisorption of gases at the surface, segregation of impurities or alloying elements to the surface, and interfacial chemical reactions can occur in some systems. Interfacial chemicals include a direct interaction between the metal and the ceramic and formation of an intermediate compound in the interface. In addition, the presence of surface defects such as cavities or microcracks may change the interface nature.

2.6 Characterization of the surface and the interface

2.6.1 Introduction to surface and interface analysis

Since the interfacial reaction in the film/substrate couple is, in many cases, assumed to involve only a few atomic monolayers in each material surface, it is very important to analyze the elemental composition and chemical binding state of the outmost atomic layers of a solid substrate before thin film metallization. After thin film deposition, the analysis of the interface can help to understand the interfacial reactions that may have occurred during the process.

For the surface analysis, the main factors in selecting the analytical techniques are spatial resolutions, sampling depths, and detection sensitivities. In table 2.4 these factors are specified for various surface analytical techniques [50]. In this work , depending on the purpose of analysis, XPS, AES, and SIMS techniques were employed. Referring to table 2.4 the following comparisons can be made among the three techniques:

- AES has the highest spatial resolution (as small as 5 nm) since the electron beam can be focused to a very small spot by adjusting lenses.

Table 2.4 Survey of some popular techniques for surface and interface analyses

(Note: spacial resolution and sensitivity are usually trade-offs.)

Techniques	Information (E: elemental C: chemical)	Spacial resolution (best)	Sampling depth(mono layers)	Sensitivity (order of)	Quantification (x : easy)	Elements not covered	input/ output radiaitons
AES	E,C	5nm	3	0.3%	x	H, He	Elec/Elec
HREELS	C	1mm	1	1%	-		Elec/Elec
RBS	E	1mm	100	1%	x	H, He	Ion/Ion
SIMS (static)	C	1μm	2	0.01%	-		Ion/Ion
SIMS (dynamic	E	20nm	10	<1p.p.m	x		Ion/Ion
imaging)					(with standard)		Ion/Ion
SIMS(dynamic	E	50μm	10	<1p.p.m	x		
depth profile)					(with standard)		Ion/Ion
UPS	C	5μm	3	1%	-	N/A	X-ray/Elec
XPS	E,C	5μm	3	0.3%	x	H,He	X-ray/Elec

- SIMS is the best in terms of detection sensitivity. Therefore, it is good for analysis of impurities.

-Due to the high peak-to-background ratio, XPS is better for analyzing chemical states than the other techniques.

Sometimes, elemental and chemical informations underneath the surface are required as a function of depth (up to ~1μm). In this case a careful use of a sputter gun is required to prevent spurious effects such as changing the surface chemical state due to preferential sputtering, producing defects in the subsurface, intermixing between dissimilar materials in the interface [51].

In the next sections, XPS, AES, and SIMS are briefly described in terms of their mechanisms and applications to surface and interface analysis.

2.6.2 X-ray photoelectron spectroscopy (XPS)

2.6.2.1 Principles of XPS

XPS is based on energy spectra from X-ray stimulated electrons. Since this technique can easily distinguish different chemical states of non-metallic atoms as well as the oxidation states of the metals, it is also frequently called Electron Spectroscopy for Chemical Analysis (ESCA). The principles of the XPS analysis are ;

1) X-rays are produced in the X-ray source (commonly Al or Mg)

2) An individual X-ray line (usually $K\alpha_1$ for the analysis) from the unresolved $K\alpha_{1,2}$ doublet, X-ray satellites, and Bremsstrallung continuum can be selected by a single crystalline monochromator.

3) X-ray photons from a nearly monoenergetic beam of energy $h\nu$ impinge on the sample.

4) The photons are absorbed by sample atoms with each absorption event resulting in the prompt emission of an electron (figure 2.3). In these events, if the X-ray energy is less than binding energies of an electron from any of the orbitals, electrons in the atom are not emitted, but excited, followed by only characteristic X-ray emmision.

5) An electron emitted in this way has a kinetic energy proportional to the incident X-ray photon energy. A constant electron binding energy in a specific orbital can be calculated if the X-ray energy is known and the electron kinetic energy is measured with the electron spectrometer. That is,

$$E_b = h\nu - E_{K.E.} - e\Phi \qquad \text{eq.(2.11)}$$

where E_b= binding energy of an electron in an orbital

$E_{K.E.}$= Kinetic energy of ejected photoelectron

$h\nu$ = characteristic energy of X-ray photon

$e\Phi$= spectrometer work function.

The spectrometer work function must be corrected through the spectrometer calibration process.

6) The resultant XPS peaks obtained in this way are plotted as a function of the binding energy. The peak positions are independent of the incident X-ray photon energy and the target materials.

In the commercial XPS, Mg and Al targets are often used. The photoelectron emmision is followed by X-ray fluorescence and/or Auger transition processes. Therefore, Auger electron spectra are also plotted with the XPS spectra. However, in XPS the spatial resolution for the Auger spectra is much lower than that of the spectra from AES due to the limitation in focusing the X-ray beam.

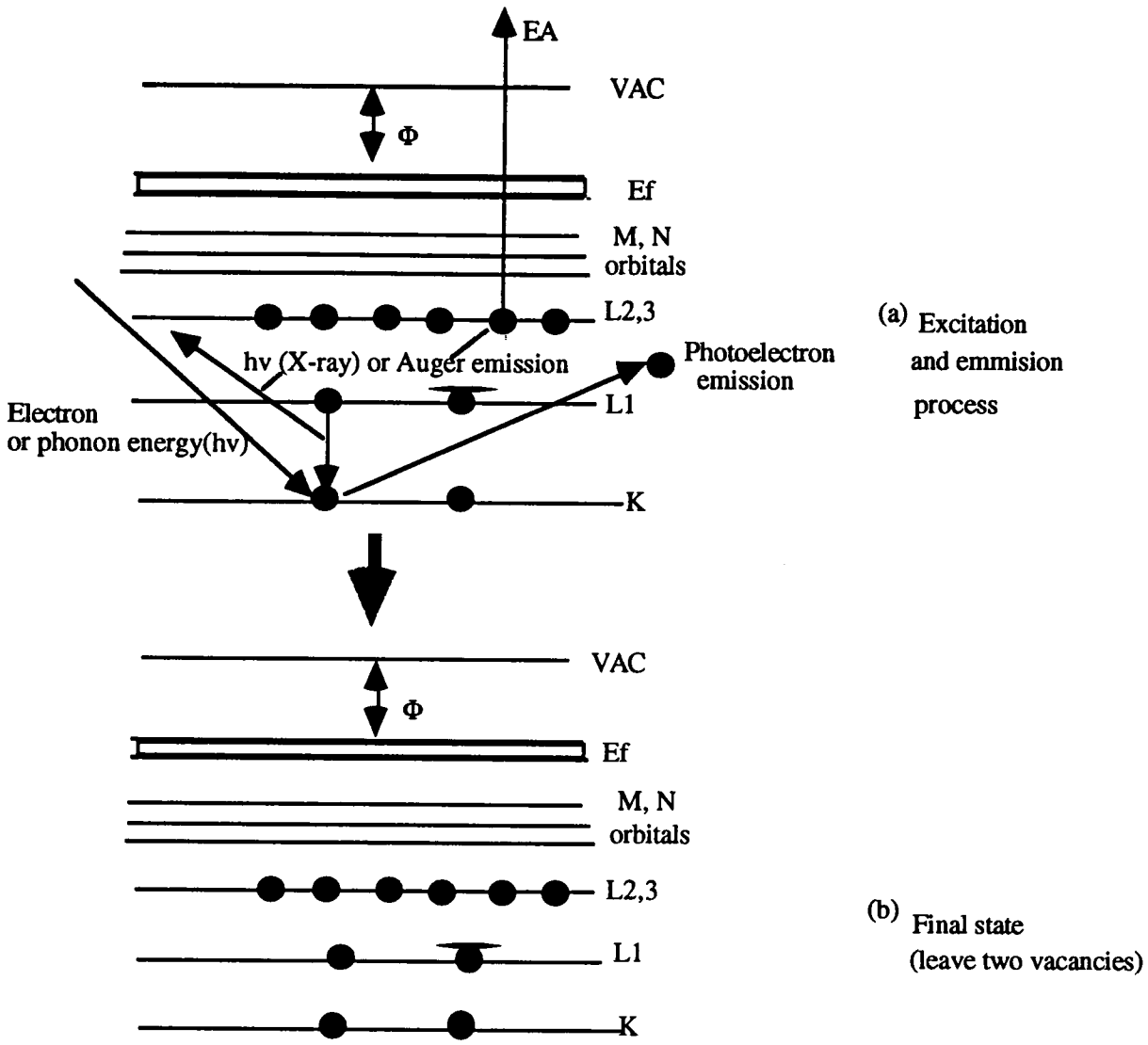

Figure 2.3 Energy level diagram depicting $KL_1L_{2,3}$ Auger transition. Once a sufficiently energetic electron or phonon energy (hv) is incident on the core level (K) electron, photoelectron is ejected, leaving an electron vacancy. The electron hole is filled by an upper level (L1) electron, followed by either X-ray emission or Auger electron emission (a). Finally, the Auger transition produces two electron holes in an atom (b).The kinetic energy of an electron (E_A) from L_2 level is equal to $E_K - E_{L1} - E_{L2,3}$.

2.6.2.2 Quantification of XPS

The number of photoelectrons produced from any given core level of an element is determined by the photoionization cross-section (σ) of that level for the incident X-ray photons. The photoionization cross-section is a function of the X-ray photon energy (hv), binding energy (Eb), atomic number (Z), and the X-ray incident angle (θ) to the surface normal [52]. The dependence of the σ on θ is, by convention, characterized by an asymmetry factor $L(\theta)$ which describes the intensity distribution of the photoelectrons ejected from the sample [52].

$$L(\theta)) = 1 + 1/2 \cdot \beta \, (3/2 \cdot \sin^2\theta - 1) \qquad \text{eq (2.12)}$$

where, b is a constant for given core-level of a given atom and X-ray photon. From eq.(2.12), we see no asymmetry correction is needed for the angle (θ) close to 54.7°, the so-called magic angle. Although calculated values of σ and β are available [52 - 54], quantitative interpretation of XPS spectra is mostly obtained via empirical and experimentally derived atomic sensitivity factors by recording spectra from standard materials. The quantification of XPS spectra can be given by

$$C_A = \frac{I_A / S_A}{\sum (I_n / S_n)}, \qquad \text{eq.(2.13)}$$

where C_A : fractional atomic concentration of element A

I_A : peak intensity (peak area over background) of the element A

S_A: atomic sensitivity factor (ASF) of the element A from the standard sample (usually a ratio of the integrated intensity of the standard sample A to that of the standard silver sample)

I_n: measured peak intensity for element n

S_n: relative atomic sensitivity factor (ASF) of the measured peak for element n.

In practice, since the small peak shifts due to various chemical states of an element in a sample produce a superimposed asymmetrical total peak, careful

deconvolution procedures are required for the quantitative as well as qualitative interpretations of the spectra. Computer softwares for this purpose are commercially available. However, the fact that an accurate quantitative analysis by XPS requires homogeneous chemical compositions within the analysis volume can be a restriction in the analysis.

2.6.2.3 Chemical shift in XPS

The chemical shift effect in XPS is the most distinctive feature among other well known surface analysis techniques. A decrease of the electron density in the valence region around an atom in a molecule produces an increase in the binding energy of core level electrons. Therefore, binding energy shifts can be readily interpreted in terms of well understood chemical concepts.

2.6.2.4 Sample Charging in XPS

The photoelectrons emitted by X-ray irradiation leave positively charged ions on the surface. The consequent positive sample charging tends to reduce the kinetic energy of the photo-ejected electrons due to the attractive force between the charging field and the photoelectron, resulting in higher apparent binding energies than the true values [57]. Generally, this phenomenon limits the amount of chemical informations obtainable from the data. Charging can be reduced in two ways: 1) The electron flooding gun can be used for charge neutralization. In this way, charging can be reduced to less than 0.1 eV. 2) Electrical equilibrium in the analysis volume should be obtained. Once the electrical equilibrium is obtained, the charge on the sample can be accurately traced and compensated using an internal or external standard. To use an internal standard, a specie is introduced into the sample matrix or substrate [58]. External standard materials are typically a vacuum deposited noble metal or carbon contamination on the sample surface [59]. Since sometimes the carbon reacts with the sample surface when the surface is chemically active, a noble metal may be the best as an external standard.

2.6.3 Auger electron spectroscopy (AES)

2.6.3.1 Auger process

The Auger effect is the de-excitation of an ionized atom by a non-radiative process. When a sufficiently energized electron impinges on an atom, an electron can be ejected from the orbitals. The resultant vacancy is subsequently filled by an electron from one of the outer shells. As a result of this transition the energy difference produces two effects; 1) release of X-ray photons which can be used in electron probe micro analysis and in X-ray fluorescence spectroscopy with the characteristic X-rays, and 2) ejection of another electron from the atom with an energy, E_A, through the so-called Auger transition which is concerned with at least two energy states and three electrons. E_A can be expressed as

$$E_A = E_1 - E_2 - E_3^*. \qquad \text{eq.(2.14)}$$

Here, E_1 and E_2 are the binding energies of the atom in the singly ionized state and E_3^* is that for the doubly ionized state. This process is schematically described in figure 2.3. X-ray fluorescence and Auger emmision are competing processes because they can not occur at the same initial core hole. For lower energy events leading to a photon or an electron with energy less than 2 keV the Auger process is dominant with more than 95% of ionizations resulting in the ejection of Auger electron [60]. The Auger electron loses energy during its motion through the solid due to inelastic collisions with bound electrons. Therefore, only Auger electrons ejected sufficiently close to the surface can escape from the surface. Then, they are detected by an electron spectrometer, producing the resultant peak spectra. Peak intensities, shapes, and positions in the Auger spectra are the main factors in analyzing the chemical composition and bonding states of the unknown materials.

The most pronounced Auger transitions observed in AES are given in figure 2.4 and these involve electrons of neighboring orbitals, e.g. KLL, LMM, MNN, NVV, MMM, and VVV families. The Auger energies for a wxy transition

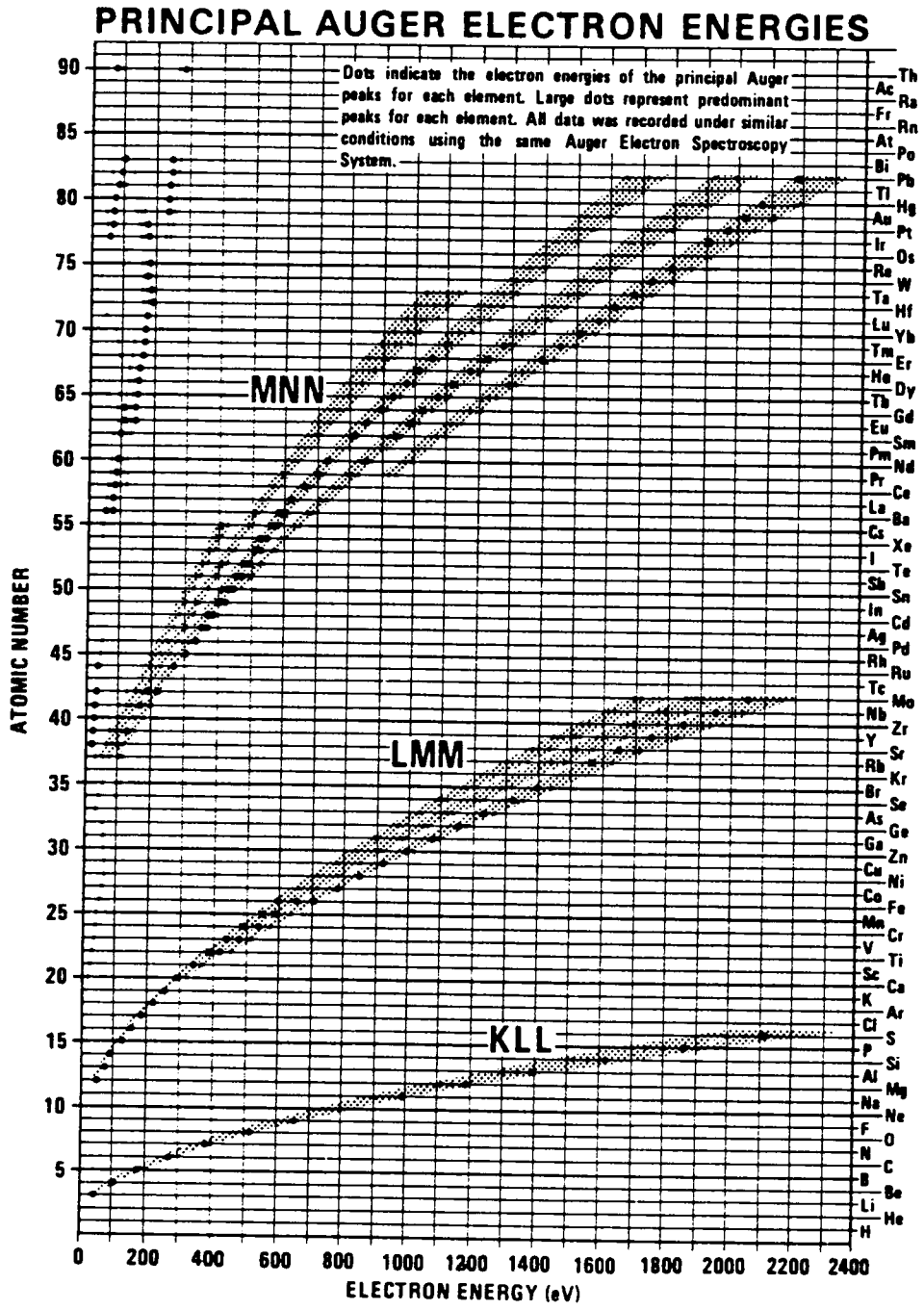

Figure 2.4 Most probable Auger transitions observed in AES

have been calculated with an empirical relation [61, 62],

$$Ewxy = Ew(Z) - 1/2\{Ex(Z) + Ex(Z+1)\} - 1/2\{Ey(Z) + Ey(Z+1)\} - \Phi, \quad \text{eq.(2.15)}$$

where Φ is the work function , Z is the atomic number, and Ei denotes the electron binding energy at the i^{th} level.. The energies calculated with eq.(2.15) are not very accurate. A physically correct expression which introduces the relaxation energy into the intermediate coupling scheme yields a very accurate KLL Auger energy [63].

$$Ezxy = Ez-Ex-Ey- F(xy:\alpha) + R^{in}_{\alpha} + R^{ex}_{\alpha} \quad \text{eq.(2.16)}$$

where F(xy:a) is the energy of interaction between the holes in x and y in the final state α, and the $R^{in}\alpha$ and $R^{ex}\alpha$ are internal and external relaxation energies, respectively. Eq.(2.16) can be used as a semi-empirical equation as experimentally determined binding energies, Ei, are incorporated in the equation together with values for the other terms. Since the calculations may involve a certain amount of error and, in many cases, the Auger peaks are differentiated to make the peaks more distinctive, a close agreement between calculated and observed Auger energies is not expected. Therefore, theoretical calculations can only identify the kind of Auger transitions for the observed Auger peaks. Standard samples and/or Auger handbooks are generally used in practical work.

2.6.3.2 Auger electron escape depth

The Auger electron escape depth, which is a function of the Auger electron kinetic energy, is generally determined empirically by depositing atomically uniform overlayers on a metallic substrate. The universal escape curve is shown in the figure 2.5 [64].

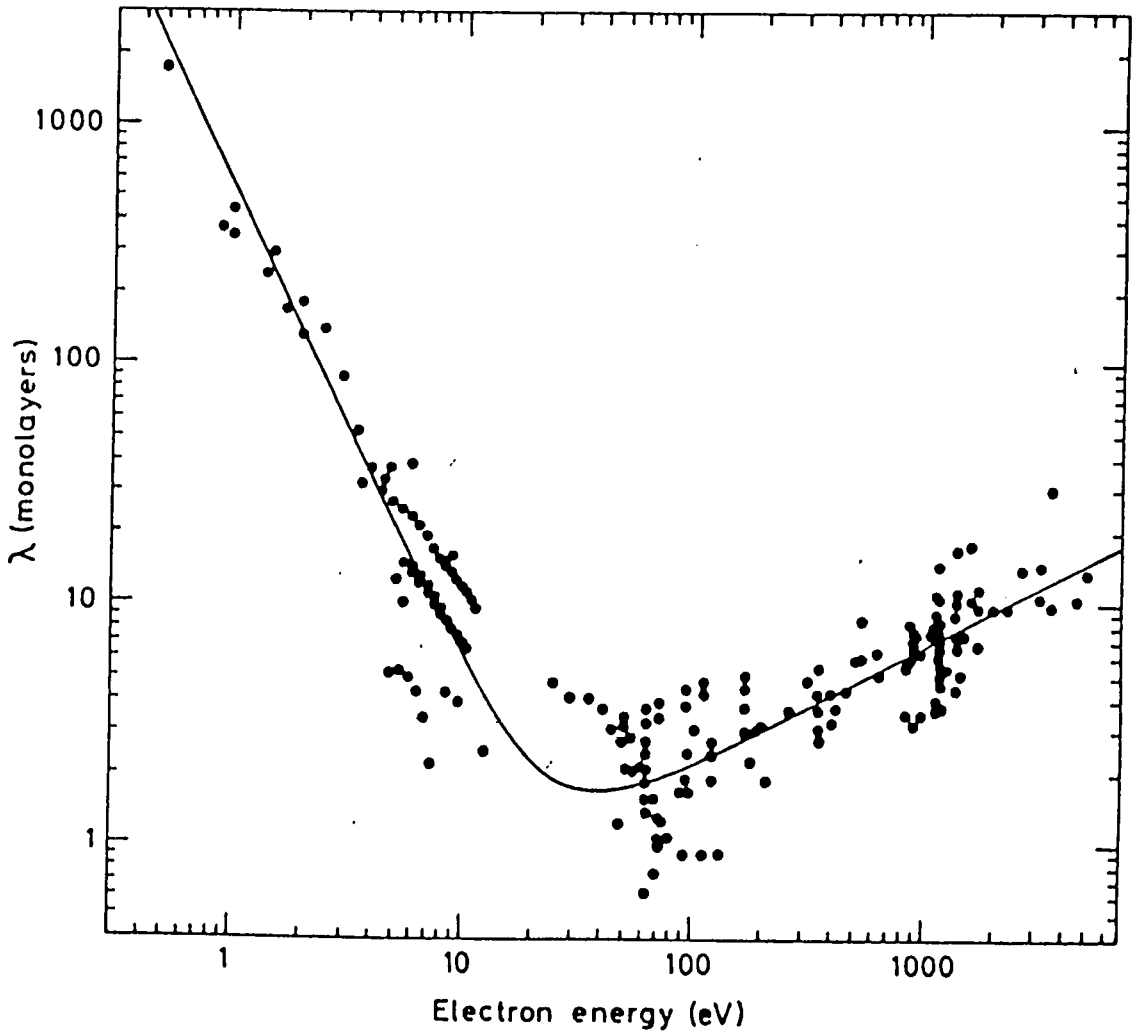

Figure 2.5 Universal curve for electron escape depth.

2.6.3.3 Chemical and charging shifts in AES

If strong chemical bonding of two or more atoms occurs, the energies of core level electrons can change by a few electron volts. In ionic bonding, for instance, electron levels of electronegative elements shift to lower binding energies, and the levels of electropositive elements shift to higher binding energies due to net charge transfer. Binding energy changes can influence the Auger electron kinetic energies, leading to the Auger peak shifts. Electropositive elements (usually metals) yield a reduction of the kinetic energy of Auger electrons coming from core level Auger transition. They combine with electronegative elements (usually non-metals). For instance, a linear energy shift of approx. 0.6 eV was found for the $L_3M_{23}M_{23}$ Auger peaks of vanadium oxides as a function of oxidation number [65]. On the other hand, energy shifts of valence electrons from the $L_3M_{23}V$ transition could not be related to the oxidation states. This means that Auger peak shifts involving the valence electrons reflect more the redistribution of the density of states in valence band than core level energy shift. Although the photoelectron energies are closely related to the Auger electron energies, the amount of the energy shifts is not the same because of the extra relaxation energies arising from the polarization of the electron clouds in the orbitals ejecting Auger electrons. Therefore, the relaxation energy is a dominant factor influencing large Auger peak shifts associated with core level transitions.

The Auger peaks can also be shifted due to artificial factors such as surface charging when analyzing insulating materials. In XPS, an accumulated charge is often positive and is reduced or eliminated by supplying low energy electrons [66, 67]. The sample charging is a function of the total electron yield, the sum of the secondary electron yield and the backscattering coefficient. A yield higher than unity produces negative sample charge, while a yield less than unity results in positive sample charge. In both cases, Auger peaks are distorted or shifted positive (negative charging) or negative (positive charging). The sample charge will cease when the numbers of incoming and outgoing electrons are

equal. In an extreme case the surface may be charged to the full incident beam potential. Several ways have been suggested to surmount the charging problem [66 - 68] :

1) reduce the primary beam current and/or the current density;
2) reduce the accelerating voltage of the primary electron beam;
3) tilt the sample stage to get a glancing incident electron beam;
4) heat the sample to several hundreds degrees C to reduce the band gap;
5) cover the sample with a conducting mask.
6) use the electron flooding gun when positively charged and supply low energy (500eV) positive charged ions when negatively charged.

However, methods 1) and 2) reduce the Auger peak resolution (low peak-to-noise ratio), spatial resolution can be reduced with 2) and 3), method 3) may work or not work depending on the surface roughness, chemical reaction can occur with 4), parts of relevant area can be hidden with 5), and the frozen period is temporary with 6). Therefore, the above methods still have problems in the analysis. In this work a new technique using the surface topography will be introduced in the experimental section.

2.6.3.4 .Quantitative aspects of AES

Since the sensitivity of Auger electrons from the outer surface layer is greater than that of electrons from the deeper levels, any quantitative analysis in AES should be carried out with some assumptions about the distribution of the elements in the surface region. Therefore, the accuracy of the results will depend on the assumption. Usually, it is assumed in AES and XPS analyses that the materials in the near surface are homogeneous. Eq.(2.13) shown in the section 2.6.2.2 is also used in AES. In AES, the intensity term stands for the peak-to-peak height of the differentiated spectrum.

2.6.3.5 Crystallographic effects on the Auger spectra

The intensity as well as the shape of the Auger spectra can be strongly influenced by the crystalline nature of the sample [70] as follows:

1) different atomic planes may yield different composition and density ,
2) anisotropic emission of the Auger electrons may occur,
3) channeling effects related to the electron diffraction may take place.

Effects 1) and 2) can be associated with the Auger intensity change. Effects 3) may produce intensity changes of the Auger peaks as well as features in the secondary electron spectrum arising from diffraction. In this case distinctive peaks which do not stand for the elemental peaks of the sample can appear on the spectra depending on the electron beam incident angle [71]. Usually, these conditions are not met on the surface which is unlikely to be well ordered. When the samples are heated in vacuum condition, the surface may become well ordered so that these features can be observed.

2.6.3.6 Auger fine structure

Auger fine structure can be seen in the spectra due to chemical effects or final state effects. Chemical effects in fine structure are associated with the chemical shift and can arise due to more than one chemical state at the surface [72, 73]. Final state effect taking part in splitting the Auger peak is associated with the two holes that are left in the atom at the end of the Auger process [74]. This is intrinsic to certain metals. In such metals the effective interaction energy between the two holes in the final state is much larger than the width of the valence band, and therefore the holes can not decay as rapidly as in the case that their interaction energy is lower.

2.6.3.7 Electron beam induced decomposition of ceramics

Ceramic materials can be decomposed during electron beam irradiation. An electron beam causes decomposition of ceramics leaving a metallic film on the surface. Under these conditions, results obtained during AES analysis contain artifacts. In general, the decomposition can be prevented by reducing the current density [75 -78]. However, this will limit the spatial resolution because reduction of the current density requires an increased analysis area for the same current. In order to increase the spatial resolution the beam current should be reduced as well, causing a reduced peak resolution. Therefore, optimized operating conditions to avoid decomposition and increase the Auger signal resolution during the data acquisition should be established before analysis.

In this work, it was studied: 1) the threshold electron fluence required to decompose Al_2O_3 for several electron fluxes and different rastering areas, 2) the kinetics of electron-beam-induced decomposition of alumina, 3) the effects of an adsorbed carbon layer and of pre-sputtering on the decomposition onset, and 4) back scattered electron effects on the Auger signal.

2.6.4 Secondary ion mass spectroscopy (SIMS)

An energetic ion impinging on a solid target is not only backscattered from surface atoms, but also it enters the target. Inside the target, the ion dissipates its energy to lattice atoms through both elastic and inelastic biparticle collisions. The phenomenon of sputtering takes place when the recoil atoms produced at or near the surface have the necessary energy and direction to escape the solid. The sputtered atoms depart the surface in a neutral, an excited, or an ionic state (either positive or negative). The positive or negative secondary ion yield $S^{\pm}$ for any specific element in the sample matrix is expressed as

$$S_i^{\pm} = \gamma_i^{\pm} C_i S, \qquad \text{eq.(2.17)}$$

where i stands for i element in the matrix, the term $\gamma_i^{\pm}$ is the ratio of secondary

ions (positive and negative) of element i to the sum of the neutral and charged particles of element i, C_i is the atomic concentration of i in the matrix, and S is the total sputter atom yield.

The mean kinetic energy of sputtered particles is typically of the order of 10 eV with the tails of the distribution extending to hundreds of electron volts [79]. The escape depth of the sputtered particles ranges from the surface to values greater than 20Å and is strongly dependent on the characteristics of the collision cascade (recoil atom angular and energy distributions) produced in the solid by the incident ion [80]. Most of the secondary ions are ejected from the first monolayer (<6Å).

2.6.5 Depth profiling

Depth profiling is the technique to analyze the elemental and chemical state distribution perpendicular to the surface of the sample. It can be obtained either by non-destructive or by destructive techniques.

Non-destructive methods for depth profiling are based on the electron escape depth. In this technique, the intensities and energies are used for the analysis. In AES and XPS, non-destructive profiling methods are based on either the energy or the emission angle dependence of the mean escape depth of the emitted electrons. Lower glancing angle generates more electrons, resulting in higher spectral intensities [81]. Monolayer resolution can be obtained by depth profiling. By comparison of the intensities between low and high electron kinetic energy peaks for the same element, the thickness of the segregation layer, an adsorbate layer, and sputtering rate can be determined [82, 83]. This technique uses the different electron escape depth for the different energy peaks.

In destructive depth profiling techniques, surface errosion by ion sputtering is used. This technique also allows monolayer depth resolution. In this method, the sample is bombarded by ions accelerated in an ion gun to an energy of typically 0.5 keV - 7 keV. A fraction of the energy is transferred to surface

atoms and causes them to leave the sample when the energy is sufficient to break the atomic bonding. Secondary Ion Mass Spectroscopy (SIMS) and Secondary Neutral Mass Spectroscopy (SNMS) techniques use the emitted particles as a result of sputtering for surface analysis, while electron spectroscopic techniques such as AES and XPS use the remaining sample surface for the analysis. Since sputtering rates at the edge and at the center of the sputter crater are different, the analysis area must be carefully selected in this method. In most cases, since the analysis area of AES is much smaller than the sputter crater and the spatial resolution of AES is much better than that of XPS, AES is often employed for depth profiling.

2.6.6 Calculation of transport of ions in matter (TRIM calculation)

As already mentioned in previous sections (2.3.2 and 2.4.1), ion bombardment produces various effects on the surface and subsurface of the materials. A Monte Carlo computer program simulating the above mentioned effects has been developed [84 - 86] and may render useful preliminary informations for either processing or characterization of the materials using ion bombardment.

TRIM was developed to determine ion ranges and damage distributions as well as angular and energy distribution of backscattered and transmitted ions. The program is primarily concerned with the quantitative evaluation of how the ions lose energy to the solid and the final distribution of these ions after they stop within the solid. The program written in FORTRAN language [85] was translated to BASIC for the use on a PC and allows the treatment of a solid made of several elements (up to 7 elements) and for layered structures (up to 3 layers). However, this program can only be applied to amorphous targets.

To determine the damage produced in the target materials, the atomic displacements should be calculated. The displacements can be defined as vacancies plus replacement collisions which reduce the number of vacancies. The vacancies can be estimated as the sum of interstitial atoms and atoms that leave the target .

For sputtering to occur, the energy of the ions impinging on the surface of the material must be above the surface binding energy. In general, the surface binding energy can be used as the heat of sublimation . The sputter yield is very sensitive to the surface binding energy and, for a real surface, the yield changes during bombardment due to surface roughness and stoichiometry changes of the compound. If the target is made of several elements, there is a separate sputtering yield for each element.

The program can calculate the above mentioned phenomena. However, the simulated results may not predict the actual damage produced and surface sputtering that takes place in the ion bombarded materials due to the restriction of the input data such as crystallographic informations (atomic packings and binding energies among dissimilar materials), actual ion's bombarding energy and fluence, etc..

2.6.7 AES analysis of metal/ceramic interfaces

Two methods have been used to study film-substrate interfaces with AES. One technique is to deposit the film in the analysis chamber and monitor the chemical changes by AES in situ as a function of film coverage. This commonly used technique has various disadvantages. For instance, the nature of the film can change as the film is built up monolayer by monolayer [87]. Therefore, the chemical shift due to interfacial reaction may combine with charging shifts. In the other method the deposited film is removed layer-by layer by sputter etching until the interface is revealed and the substrate is exposed [88]. The main problem of this de-constructive method is the possible ion-beam damage of the interface under study. Although the damaging problem can be mitigated by reducing the ion beam energy for sputter etching, the de-constructive method requires a careful control of the sputtering rate depending on the interface thickness. Therefore, several trial and error runs may be needed to detect elements at the interface region. However, this method can be used in analyzing a relatively thick interface.

In this work, it has been shown that a new method proposed here

eliminates or mitigates the problems described above.

2.7 Copper/SiO_2 couple

As introduced in section 2.1, copper is the material that can substitute for aluminum for better performance metallization level. However, copper can migrate into the silica under an electric field [89] causing an increased resistivity in the metal line and a dielectric loss of the oxide substrate, eventually, it will lead to the failure of the device. This will be a big restriction in introducing copper for the future material for multilevel metallization. It was found previously that adding a layer of titanium between the copper and the SiO_2 substrate can greatly reduce the copper drift and that a certain thickness ($\geq$ 5 nm) of the layer is required for the prevention of diffusion [90]. Also, Cu and Ag do not drift into the silicon oxide when the electric field is applied to the couple in vacuum (~ 10^{-6} torr.) [91].

The mechanism of migration is studied here using AES and SIMS without coating any anti-drift layer at the interface .

CHAPTER 3

EXPERIMENTS

The experimental sections describe the sample preparation (processing) and the testing and analysis (characterization). Sample preparation comprises laser and ion beam surface treatments, thin film deposition, and heat treatment. Chracterizations include pull adhesion testing and surface and interface analysis using surface sensitive analytical techniques such as XPS, AES, and SIMS.

3.1 Sample preparation

3.1.1 Sample materials

1) Al_2O_3 : The alumina (polycrystalline Al_2O_3) substrates were finished to a surface roughness of approx. 0.1 μm as measured with a Dektak profilometer and had a relatively uniform grain size of 2 μm, on the average . The nominal purity was 99.6% and the main impurities were SiO_2 and MgO. The alumina samples were tape-cast processed by the Coors Ceramic Company. Commercial sapphire (single crystalline Al_2O_3) samples of 99.6% purity with an optical finish slightly off the $\{2\bar{1}\bar{1}0\}$plane were supplied by Saphikon Company.

2) AlN : The AlN substrates were ≥ 99% pure. The surface roughness was ≤ 0.4 μm, as specified by the manufacturer (ANCeram GmbH & Co. KG of Germany). The average grain size was approx. 3 μm.

3) SiO_2 /Si: These substrates are used for the copper drift test. A highly doped n-type silicon wafer (thickness; approx. 1 mm) was thermally oxidized to form SiO_2 with a thickness of approx. 5500 Å, as measured with SIMS depth profiling and profilometry techniques.

4) Pure copper and gold were used for the thin film.

3.1.2 Surface modification of the substrates

Laser irradiation

Ceramic substrates, e.g., Al_2O_3, AlN, and SiO_2, were irradiated with a pulsed XeCl excimer laser (308nm wavelength and 41 ns pulse duration at FWHM) in oxidizing or reducing (Ar-4%H_2) atmospheres. Substrates were laser-irradiated at various energy densities 0.3, 0.5, 1, 1.5, 2, and 3 J/cm^2. Each area was irradiated with 10 sequential pulses unless otherwise specified. Laser energy densities were determined from output laser energy as measured by the energy calorimeter, divided by the irradiation areas. A set-up of the laser processing is schematically described in figure 3.1

Ion beam bombardment

Sapphire substrates were treated in three different ways: 1) annealed, 2) sputtered, and 3) annealed and pre-sputtered. Annealing was conducted at 1350°C for 3 days in air to appreciably reduce all possible organic surface contaminants and surface defects. The sputtering was carried out with Ar ions and neutrals of 7 keV beam energy, and 1 mA beam current .

3.1.3 Surface cleaning of AlN substrate

Surface cleaning effects of the substrate on film adhesion were investigated for AlN substrate. The cleaning procedures were as follows.

1) ultrasonic cleaning in water with detergent for 10 min.
2) ultrasonic cleaning in ethanol for 10 min.
3) washing with distilled water
4) drying with hot air
5) additional drying on hot plate at 150°C for 15 min.

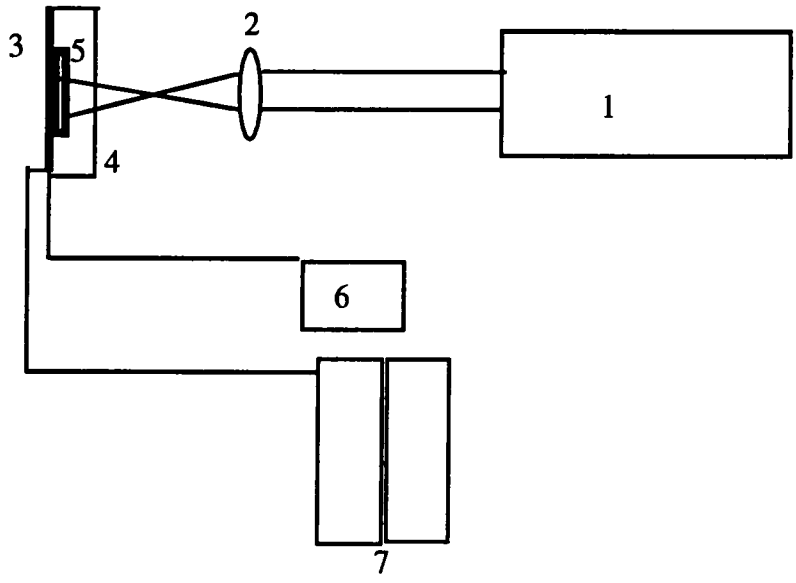

1. Laser source
2. Lenz
3.Sample stage
4.Gas chamber
5. Sample
6.Vacuum pump
7. Processing gas tanks
(oxygen or Ar-H)

Figure 3.1 A schematic of laser processing.

3.1.4 Thin film deposition

Copper and gold targets were bombarded with Ar neutrals and ions at 7 keV beam energy and 1 mA current. A Paulus and Reverchon type ion gun was used for sputter-etching [92]. The beam incident on the target is largely composed of neutral Ar because most of the ions transfer their energy to gas atoms. Particles from the target were deposited to a thickness of about 800Å on the substrates in a vacuum pressure of approximately 10^{-4} torr. The base pressure of the chamber was $2x10^{-6}$ torr. A schematic of the deposition process is shown in figure 3.2.

For the pull adhesion test of the gold film/substrate couples, about 200Å of copper film was deposited on the top of gold film, because the adhesion strength between the gold film and epoxy resin is very weak. Our experiment showed that the adhesion between copper and gold films is much stronger than that between copper and epoxy resin.

3.1.5 Annealing and curing of the film - substrate couples

Some of the sapphire substrates were annealed in air at 1350°C for 3 days to remove organic contaminants and defects. Heating and cooling were done for 8 hours each in order to eliminate the possibility of a thermal shock in the substrate which may lead to the fracture.

Metallic film/ceramic couples were annealed at 300°C and 500°C in a vacuum atmosphere ($5x10^{-6}$ torr) for 1h. For the adhesion pull-testing, an aluminum-pin coated with epoxy resin was positioned on the film surface of the test couples (figure 3.3) and cured in an argon atmosphere. Maximum strength of the copper/epoxy interface was obtained by curing the couples at 150°C for 1.5 h. The heating and cooling rates were designed to obtain the best adhesion and avoid residual stresses that could affect the gold/sapphire bonding. The heating-up time was 30 min and the cooling-down time was 2 hrs.

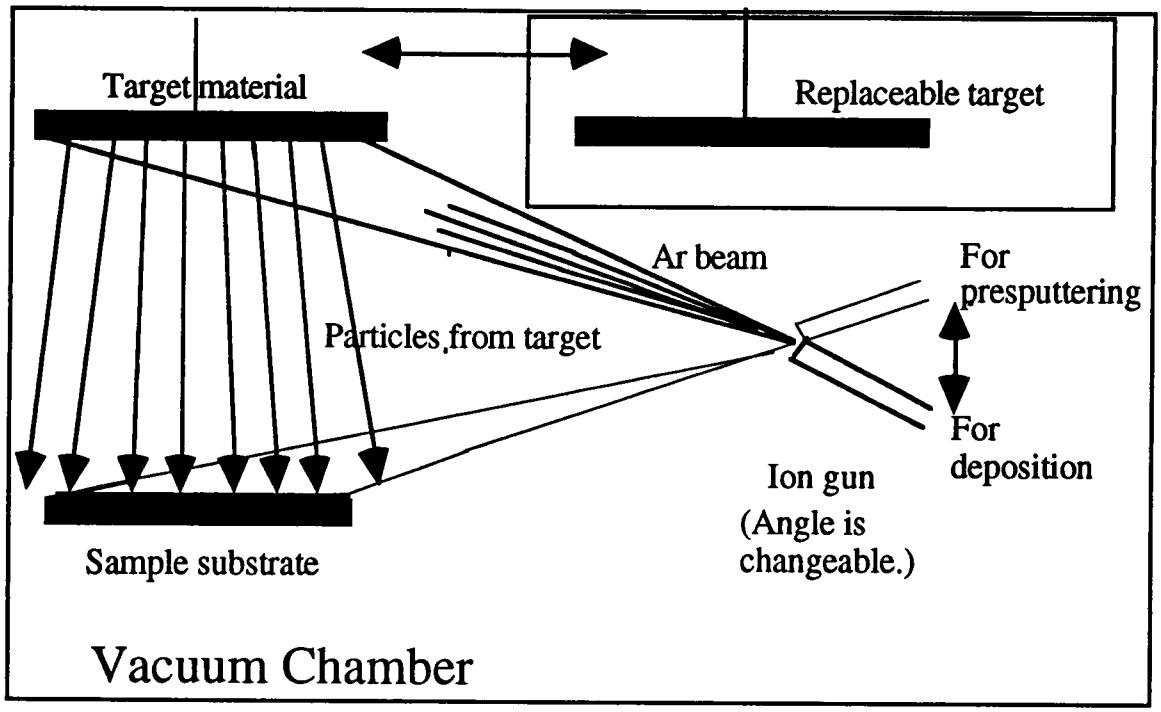

Figure 3.2. Schematic illustration of sputtering process.

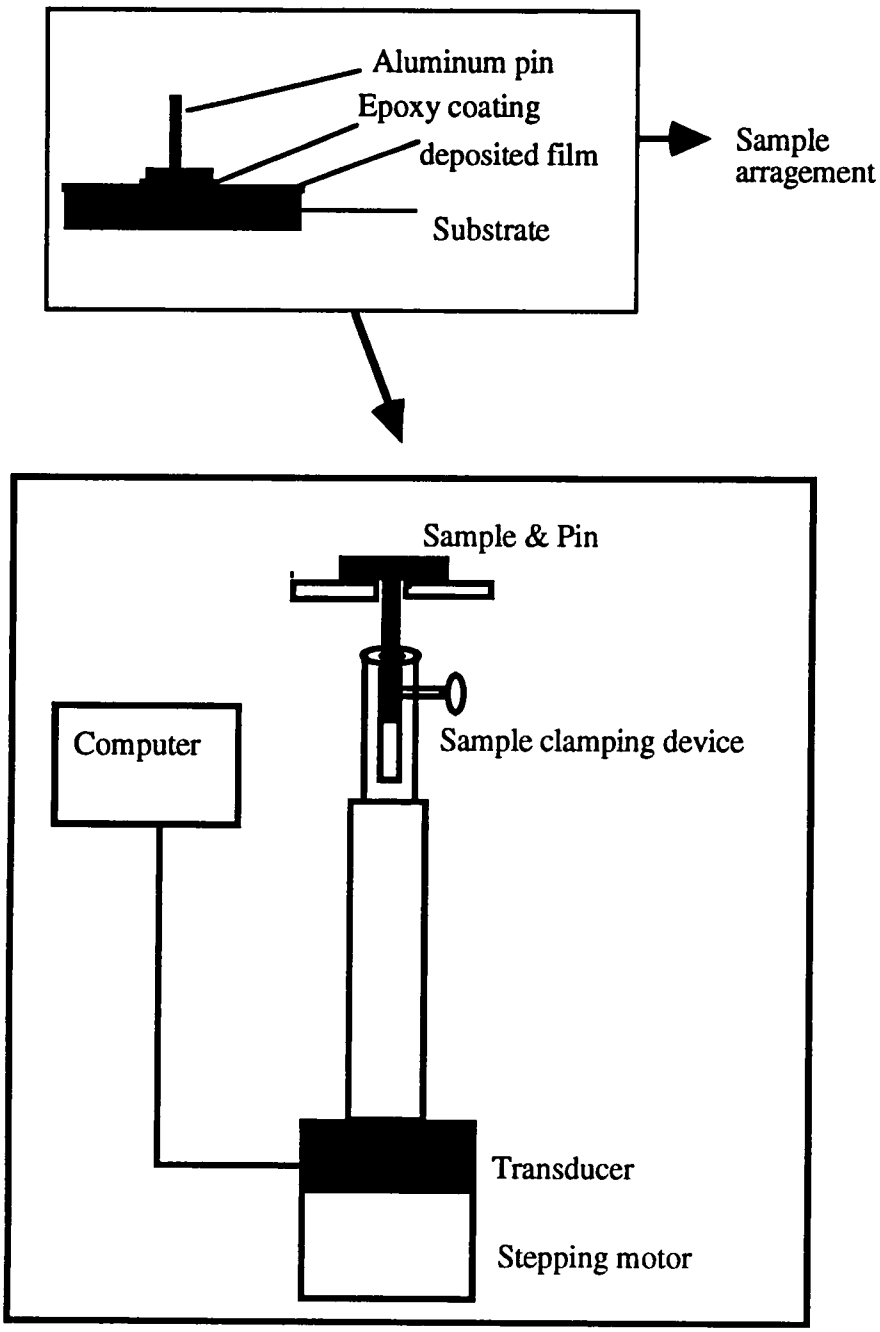

Figure 3.3 Schematic illustration of sample prepared and pull-testing device

3.1.6 Copper drift test into the SiO_2 layers developed on Si

Copper films of ~ 100 nm thickness were sputter-deposited on a SiO_2 layer ~550 nm in thickness thermally grown on a Si substrate. Two samples were prepared; 1) one was annealed at 300°C for 12 hrs under the presence of 1 MV/cm electric field and 2) the other was annealed with no electric field.

3.2 Testing and analysis

3.2.1 Adhesion pull-testing of the couples

Copper and gold films deposited onto laser irradiated Al_2O_3 and AlN substrates and gold film deposited onto ion bombarded sapphire substrates were pull-tested. An aluminum-pin coated with epoxy resin was glued to the metallic film to be tested. In the case of gold films, as already mentioned, an intermediate copper film was deposited to ensure good bonding of the metallic film to the epoxy resin. The interface between copper film and gold film was stronger than any of the other interfaces in the sample. Each adhesion strength value reported is the average of measurements done on 5 different specimens. The accounted error is the standard deviation of these five measurements.

After firmly clamping the epoxy coated aluminum pin attached on the film of the couple, the pin was pulled down at a speed of 3 μm/sec by means of a stepping motor. The signals from the load cell were transferred to and recorded by computer. The strength of the aluminum pin was 10 Ksi and the capacity of a load cell was 100 Ib. The strength of the glue that connects pin and copper film, ~ 70-75 MPa, is the test upper limit for the adhesion strength between the film and the substrate. Since the pulltester utilizes a very rigid frame, an accurate sample alignment was achieved and possible shear stresses at the interface during pulltesting could, thus, be avoided . A schematic cross section of the test set-up is shown in figure 3.3.

3.2.2 XPS analysis of the surface of the ceramic substrates

As-received, annealed (72 hrs at 1350°C), and laser-irradiated ceramic substrates were analyzed with XPS . A schematic cross section of the XPS equipment that was used in this work is shown in figure 3.4. The laser irradiation was performed in air and Ar-4%H2 atmosphere with laser energy densities of 0.4, 1, 3, and 5 J/cm^2. The samples were sputtered in order to perform chemical and damage analysis at different depths from the surface. A Perkin Elmer 5600 ESCA Spectrometer was used for XPS analysis. By setting the aperture for the analyzer lens, an analysis area of 400 μm diameter on the sample was selected . Survey scans were obtained for each sample using 1253.6 eV Mg Kα X-rays and an analyzer pass energy of 93.9 eV, over a binding energy range of 0 to 1100 eV. Measured peaks were corrected for detector sensitivity and photoionization cross-section differences and subsequently used to estimate the atomic concentration of the present elements. When necessary, intensity peak positions were corrected with a carbon peak as an internal reference. To detect the formation of metallic aluminum as a result of the irradiation assisted decomposition of the alumina, multiplex scans of the Al 2p core spectrum were obtained for alumina samples as- received and laser-irradiated at 5J/cm^2 in Ar-4%H_2.

3.2.3. Auger Electron Spectroscopy (AES) analysis

The interface of Cu/Al_2O_3, Au/Cu/Al_2O_3,, Cu/AlN, Au/AlN, and Cu/SiO_2 couples and the surface modification of the substrates were analyzed with a Scanning Auger Microprobe (SAM) Phi model 660 combined with ion sputtering gun at a pressure of ~ 5x10^{-10} torr. A schematic description of the AES system is given in the figure 3.5. An accelerating voltage of 3 kV and a beam current of 20 nA were used for the analyses. Unless otherwise mentioned, the Auger peaks are differentiated. Electron beam induced decomposition and sample charging that are general problems during AES analysis of the insulating materials were studied prior to the analyses .

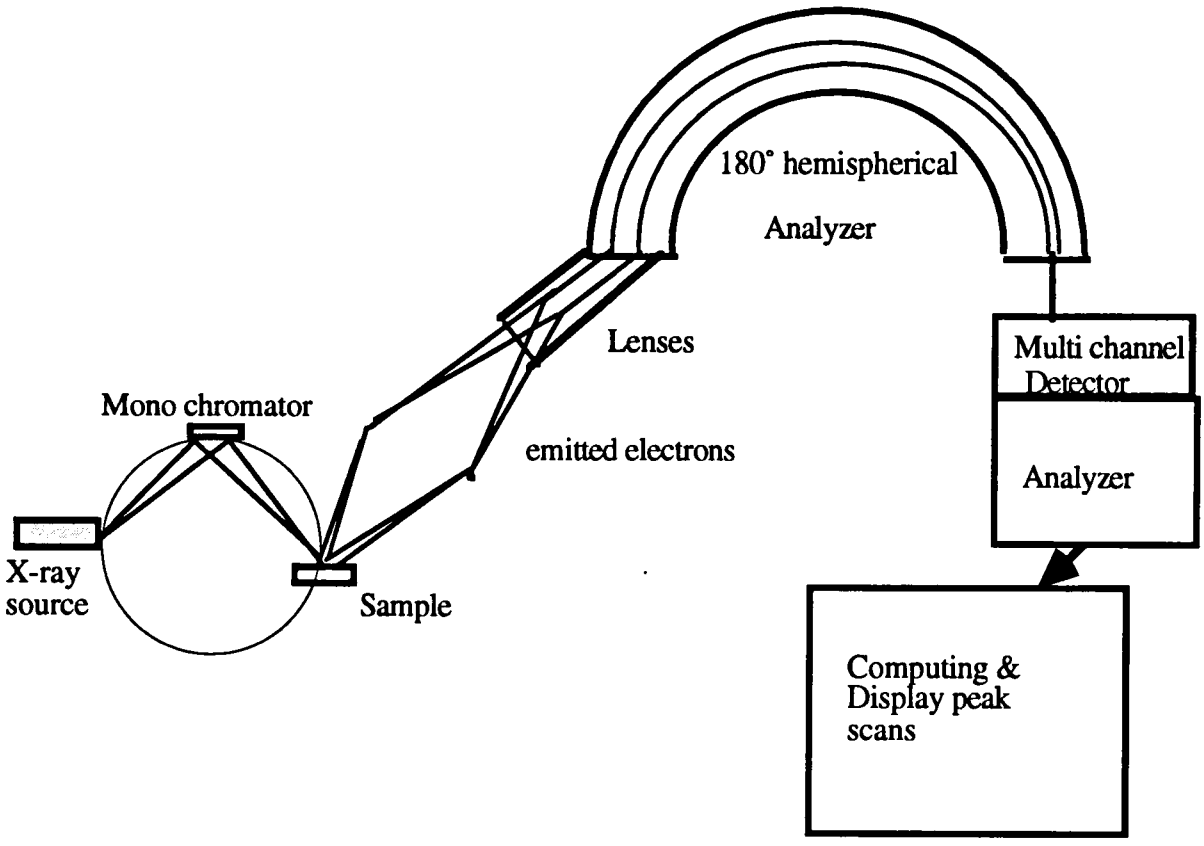

Figure 3.4. Illustration of X-ray Photoelectron Spectroscopy equipment.

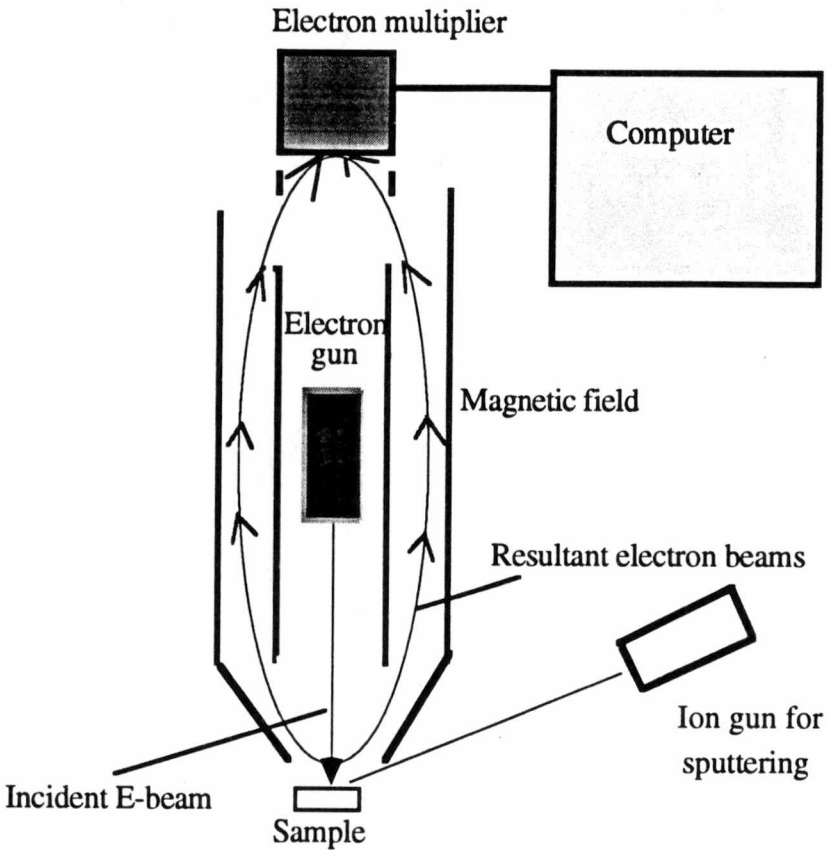

Figure 3.5 Schematic description of Auger electron spectroscopy apparatus.

3.2.3.1 Study of sample charging in AES

Sample charging of the insulating sample is due to secondary electron yield and backscattering coefficient. The sample charging could be reduced or eliminated by considering the mechanism of the secondary electron emissions. The methods are described here and will be discussed in the discussion chapter.

Sample charging of the flat sapphire substrate was eliminated by tilting the sample stage by 30° in order to increase the electron impingement area and to generate more secondary electrons in a volume lying closer to the surface.

For polycrystalline ceramic samples, the charging problem was more complicated due to the surface roughness. A very simple and effective way to eliminate the charging effect was found as follows;

1) The tilting angle was increased till a SEM image could be clearly obtained.
2) The magnification of the SEM image was raised to 5000X.
3) The analysis area was reduced as much as possible and the beam current was adjusted so that no decomposition occurred.
4) The top of the grain was selected as the analysis area.
5) The tilt angle was adjusted to a value that depended on the analysis areas.

3.2.3.2 Study of decomposition during AES

Commercial sapphire substrates of 99.6% nominal purity having an optical finish were used in this work. A Perkin Elmer model 660 Scanning Auger Microprobe (SAM) was employed to perform *in-situ* electron beam irradiation and characterization at a pressure of $3x10^{-9}$ torr. A 3 kV accelerating voltage was used in most of the experiments. For selected experiments, the accelerating voltage was varied from 2.2 to 10 kV. The sample stage was tilted by 30° in order to increase the electron impingement area and to get the secondary electrons

generated in a volume lying closer to the surface. This set-up reduces the electron accumulation in the insulating sample by generating more secondary electrons and also reduces, or even eliminates, charging effects. Tilting is also necessary to produce a geometry suitable for sputter-cleaning. The change in the analysis area due to stage tilting was accounted for in the electron flux calculations. The beam currents used in the decomposition study were 21.2, 53, 106, 159, and 224 nA as measured with a Faraday cup for analysis areas of 38, 76 and 140 μm^2, and 21.2 to 53 nA for circular areas of 0.4 mm-diameter (the beam cross sectional area at 3 kV). The difference between the sample current and the current measured with the Faraday cup was 6% at the potential of 3 kV, in the experimental set-up used here. The electron beam current in the sample was measured under a positive bias field of 90 V applied to the specimen. All secondary and backscattered electrons with energy less or equal to 90 eV were trapped in the sample and contributed to the sample electronic current. The difference between the sample current and the current in the Faraday cup is due to the fact that ~ 6 % of the secondary and backscattered electrons had a kinetic energy larger than 90 eV. All the measured fluxes were corrected for this difference.

The analyzing electron beam was used in a rastering mode. Therefore, the electron fluences determined in these experiments were averaged over the analysis area. The electron fluence ϕ was calculated as $\phi = J_a t_r$ where J_a is the average electron flux in electrons/cm^2.s, and t_r is the total rastering time in seconds. The average flux was calculated by dividing the electron current upon the total rastering area. The fluence can also be expressed as $\phi = J_i t_i$ where J_i is the instantaneous flux and t_i is the irradiation time for each given region. The instantaneous flux was calculated by dividing the electron current by the cross sectional area of the beam. The rastering periods were 0.1, 0.2, and 0.37 ms for the rastering areas of 38, 76, and 140 μm^2, respectively.

The analysis area was sputter-cleaned to eliminate surface contamination effects on the decomposition behavior. Sputter cleaning was done by 1 keV Ar^+ ion bombardment until the surface carbon was effectively removed. Non-sputtered, ethanol-cleaned, areas were also analyzed and the decomposition kinetics were compared with those of the sputtered area. The decomposition rates

of alumina were determined under various conditions by calculating the atomic concentrations from the peak-to-peak values of the differential Auger energy spectrum. The atomic concentrations, in turn, were determined using the corresponding atomic sensitivity factors found in the tabulated Perkin Elmer standard library.

The 54 eV Al peak from sapphire and the 68 eV Al peak from metallic aluminum were monitored for the decomposition onset studies. These peaks are very sensitive to the near surface condition of the substrate because the corresponding Auger electron escape depth is approximately 4 Å.[50] . The decomposition behavior was also examined through the evolution of the higher kinetic energy peaks of aluminum from sapphire (1388 eV) and from metallic aluminum (1396 eV) whose escape depth is approx. 20 Å [50] . Each peak multiplex cycle was an average of peak scans acquired for approximately 30 s. Generally, one half of the scanning time for a certain multiplex cycle where metallic aluminum peaks were initially detected was regarded as the decomposition onset time. Therefore, the accuracy of the decomposition onset time is about 15 seconds. However, for short decomposition times the relative error of the onset decomposition time determined in this way becomes large. For onset times under 200 s, the decomposition onset time was determined *during* data acquisition thus reducing the error, due to background fluctuations on the Auger spectra, to a few seconds.

3.2.3.3 AES Analysis of ion bombarded sapphire surface

The effects of ion beam bombardment on the sapphire substrate were investigated in situ with a Perkin Elmer model Phi 660 Scanning Auger Microprobe combined with an ion sputtering gun. The gun was manufactured by Perkin Elmer and is different from the gun used for pre-sputtering the substrates prior to gold deposition. The sapphire substrates were irradiated at a pressure of 10^{-9} Torr with 7 keV Ar^+ ions and a beam current of 130 nA, and with 3 keV Ar^+ ions and a beam current of 70 nA. The changes in the surface layers were investigated comparing the Al LVV spectrum before and after irradiation.

3.2.3.4 AES interface analysis

Two different analytical techniques have been considered as described in the following.

1. Au/presputtered sapphire couple: Since the interface thickness of this couple was very thin, a technique using Auger electron escape depth was devised to analyze the interface.

Gold films deposited on as-received substrates (weakly-bonded) and on annealed and ion bombarded substrates (strongly-bonded) were analyzed with AES. Approx. 100Å thickness of gold film was in situ deposited on sapphire substrates presputtered with 7 keV Ar^+ ion energy. AES analysis showed that the gold film completely covered the sapphire substrate without forming any island on the substrate when no annealing of the couple was performed. Sputter-etching of the film in the AES vacuum chamber (approx. 10^{-9} torr) was performed at an angle of 53° with respect to the specimen normal using the ion gun. An area of 200 μm x 200 μm was bombarded with a 0.5 keV ion beam until a portion of the substrate in the selected area became exposed forming a crater-like region surrounded by gold film. This process was conducted by detecting Al LVV Auger signals with AES. The damage produced by sputtering was estimated with TRIM calculation.

A schematic drawing of the wedge produced by sputtering is shown in figure 3.6. The edge of the sputter-produced crater can be observed by secondary electron imaging and the analysis position can be approximately determined assuming that the slope of the crater edge is linear. The slope generated by this sputtering gun is very shallow: the film thickness increases by 0.5 nm when the electron beam is displaced 5 mm in the radial direction away from the film denuded area (figure 3.6 a). As described schematically in figure 3.6 b, different analysis positions on the edge of a sputter-produced crater can provide different elemental and/or chemical information because the Auger electron escape depths from different Auger transitions are different. Three main different positions relative to the crater

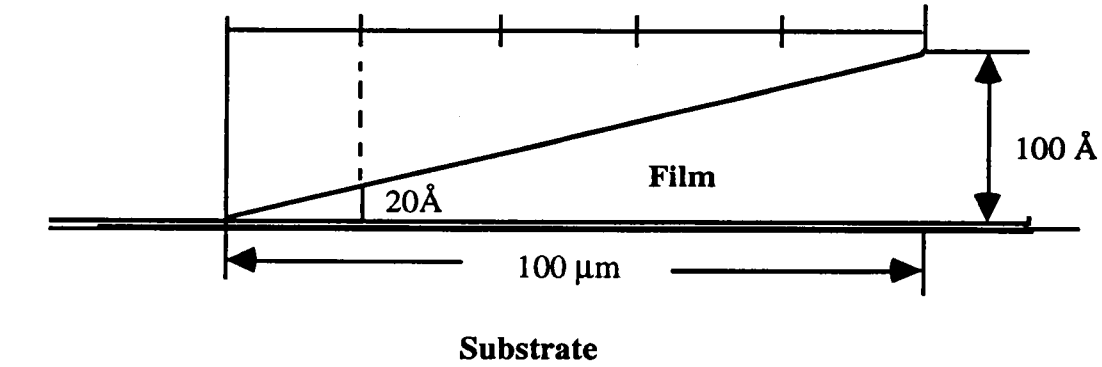

(a)

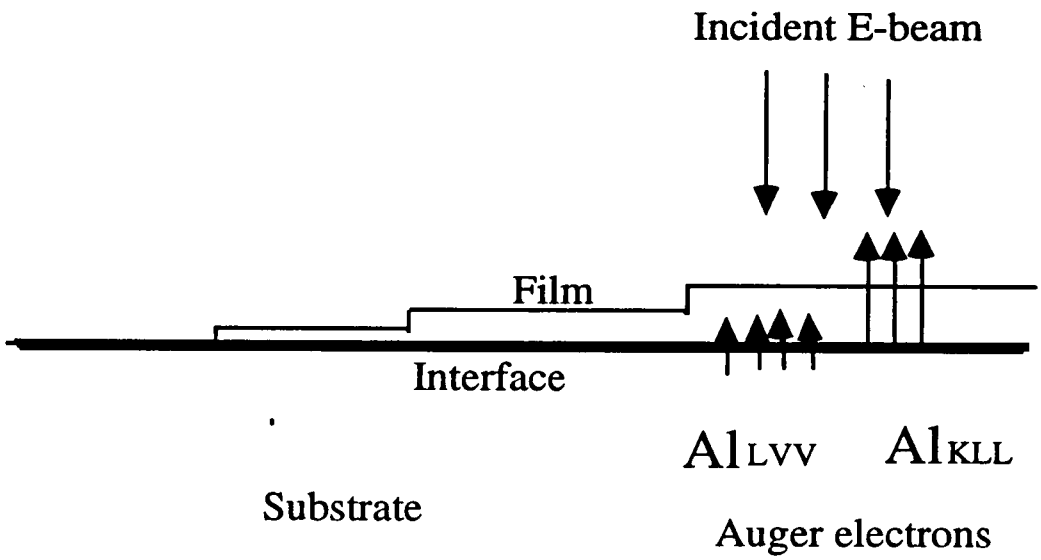

(b)

Figure 3.6. a) Schematic of the wedge produced in the gold film by sputter-etching in the AES chamber. b) Schematic of the relation between the Auger electron escape depth and the film thickness. Since the wedge length is too long as compared to the film thickness, atomic layers on the wedge should be ledge shaped.

edge were selected to study the gold, oxygen, and aluminum peaks at the interface. Low kinetic energy Au NVV (71 eV), high kinetic energy Au NVV (249 eV), oxygen KLL (506 eV), and aluminum KLL (1388 eV) Auger spectra were acquired for analysis. An accelerating voltage of 3kV was used for the analysis. This method can eliminate the artificial peak shift due to the charging and decomposition, because the first monolayer at least is a conductive film. In this method the beam current can also be increased to get higher peak signal resolution without raising a charging problem.

2. Metallic films / alumina and aluminum nitride couples: In these couples, there are two problems in interface analysis due to the surface roughness; one is sample charging, the other is non-uniform interfacial reaction due to non-uniform melting and decomposition behaviors during laser irradiation. Therefore, the analysis area should be the top part of a grain. Since most of these couples are annealed at 300°C or 500°C, the interface thickness may be relatively thick. The following method has been devised and used in this case;

1) tilting the sample stage to approx. 60°

2) enlarging SEM image and selecting the analysis area in one grain

3) using an ion beam energy of 500 eV and an ion current of 2 nA minimize the damage that may be produced during sputtering (TRIM calculations were also conducted) .

4) removing the metallic film layer-by-layer with an Ar^+ gun. The Auger peaks were scanned after each sputtering cycle. The sputtering cycle lasted 6s and the sputtering area was 35μm x 35μm; in the vicinity of the interface a thickness of only 1 - 2Å was removed per cycle. The sputtering rate was measured using the number of sputtering cycles and the film thickness.

5) using an accelerating voltage of 3kV and electron beam current of 20 nA for the analysis. These potential and current levels eliminate the decomposition of alumina and aluminum nitride and reduce sample charging effects.

3.2.3.5 Auger mapping

Auger mapping can provide information about the distribution of an element in a matrix material. The procedure for mapping is as follows;

1) Choose an energy peak for a specific element
2) Set the background to get the integrated intensity properly
3) Select the analysis area and set the data acquisition time.

Metallic aluminum distribution in laser-irradiated AlN was investigated along with other elements and compared with cross sectional TEM results.

3.3 SIMS study on copper drifted into SiO_2 and Si

The copper concentration in silica was measured with SIMS techniques since the concentration was expected to be very low. To evaluate the motion of copper and other species in the oxides, electrical measurements can also be used and they are more sensitive than SIMS. However, they can not distinguish copper from other positive ions such as sodium. SIMS was thus used to measure the copper concentration. Since the positively charged Ar ions often produce sample charging during SIMS analysis, a simpler way to surmount this problem was devised on the basis of the conventional negative ion bombardment technique.

3.4 High Resolution Transmission Electron Microscopy (HRTEM), conventional TEM (c-TEM), and Scanning Electron Microscopy (SEM) of the surface and interface

The interface morphology and thickness and phase distributions were directly observed with HRTEM and/or c-TEM. Parts of this work was correlated with the results from the AES analysis.

SEM was employed to observe the surface topographic change after laser

irradiation on the ceramic substrate. Depending on how the secondary electron yield is controlled, the surface coating with conductive film such as gold or carbon may or may not required. Without conductive film coated on the ceramic surface, SEM image was successfully obtained. A detail will be presented in the results section. The experimental set-up is aimed at controlling the secondary electron yield and minimizing the electron accumulation on the surface.

3.5 Validation of the pull adhesion test

Metallic films deposited onto the ceramic substrates can form the island morphology due to different surface energies between the deposited film and the substrate. It can occur with or without annealing depending on the deposited film thickness. The wetting angle formed by island formation of a thin film can reflect the adhesion between a film and a substrate as explained in section 2.5.2. If this happened, however, pull adhesion testing may not be validated because epoxy pin may adhere to not only film but also substrate. An experiment was conducted to verify if 80 nm film thickness is quite safe in pull testing to investigate the adhesion that takes place only at the film/substrate interface. For this work, copper films with the thickness of 10 nm and 50 nm were deposited onto the AlN substrate and AES technique was used to examine the surface film coverage. 3 kV accelerating voltage and 50 nA electron beam current were used for the analysis and analysis area was 500μm x 500μm.

CHAPTER 4

RESULTS

Experimental results presented in this chapter include i) pull adhesion testing of metallic films/ceramics couples, ii) the formation of metallic islands during annealing, iii) in situ decomposition study of Al_2O_3, iv) sample charging of the ceramic substrate during AES analysis, v) XPS and AES characterization of surface modified ceramics prior to the film deposition, vi) SEM and TEM studies on surface topographical changes after laser irradiation of the ceramic substrates, vii) interface analysis of the strongly and weakly bonded metal/ceramic couples with AES , and viii) SIMS and AES analysis of Cu/SiO_2 couple.

4.1 Pull adhesion testing

Pull adhesion testing conducted in this work is for metallic film/ AlN couples and the results will be presented in this section.

The results of pull adhesion testing on metallic film/Al_2O_3 couples previously conducted by Dr. Desilva and Mr. Kumar during their Ph. D and MS dissertation works will be briefly described in this section.

4.1.1 Cu film/ AlN substrate

Pull adhesion tests of Cu/AlN couples laser irradiated in air and Ar-4%H_2 atmospheres were conducted and the adhesion strengths are plotted as a function of laser energy density in figures 4.1 and 4.2. Here, we can notice that an increased laser irradiation results in the reduction of adhesion strength and higher temperature post-deposition annealing is required to enhance the adhesion between the film and laser-irradiated substrate. Obviously, this is a quite different

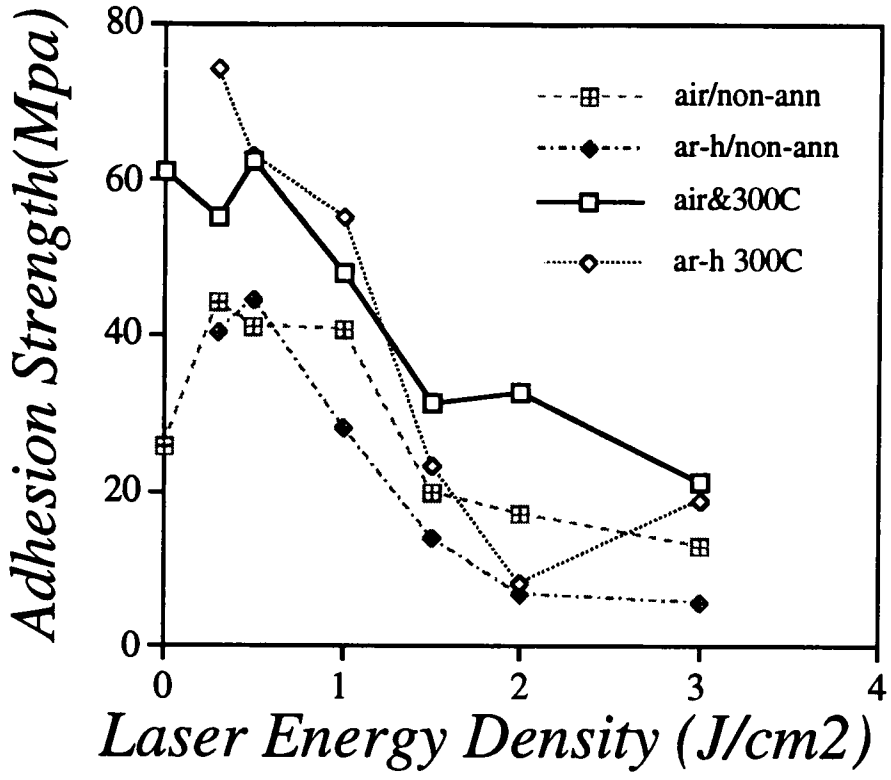

Figure 4.1. Adhesion strength of the copper films deposited onto AlN substrates laser-irradiated in air and Ar-4%H2 atmospheres as a function of laser energy density. Annealing was done at 300°C for 1 hr. (The zero laser energy density stands for as-received condition.)

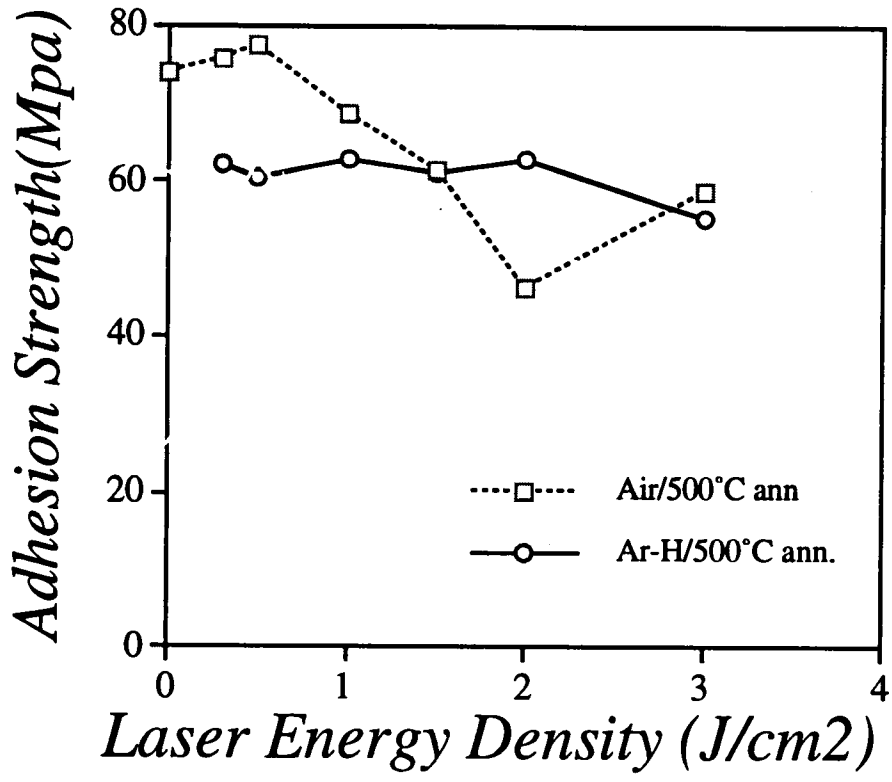

Figure 4.2. Adhesion strength of the copper film deposited onto AlN substrates laser-irradiated in air and Ar-4%H2 as a function of laser energy density. Couples were annealed at 500°C for 1 hr.

trend to the result obtained from the adhesion test of the metallic films/Al_2O_3 couples [93, 94] . The result can be described as follows:

1) The adhesion strength of Cu/as-received AlN couple is weak without annealing (~25 Mpa) (figure 4.1).

2) Laser irradiation with low energy densities ($\leq 1 J/cm^2$) in both air and Ar-4%H_2 increases the adhesion strength to ~40 Mpa. As the laser energy density increases, the adhesion strength decreases and becomes even lower than the strength of the couple with non-irradiated substrate. The couple irradiated in air shows higher adhesion strength than the couple irradiated in Ar-4%H_2. The difference of the adhesion strength between the couples irradiated in air and Ar-4%H_2 becomes larger as increasing the laser energy density (figure 4.1).

3) When the couples are annealed at 300°C, the couples laser-irradiated with low energy density ($\leq 1 J/cm^2$) show the maximum strength, but 300°C annealing enhances the adhesion of the couples laser-irradiated with $\geq 1 J/cm^2$ in both oxygen and Ar-4%H_2 atmosphere to only about 1.5 times. This is still below the maximum strength. The couples irradiated in air show slightly higher adhesion strength than the couples irradiated in Ar-4%H_2 (figure 4.1).

4) With 500 °C annealing, all the specimens laser irradiated with $\geq 1 J/cm^2$ energy density in both oxygen and Ar-4%H_2 atmosphere also show the maximum adhesion strength (figure 4.2).

4.1.2 Au film/AlN substrate

Figures 4.3 and 4.4 are plots of the adhesion strength of the gold film deposited onto AlN substrate as a function of laser energy densities. The pull testing data of the couples irradiated in air and Ar-4%H_2 are incorporated in the same plot. It is notable that the overall adhesion strength decreases after 300°C annealing and increases after 500°C annealing. Figures 4.3 and 4.4 can be

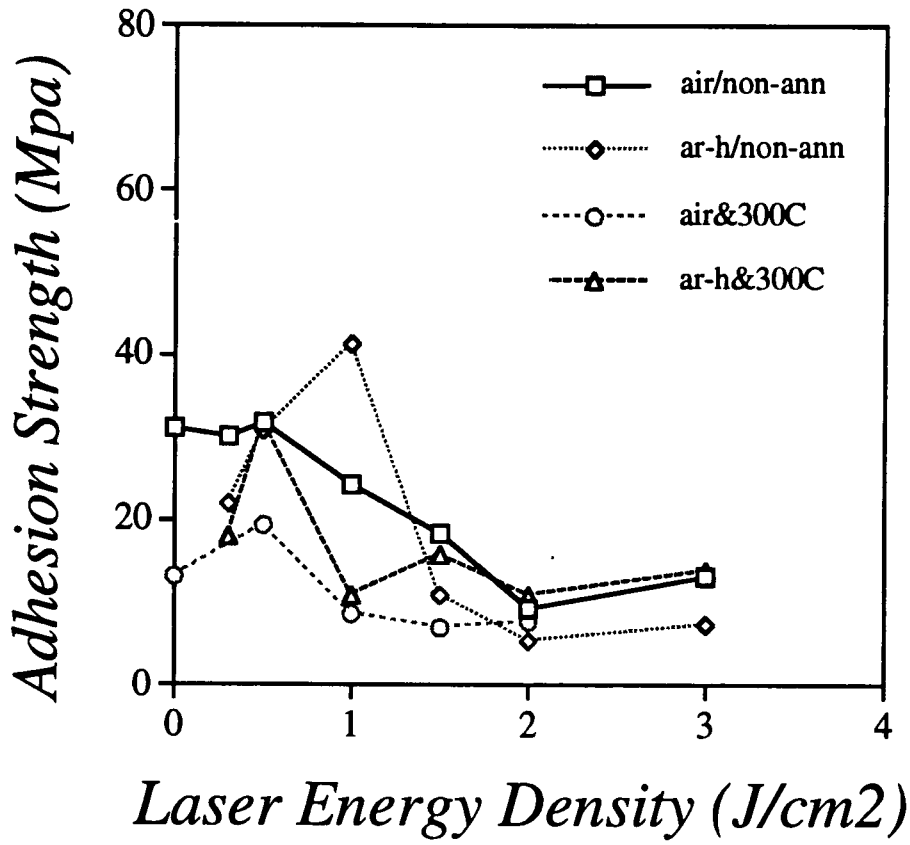

Figure 4.3. Adhesion strength of the Au film/AlN substrate couples as a function of laser energy density. Substrates are laser irradiated in both air and Ar/H atmosphere. Laser irradiation tends to reduce the adhesion strength, 300°C annealing does not improve the adhesion.

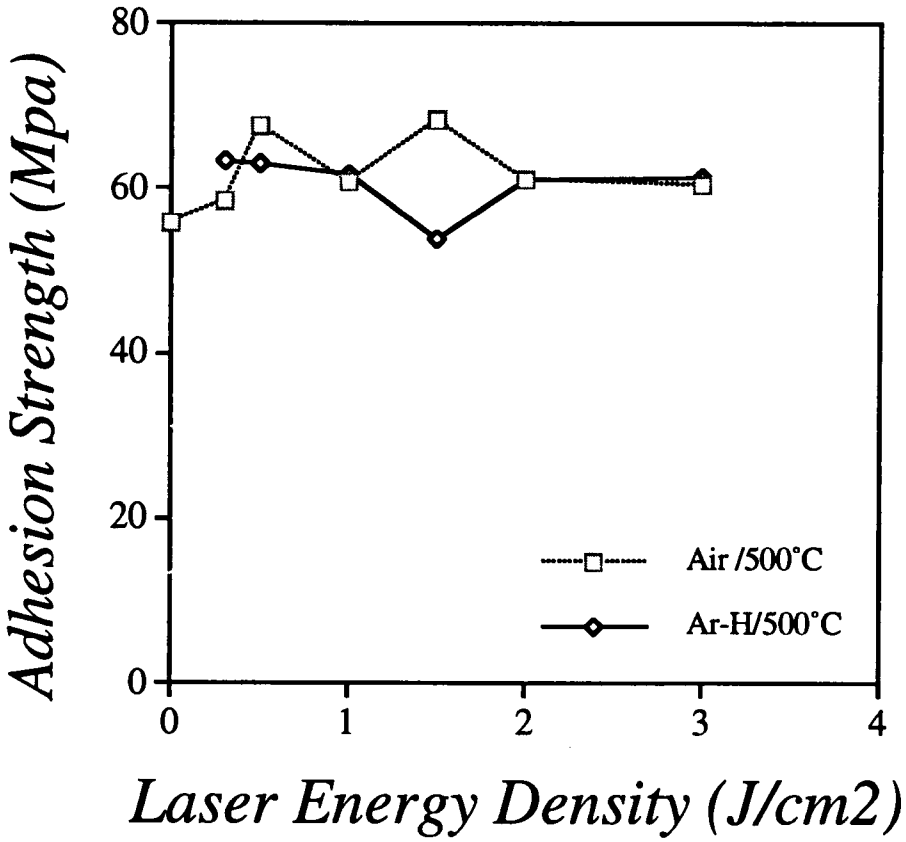

Figure 4.4. Adhesion strength of the Au/AlN as a function of laser energy density. Laser irradiation was done in air and Ar/H atmospheres and the couples were annealed at 500°C for 1 hr. The adhesion strength increased to the maximum measurable in this work.

analyzed as follows:

1) Similarly to the Cu/AlN couple, laser irradiation with more than $1J/cm^2$ energy density reduces the adhesion strength when the substrates are irradiated in both air and Ar-4%H_2 (figure 4.3). For the energy density less than $1J/cm^2$, laser irradiation in air does not show any difference in the adhesion, while the adhesion of the couples irradiated in Ar-4%H_2 increased from ~20 Mpa at 0.3 J/cm^2 to ~40 Mpa at $1J/cm^2$ (figure 4.3).

2) 300°C annealing decreases the adhesion strength of all the couples with the substrates irradiated in air and the couples irradiated with $\leq 1J/cm^2$ in Ar-4%H_2 and slightly increases the adhesion of the couples irradiated with $\geq$ 1J/cm2 in Ar-4%H_2(figure 4.3). 500°C annealing increases the adhesion strength to the maximum for the couples irradiated in both air and Ar-4%H_2(figure 4.4).

3) As a result of the pull adhesion testing, the couples with as-received substrates are broken at the interface between the film and substrate regardless of the annealing temperature, but the couples with laser irradiated substrates are broken at the epoxy glue after 500°C annealing (figure 4.4).

4.1.3 Cu film/Al_2O_3 substrate couple

The pull adhesion testing for these couples was previously conducted by Dr. DeSilva during his research for Ph.D thesis [93]. Adhesion testing of the couples was conducted for the substrates irradiated in air and Ar-4%H_2 atmosphere, respectively. Couples with the substrates irradiated in air were annealed at 300°C for 1 hr, because the couples showed very strong bonding with 300°C annealing. On the other hand, the couples irradiated in Ar-4%H_2 atmosphere were annealed at 500°C since the adhesion strength of these couples after annealing at 300°C was very weak. The adhesion testing results are summarized as follows:

1) The laser irradiation in air doubles the adhesion strength without annealing the couples and subsequent annealing of the as-deposited couples increases the adhesion strength further to the maximum strength (epoxy strength) measurable in this test.

2) The laser irradiation in Ar-4%H_2 does not increase the adhesion strength with low temperature annealing (≤300°C), but as increasing the annealing temperature above 300°C the adhesion strength increases and reaches to the maximum strength at 500°C annealing.

Three differently prepared samples, which have shown strong and weak bonding , i.e., a couple irradiated with 1 J/cm^2 energy density in air and annealed at 300°C, a couple irradiated with 1 J/cm^2 energy density in Ar-4%H_2 and annealed at 300°C, and a couple irradiated with 1 J/cm^2 energy density in Ar-4%H_2 and annealed at 500°C, were AES-analyzed to investigate the adhesion mechanisms. The results are presented in the section 4.5.1.

4.1.4 Au film/Al2O3 substrate couple

The adhesion pull testing for this couple was done by Mr. Kumar for his MS thesis [94] . The results he obtained are as follows:

1) The adhesion of gold film deposited onto the as-received alumina is very weak (~ 0.1 Mpa) even after annealing and laser irradiation of the substrate increases the adhesion strength,

2) Laser irradiation of the substrate in Ar-4%H_2 produces some increase in the adhesion strength (~ 1.2 Mpa), and post-deposition annealing increases the adhesion strength slightly more (about 3 Mpa),

3) The substrate laser-irradiated in air produced very strong bonding (~30 Mpa) as shown in figure 4.2b and the irradiation in pure oxygen produced the

maximum strength since the failure of the samples during pull test occurred in epoxy .

His results also showed that the maximum adhesions were obtained when the substrates were irradiated with 1 to 1.5 J/cm^2.

For the analysis of the interface, two samples shown strong and weak bonding were selected. Those are the couples laser-irradiated in oxygen and Ar-4%H_2 with 1 J/cm^2 energy density and the results will be presented in the section 4.5.2.

4.1.5 Gold film/pre-sputtered sapphire

Pull adhesion testing results of gold film/sapphire couples are shown in table 4.1.

The adhesion strength of gold films deposited on as-received sapphire is very weak (4.7 Mpa), but inceases ~ 6 times (31.7 Mpa) when the substrate is annealed at 1350 °C and 10 times (41.9 Mpa) when the substrate is pre-sputtered. The adhesion strength of gold film sputter-deposited onto annealed and pre-sputtered sapphire is over 15 times (70.4 Mpa) higher than that of the film deposited onto as-received sapphire. Except for the gold film deposited on annealed and presputtered sapphire, all the other couples were broken at the interface.

The adhesion strength of the gold film to the sapphire substrate annealed and ion-bombarded probably increases more than the value reported in the table because failure took place in the glue during pull testing. In this table the interface means the film/substrate interface.

The ion bombarding effects on the sapphire substrate and the interface of the couple shown strong adhesion were studied with AES techniques. These studies will be presented in the later sections.

Table 4.1

Pull testing results for various conditions of the gold film-sapphire substrate couples.

Heat treatment of the substrate	Surface treatment of the substrate	Adhesion strength (Mpa)		Remarks
as-received	non-sputtering	4.7	±4.7	broken in interface
as-received	pre-sputtered	41.9	±15.6	broken in interface
Annealed(1350°C for 1h)	non-sputtering	31.7	±13.9	broken in the interface
Annealed(1350°C for 1h)	pre-sputtered	70.4	±10.5	broken in the epoxy

4.2 The formation of metallic islands during annealing

Figure 4.5a shows AES survey scanning of the surface of copper film deposited to 50 nm thickness on AlN substrate after annealing at 500°C. As can be expected, the surface is heavily contaminated with carbon KLL. Oxygen KLL and copper LMM peaks are also detected. However, there are no Auger peaks in the low Auger kinetic energy range and the resolution of the peaks other than the carbon peak is very poor. The Auger electron escape depth in this energy range is only one or two monolayers. This means that the thickness of carbon contamination may be more than one or two monolayers.

Subsequently, the surface in the same analysis area was sputtered with Ar^+ ion of 0.5 keV energy and 1 nA current under the pressure of $5x10^{-9}$ torr and the sputtering was done till the carbon signal disappears. An AES survey scan of the sputtered surface is shown in figure 4.5b. Here, the carbon peak is reduced considerably, and, thus other peaks became more distinctive. The low energy region (less than 100 eV) in the peak scan is expanded and shown in figure 4.5c. One noticeable detail in this spectra is the appearance of the distinctive copper MVV Auger peak without superimposing any Al LVV peaks in the energy range less than 100 eV (figure 4.5c). It seems that the substrate is not exposed since at least one or two monolayers are covered with the copper film. Al KLL peaks that should appear in the range of 1300 to 1400 eV are not seen in the survey scan (figure 4.5b). Electron escape depth in this energy range is ~ 2 nm (4 - 5 monolayers). The full coverage of the copper film ensures that only the metal-ceramic interface is being tested. There is no contact between the ceramic substrate and the glue from the pulling stud.

Figure 4.6 is an AES survey scan of the film deposited to 10 nm thickness on the AlN substrate after annealing at 500°C. The surface was slightly sputtered, but still a considerable amount of surface contaminants such as S and C exists. In figure 4.5a only carbon exists on the surface as a contaminant. The fact that nitrogen and sulfur are detected on the surface of this couple is noticeable. These elements may be from the substrate: Sulfur may be a surface contaminant too in substrate and nitrogen should be from the AlN substrate. The strong oxygen

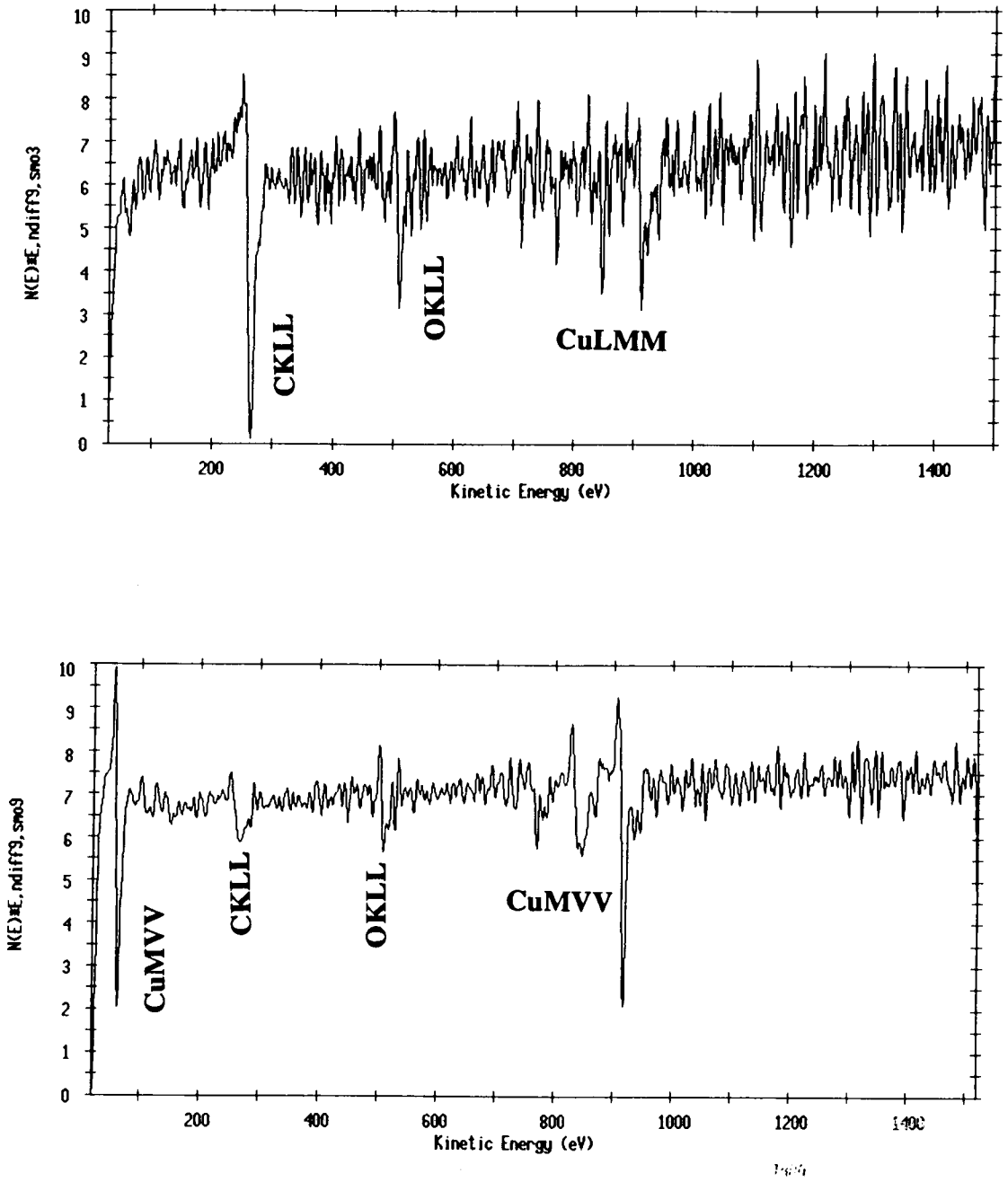

Figure 4.5. (a) A differentiated AES survey scan of the surface of the deposited copper film to 50 nm thickness on AlN substrate after annealing at 500°C. The surface is heavily contaminated with carbonaceous materials. (b) An AES survey scan of the sputtered surface. Here, peak to peak height of differentiated carbon auger peak reduced considerably, and, thus other peaks became more distinctive.

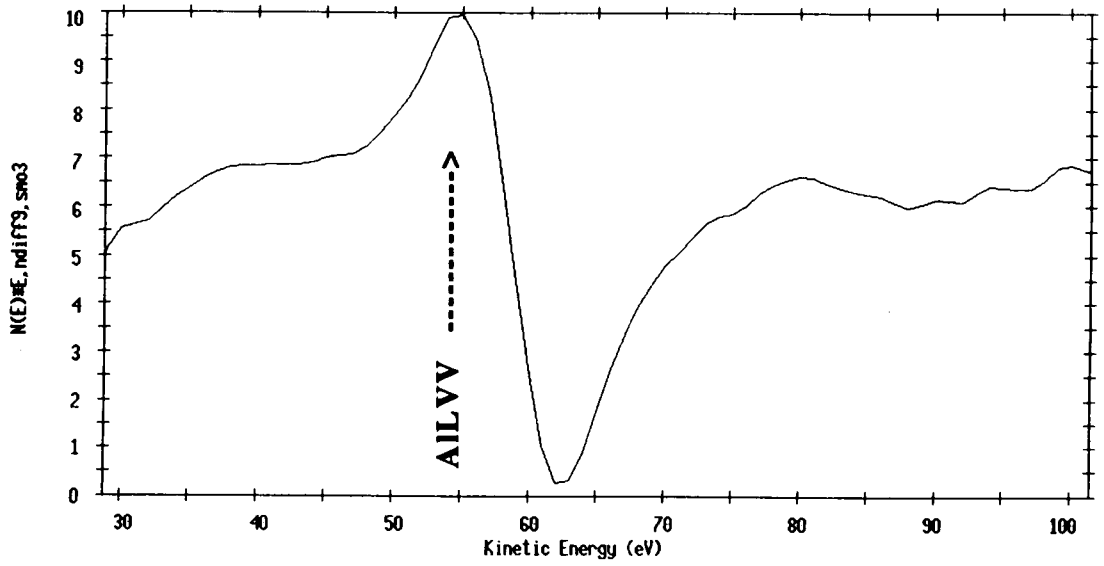

Figure 4.5 Continued. (c) Low energy region (less than 100 eV) in the peak scan is expanded and shown in figure 4.5c. One noticeable thing in this spectra is the appearance of the distinctive copper MVV Auger peak without superimposing any Al LVV peaks in the energy range less than 100 eV (figure 4.5c).

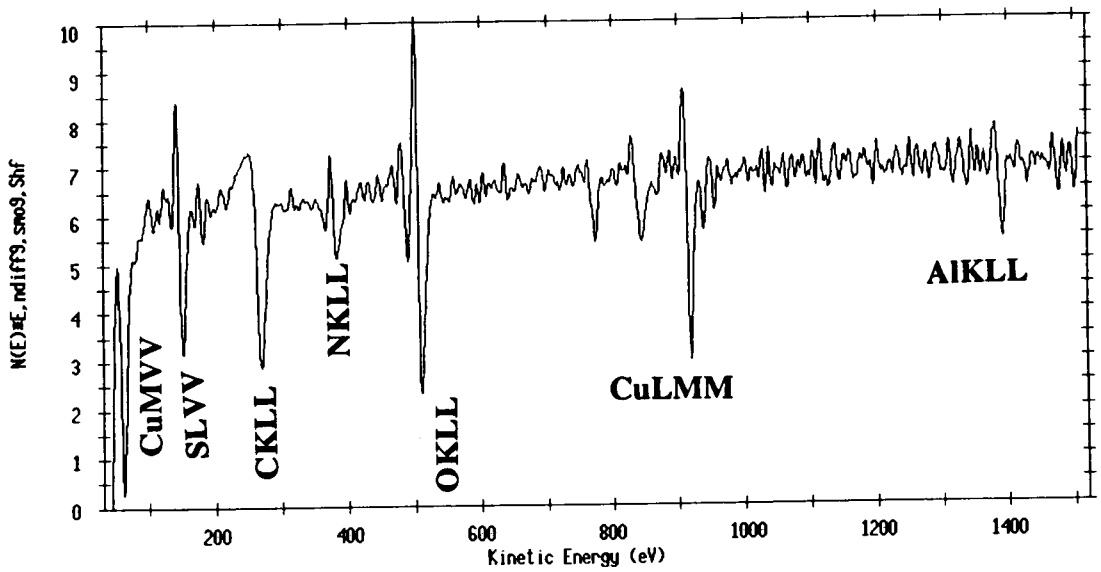

Figure 4.6 A differentiated AES survey scan of the film deposited to 10 nm thickness on the AlN substrate after annealing at 500°C.

Auger peak shows that the surface of AlN substrate is considerably covered with Al_2O_3. In this experiment the carbon was not completely sputtered-off to ensure that the very thin metallic film was not removed. In this case, Cu LMM peak at 61 eV exist with Al KLL peak at ~ 1390 eV (figure 4.6) together and Cu MVV peak is not superimposed with Al LVV peak. However, Al LVV peak (54 eV) does not appear probably indicating that very small islands are scattered over the whole surface due to the surface roughness, or small aluminum Auger peaks may have been buried in the copper MVV peak, since atomic sensitivity factor of copper is higher than the that of aluminum,. The thickness of the layer or the small islands should not exceed one or two monolayers because the signal of the Al KLL peaks coming from 4 - 5 monolayers depth are very distinctive.

In conclusion, copper film deposited on AlN substrate tends to form island after 500°C if the film thickness is ~ 10 nm. If the film thickness is about 50 nm, the film can cover the AlN substrate uniformly even after 500°C annealing. Therefore, pull testing with 80 nm film thickness is quite reliable after 500°C annealing.

The gold film/substrates were not studied because for the pull testing of these couples approx. 20 nm thickness of copper film is deposited additionally onto an 80 nm thick gold film to increase the adhesion of the epoxy pin with the film. Therefore, the possibility to expose the substrate by forming the islands after annealing is almost zero in these couples.

When 10 nm thickness of gold film is deposited onto the sapphire substrate, the film islands were not formed on the substrate without annealing. It seems that the

4.3. Surface studies of ceramic substrates with AES and XPS

In this section, the analysis of the surface modified sapphire, alumina, and AlN substrates will be presented. The surfaces of the substrates were analyzed with XPS and AES techniques.

Studies on sample charging and decomposition during AES analysis of ceramics were conducted and will be presented prior to presenting the surface

analysis results of the samples.

4.3.1. Artifacts during AES analysis of ceramics

Decomposition and charging effects during analysis of ceramic materials are two important drawbacks of AES studies that often lead to artifacts in the results obtained during AES analysis. A reference sample for the study of the electron beam induced decomposition was Al_2O_3 and this study may render useful informations not only to prevent an artifact during AES analysis but also for surface modifications. A reference sample for the study of sample charging during AES was AlN substrate. Detailed studies on these phenomena have been conducted and are described in the sections 4.3.1.1 and 4.3.1.2 .

4.3.1.1. Decomposition of Al_2O_3 during AES analysis

Although Auger signals are also produced during XPS analysis, electrons are mainly used for the AES analysis due to the spatial resolution. Ceramics can be decomposed by electron beam irradiation. Unfortunately, the threshold electron dose for the decomposition are various depending on the materials. Therefore, a study on the threshold conditions on the decomposition should be proceeded to the ceramic sample analysis.

Al LVV peak positions from the metallic aluminum and aluminum oxide are differ by ~ 14 eV. Therefore, AES technique is good for the study of the Al_2O_3 decomposition, besides the study on the determination of the decomposition threshold electron dose for the analysis purpose.

Differential Auger spectra of sapphire in the 40 to 70 eV electron energy range are shown in figure 4.7 for increasing irradiation times and several electron fluxes. At a flux of 9.36×10^{16} electrons/cm^2.s, the aluminum peak from alumina (54 eV) is very prominent even after 800 s of irradiation (Figure 4.7a). The aluminum peak from metallic aluminum (68 eV) appears after 210 s of electron irradiation at a flux of 3.5×10^{17} electrons/cm^2.s (figure 4. 7b). At electron fluxes

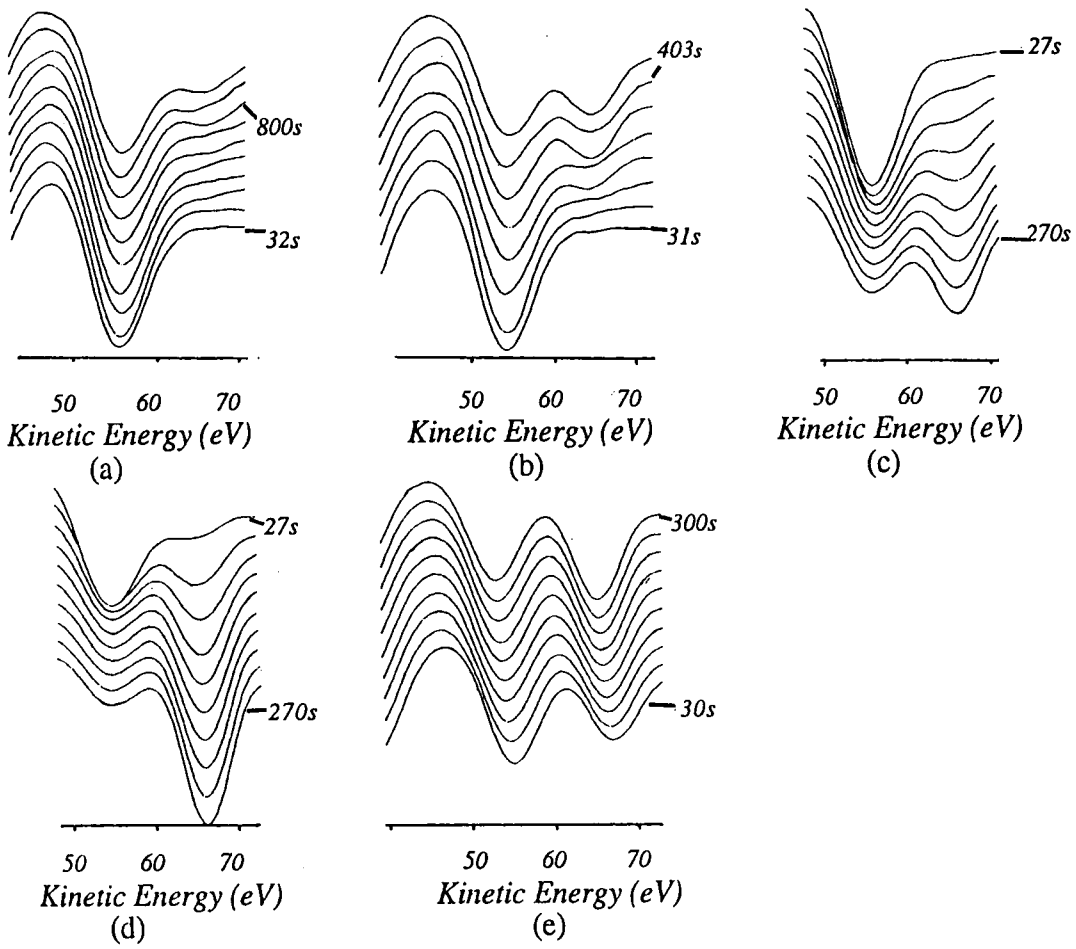

Figure 4.7. AES peak scans showing decomposition behavior of sapphire. Decomposition starts earlier at increasing electron flux: a) 9.36×10^{16} electrons/s.cm^2; b) 3.5×10^{17} electrons/s.cm^2; c) 7.12×10^{17} electrons/s.cm^2; d) 1.7×10^{18} electrons/s.cm^2; e) 2.87×10^{20} electrons/s.cm^2.

of 7.1×10^{17} and 1.7×10^{18} electrons/cm^2.s, decomposition occurs after 68 and 27 s, respectively (Figure 4.7c and -d). In figures 4.7 -c and -d the cycle axes are reversed in order to display the peak scans more clearly. Decomposition of alumina at an electron flux of 2.9×10^{20} electrons/cm^2.s (spot-size beam) takes place after a very short irradiation time. As can be seen in figure 4.7e, after 30 s the aluminum peak from metallic aluminum is very prominent.

The electron fluence and time required for initiating the decomposition of alumina as a function of instantaneous and average electron fluxes for electron beam rastering areas of 38 and 140 μm^2 are presented in detail in table 4.2. The electron fluence required for the decomposition onset is $4.78 \pm 0.07 \times 10^{19}$ electrons/cm^2 for a rastering area of 38 μm^2, and $5.05 \pm 0.17 \times 10^{19}$ electrons/cm^2 for a rastering area of 140 μm^2. The electron fluence for decomposition is almost constant, i.e., flux-independent, except at the lower electron flux, as can be seen in table 4.2. At a flux of 3.5×10^{17} electrons/cm^2.s the fluence for decomposition onset increases to 9.45×10^{17} electrons/cm^2.

The metallic aluminum fraction plotted as a function of electron fluence yields an S-shaped curve, as can be seen in figure 4.8. This fraction is defined as the number of metallic aluminum atoms over the total number of aluminum atoms in the first monolayer of the analysis area.

In order to study the effect of the irradiated area on the decomposition, sapphire was irradiated with 3 kV electrons using a spot-size electron beam, a rastering area of 38 μm^2 and a rastering area of 76 μm^2. The electron fluxes used in this study were 2.9×10^{20} electrons/cm2.s for a spot beam size, 9.7×10^{17} electrons/cm^2.s for a rastering area of 38 μm^2, and 4.9×10^{17} electrons/cm^2.s for a rastering area of 76 μm^2. The corresponding spectra of the irradiated sapphire are shown in Figure 4.9 (lines b, c and d, respectively) together with the differential spectrum of the kinetic energy peak of aluminum from Al_2O_3 (line a in figure 4.9). In the three cases the spectra were taken after no further decomposition was detected. The ratio of the aluminum peak from metallic aluminum (68 eV) to the aluminum peak from alumina (54 eV) increases as the scanned area increases. This

Table 4.2

Electron-Induced Decomposition of Alumina

Electron Flux		Decomposition onset time (s)	Electron fluence ($x10^{19}$ electrons /cm^2)
Instantaneous ($x10^{20}$ electrons / $s.cm^2$)	Average ($x10^{17}$ electrons / $s.cm^2$)		
1.1	3.5*	217	7.6
1.1	0.9**	784	7.4
2.6	8.7*	55	4.8
2.6	2.4**	210	5.0
5.3	17.4*	27	4.7
5.3	4.7 **	109	5.2
7.9	27. 0*	18	4.9
7.9	7.1 **	68	4.8
11.2	36.7*	13	4.8
11.2	10.4**	50	5.2

Notes:

* Rastering area : 38 μm^2

** Rastering area : 140μm^2

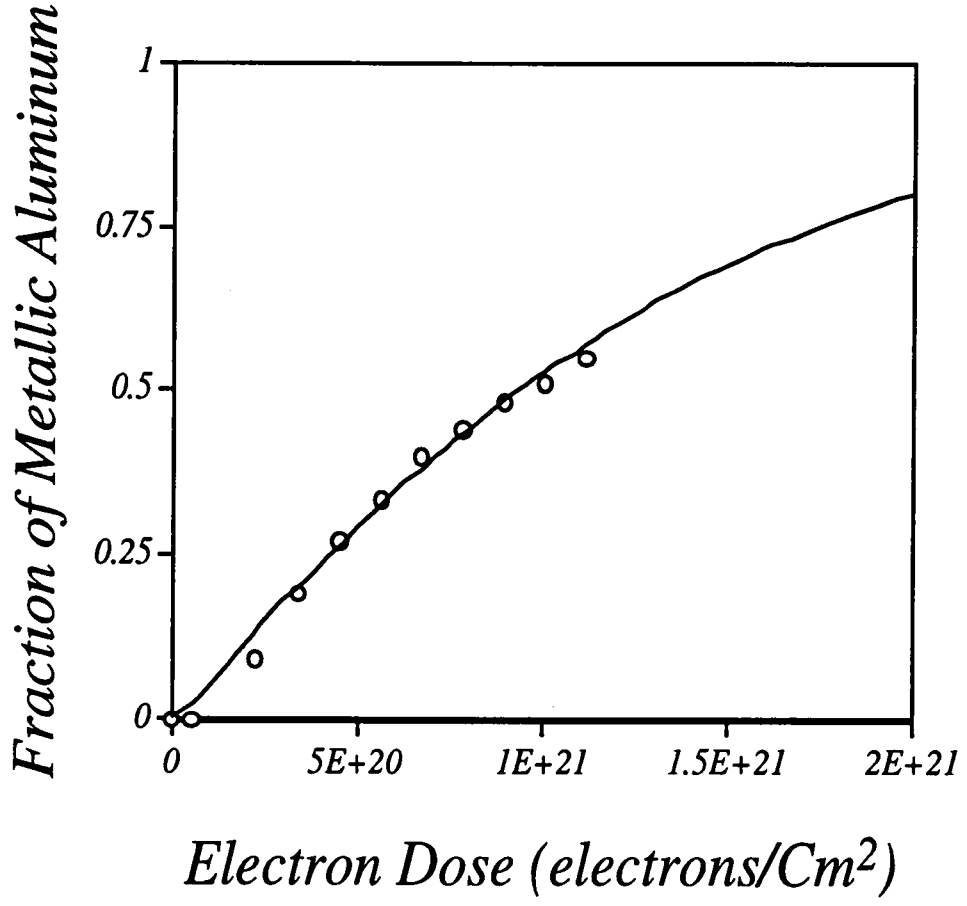

Figure 4.8. Fraction of metallic aluminum in sapphire versus electron fluence. The data points have been fitted with the function $F = 1 - \exp(-3 \times 10^{-24} \phi^{1.13} t^{1.13})$. For more detail see equation 6 in text.

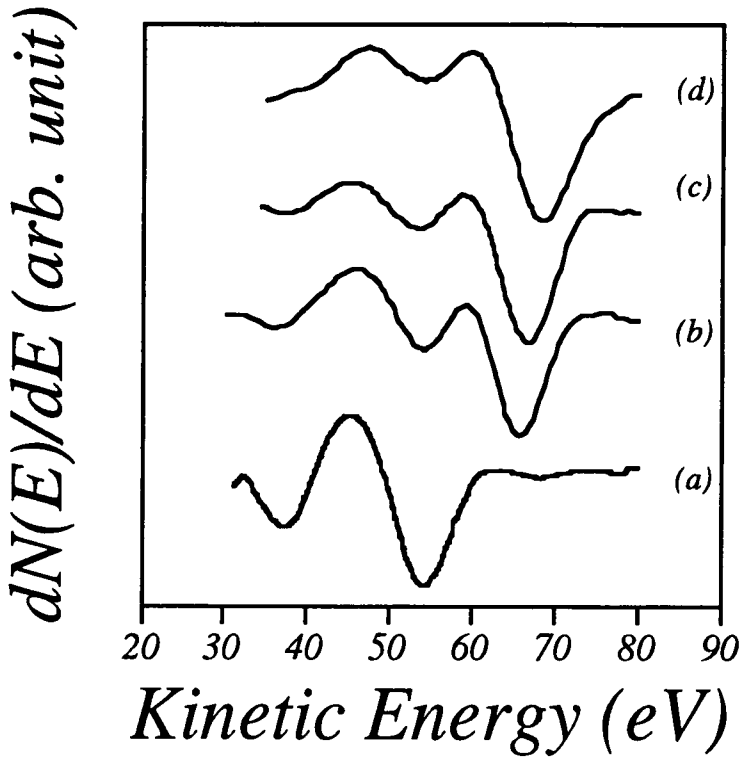

Figure 4.9. Al LVV Auger peak spectrum for sapphire (54 eV) and Al Auger peak spectrum for metallic aluminum (68 eV). In (a) an Al LVV peak spectrum for Al_2O_3 is shown as a reference. In (b), (c) and (d) the Al LVV Auger peak spectra for sapphire (54 eV) are shown together with the Al Auger peaks for metallic aluminum (68 eV) produced by decomposition of alumina by 3 keV electrons. The proportion of decomposed Al_2O_3 after irradiation with 3 keV electrons is shown in (b), (c), and (d). The area irradiated by the electron beam was a spot size electron beam (b), a rastering area of 38 μm^2 (c) , and a rastering area of 76 μm^2 (d). In the three cases irradiation was performed after no further decomposition was detected. The proportion of decomposed sapphire seems to increase as the scanned area is increased.

is due to Auger electrons excited by backscattered electrons emerging from an area other than the primary beam incident area [96, 97] and this will be further discussed in the section 5.5.

We may be asked if electron-induced decomposition also occurs at subsurface levels. To answer the question the high energy Al (Al KLL) peaks were also examined, since the low kinetic energy Auger peaks can only provide information about the decomposition taking place approximately in the first surface monolayers only. The electron escape depth of these electrons (20 Å) is ~ 5 times larger than the corresponding escape depth for the low kinetic energy peaks. The decomposition kinetics of sapphire at a 3 kV accelerating potential and a flux of 2.87×10^{20} electrons/$cm^2 \cdot$ s, using the high kinetic energy aluminum peaks, are shown in figure 4.10. The bottom spectrum corresponds to aluminum from sapphire while the top corresponds to aluminum KLL from metallic aluminum. The various features of the fine structure associated with each main peak are also shown in figure 4.10 for both spectra. The metallic aluminum fine structure is due to plasmon loss peaks [98]. After irradiating Al_2O_3 for 110 s the spectrum from the first few monolayers is very similar to that of Al_2O_3, indicating almost no decomposition. After 990 s of the irradiation the differential spectrum of the same region exhibits superposition of the spectra of aluminum from Al_2O_3 and of metallic aluminum, showing that only partial decomposition of alumina has taken place. After 3000 s of irradiation the spectrum looks very similar to that of metallic aluminum indicating that most of the first ~2 nm of alumina have been decomposed. At this electron flux a very significant portion of the surface monolayer is decomposed after only 30 sec of irradiation (figure 4.6e). These results indicate that electron-induced decomposition takes place at least in the first five atomic layers of the substrate and that the decomposition kinetics are much faster for the first monolayer than for the subjacent atomic layers.

High carbon content of the surface of ethanol-cleaned sapphire was greatly reduced by sputter-cleaning for 1 min with 3 keV Ar^+ ions. However, after sitting for a few hours at a pressure of 10^{-9} torr in the AES chamber, the surface carbon content increased anew. Figure 4.11 shows different

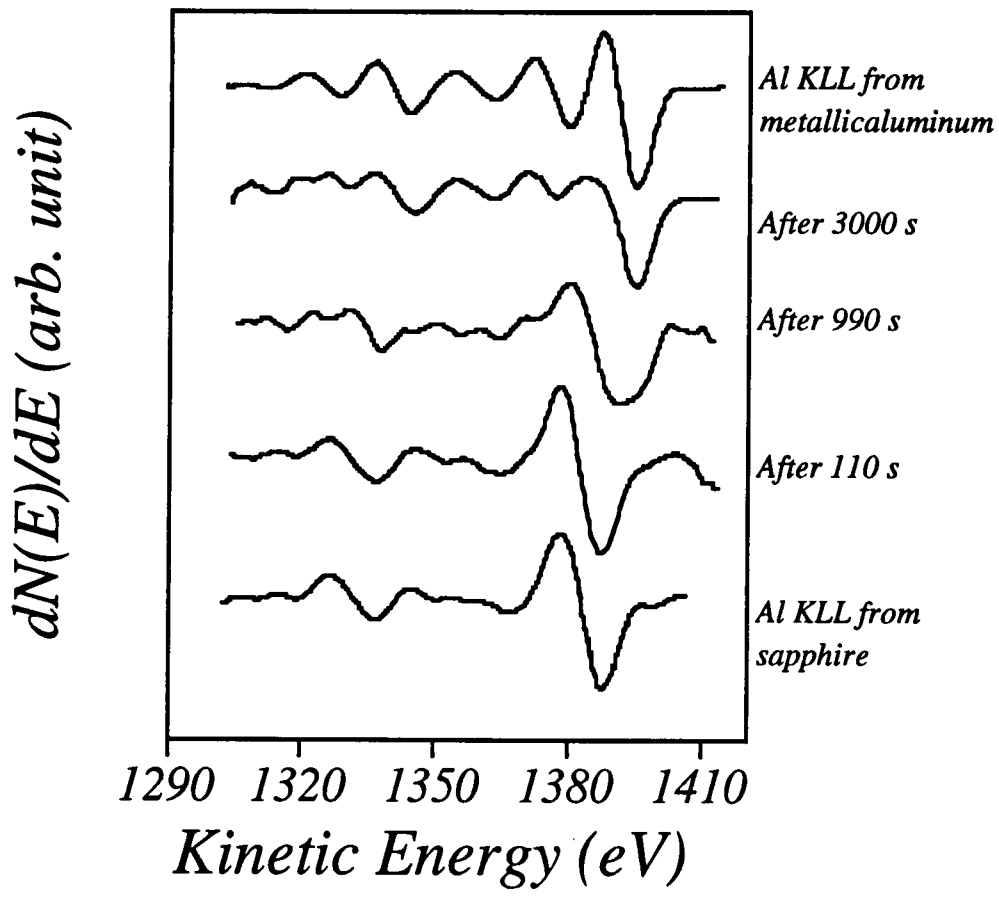

Figure 4.10. The decomposition kinetics of sapphire at 3 keV electron accelerating potential and a flux of 2.87×10^{20} electrons/cm^2·s, using the high kinetic energy aluminum peaks. The bottom spectrum correspond to aluminum KLL from sapphire while the top correspond to aluminum from metallic aluminum. The amount of aluminum increases at increasing irradiation time. After 3000 s irradiation the spectrum is very similar to that of metallic aluminum, indicating that most of the first 20 Å of alumina have been decomposed.

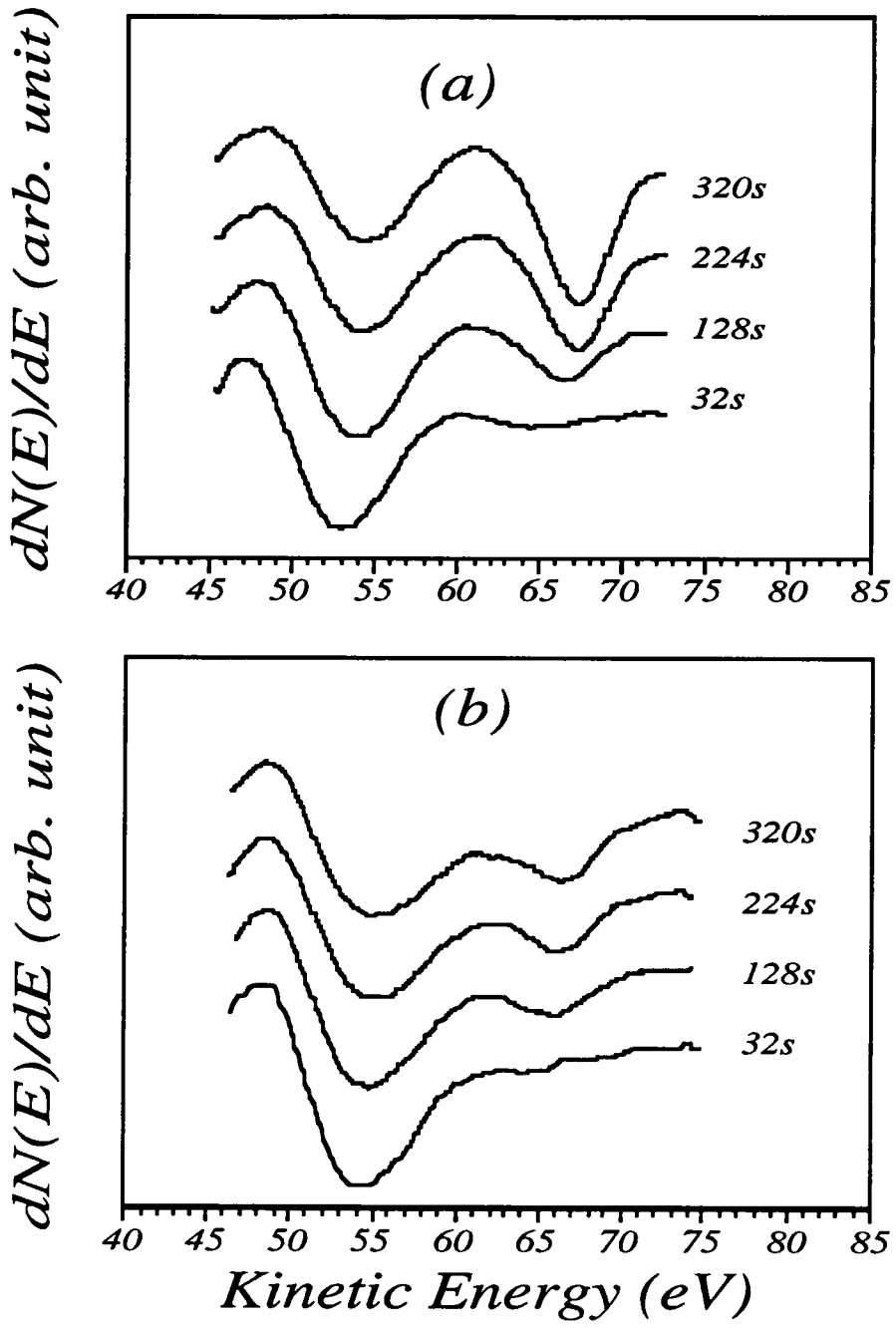

Figure 4.11. AES scans of sputter-cleaned sapphire (a), and of ethanol-cleaned sapphire (b). The decomposition rate of alumina at the ethanol-cleaned surface is much slower than that of the sputter-cleaned sapphire.

decomposition rates for sputter-cleaned and ethanol-cleaned sapphire surfaces. The electron irradiation induced decomposition of Al_2O_3 is strongly affected by the surface condition. The decomposition in sputter-cleaned surfaces starts after less than 108 s of electron irradiation at a flux of 2.6 x 10^{20} electrons/cm^2.s (figure 4.11a), but the decomposition rate of sapphire is extremely slow when a carbonaceous layer is present on the surface. For instance, about 240 s are required at the same flux to initiate the decomposition in this case, as can be seen in figure 4.11b.

The decomposition behavior of sputter-cleaned sapphire immediately after sputter-cleaning and after re-contamination with carbon in the ultra high vacuum chamber is shown in figure 4.12. It can be seen that the decomposition rate of the sapphire surface re-contaminated with carbon after sputter-cleaning (figure 4.12b) is much slower than the rate of the as-sputtered surface (figure 4.12a), revealing that the observed effect is not due to ion irradiation damage during sputter cleaning.

4.3.1.2. Sample charging during AES

Figure 4.13a shows analysis areas for the charging study of aluminum nitride. Figure 4.13b shows the different charging depending on the different analysis areas on AlN surface. Before selecting the analysis area, SEM image enlarged to 5000X and sample stage was tilted to 60°.

The surface of AlN substrate was covered with Al_2O_3. O KLL peaks were used in this study. Reference peak position of the oxygen KLL in the Al_2O_3 is 506 eV.

In area (1) in figure 4.13a, no oxygen KLL peak appears in the energy range of 490 - 550 eV. This means oxygen peak shifts to more than 50 eV. Area (2) produces oxygen KLL Auger peak at 528 eV. Oxygen KLL at area (3) is about the same as the reference peak position. In area (4), the peak shifts approx. - 2 eV as compared to the reference peak position, implying that the positive sample charging occurred on the sample surface. This means that the secondary electrons emitted is more than the incident electrons. Auger peaks from area (4)

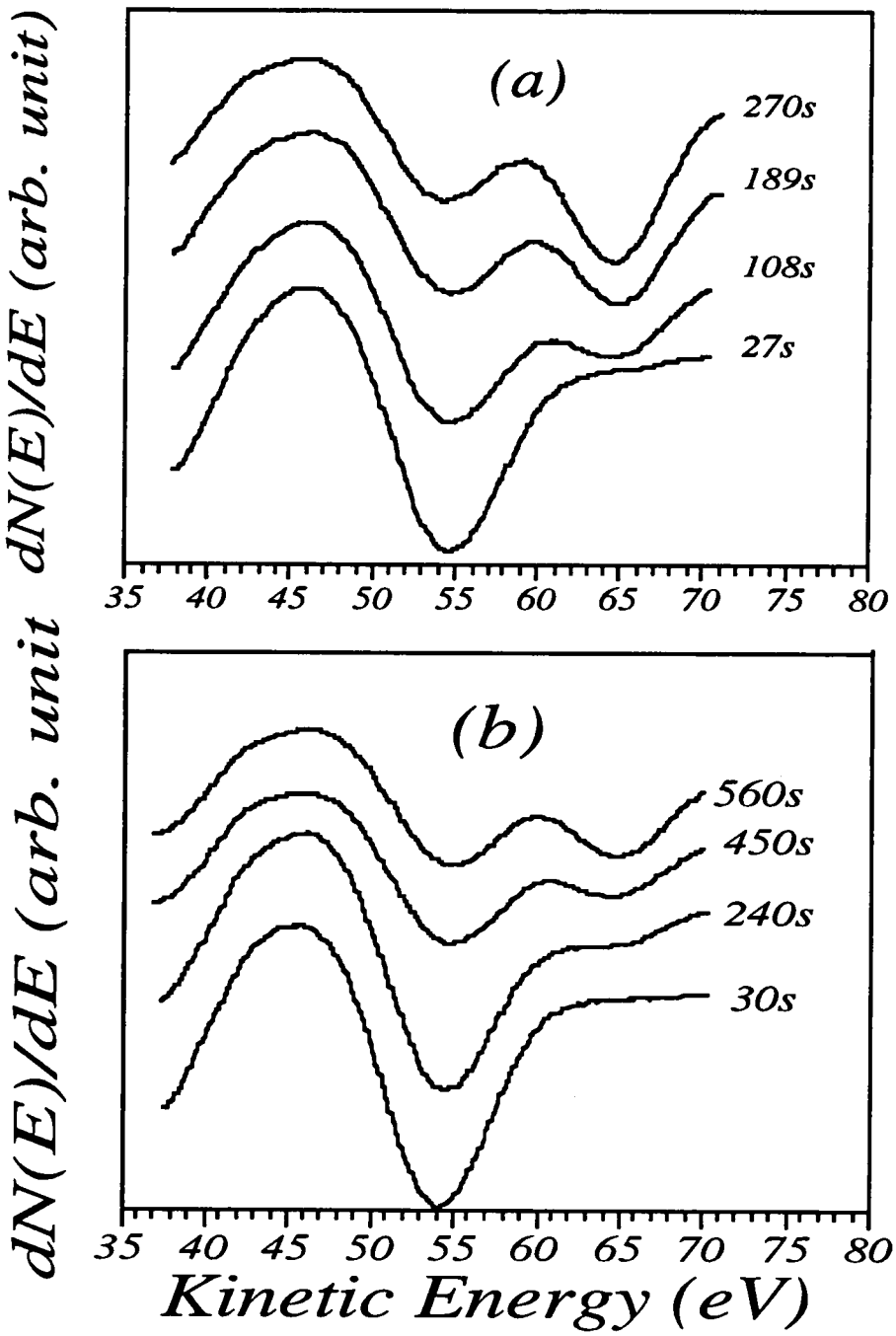

Figure 4.12. Comparison of decomposition behavior of sputter-cleaned sapphire surface and surface re-contaminated with carbon after sputtering in the vacuum chamber (10^{-9} torr) a) as-sputtered sapphire; b) sapphire with carbon re-deposited after sputtering.

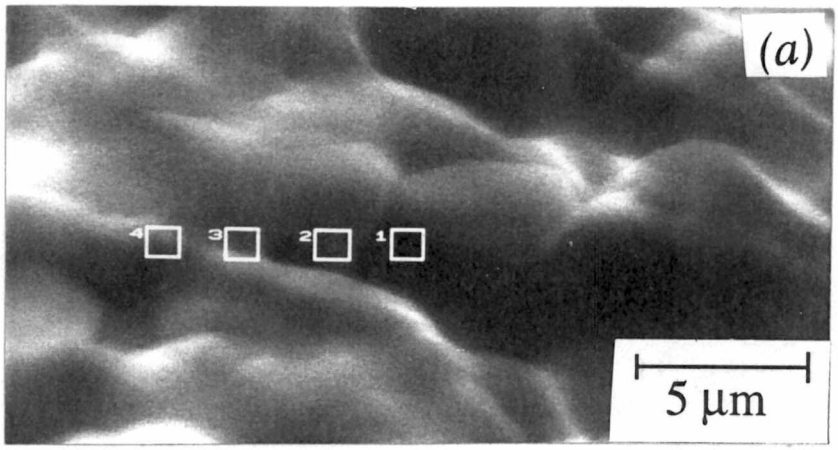

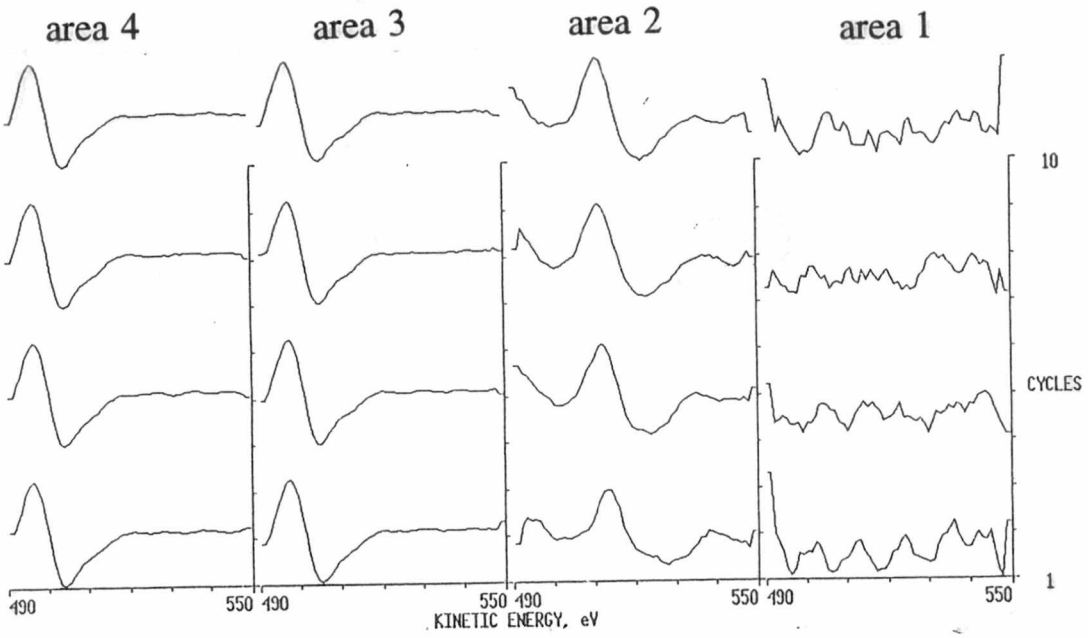

(b)

Figure 4.13. (a) Areas used for the charging study, (b) Auger peak scans for four analysis areas shown in (a).

can be used for the analysis with small correction using the reference peak. The mechanisms of the changes of the charging will be discussed in detail in the section 5.6.

4.3.2. AES analysis of laser-irradiated Al_2O_3 substrates

Alumina substrates irradiated in oxygen and in Ar-4%H_2 at 2 J/cm^2 were studied with AES. The surface chemical composition of the specimen irradiated in oxygen corresponds to Al_2O_3 (peak *i* in figure 4.14), while in the subsurface regions some metallic aluminum or substoichiometric aluminum oxide is observed (peaks *ii* and *iii* figure 4.14).

When the alumina specimen is irradiated in reducing atmosphere (Ar-4%H_2) with 2 J/cm^2 energy density, the surface chemical composition is stoichiometric Al_2O_3 (peak *i* in figure 4.15a), indicating that the irradiated surface may have re-oxidized when exposing in air. However, distinctive metallic aluminum or substoichiometric alumina is formed in the subsurface (peak *ii* in figure 4.15a). The amount of the metallic aluminum and substoichiometric alumina in this specimen is less than that of the specimen irradiated in oxygen.

The formation of metallic aluminum or substoichiometric alumina is also evidenced with Al KLL Auger peak spectra (figure 4.15b). Since Al Auger electrons from KLL transitions are more energetic than those from LVV transitions, Al KLL peak has more escape depth than the Al LVV. Therefore, the informations obtained from Al LVV peak can be different to those from the Al KLL peak. Al KLL Auger spectra is more averaged over the distance from the surface. Comparing figure 4.15a with figure 4.15b, the relative amounts of metallic aluminum are different. This implies that the distributions of the metallic aluminum in the irradiated alumina are not uniform. When metallic aluminum features appear in Al LVV spectra, Al KLL spectra may not show the existence of metallic aluminum. This results can be compared to the TEM micrographs that will be shown in the later section.

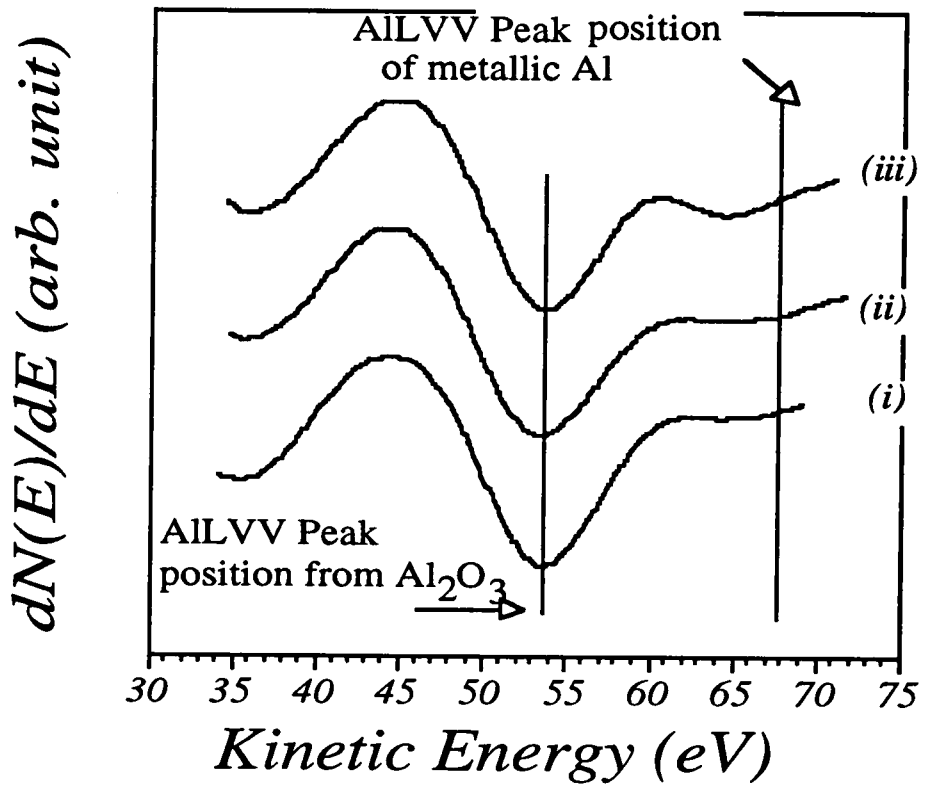

Figure 4.14. Al LVV peaks from the surface (*i*) and subsurface (*ii* and *iii*) of alumina laser irradiated in air at 2 J/cm^2. Metallic and/or substoichiometric aluminum oxide is detected in the subsurface region.

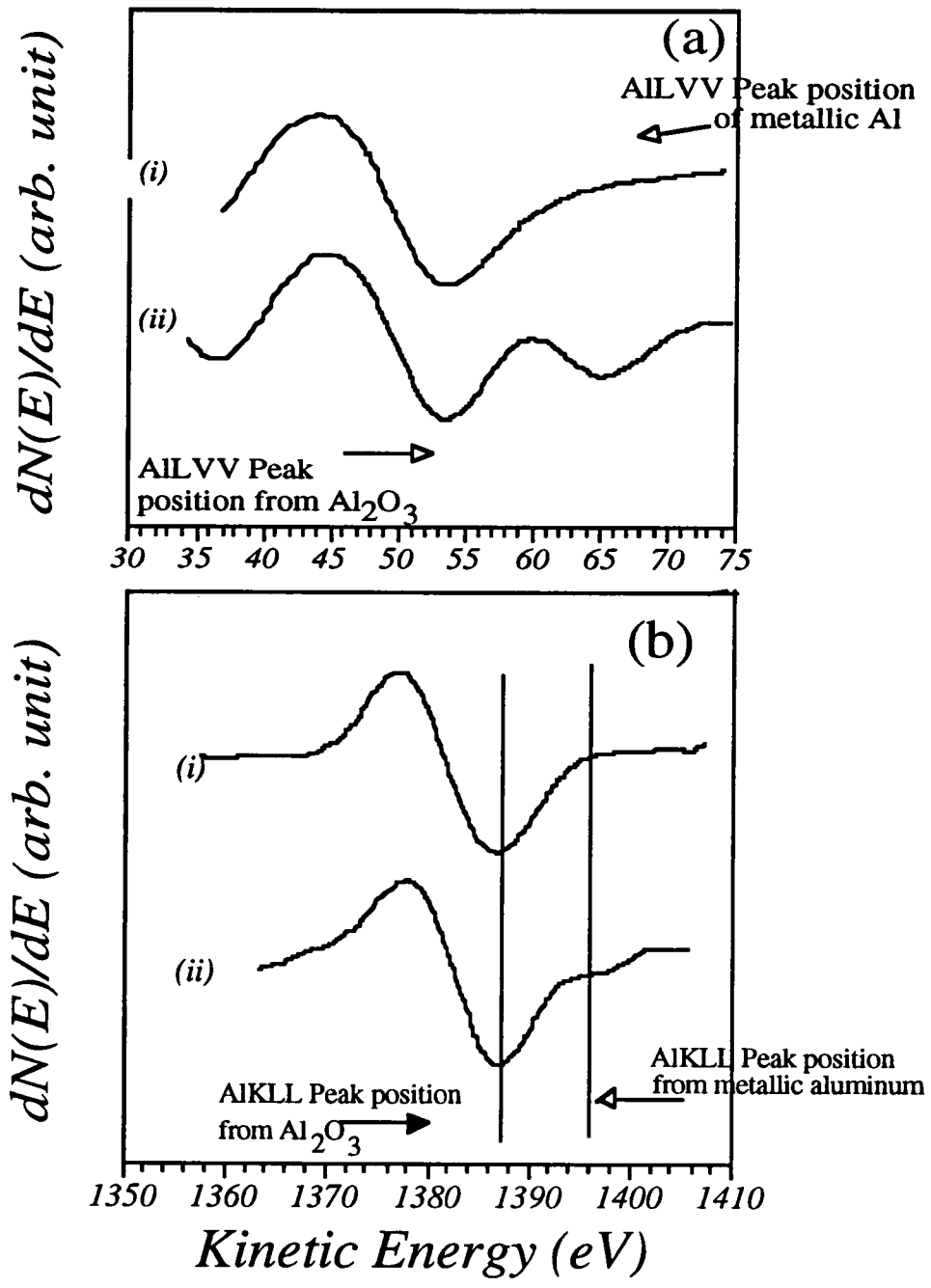

Figure 4.15. Al LVV (a) and Al KLL (b) peaks each from the surface (*i*) and subsurface (*ii*) of alumina laser-irradiated in Ar-4%H_2 at 2J/cm^2. Distinctive metallic (or substoichiometric alumina) feature appears in the subsurface (peaks of *ii*). On the other hand, the surface peak is from stoichiometric alumina (Al_2O_3) (*i*), implying that the surface is reoxidized when the irradiated area is exposed in air.

4.3.3. AES analysis of laser-irradiated AlN

Figure 4.16 is Al LVV peak spectra of as-received AlN as a function of depth from the surface. Although the position of peak *i* in figure 4.16 is that of Al LVV from alumina, however, the peak is much more broadened than the peak from pure alumina shown in 4.14 (*i*). That means the surface of as-received aluminum nitride consists mostly of aluminum oxide layers but partly of aluminum nitride. This is consistent with aluminum oxide being thermodynamically more stable than aluminum nitride [95].

It is shown in figure 4.17 that the surface of an AlN substrate laser-irradiated at 2 J/cm^2 in a reducing atmosphere (Ar-4%H_2) consists of a mixture of AlN and Al_2O_3 (peak *i*), while the subsurface was a mixture of metallic Al and AlN (peaks *ii* and *iii*). The oxide layer after laser irradiation was one to two monolayers thick, whereas that of as-received AlN was much thicker, but varied depending on the area.

The nitrogen and oxygen Auger peaks were measured on the near-surface of as-received and laser irradiated AlN (figure 4.18 -a and -b). Figure 4.18a shows nitrogen and oxygen Auger peak spectra from the surface and the subsurface region of as-received AlN. The spectra from the surface is mostly from Al_2O_3 (*i*) since nitrogen peak is very weak. Subsequent sputter etching reveals increasingly stronger N KLL peaks in the subsurface (*ii* and *iii*). Figure 4.18b is nitrogen and oxygen Auger peaks from the surface and the subsurface of AlN substrate laser irradiated in Ar-4% H_2 with 2 J/cm^2 energy density. In the surface both AlN and Al_2O_3 are distinctive. This means that oxide layers on the surface of as-received AlN may be ablated during laser irradiation, exposing the bulk AlN substrate. Only decomposed metallic aluminum on the surface may have been reoxidized as shown in spectra (*i*).As the sputter etching progresses, nitrogen peak becomes more prominent and oxygen peak disappears (*ii* and *iii*) .

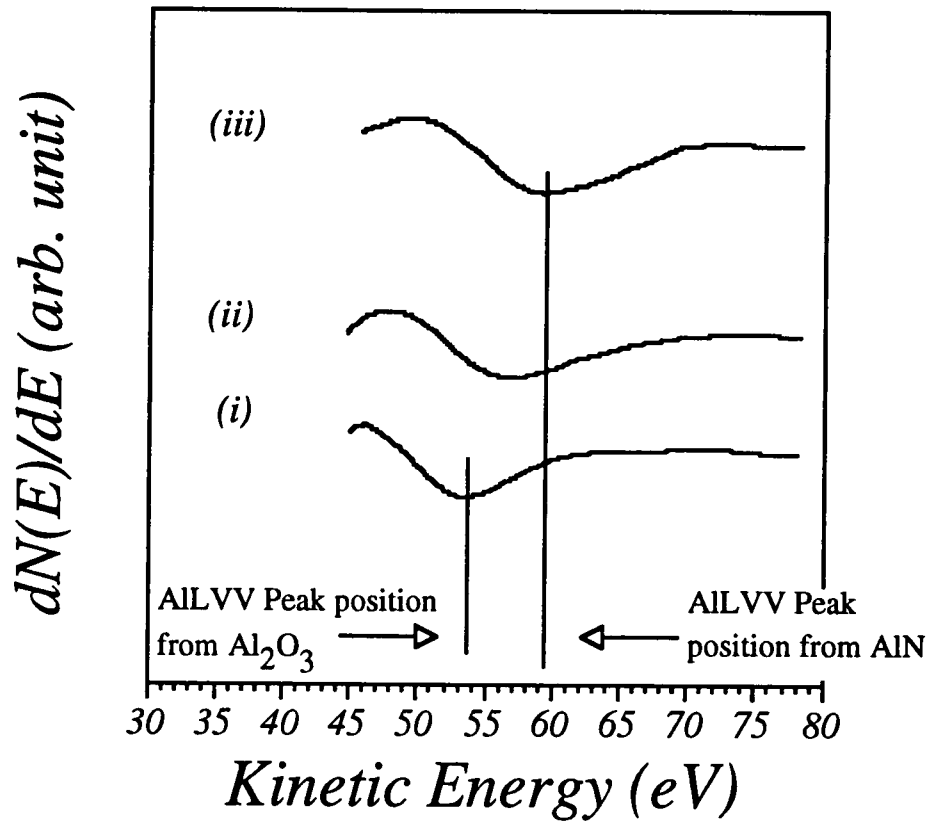

Figure 4.16 - Al LVV peak spectra from the surface (*i*) and the subsurface (*ii* and *iii*), of as-received AlN substrate. To obtain the subsurface AES peaks the surface was gently sputter-etched in situ. The spectra from the surface is that of stoichiometric alumina (*i*). As sputter etching advances to deeper substrate layers, the surface chemistry changes from aluminum oxide to aluminum nitride (*ii* and *iii*).

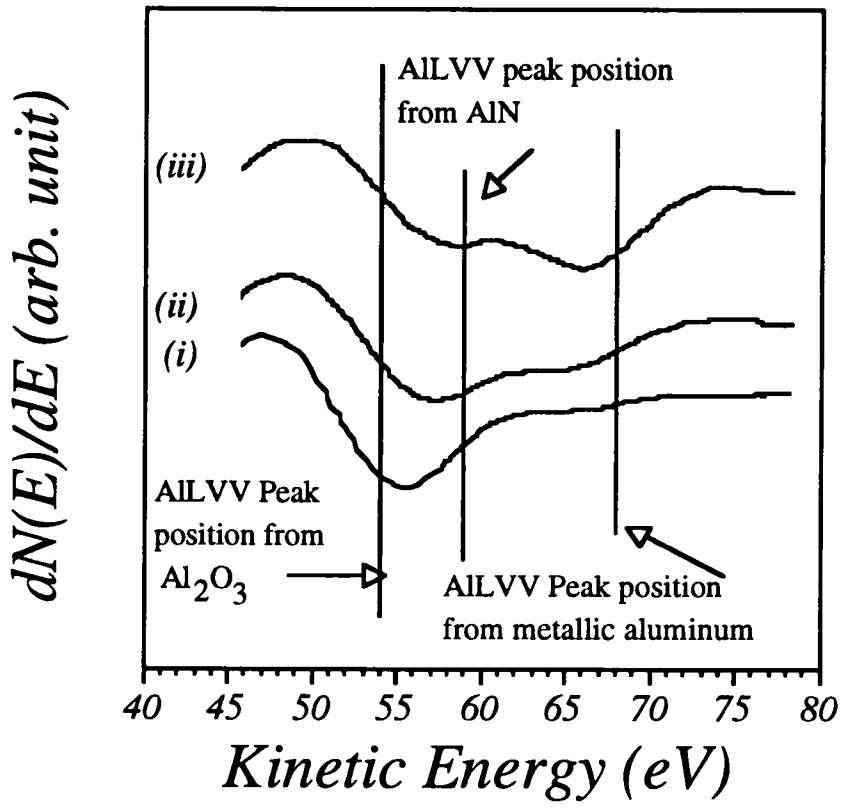

Figure 4.17- Al LVV peak spectra from the surface (*i*) and subsurface (*ii* and *iii*) of AlN laser-irradiated in Ar-4%H_2 at 4J/cm^2. Al LVV from the surface (*i*) is a superposition of peaks from Al_2O_3 and AlN, while sputter etching reveals that the subsurface peaks are from both AlN and metallic aluminum (*ii* and *iii*).

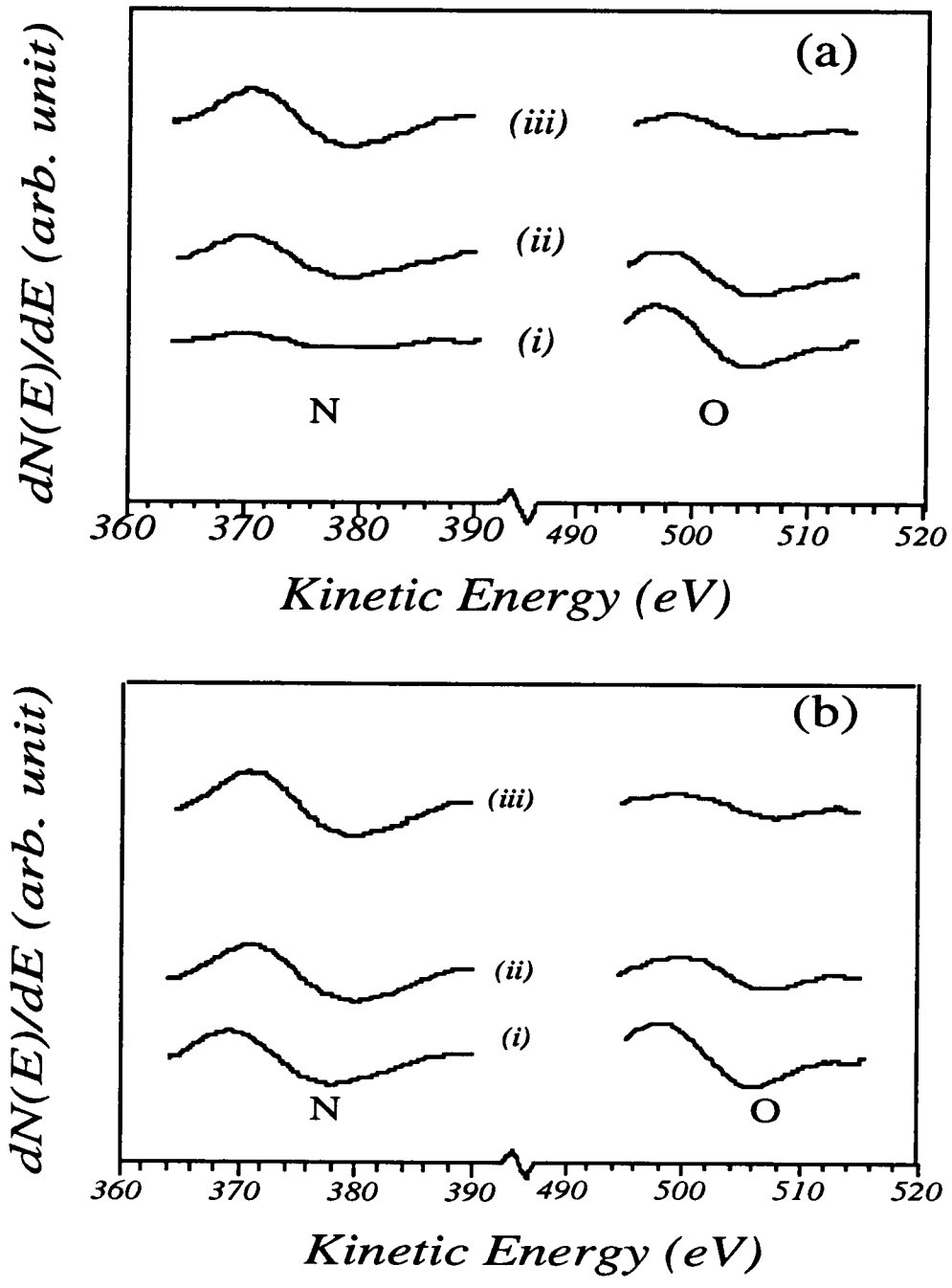

Figure 4.18. (a) Nitrogen and oxygen Auger peak spectra from the surface (i) and the subsurface (ii and iii) of as-received AlN. (b) Nitrogen and oxygen Auger peak from the surface (i) and subsurface (ii and iii) of AlN substrate laser irradiated in Ar-4% H_2 with $2J/cm^2$ energy density.

4.3.4. XPS analysis of Al_2O_3

The XPS can not resolve the small areas due to its limited spatial resolution, but gives overall surface chemistry produced by the laser irradiation. Except for the disadvantage of spatial resolution, XPS has a merit over AES in terms of peak resolution. The surface of as-received, annealed, and laser-irradiated alumina and sapphire were studied with XPS and the results were compared with AES analysis.

Figures 4.19-a and -b are XPS survey scans of annealed and laser-irradiated alumina, respectively. The annealing were conducted at 1350°C for 48 hr and laser irradiation was conducted in Ar-4%H_2 with ten sequential shots at 3 J/cm^2 energy density. Silica, which exists probably at the boundary between the alumina particles, was largely ablated during the irradiation and the amount of carbon as a surface contaminant increased after irradiation.

Quantitative analyses of the specimens treated in various ways were conducted using XPS survey scans and are presented in tables 4.3 and 4.4, respectively. The atomic percentages of carbon, oxygen, aluminum, and magnesium plus silicon (C/O/Al/bal.) are shown in the second column of the tables. Most of the carbon was removed by a 30 s sputtering with 2 keV Ar^+ ions, indicating that the carbon atoms were adsorbed at the surface. The amount of carbon present in as-received sapphire and alumina substrates varied significantly from sample to sample. The data for the two as-received specimens presented in table 4.4 illustrate this situation. The carbon content significantly decreased immediately after annealing. However, the carbon concentration in the annealed specimens increased as a function of time even though the specimens were kept in a vacuum jar at a pressure of 10^{-2} torr. We also found that the carbon increases as a function of time even in ultra high vacuum. Ten pulses of laser irradiation with 3 J/cm^2 applied to the sapphire may be enough to not only desorb the impurities but also ablate the sapphire. The carbon detected in the irradiated areas was most likely deposited from the air after the irradiation.

The binding energy of C-1s of free carbon (amorphous) or hydrocarbon is

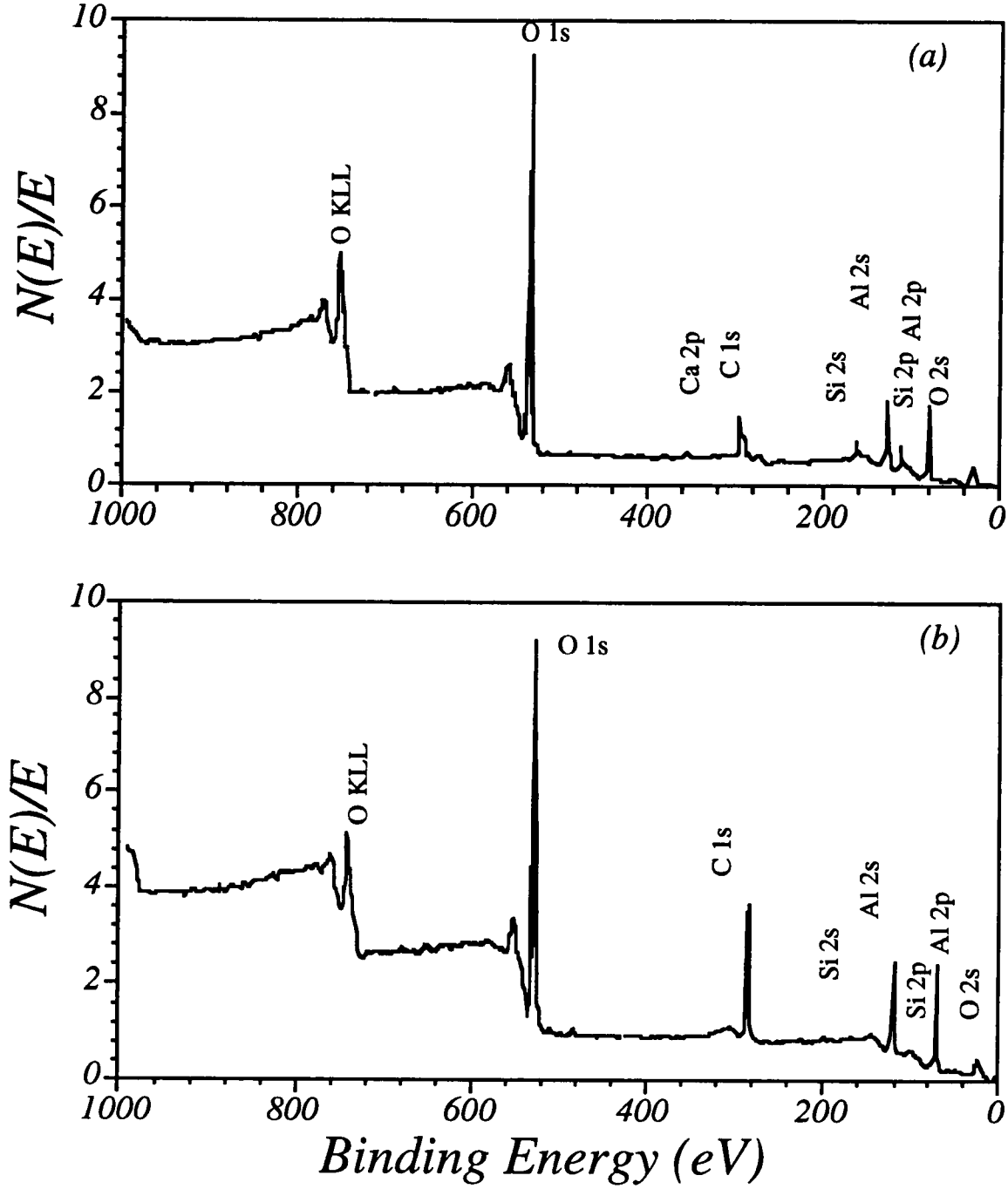

Figure 4.19. (a) XPS survey scan of annealed alumina. (b) XPS survey scan of alumina laser-irradiated under Ar-4% H^2 with $3J/cm^2$

Table 4.3.

Summary of XPS observations in Sapphire Specimens

Surface Condition	Atomic % C-O-Al-bal	O/Al ratio	O_{hyd}/O_{tot} ratio	% metallic Al	FWHM O-1s Peak	FWHM Al-2p Peak
As-received	12-57-26-5	2.2	0.19	0	2.8	2.3
As-received	46-32-13-9	2.4	2.5	0	2.7	1.8
Annealed	7-59-30-7	2.0	0.29	0	2.1	1.7
Annealed (0.5m)*	0-64-36-0	1.8	0.15	0	2.3	1.9
Annealed (10m)*	0-62-38-0	1.6	0.08	0	2.2	1.9
Laser irrad. (Ar-4%H_2) 3J/cm^2	29-41-30-0	1.4	0.10	3	2.8	2.4
Laser irrad. (Ar-4%H_2) 3J/cm^2 (1.2m)*	~1-60-38-1	1.6	0.09	6	2.6	2.2
Laser irrad. (Ar-4%H_2) 3J/cm^2 (10m)*	0-61-39-0	1.6	0.08	2	2.4	2.0
Laser irrad.(air) 3J/cm^2	24-54-22-0	2.5	0.40	0	2.9	2.1
Laser irrad.(air) 3J/cm^2 (0.5)*	7-60-33-0	1.8	0.09	0	2.7	2.1

*Sputtering time

Table 4.4.

Summary of XPS observations in Alumina Specimens.

Surface Condition	Atomic % C-O-Al-bal	O/Al ratio	O_{hyd}/O_{tot} ratio	% metallic Al	FWHM O-1s Peak	FWHM Al-2p Peak
Annealed	16-55-28-1	2.0	0.17	0.0	2.5	1.9
Laser irrad.(Ar-4%H_2) 0.4 J/cm^2 (30s)*	26-45-27-2	1.7	0.14	1.6	2.5	2.1
Laser irrad.(air) 0.4 J/cm^2 (30s)*	7-56-33-4	1.7	0.13	1.2	2.5	2.2
Laser irrad.(Ar-4%H_2) 1 J/cm^2 (30s)*	3-60-37-	1.6	0.17	3.0	2.6	2.2
Laser irrad.(air) 1 J/cm^2 (30s)*	9-57-33-	1.8	0.18	0.0	3.2	2.7
Laser irrad.(Ar-4%H_2) 3 J/cm^2 (30s)*	2-58-40-0	1.5	0.06	6	2.3	2.1
Laser irrad.(Ar-4%H_2) 5 J/cm^2	31-40-28-1	1.4	0.17	4	2.6	2.1
Laser irrad.(Ar-4%H_2) 5 J/cm^2 (30s)*	2-57-41-0	1.4	0.07	5	2.3	2.1
Laser irrad.(Ar-4%H_2) 5 J/cm^2 (5m)*	2-60-38-0	1.6	0.10	2	2.3	2.1
Laser irrad.(Ar-4%H_2) 5 J/cm^2 (10m)*	1-60-39-0	1.5	0.08	1	2.3	2.1

*Sputtering time

285 eV and that of carbon bound to either oxygen and/or nitrogen is ~ 288eV. Approx. 90% of the carbon came from the amorphous carbon for as-received sapphire and sapphire irradiated in Ar-4%H_2, while for sapphire irradiated in oxygen atmosphere only 60% of the carbon was from the free carbon. That means carbon tends to be oxidized when the irradiation is performed in an oxygen atmosphere. However, the thickness appeared to be non-uniform or less than a few mono layers, since O 1s peak having less photoelectron escape depth than C 1s is mostly from Al_2O_3 (tables 4.3 and 4.4).

The oxygen to aluminum atomic concentration ratio (O/Al) was measured from XPS survey spectra of sapphire and alumina specimens (tables 4.3 and 4.4). O 1s and Al 2p peaks were used for the measurement. Since O 1s is from the shallower depth from the surface than Al 2s, the ratio is strongly dependent upon the surface oxygen concentration. The O/Al ratio in as-received sapphire was substantially higher than the stoichiometric ratio (1.5). This ratio decreased to 1.4 at the surface of alumina and sapphire samples irradiated in argon-4% hydrogen. On the other hand, when the substrates were irradiated in air the O/Al ratio at the surface was 2.5, a value substantially higher than that of as-received sapphire. As the near-surface layer was sputtered away, the measured composition tends to be the stoichiometric ratio of 1.5.

Figures 4.20 -a and -b show the change in the binding energy of Al 2p at the surface of sapphire as-received and laser irradiated in Ar-4%H_2 with 10 pulses of 5 J/cm^2. In both cases the surfaces were slightly sputter-cleaned prior to data acquisition. In the irradiated specimen a small peak can be seen and this peak is 2.5 to 3 eV away from the aluminum oxide peak in the Al 2p spectrum and is due to the metallic aluminum formation. The amounts of metallic aluminum present after the various treatments performed in sapphire and alumina are shown in tables 4.3 and 4.4 as a percentage of the total aluminum signal, i.e. metal/(metal + oxide). The amount of aluminum after irradiation increased as increasing the laser energy density when the substrates are irradiated in argon-4% hydrogen (Figure 4.21). Only a small amount of aluminum was detected in samples irradiated in air with a laser energy density of 0.4 J/cm^2. These results demonstrate that a thin layer of metallic aluminum is formed on the surface of sapphire and alumina

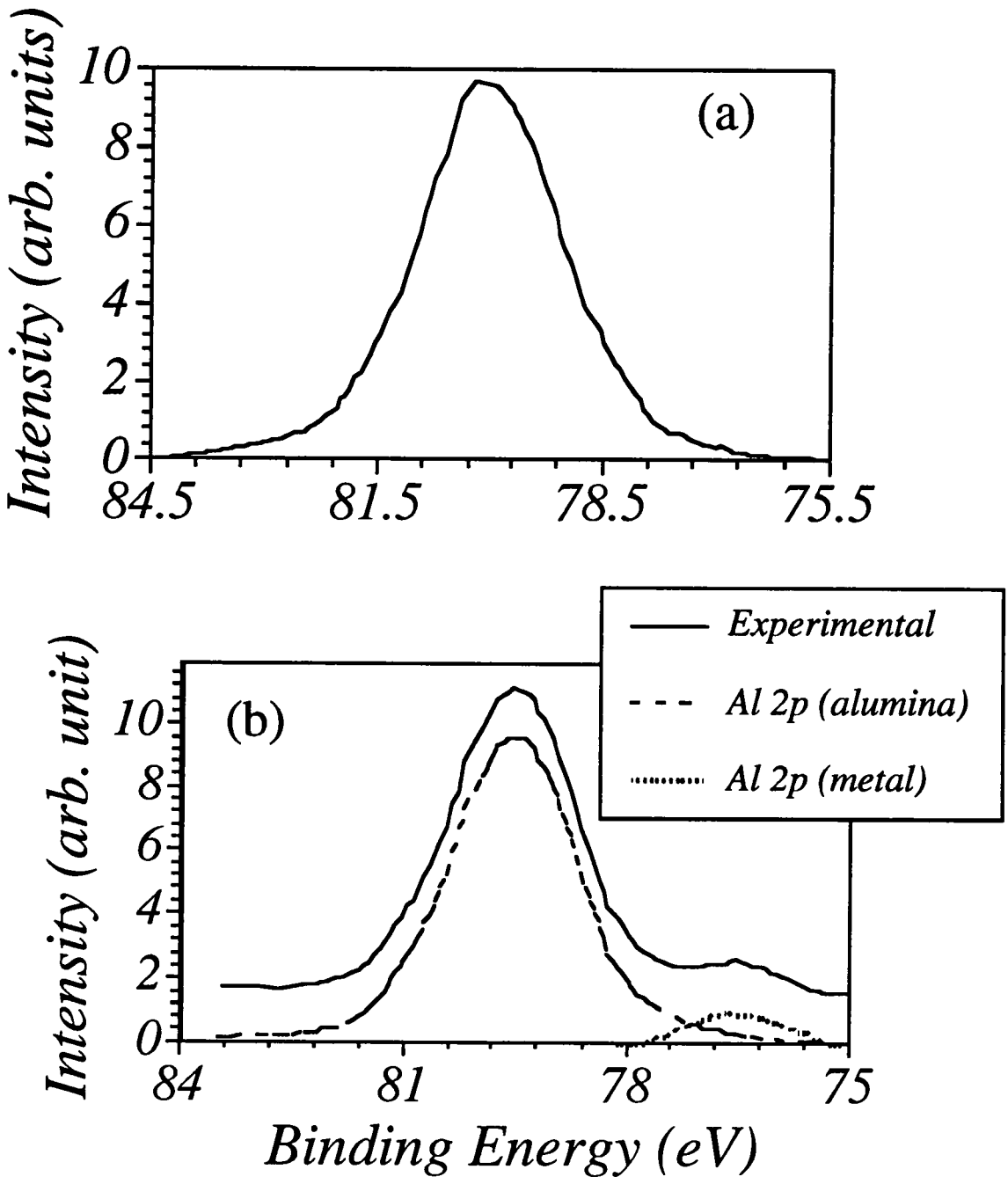

Figure 4.20. Al 2p XPS spectra of as-received alumina (a) and alumina laser-irradiated in Ar-4%H2 with 10 pulses of 5J/cm^2 (b).

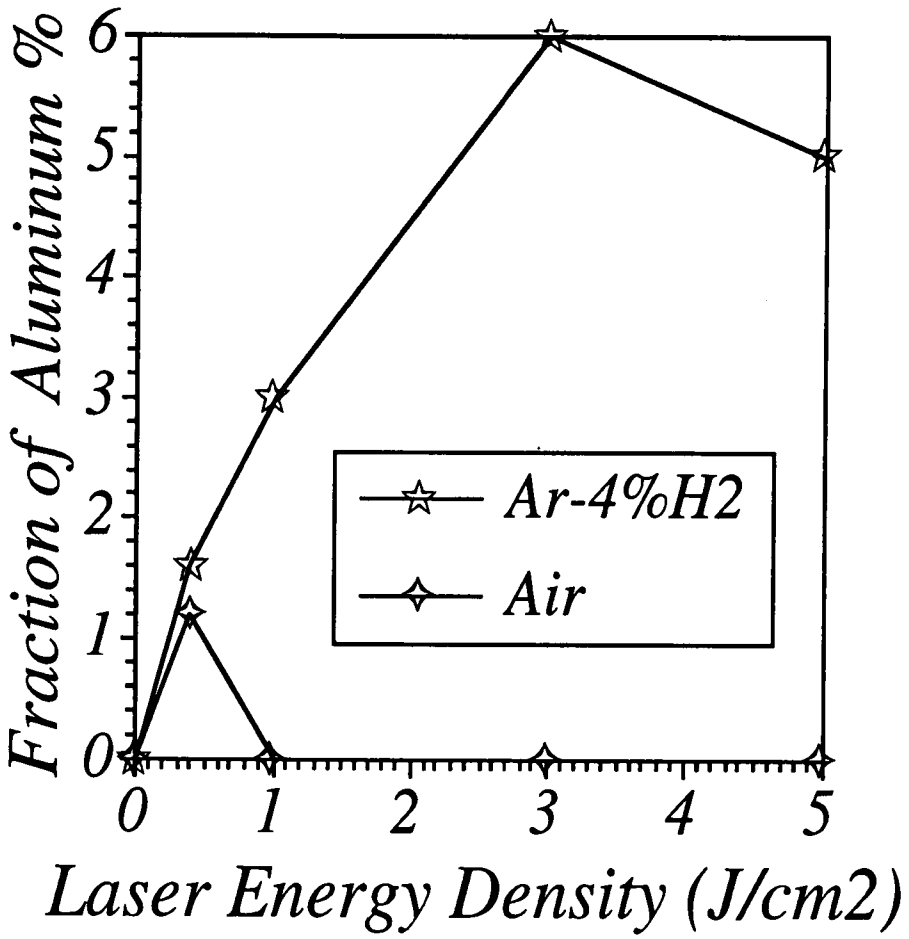

Figure 4.21. Percentage of the fraction of metallic aluminum over the total aluminum signal, i.e., metal/(metal + oxide), present in the near-surface region of the alumina substrate.

laser-irradiated in a reducing atmosphere.

The metallic aluminum signal from sapphire laser-irradiated in Ar-4%H_2 at 3 J/cm^2 doubled after the surface was sputtered for 72 s. The metal/(metal + oxide) ratio increased from 3 to 6%, while the O/Al ratio decreased. This means that the decomposed aluminum on the as-irradiated surface reoxidized in air and the sapphire matrix was oxygen depleted by the laser irradiation in a reducing atmosphere. After sputtering, the oxide film was removed and the metallic aluminum from the subsurface is exposed.

The full width at half maximum (FWHM) of both the 1s oxygen line and the 2p aluminum line (Tables 4.3 and 4.4) were calculated from the corresponding profiles and used to measure the line broadening. The width of a measured core level is a convolution of many effects, including (1) the natural line shape of the energy level of the element of interest, (2) the instrument broadening function, and (3) the distribution of different chemical states within the analyzed volume. It can be assumed that effects (1) and (2) were kept constant during the measurements. Therefore, changes in FWHM can be attributed to changes in the distribution of closely related chemical environments found in alumina.

Figure 4.22 a shows the valence band photoelectron spectra of as-received and annealed alumina specimens. The scans were taken after the samples were slightly sputter-cleaned. Two prominent peaks separated by ~ 3.2 eV are observed in the valence band as the main features. The FWHMs of the valence spectra for both the annealed and the as-received samples are equal to ~ 7.2 eV. The annealing produces a small broadening in the upper part of the spectra. These spectra are similar to those reported by Ohuchi et al [99, 100].

Upon laser irradiation in either air or an Ar-4%H_2 atmosphere two main changes happen in the valence band spectra: their width decreases by ~ 10% and the reduction occurs in the low binding energy peak, as seen in Figure 4.22b.

4.3.5 Laser induced topographical change of AlN surface

The surface topographical change of the substrates due to the irradiation was observed with SEM.

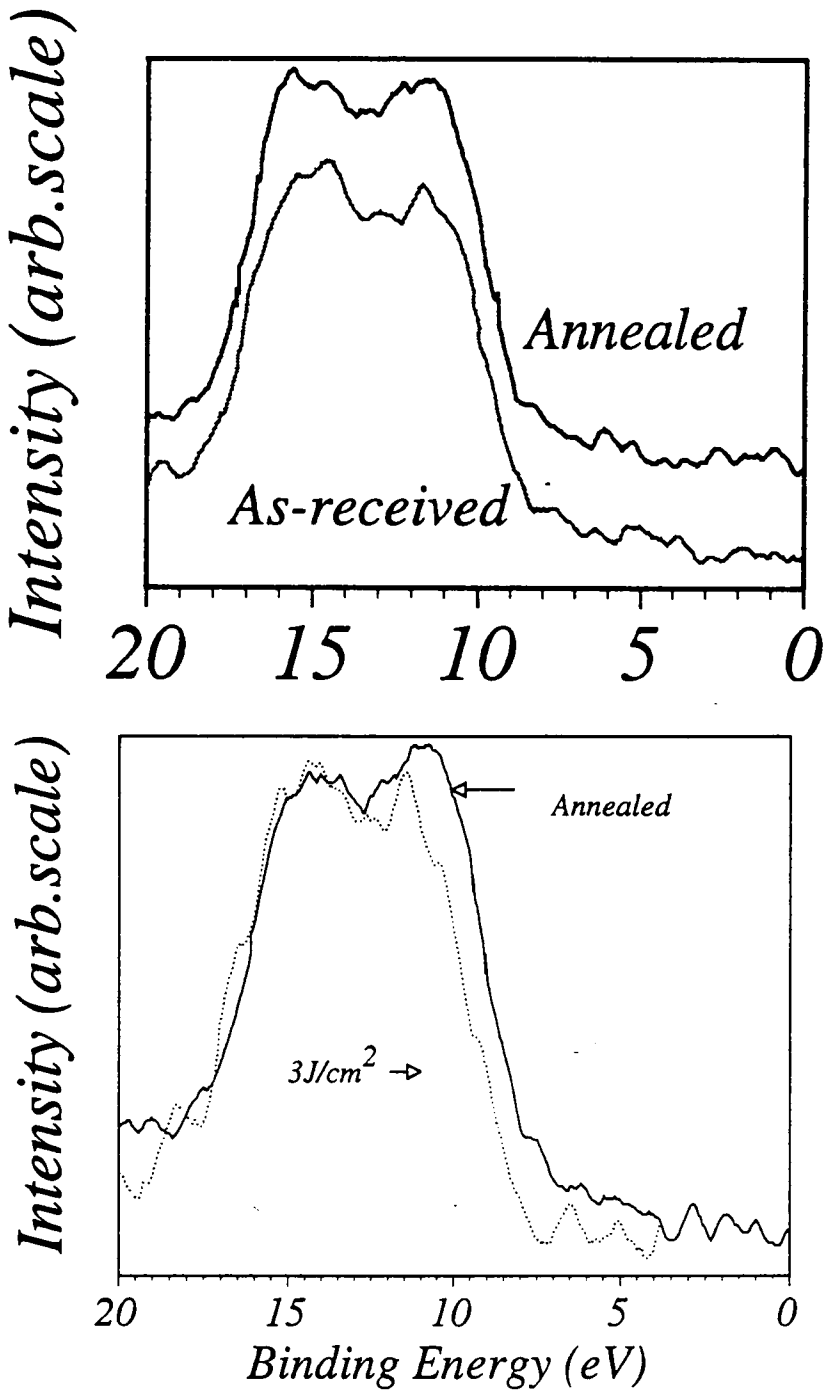

Figure 4.22. (a) Valance band photoemission spectra of as-received and annealed alumina.(b)Valence band photoelectron spectra of annealed and 3J/cm^2 laser irradiated sapphire.

The ceramic surface is usually coated with conductive film for SEM observation because the sample charging due to the excess electrons on the surface often produces distorted SEM images. In this work, although some AlN substrates were not coated with the conductive film, SEM micrographs were successfully obtained. SEM image distortion can be produced by controlling the secondary electron emission. As already explained in the section 2.5.3.3, the factors governing the secondary electron emission are the incident electron energy and current, specimen surface topography, and specimen geometry (tilting angle). The threshold conditions for undistorted imaging of AlN substrate changed before and after the laser energy irradiation. For as-received sample the undistorted image was obtained with *10* kV and 3 nA of incident electron beam, whereas for laser irradiated samples the images could be successfully obtained even with *15* kV and 3 nA of incident electron beam. In both cases the sample stage was tilted to 60°. The fact that the sample charging is less after laser irradiation may be attributed to two reasons, i.e., 1) the surface smoothening that affects to the secondary electron emission and 2) the formation of the metallic aluminum by laser induced decomposition of AlN. However, the major factor must be the metallic aluminum formation because it gives some conductive path in the insulating matrix.

The surface roughness of as-received AlN substrate is $\leq 0.4\mu m$. Figure 4.23 -a and -b are the SEM micrographs of AlN laser irradiated with 0.5 and 0.7 J/cm^2 energy densities in air, respectively. The melting flows can be observed on the surface laser irradiated at 0.7 J/cm^2 , but no melting occurs at 0.5 J/cm^2. Therefore, the threshold energy density for the initiation of the melting may be around 0.7 J/cm^2. The surface topographic changes are significant after laser irradiation as shown in figures 4.24, 4.25a and 4.25b that are obtained from AlN substrates as-received and laser irradiated at 2 and 4 J/cm^2, respectively. The AlN substrates becomes smoother when they are irradiated with higher energy densities. Since the image is obtained with 60° tilting angle, the surface roughness appears more distinctively here than the planar observation as shown in figure 4.23. These three SEM micrographs were obtained without conductive material coating.

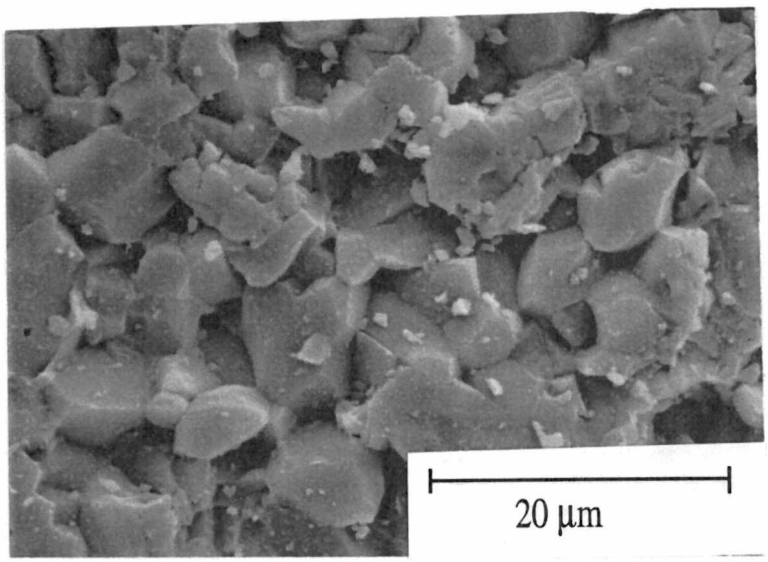

(a)

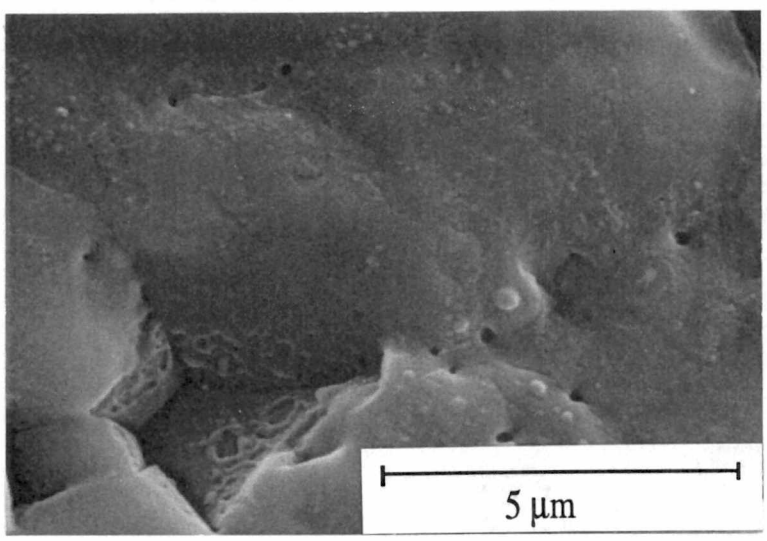

(b)

Figure 4.23. SEM micrographs of the aluminum nitride substrate laser irradiated at 0.5 J/cm^2 (a) and 0.7 J/cm^2 (b) in air.

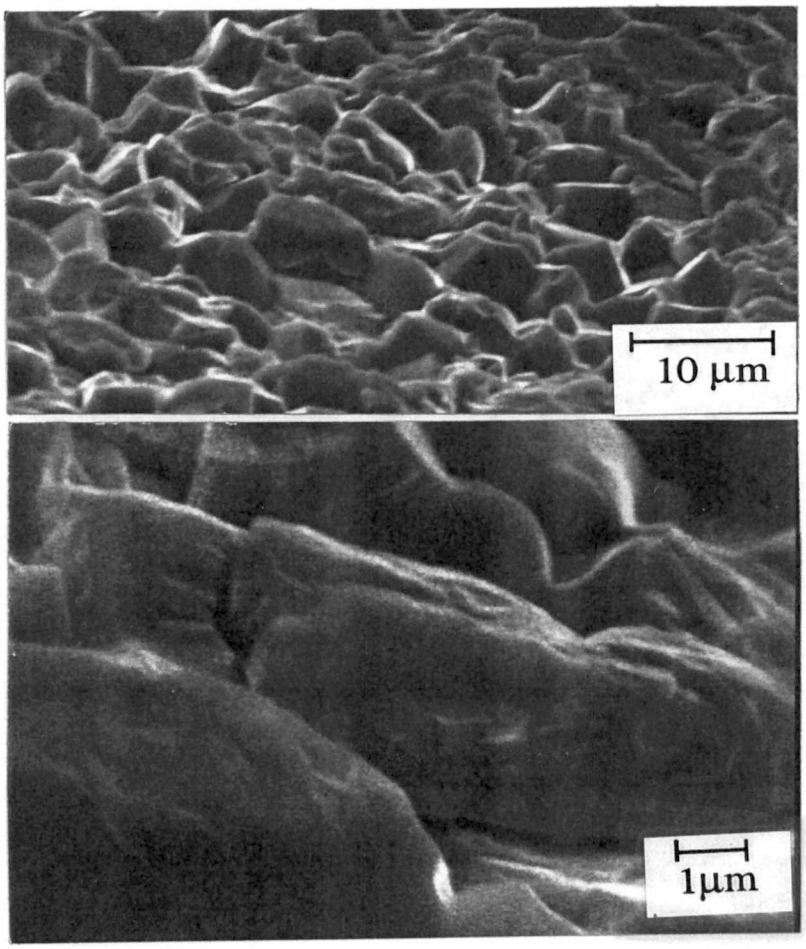

Figure 4.24. SEM micrographs of as-received aluminum nitride substrate. The sample was tilted by 60°.

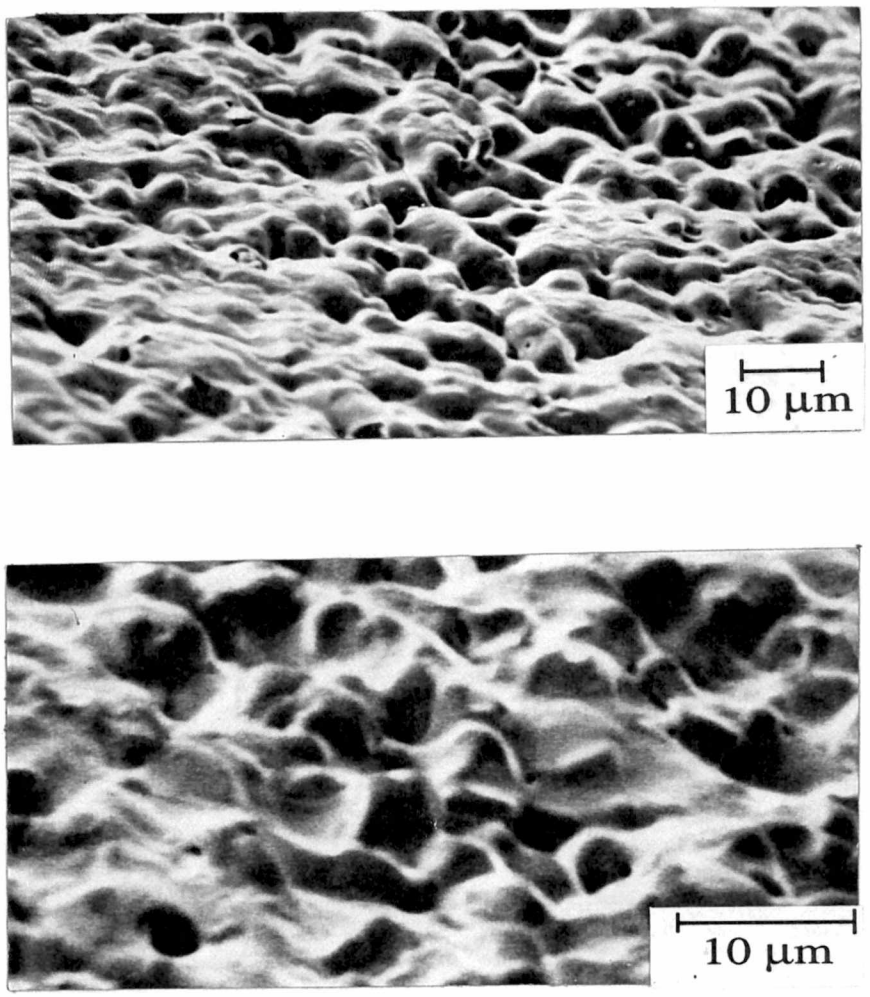

Figure 4.25. SEM micrographs of an aluminum nitride substrate laser-irradiated with 2 J/cm^2(a) and 4 J/cm^2 (b) in Ar-4%H_2. The sample was tilted by 60°.

4.3.6 Distribution of metallic aluminum in the laser irradiated Al_2O_3 and AlN

As shown by AES and XPS analyses, metallic aluminum forms in the laser irradiated alumina and aluminum nitride. AES mapping and TEM techniques have been employed to investigate how the metallic aluminum is formed in the laser irradiated alumina and aluminum nitride substrates. The minimum diameter of the electron beam of AES used in this work is ~2.5 nm as specified in the equipment manual. Therefore, Auger mapping can not resolve the particles or phases whose sizes are less than 2.5 nm.

The mappings were done for AlN substrate laser-irradiated with 1 J/cm^2 in Ar-4%H_2 at 10 kX magnification (figure 4.26). White areas in each mapping denote distributions of the elements under investigation. The metallic aluminum oxidized after it had been exposed for about 10 minutes in the vacuum chamber at a 10^{-9} torr pressure. Therefore, the surfaces were gently sputtered with 0.5 keV for 10 s at every 5 minutes during the data acquisition for metallic aluminum mapping.

Figures 4.26 -a and -b are , respectively, the mappings of metallic aluminum and nitrogen. The holes that appear consistently in each figure are due to the surface topography which electron beams can not reach to or Auger electrons can not emit due to the specimen geometry. Except for the holes, elemental distributions are well consistent. In figure 4.26a, the sizes of the metallic aluminum clusters are $\leq$ ~3 μm. The white area in figure 4.26b roughly corresponds to the dark area in figure 4.29a and vice versa. This means that metallic aluminum and AlN exist in the laser irradiated AlN surface.

Figures 4.27 and 4.28 are TEM micrographs of Al_2O_3 and AlN laser irradiated with 3J/cm^2 in Ar-4%H_2. In figure 4.27, metallic aluminum forms clusters in the alumina matrix and the sizes are $\leq$ ~ 20 nm. Therefore, Auger mapping of the laser-irradiated alumina to detect the metallic aluminum distribution was not applicable in this work. Figure 4.28 shows that Al patches are formed on the irradiated AlN surface and non-decomposed AlN particles are embedded in the Al patch. The result of figure 4.28 agrees with the results obtained by Auger mapping technique shown in figure 4.26.

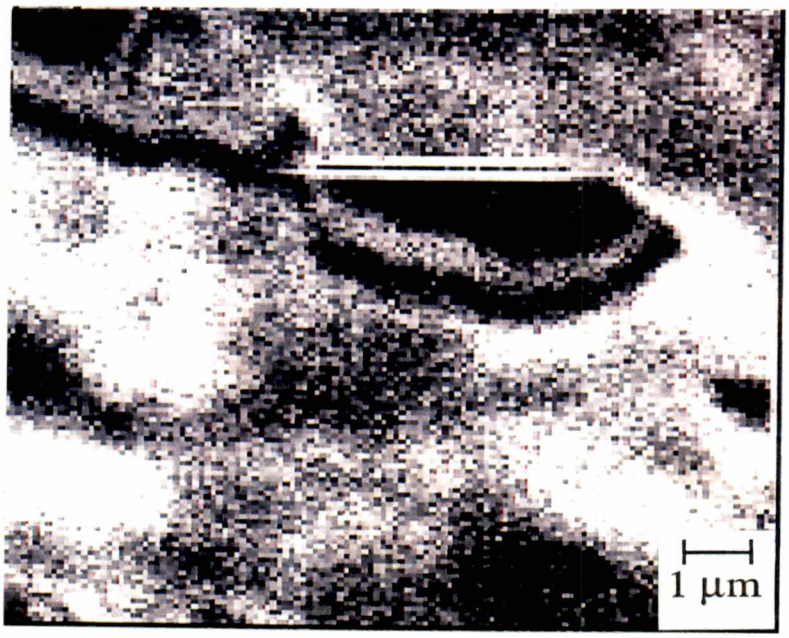

(a)

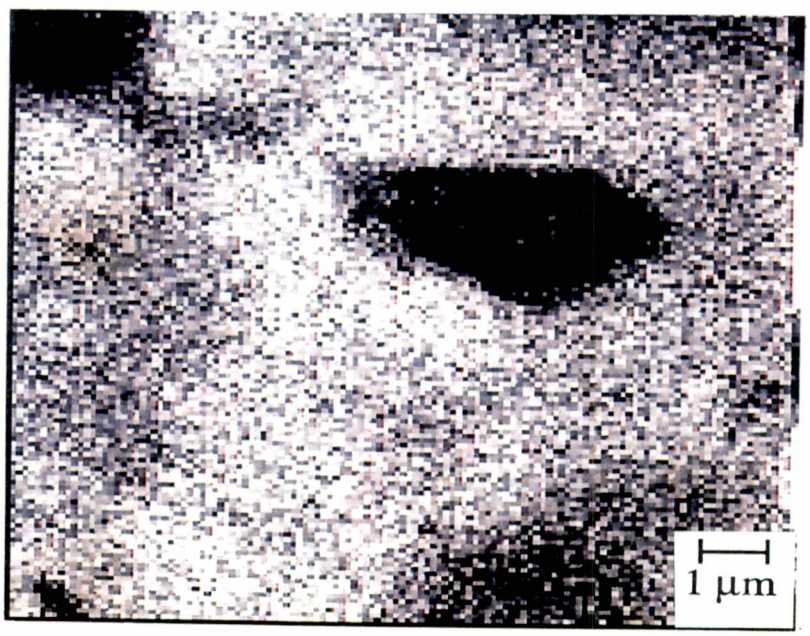

(b)

Figure 4.26. Auger mappings of metallic aluminum (a) and nitrogen from AlN (b) in AlN substrate laser-irradiated with 1 J/cm^2 in Ar-4%H_2.

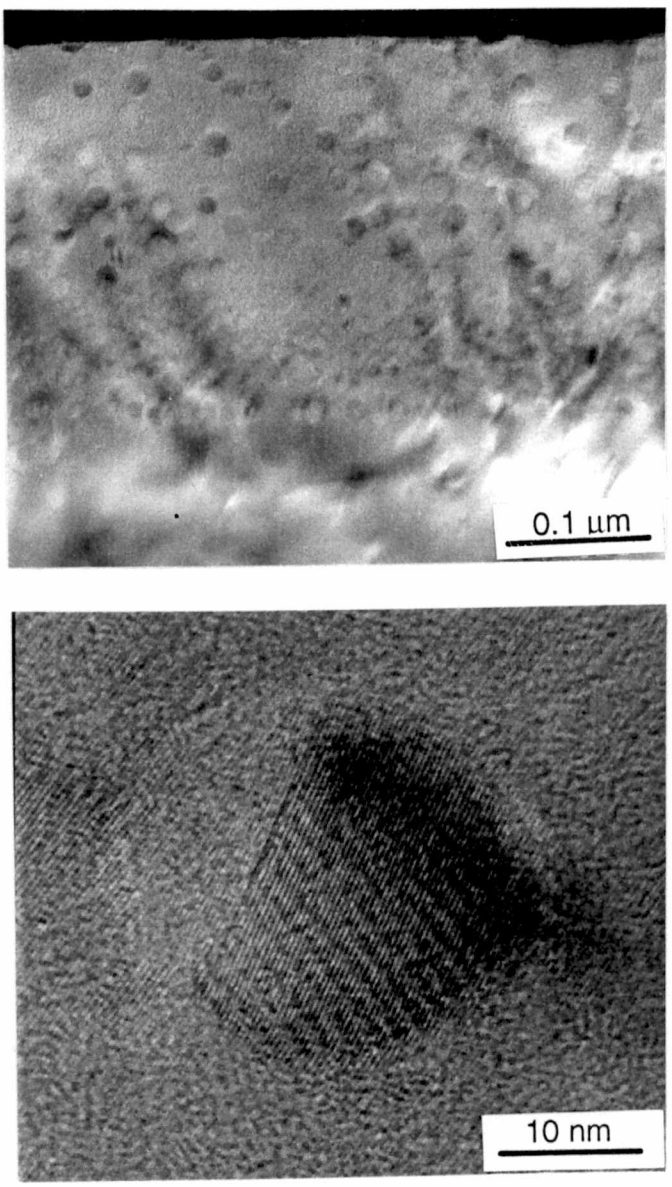

(a)

(b)

Figure 4.27. TEM micrographs of alumina laser-irradiated with 3 J/cm^2 in Ar-4%H_2 atmosphere. The size of metallic aluminum particles is ~ 20 nm. Small aluminum particles are seen in melted and solidified region by laser irradiation (a) . Micrograph (b) is a high resolution TEM of an aluminum particle.

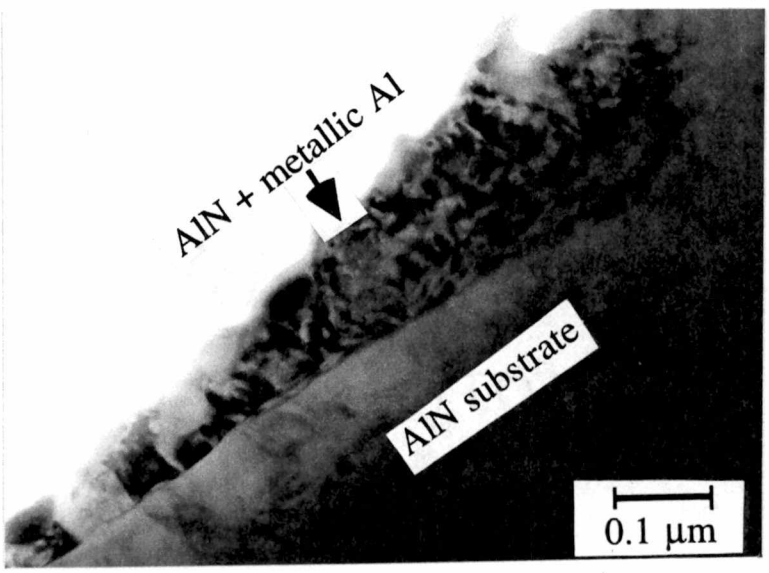

Figure 4.28. Cross-sectional TEM micrograph of AlN laser-irradiated with 50 pulses of 3 J/cm^2 energy density. Undecomposed AlN particles are embedded in the metallic aluminum cluster.

4.4 Ion bombardment effects of sapphire surface

No alumina reduction was detected after 3 keV Ar^+ ion irradiation at a current of 70 nA for 3 min. In this case, the Al LVV spectrum remained unchanged as compared to that from as-received sample, as shown in figure 4.29. After bombardment with 7 keV Ar^+ ions for the same time and a current of 130 nA, the 68 eV Al LVV peak from metallic aluminum became visible, indicating the reduction of the sapphire (figure 4.29). The amount of metallic aluminum increased further after 4 min. irradiation. Together with metallic aluminum, Al KLL from Al_2O_3 was also detected, indicating that reduction took place in part of the surface only.

The sputtering yields of oxygen and aluminum atoms from an Al_2O_3 target bombarded with 3 keV and with 7 keV Ar^+ ions were calculated using the TRIM computer simulation program [85]. The calculated ratio of oxygen to aluminum sputtering rates indicates that the Al_2O_3 surface bombarded with either 3 or 7 keV Ar^+ ions should become enriched in aluminum by ~6%. In the case of 3 keV ions the sputtering yields of aluminum and oxygen atoms per incident ion are 25% less than that for 7 keV ions. These results suggest that at a sufficiently high fluence Al_2O_3 would also be reduced by 3 keV Ar^+ bombardment.

4.5 AES studies on the metallic films/ceramics interfaces

The metal/ceramic interfacial reactions can be studied with AES as a function of metallic film deposition on the substrate. In our work, however, the real processing conditions could not be reproduced in the AES instrument. For instance, we could not attach the laser equipment to the AES vacuum chamber. Besides the practical problems, this method gives arise to another problem when the substrate is a wide band gap material. That is, surface charging during AES analysis can be changed as a function of deposited film thickness causing artificial peak shifts.

In this work the interface was analyzed as a function of reducing film thickness. In spite of several problems with this method such as ion-bombardment

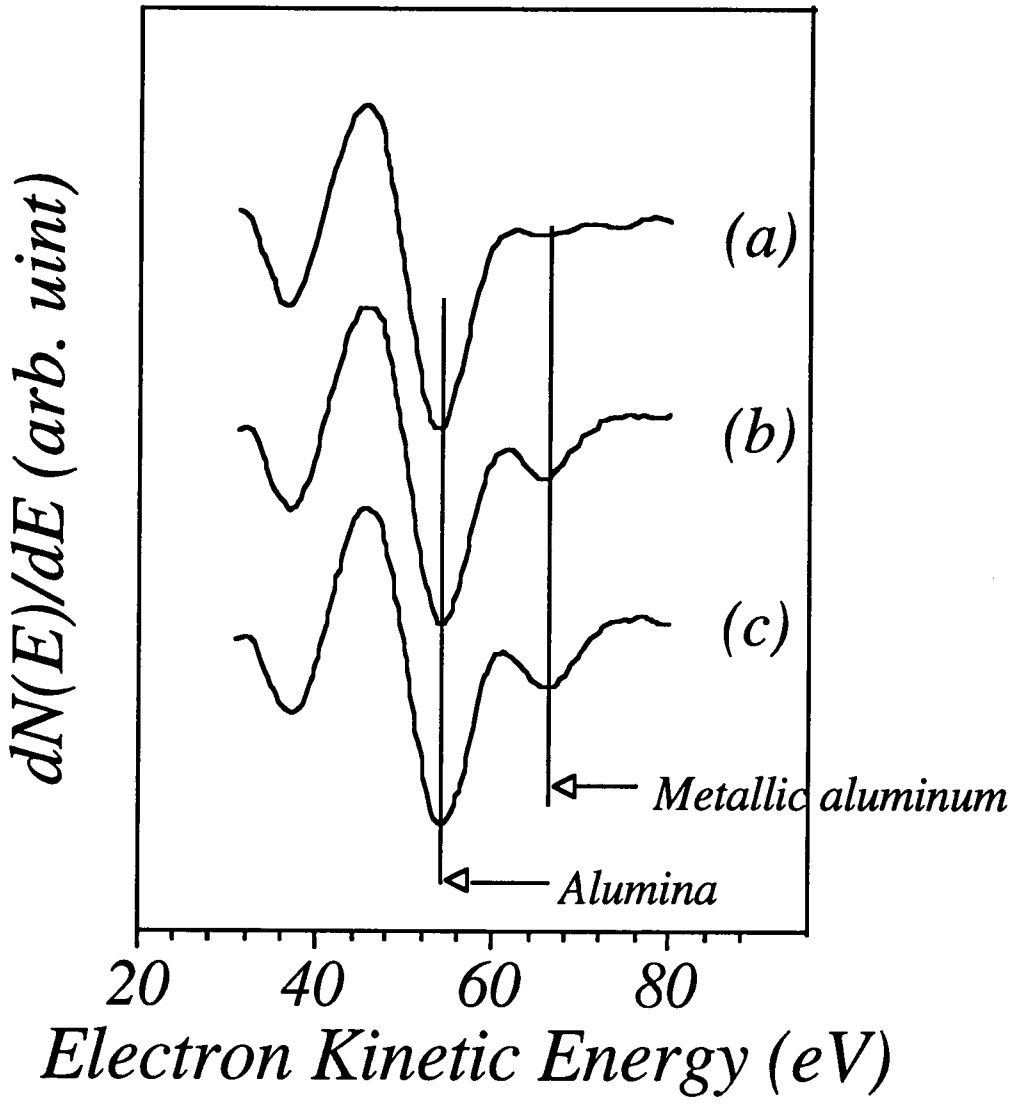

Figure 4.29. Al LVV spectrum of Ar^+ ion bombarded Al_2O_3 : (a) 3 keV ions, 70 nA, 3 min; (b) 7 keV, 130 nA, 3 min; (c) 7 keV, 130 nA, 4 min.

induced damages, mixing, and the sputtering depth resolution [101, 102] , careful use of sputter-etching (using low energy ion) allowed us to analyze the interface formed by the real processing.

Unless otherwise mentioned, in this work all the Auger spectra were differentiated.

4.5.1 Interface of copper/alumina couples

Although copper and alumina are non-reactive to each other, sometimes a strongly adherent copper film on as-received alumina was produced upon a 500°C anneal. However, strong bonding in these couples was not always obtained. Strong adhesion was always obtained when the couple with the substrates irradiated in air at ≥ 1 J/cm^2 were annealed at 300°C for 1 hr. When the couple irradiated in Ar-4%H_2 was annealed at 300°C for 1 hr, the adhesion was very weak; however, an elevated temperature annealing (500°C) produced very strong bonding. The interface of these strongly and weakly bonded couples were analyzed with AES to discover the adhesion mechanism. Prior to the interface analysis, the copper oxides thermally produced on the surface of copper films were studied and the standard peak positions were obtained.

4.5.1.1 Copper oxide thermally produced on the deposited copper film

When the copper film is annealed at 500°C in $5x10^{-6}$ torr vacuum pressure, copper oxides formed on its surface with a thickness of ~ 6 nm. The thickness of the oxide layer generally depended on the annealing conditions such as vacuum pressure and temperature. AES peak spectra showed distinctive differences for both copper and oxygen in the oxidized and elemental states of copper. On the surface of this sample the peak positions of differentiated O KLL and Cu LMM were ~ 512 eV (figure 4.30a (i)) and ~ 918 eV (figure 4.30b), respectively. When the surface was slightly sputtered, the O KLL peak shifted in the lower kinetic energy direction by ~ 3 eV (figure 4.30a (ii)) and the Cu LMM toward a higher kinetic energy by ~ 1 eV (figure 4.30b(ii)) and then further by ~1

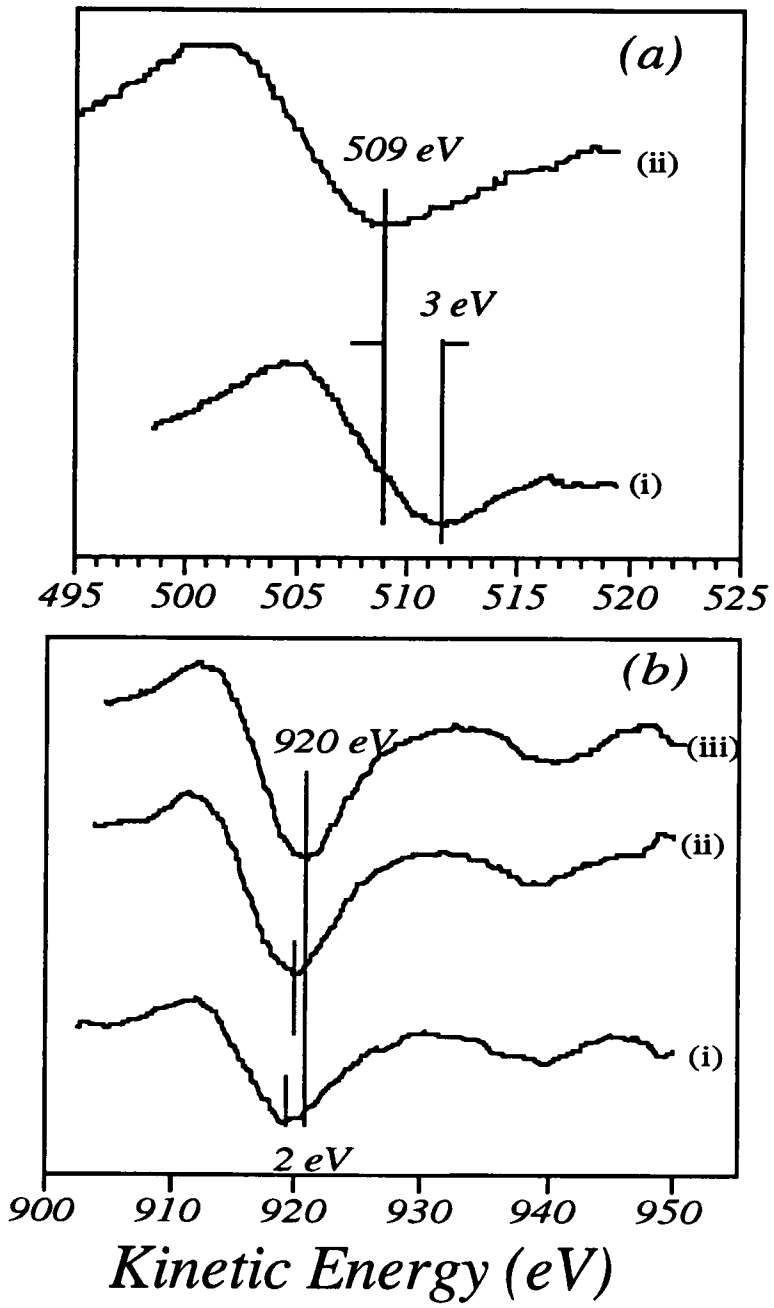

Figure 4.30. O KLL (a) and Cu LMM (b) peak spectra from the copper oxide grown on the copper film. Cu_2O and CuO form, respectively, on the surface and in the subsurface. Peak (i) is from the surface, and peaks (ii) and (iii) are from the subsurface.

eV (iii). Peak iii in figure 4.30b is from elemental copper, because further sputtering did not change the peak positions any more.

Assuming that two possible oxidation states of copper are cuprous oxide (Cu_2O) and cupric oxide (CuO), the 918 eV peak should be from Cu_2O that was detected on the surface and the 919 eV peak should be from CuO detected in the subsurface, because it was reported that Cu LMM peak position from Cu_2O is ~1 eV less than that from CuO [103, 104]. Accordingly, the 512 eV O KLL peak should be from Cu_2O and the 509 O KLL from CuO. However, the peak positions determined in this work are slightly different from those they reported [103, 104] . The difference may be due to different energy calibration and static charging of the samples. However, the differences of peak positions obtained in this work were consistent with their works. Here, our standard O KLL peak positions from Al_2O_3, CuO, and Cu_2O were, respectively, ~ 506 eV as obtained from as-received Al_2O_3 substrate, ~ 509 eV, and ~ 512 eV, and the Cu LMM peak positions from elemental copper, CuO, and Cu_2O were ~ 920 eV, ~ 919 eV, and ~ 918 eV, respectively. The analysis was focused on the relative peak shifts and shape changes.

4.5.1.2 The interface of Cu/as-received Al_2O_3 couple annealed at 500°C

O KLL and Al KLL peaks were used for the analysis. As the interface was approached by sputter etching, the O KLL peak at ~ 512 eV (figure 4.31a(i)) and the Al KLL at ~ 1392 eV (figure 4.31b(i)) were detected. As progressing the sputter etching, oxidation states are changing from Cu_2O (~ 512 eV) to Al_2O_3 (~ 506 eV). Peaks (iii) and (iv) in figure 4.31a located at ~ 508 eV appear to correspond to oxidation states other than Cu_2O (512 eV), CuO (509 eV), and Al_2O_3 (506 eV). On the other hand, the Al KLL peaks are firstly detected at ~ 1392 eV and then from stoichiometric alumina (~ 1388 eV).

4.5.1.3 Couple with substrate laser-irradiated in air at 1 J/cm^2

This couple showed very strong bonding after annealing at 300°C for 1 hr.

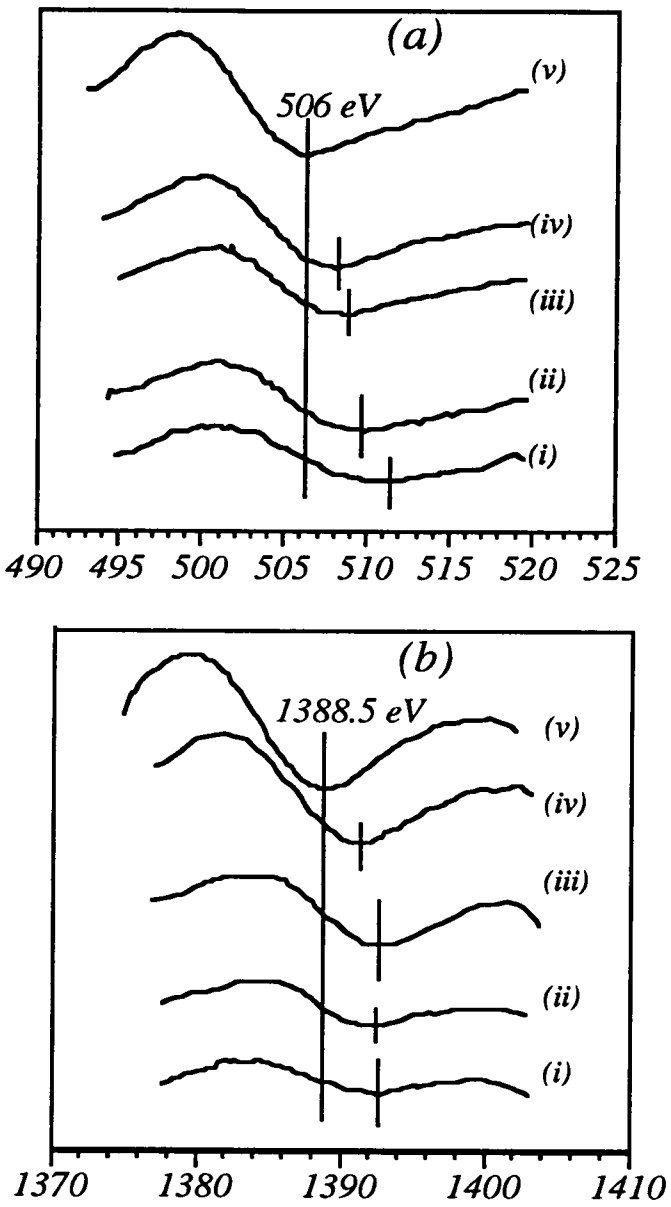

Figure 4.31 O KLL(a) and Al KLL(b) Auger spectra at the interfacial region of Cu/ as-received Al_2O_3 couple annealed at 500°C. As progresses sputtering the O KLL peak changes from that of copper oxide (peak 1) to that of Al_2O_3 (peak v) (a), and Al KLL peaks are firstly at 1392.5 eV (peaks i, ii, and iii) and then at 1388 eV (peak v) (b).

Figure 4.32 shows the differential oxygen Auger peaks that appear between the surface of the copper film and the bulk substrate. The peak position of Cu LMM Auger spectrum from the surface is about ~ 918.3 eV whereas inside the film it is ~ 920 eV. The difference in kinetic energy between the copper peak measured at the surface and the one measured inside the film is ~1.7 eV. Therefore, it seems that surface oxygen is in Cu_2O. The copper peak at the interface is also shifted ~ 1.7 eV towards the lower values of the kinetic energy, consistent with the presence of an oxide at the copper/alumina interface (figure 4.32).

The oxygen peak that corresponds to the copper oxide on the surface disappeared when the surface was slightly sputtered (figure 4.33). Further sputtering revealed two oxygen Auger peaks (figure 4.33). The peak positions are ~ 508 eV and ~ 512 eV. The higher kinetic energy peak should be from Cu_2O, but the lower kinetic energy peak does not appear to come from Al_2O_3 since the O KLL kinetic energy from Al_2O_3 is 506 eV. Copper oxide and aluminum oxide may exist at the interface in Cu-O-Al compound. This will be shown more in detail in the next sections.

4.5.1.4 Couple with substrate laser-irradiated in Ar-4%H_2 at 1 J/cm^2

Pull test showed that the adhesion of copper thin film sputter-deposited onto alumina substrate laser-irradiated with energy density ≥ 1 J/cm^2 in Ar-4%H_2 atmosphere was very poor on low temperature (300°C) annealing, but higher temperature (500°C) anneal produced very strong adhesion of the couple. AES studies were also performed for these couple to investigate the interfacial reactions.

Figure 4.34 shows oxygen KLL Auger peak spectrum across the interface. Right below the copper film O KLL Auger peak (i) is from the copper oxide (512 eV) and subsequent sputtering reveals the oxygen KLL at ~ 507 eV (ii). Further sputtering reveals slightly broadened O KLL peaks (iii-iv). Eventually the stoichiometric alumina is revealed (v).

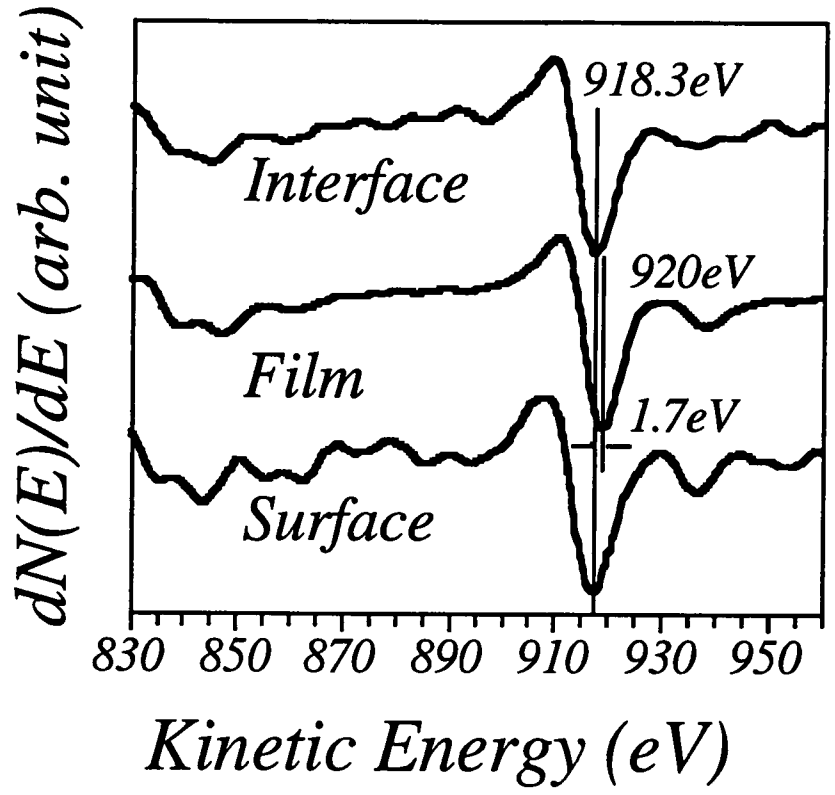

Figure 4.32. Cu LMM Auger peaks from copper film / laser-irradiated ($1J/cm^2$) alumina couple annealed 1h at 300°C. The copper Auger spectrum at the interface are very similar to the surface spectrum, revealing the existence of copper oxide at the interface.

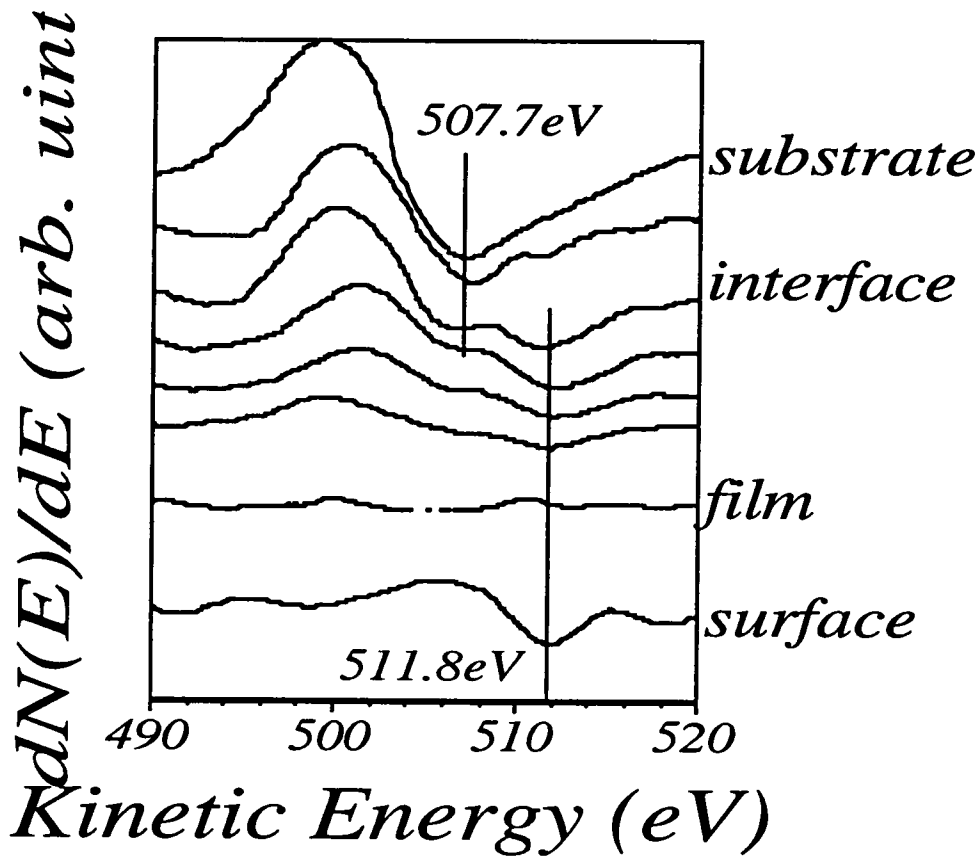

Figure 4.33. Auger peaks from a copper film / laser-irradiated alumina couple annealed 1h at 300°C. At the interface, the oxygen exists in two different oxidation states, implying that a Cu-Al-O compound formed at the interface.

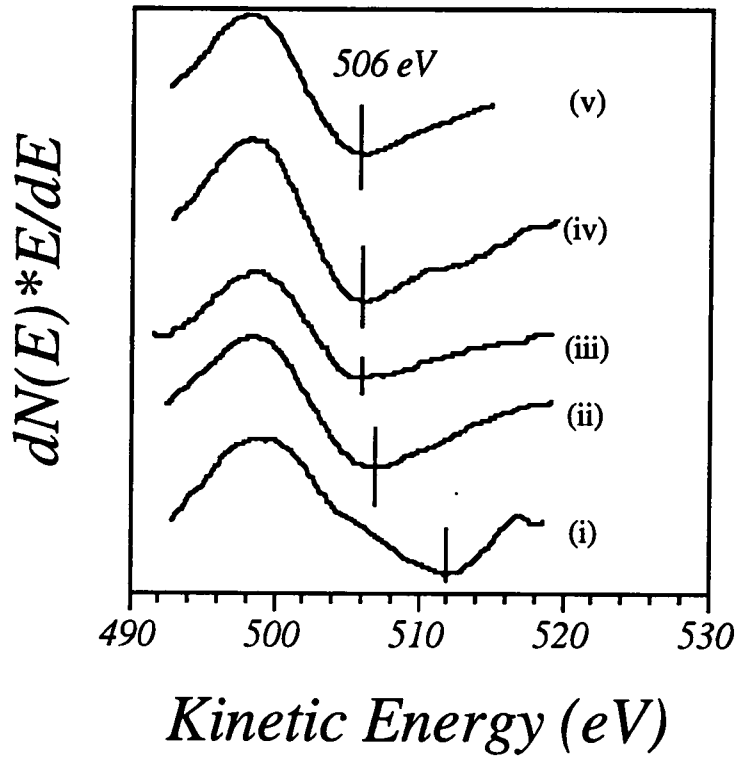

Figure 4.34. Oxygen KLL Auger spectra across the interface of copper film/ alumina couple with substrate laser irradiated in Ar-4%H_2 atmosphere at 1 J/cm^2. Annealing was done at 500°C for 1 hr.

Direct Auger peaks were also used to investigate the changes associated with reactions between copper and the irradiated alumina substrate. The CuLMM Auger peak in the kinetic energy range of 900 to 940 eV was used for the analysis.

The variations of the copper Auger peaks across the interface are shown in figure 4.35. Peak (i) is Cu LMM from the film. Peak (ii) is shifted toward lower kinetic energies by about ~ 2 eV relative to peak (i), thus, it is from a copper oxide that is in the interface. As the sputtering progresses further, copper Auger peak similar to that from the film appears (iii), but it is broadened in the lower kinetic energy direction and new fine structures are also seen in the lower kinetic energy region.

Figure 4.36 is Al KLL spectra across the interface. When acrossing the interface by sputter etching, Al KLL peaks with metallic aluminum features are detected (i and ii). Peaks i and ii are from different sputtering cycles. Peak (i) shows more distinctive metallic aluminum than peak (ii) . This result is consistent with AES analysis of laser irradiated alumina surface. That is, metallic aluminum and substoichiometric (oxygen deficient) alumina exist in the subsurface of the irradiated alumina.

4.5.1.5 Interface of Cu/alumina irradiated in Ar-4%H_2 at 3 J/cm^2

The adhesion of this couple was very weak when it was annealed at 300°C, but, similar to the case with the substrate irradiated at 1 J/cm^2, a 500°C anneal produced very strong adhesion.

O KLL peaks in the vicinity of the interface were investigated (figure 4.37) . In this couple the copper oxide layer at the interface is much narrower than the layer present in the couple irradiated with 1 J/cm^2, as obtained by the AES depth profiling. As the interface is approached, the O KLL peak was first at ~ 508.5 eV (i) and then at 506 eV (ii) from the substrate. Obviously, the O KLL is not from cuprous oxide (Cu_2O).

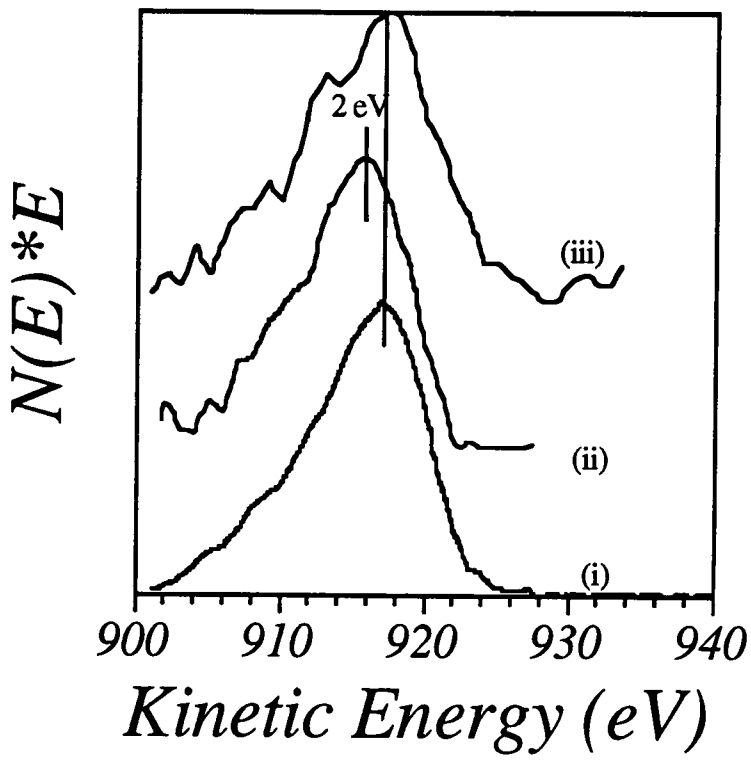

Figure 4.35. Direct Auger spectra of Cu MLL at the interface between copper film and alumina substrate laser irradiated in Ar-4%H_2 atmosphere with 1 J/cm^2. The couple was annealed at 500°C for 1 hr.

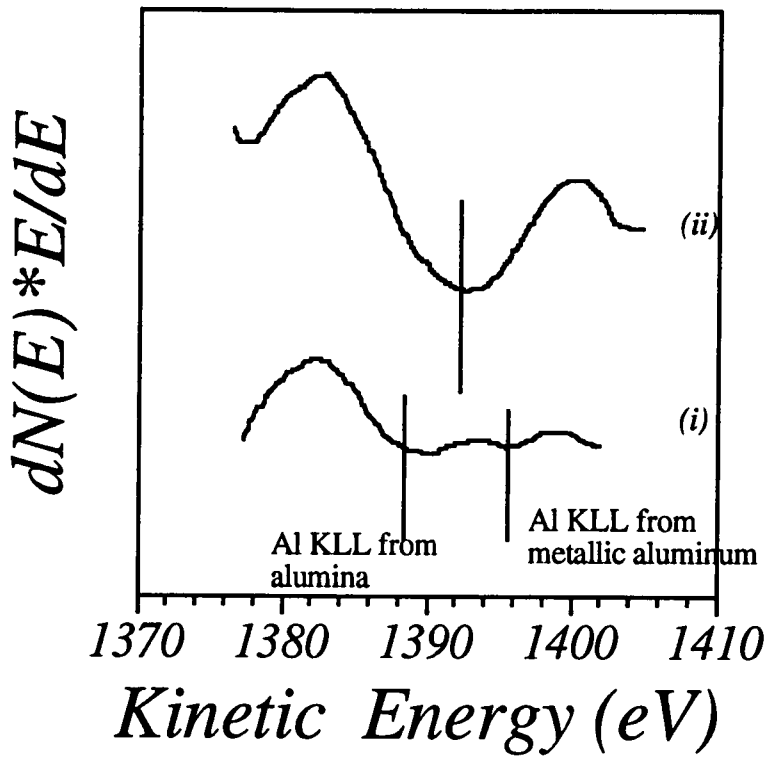

Figure 4.36. Al KLL Auger spectra across the interface of copper film/ alumina couple laser irradiated in Ar-4%H_2 at 1 J/cm^2. Annealing was done at 500°C for 1 hr. Peak (i) is closer to the interface than peak (ii).

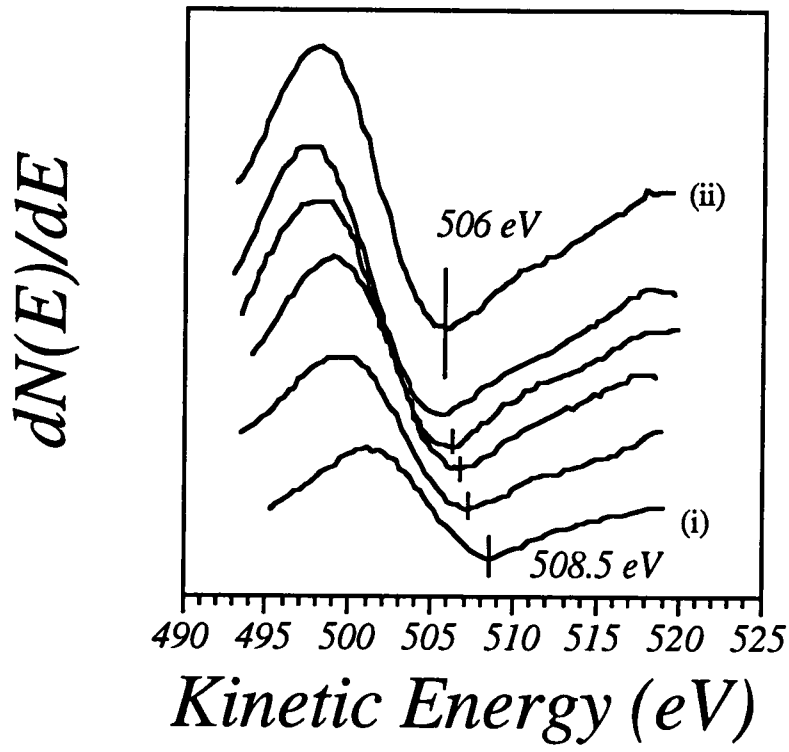

Figure 4.37. O KLL peaks across the interface of copper film/alumina irradiated in Ar-4%H_2 at 3 J/cm^2. The couple was annealed at 500°C for 1 hr. Peak (i) is toward the film and peak (ii) is from the substrate.

4.5.2 Interface of gold/alumina couples

Substrate irradiation in oxygen promotes a very strong bonding in Au / Al_2O_3 couples while the irradiation in Ar-4%H_2 generates very weak bonding in these couples [105]. A post-deposition annealing at 300°C for 1 hr increases the adhesion strength by approximately one order of magnitude relative to gold film deposited on unirradiated substrates [105]. The interfaces of weakly and strongly bonded couples with irradiated substrates were analyzed with AES.

Figures 4.38 -a and -b show the differential Auger electron spectra of Au NVV and Al LMM peaks, for gold- alumina couples. The alumina substrates were irradiated in oxygen (figure 4.38a) and in Ar-4% H_2 (figure 4.38b), as described above. The spectra presented here for different sputtering times were selected from a large data base in order to encompass the gold-alumina interface region. The Al peaks from the alumina with kinetic energies of 38 and 54 eV overlap with the Au peaks at 44 eV and 56 eV.

Oxygen KLL peaks for the same sputtering times as those of figure 4.38, and with substrates irradiated in oxygen and in Ar-4% H_2 are shown in figures 4.39 -a and -b, respectively. In figures 4.40 -a and -b the Al KLL peaks are shown for the same conditions as those of figures 4.38a and b. (1) and (2) peaks in each figure are mostly from the gold film and (3) and (4) peak signals are mostly from the interface. Peaks (5) in each figure are from the substrate.

In the interface region of Au-alumina couples with substrates irradiated in oxygen, the Au NVV Auger peak shifts 1.5 eV to a lower kinetic energy relative to pure gold (figure 4.38a). For the couple whose substrate has been irradiated in oxygen, the O KLL and Al KLL peaks shift 1.6 eV and 1.2 eV (figure 4.39a), respectively, from their bulk values toward higher kinetic energies (figure 4.40a). In contrast, no shift in the Au NVV Auger peak is detected at the interface level when the substrate was irradiated in Ar-4%H_2 (figure 4.38b). Also, there is no shift in the Al KLL and O KLL peaks when the substrate was irradiated in Ar-4%H_2 (figure 4.39b and 4.40b). These results indicate that there is no reaction

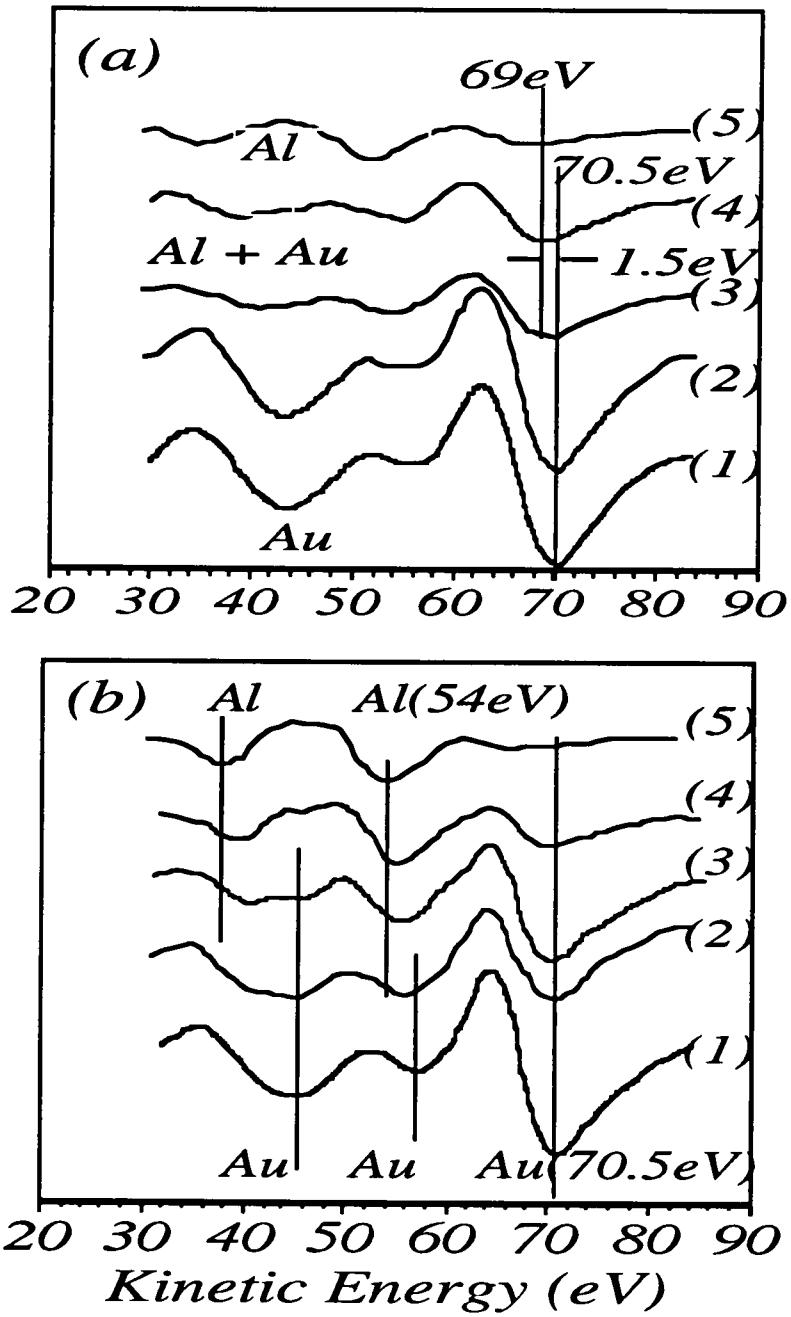

Figure 4.38. Au NVV peaks for gold films deposited on alumina substrates laser-irradiated at 1J/cm^2 in oxygen (a) and in Ar-4%H_2 (b). When the film-substrate interfaces are exposed, upon sputtering with Ar^+ ion, the Auger peaks for gold are shifted from the film peaks about 1.5 eV toward lower kinetic energies in (a), and do not shift at all in (b).

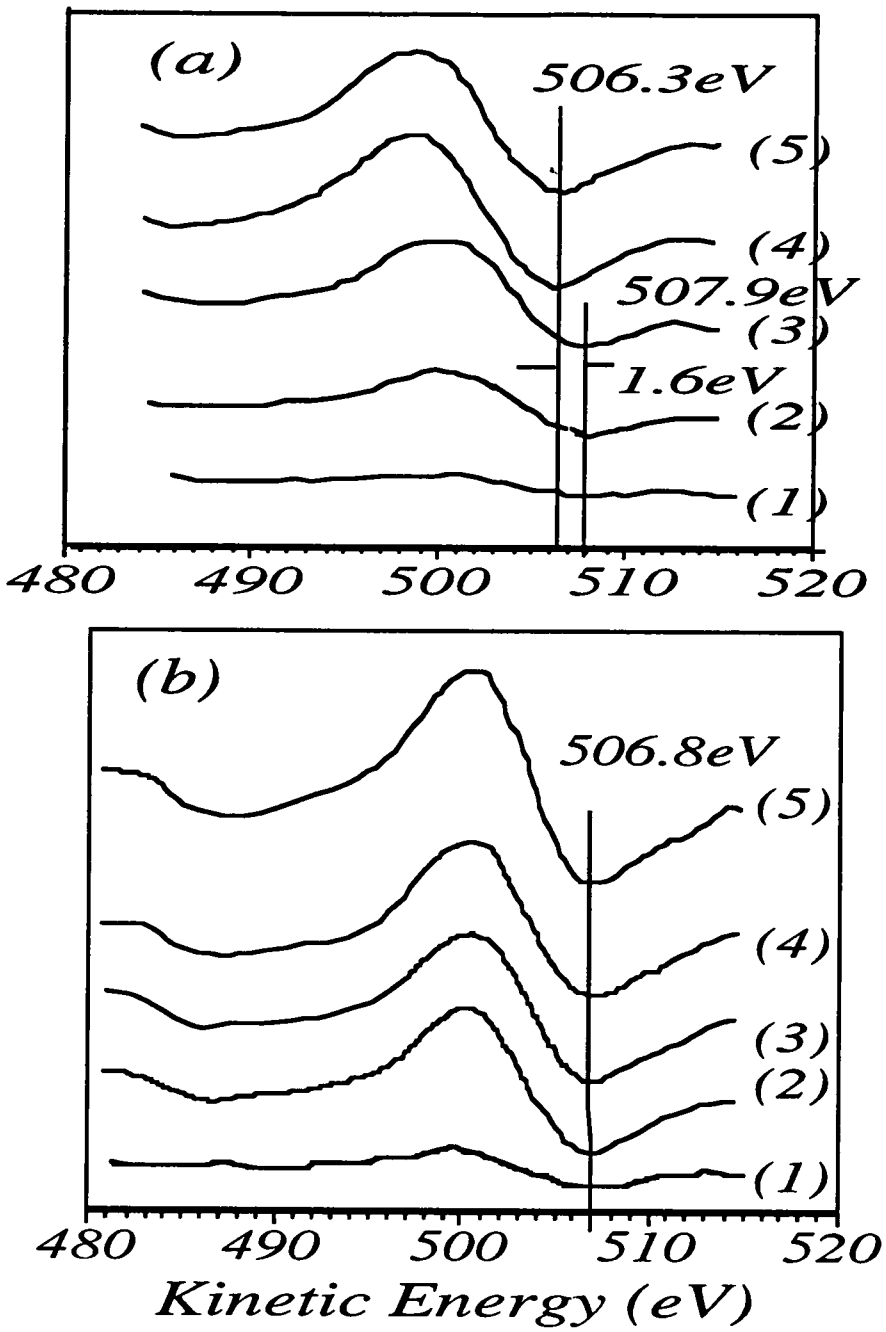

Figure 4.39. Oxygen KLL peaks for gold films deposited on alumina substrates irradiated with a laser energy density of 1J/cm^2 in oxygen (a) and in Ar-4%H_2 atmosphere (b). At the interface, the oxygen peak shifted by 1.6 eV from the peak of bulk alumina to lower kinetic energies for laser irradiation in oxygen but no shift was detected for the irradiation in Ar-4%H_2.

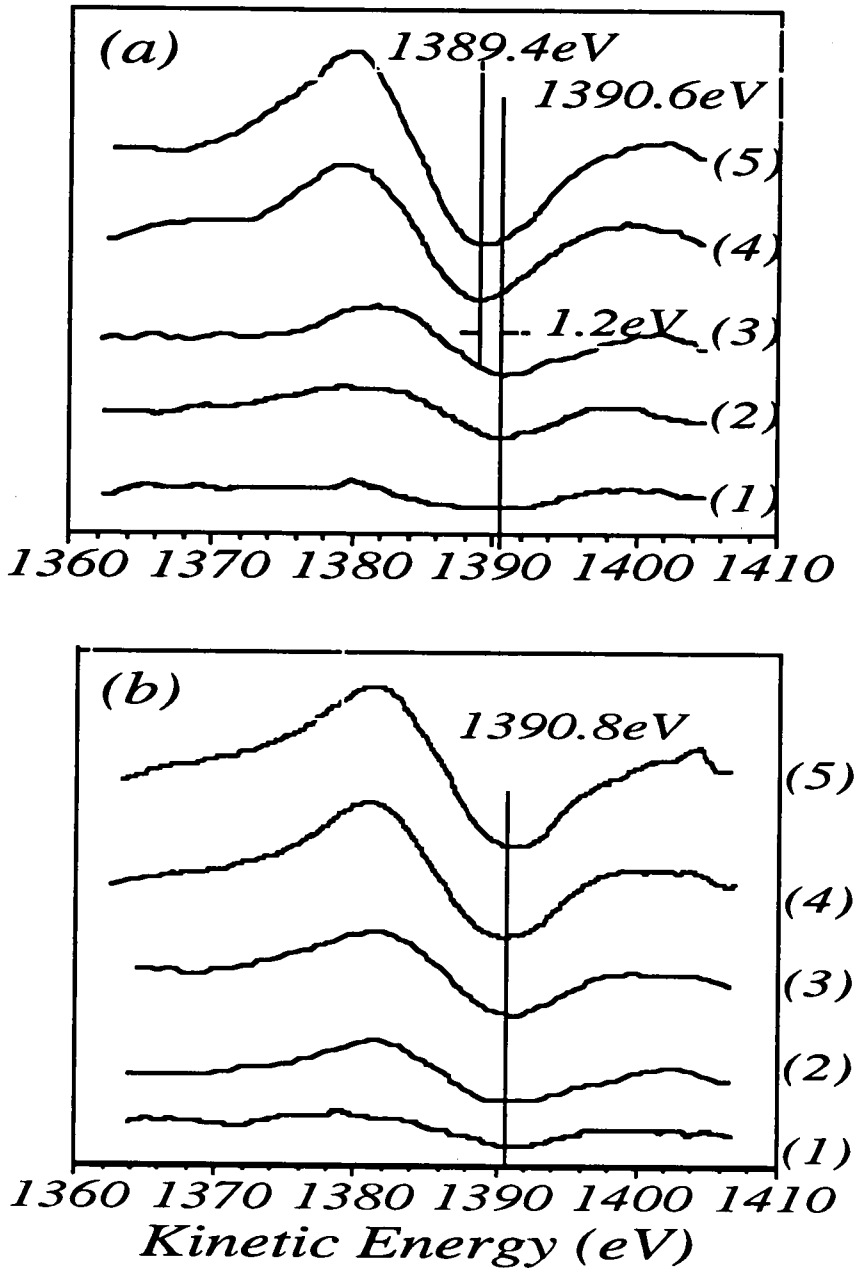

Figure 4.40. Al KLL peaks for gold films deposited on alumina substrates irradiated with a laser energy density of 1J/cm^2 in oxygen (a) and in Ar-4%H_2 atmosphere (b). The peak positions from two substrates are different: (a):1389.4 eV, (b): 1390.6 eV. This implies that there is a different stoichiometry at each surface.

4.5.3 Interface of copper/aluminum nitride couples

As shown in figure 4.1 the adhesion strength of Cu/AlN couples is lower for laser irradiated substrates than for unirradiated ones annealed at 300°C annealing. However, 500°C annealing of couples with irradiated substrates enhanced the adhesion to the maximum strength measured in this work (figure 4.2). The interfaces of couples with substrates irradiated at laser energy densities of 0.3 and 3 J/cm^2 in air and 1 and 1.5 J/cm2 in Ar-4%H_2 were analyzed with AES. The first two samples were annealed at 300°C and the third sample was annealed at 500°C. Preliminary analysis of these couples indicated that there is a strong relationship between the amount of oxygen at the interface and bonding strength. As shown in previous sections, the surface of aluminum nitride substrates used here exhibited a mixture of Al_2O_3 and AlN. Therefore, the analysis was focused on the elemental profiles as well as their chemical states. Cu LMM, Al KLL, O KLL, and N KLL peaks were used for the depth profiling at the interface. Sputtering conditions used in this work were almost the same for all the profiles (1 KV and 20 nA).

4.5.3.1 Interface of copper/AlN irradiated in air at 0.3 J/cm^2

Figure 4.41 is a depth profile of the Cu/AlN irradiated in air at 0.3 J/cm^2. Oxygen increases as the interface is approached along with aluminum and nitrogen, implying that the substrate surface oxide layer was not eliminated by the laser irradiation. Similarly to the strongly adherent copper/alumina couples, at the interface copper oxides were detected (figure 4.42a). In figure 4.41a, differentiated O KLL was first detected at ~512 eV , and then, after copper oxide layers disappear, the O KLL shifts to 507 eV and nitrogen from AlN was detected.

In the interface the copper peak shift by ~ 1 eV as sputtering progresses, implying the formation of copper oxide (figure 4.42b). Al KLL detected at the interface in this couple is ~ 1391 - 1392 eV (figure 4.42c). This is indicative of the non-stoichiometric Al_2O_3 and/or AlN at the interface.

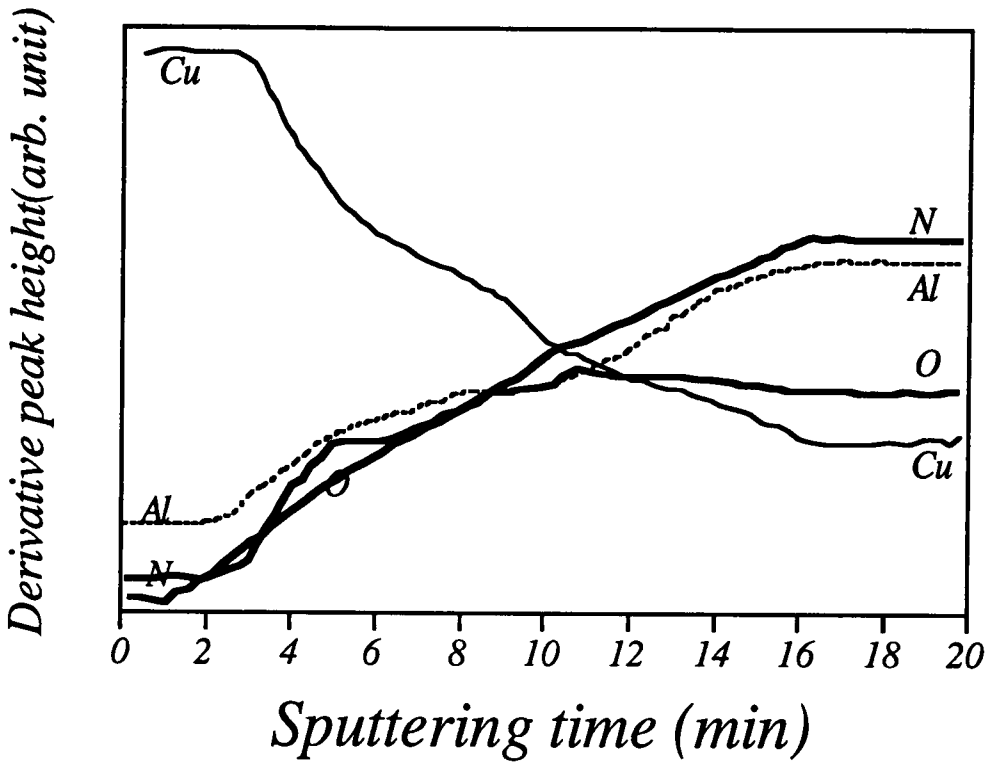

Figure 4.41. Depth profile of Cu/AlN laser-irradiated with 0.3 J/cm^2 in air atmosphere. The couple was annealed at 300°C for 1 hr in a vacuum pressure of 10^{-5} torr. As the interface is approached to the oxygen increases along with the aluminum and the nitrogen.

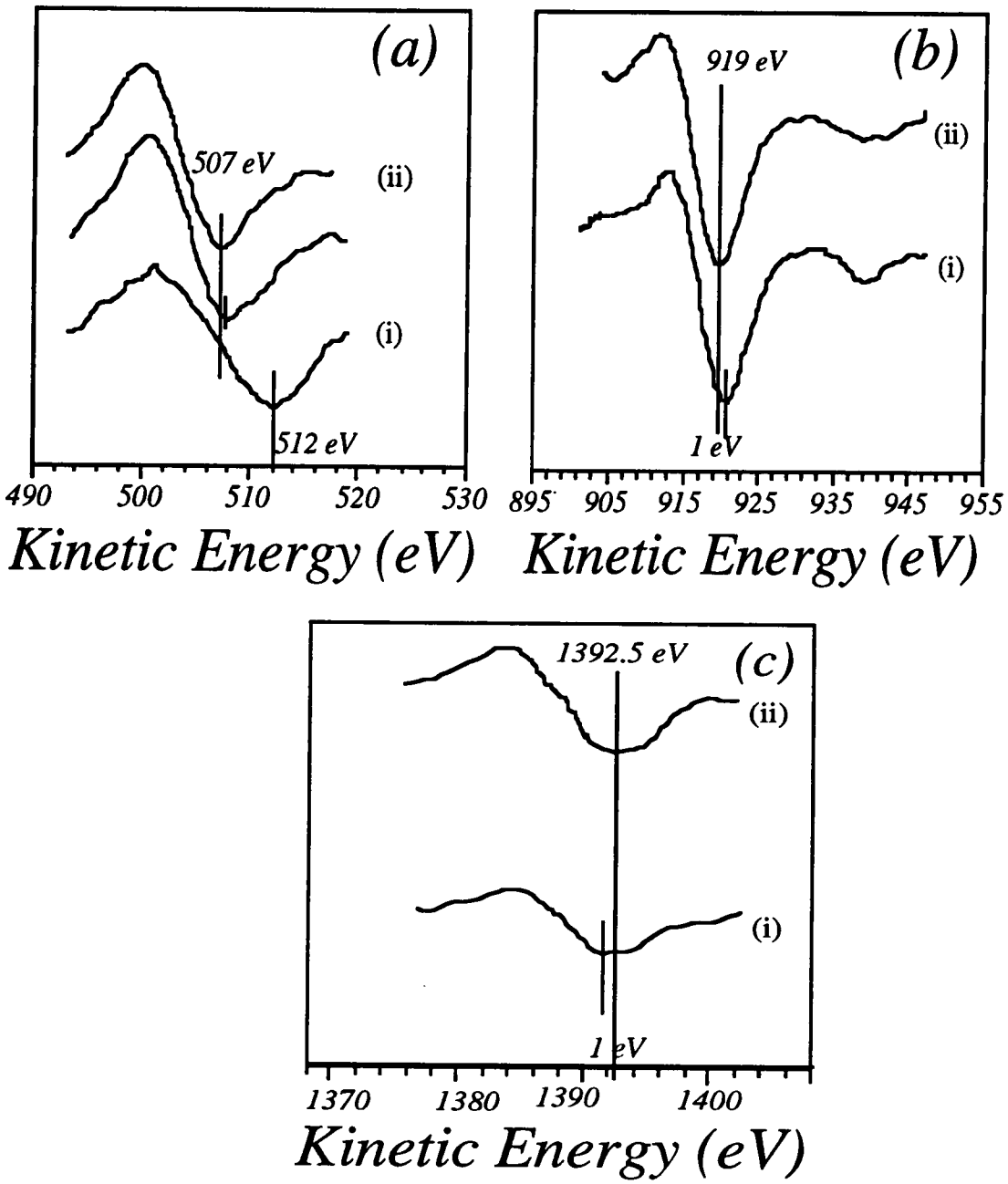

Figure. 4.42 O KLL, Cu LMM, and Al KLL peaks across the interface of Cu/AlN couple irradiated in air at 0.3 J/cm^2. Copper oxide and non-stoichiometric Al_2O_3 or AlN exist at the interface.

4.5.3.2 Interface of Cu/AlN couple irradiated in air at 3 J/cm^2 followed by 300°C annealing

This couple showed very weak bonding. A depth profile was also obtained across the interface of this couple (figure 4.43). In contrast with the couple irradiated in air at 0.3 J/cm^2, the amount of oxygen at the interface is relatively very small (figure 4.44), but there is some. Most of oxygen is from copper oxide as evidenced by O KLL intensity peak position at ~ 508.5 eV (figure 4.44a). Therefore, copper is mostly from CuO. However, Cu from copper oxide is not seen in the Cu LMM spectra (figure 4.44b), denoting that copper oxide concentration is very low as compared to the non-oxidized elemental copper. Encompassing the interface, Al was mostly from the metallic aluminum as evidenced by the Al KLL peak at ~1393 eV (figure 4.44c). This means that the substrate is mostly decomposed to form metallic aluminum. However, nitrogen was also detected along with metallic aluminum (figure 4.44d). This nitrogen should be from the undecomposed AlN substrate.

4.5.3.3 Interface of Cu/AlN irradiated in Ar-4%H_2 at 1.5 J/cm^2 followed by 500°C annealing

This couple showed very weak bonding after 300°C annealing, but became very strong after 500°C annealing.

Depth profiling of this couple shows that a considerable amount of oxygen exists in the vicinity of the interface and the concentration increases very steeply as the interface is approached (figure 4.45). The oxygen concentration decreases as the copper concentration decreases.

Chemical analysis of this couple was also conducted (figure 4.46), Oxygen was detected at every place in the film. In this respect, this couple is very different from other couples such as all the Cu/Al_2O_3 couples and Cu/AlN couples annealed at 300°C. The oxygen in the latter was from copper oxide (figure 4.46a). In this case, the O KLL kinetic energy is ~ 512 eV (Cu_2O) in the film, while as the interface is approached to the oxygen peak was detected at ~ 509

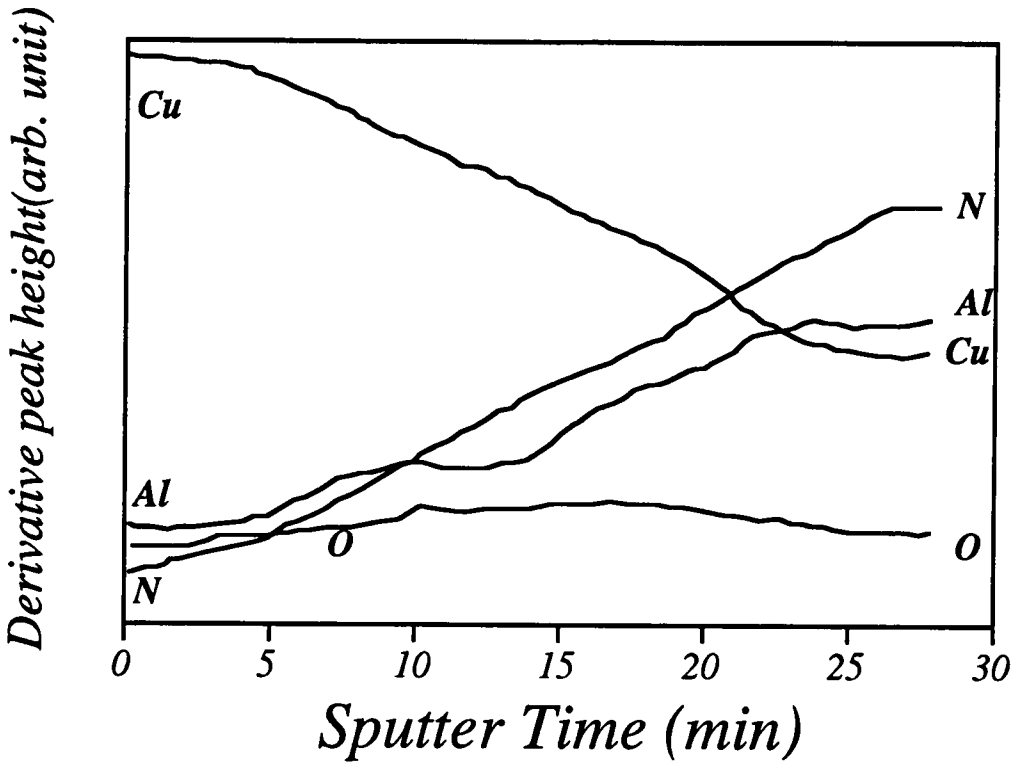

Figure 4.43. Depth profile of Cu/AlN irradiated in air with 3 J/cm^2. The couple was annealed at 300°C for 1 hr. Oxygen exists at the interface, but the amount is very small, indicating that the aluminum oxides layers on the surface of AlN substrate are almost entirely ablated during laser irradiation. This couple showed very weak bonding.

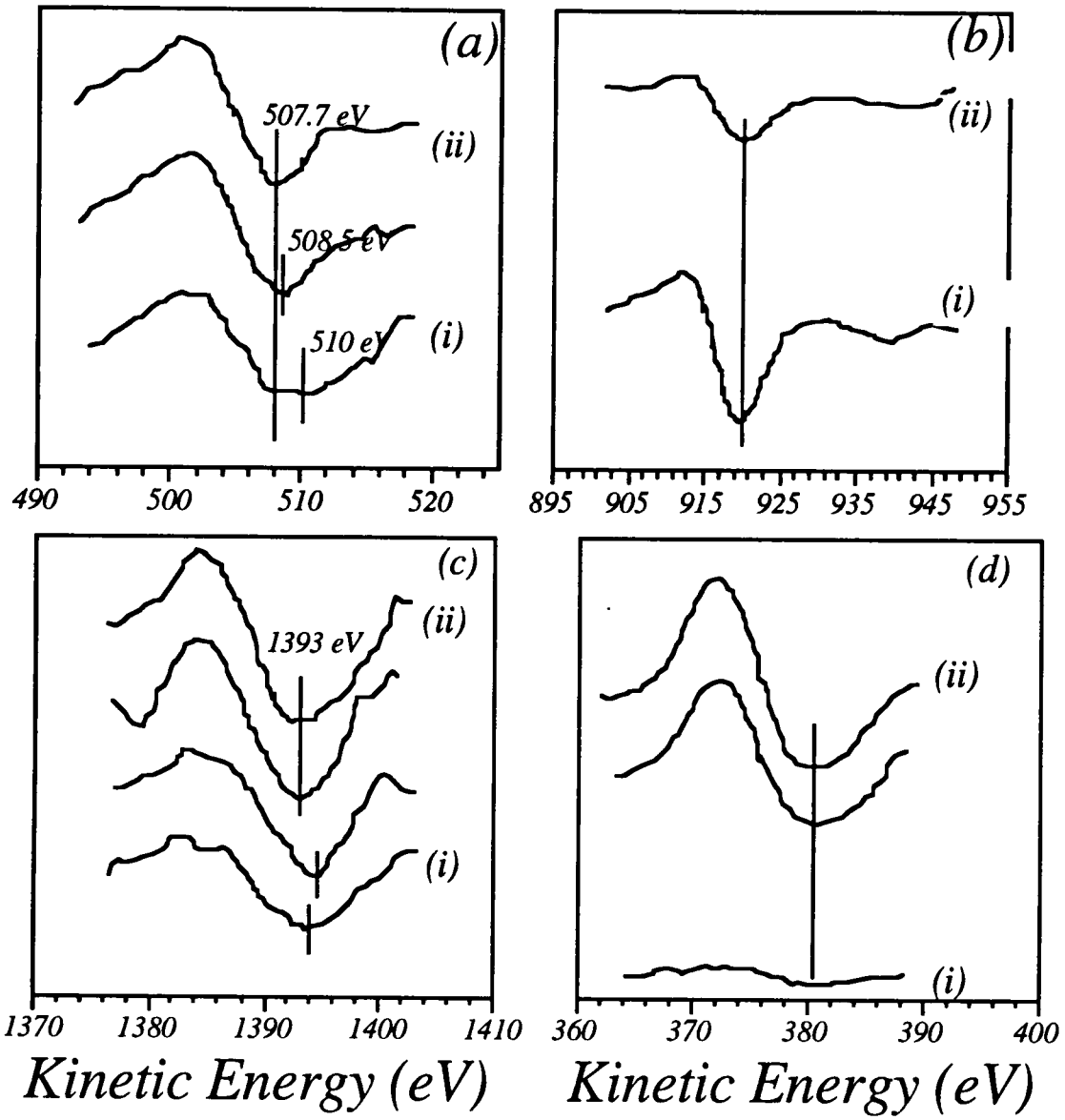

Figure 4.44. O KLL (a), Cu LMM(b), Al KLL(c), and N KLL(d) across the interface of Cu/AlN couple irradiated in air at 3 J/cm^2. The couple was annealed at 300°C for 1 hr. Copper oxide is formed at the interface and aluminum is mostly metallic aluminum. However, AlN exists also along with metallic aluminum. Therefore, it appears that most of Al_2O_3 layers were ablated during laser irradiation.

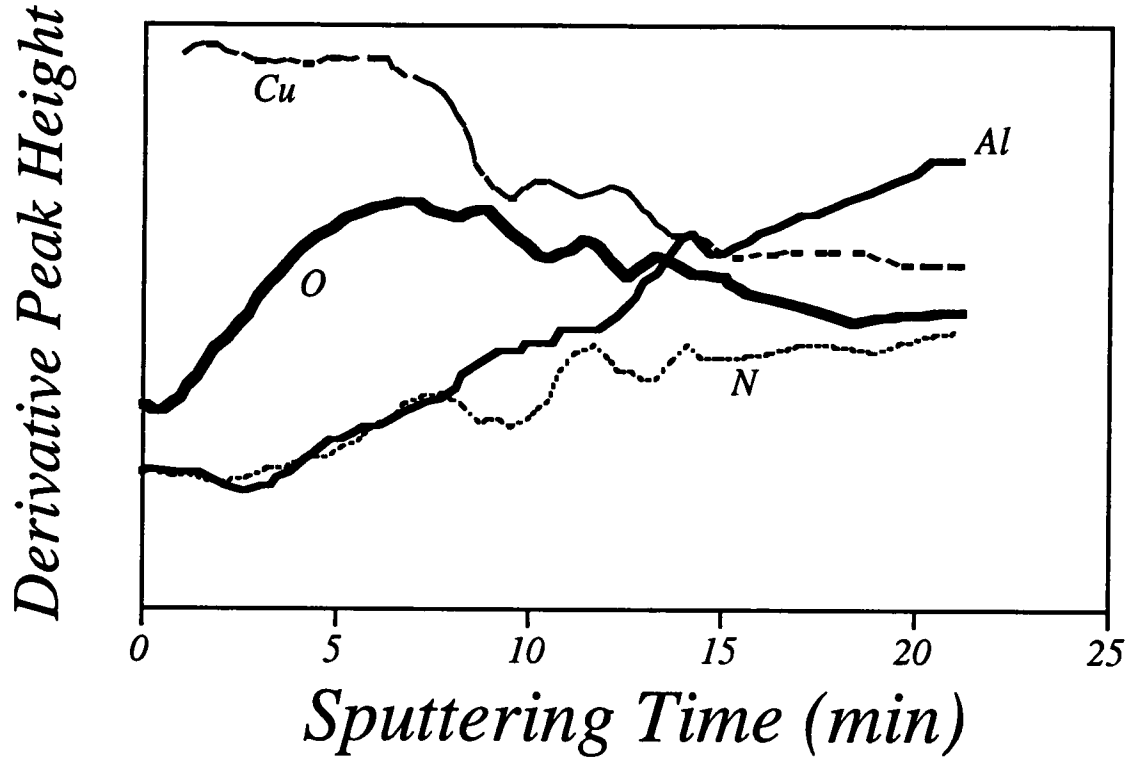

Figure 4.45. Depth profiles at the interface of Cu/AlN couple irradiated in Ar-4%H_2 with 1.5 J/cm^2. The couple was annealed at 500°C for 1 hr. Thick layers of copper oxide were developed in this couple.

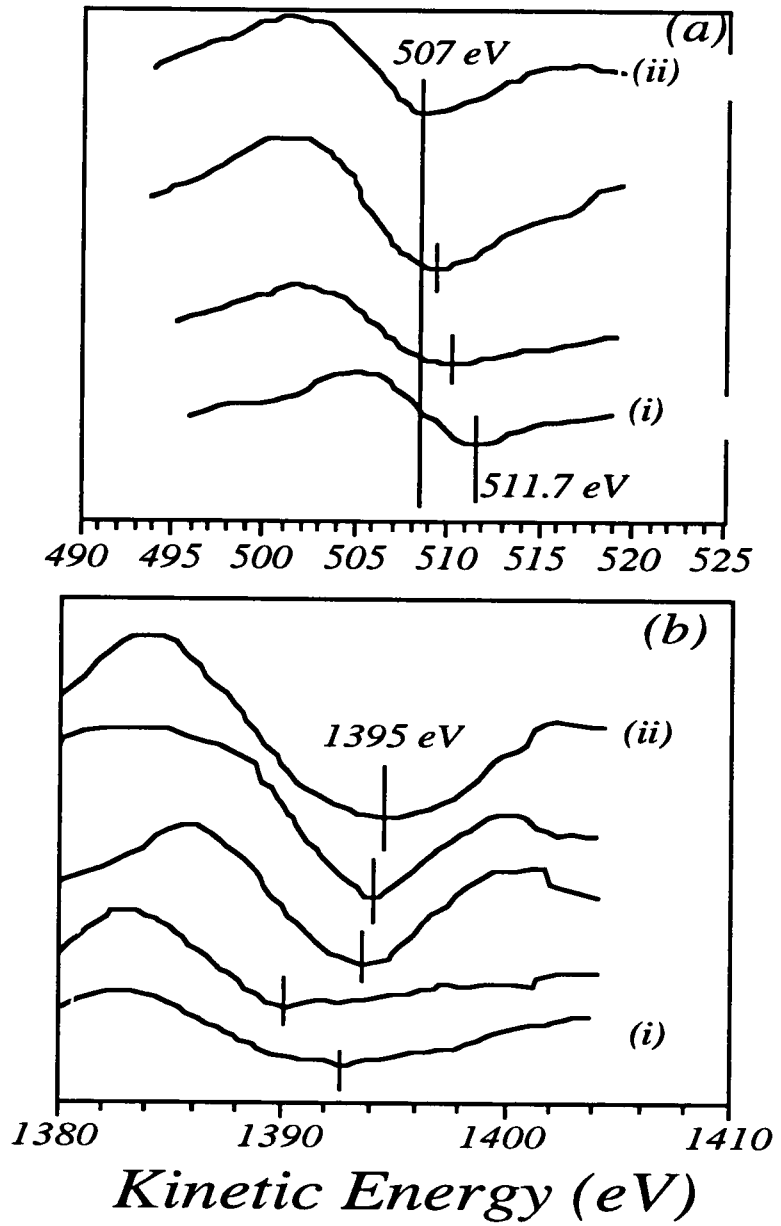

Figure 4.46. O KLL (a) and Al KLL (b) across the interface of Cu/AlN couple irradiated in Ar-4%H2 with 1.5 J/cm^2. The couple was annealed at 500°C for 1 hr. Various copper oxides are detected at the interface (peak i - peak ii)(a). Al at the interface is from non-stoichiometric alumina and aluminum nitride (peak i), while Al in the sub-surface is mostly from metallic aluminum (peak ii) (b).

eV (figure 4.46a). However, the concentration of the copper oxide is very small, because Cu LMM peaks are those of elemental copper in the film.

Al KLL peaks at the interface are located at 1391 eV, implying that the aluminum is not from stoichiometric alumina (figure 4.46b). After removing the interfacial layers considerably, most of Al KLL signals are from metallic aluminum since the kinetic energies are around ~ 1395 eV (figure 4.46b). However, the substrate was not decomposed fully to form metallic aluminum, since nitrogen was also detected (figure 4.46c). The nitrogen is from AlN. It seems that aluminum from AlN in this analysis volume is very small, because no significant Al KLL from AlN appears in the peak.

4.5.3.4 Interface of Cu/AlN irradiated in air at 1 J/cm^2 followed by 500°C annealing

The adhesion of this couple was very weak with 300°C annealing, but very strong after 500°C. The couple showing strong bonding (annealed at 500°C) was analyzed with AES in the same way as the other samples.

Depth profiling was conducted at several areas of this sample. Two different trends were found(figures 4.47 -a and -b). In figure 4.47a the concentration of aluminum increases along with the oxygen concentration as the interface is approached, while in the other analysis area the aluminum increases with the increase of nitrogen (figure 4.48b). However, the latter was more representative, because only one area showed the former profile among four analysis areas. These profiles denote that copper film is in contact with AlN as well as Al_2O_3 at the interface. In both cases, however, the concentration of copper oxide was much higher near the interface than at the surface and subsurface of the film. This implies that the oxygen source is in the interface. However, oxygen from copper oxide was detected in the whole film.

O KLL and Al KLL peaks were analyzed for the two areas. Figures 4.47 and 4.47 are, respectively, for the cases of enriched Al_2O_3 and AlN at the interface. In both cases, various oxidation states of copper were detected from the film surface to the interface. O KLL kinetic energies are from ~ 512 eV to 506 eV.

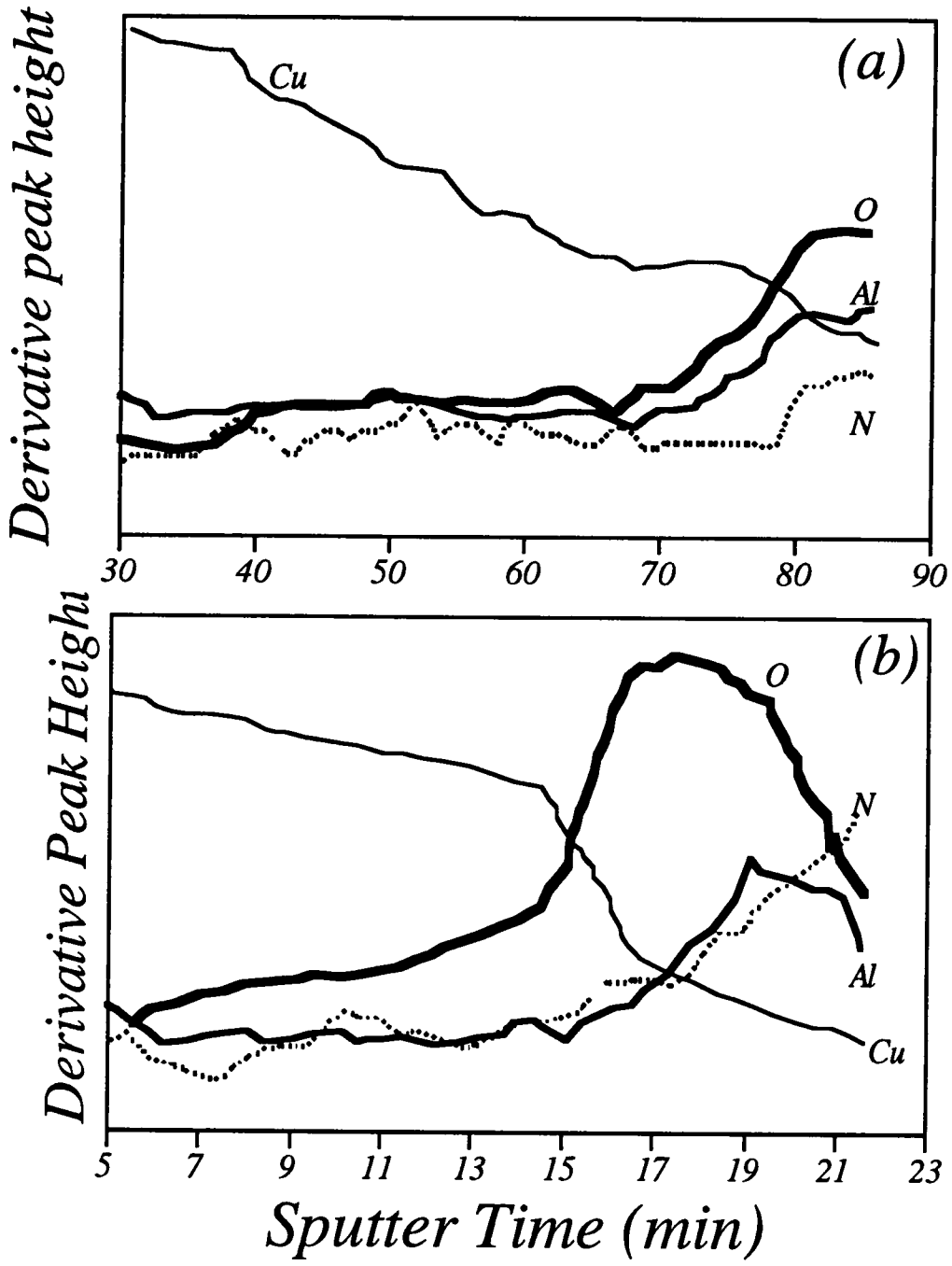

Figure 4.47. Derivative peak-to-peak height vs. sputtering time across the interface of Cu/AlN couple laser-irradiated in air at 1J/cm^2. The couple was annealed at 500°C for 1 hr.

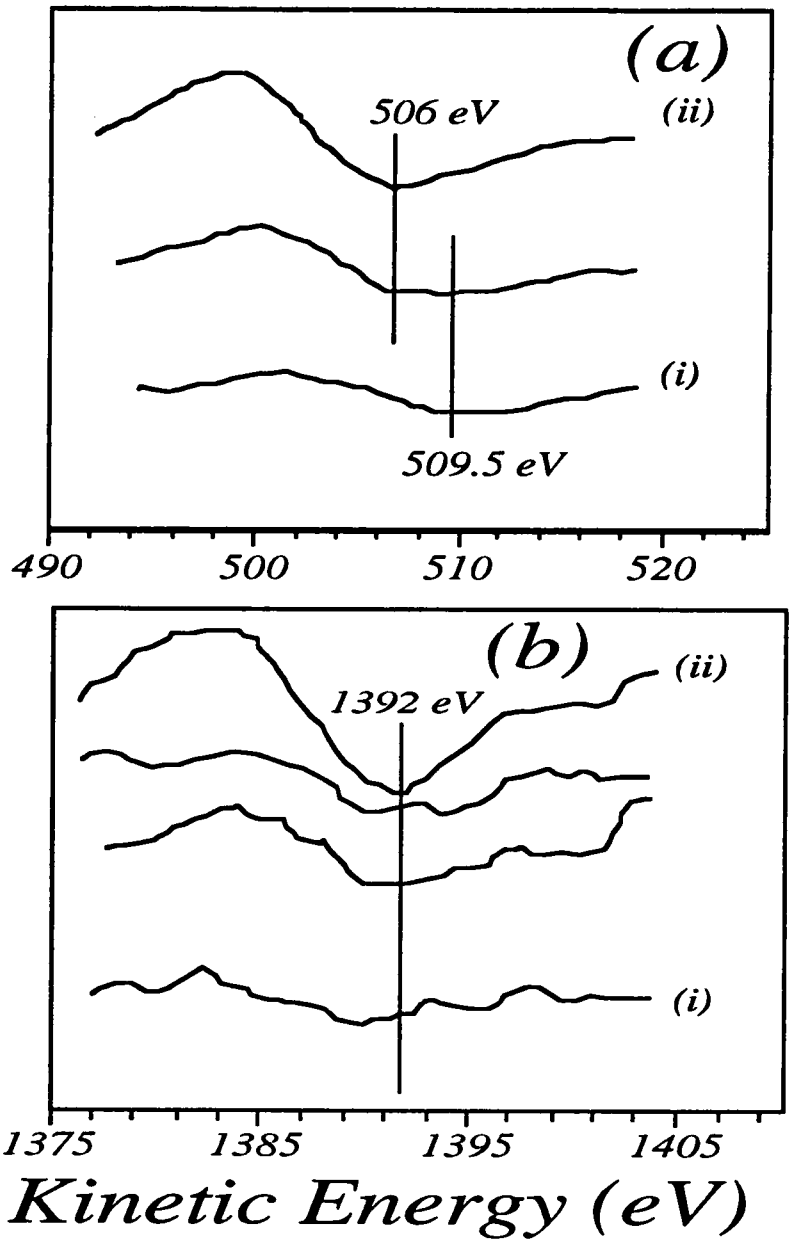

Figure 4.48. O KLL (a) and Al KLL(b) peaks across the interface of Cu/AlN couple. The AlN substrate was irradiated in air at 1 J/cm^2 and the couple was annealed at 500°C for 1 hr. These peak spectra were obtained from the interface of a Cu/AlN couple with enriched Al_2O_3 .

However, a clear difference between these two cases exists. In the case of copper in contact with the enriched Al_2O_3 (figure 4.49) oxygen in the film close to the interface is mostly from CuO, since differentiated O KLL peak position from those areas was ~ 509 eV (figure 4.49a). On the other hand, in the case of the copper film mainly in contact with AlN substrate, the oxygen in the film is mostly from Cu_2O, because O KLL kinetic energy is ~ 512 eV (figure 4.49a). The oxygen KLL peaks are abruptly changed closer to the interface. However, in both cases Al_2O_3 was detected at the interface as shown by peak (ii) in figures 4.48a and 4.49a.

Figures 4.48a and 4.49b are Al KLL spectra across the interface. The peak position at the interface is ~ 1391 eV and then changes to ~ 1388 after passing the interface by further sputtering.

4.5.4 Interface of gold/aluminum nitride couples

Among other couples the couples with the substrates irradiated in air with 2 J/cm^2 were selected for the interface analysis to explore the adhesion mechanism. They were annealed at 300°C and 500°C, which respectively produced weak and strong bonding. Since strong adhesion was also obtained for the gold film deposited on AlN substrate cleaned as described in section 3.1.3 after a 150 °C anneal, this was also analyzed.

Auger spectra of Au NVV in the 230 eV - 260 eV range, N KLL, O KLL, Al KLL were investigated.

<u>Annealed at 300°C for 1 hr</u>

As shown in figure 4.50 of depth profiling, nitrogen was not detected till significant amount of aluminum and oxygen were detected, implying that the film in this analysis area was in contact with Al_2O_3.

The oxygen detected in this couple is from Al_2O_3 as shown in figure 4.51a. The aluminum is from stoichiometric alumina at the interface (figure 4.51b(i)), however, as the sputtering progresses, metallic aluminum features become distinctive (figure 4.51b(iii)). This implies that metallic aluminum from the

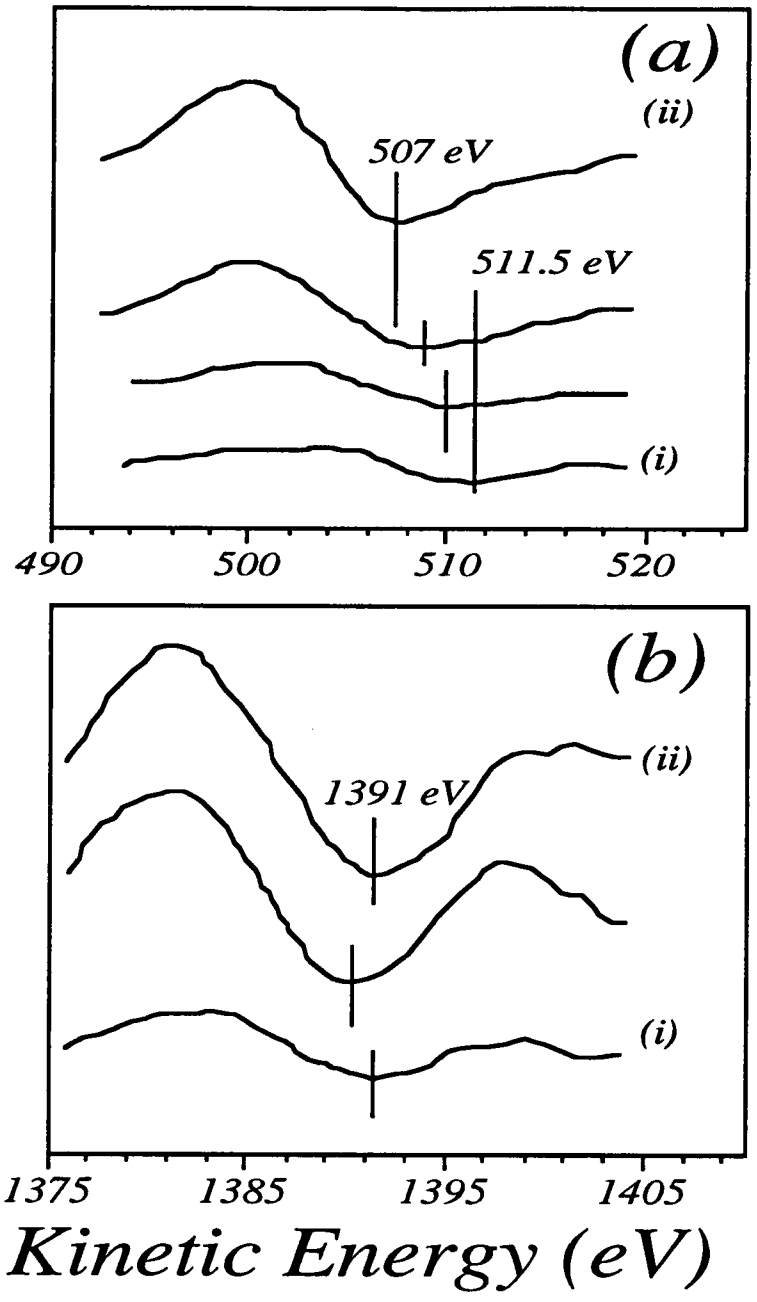

Figure 4.49. O KLL And Al KLL peaks at the interface of Cu/AlN couple laser-irradiated in air with 1 J/cm2. This couple was annealed at 500°C for 1 hr. In this interface, aluminum is mainly from AlN. Peaks (i) and (ii) are closer, respectively, to the film and substrate.

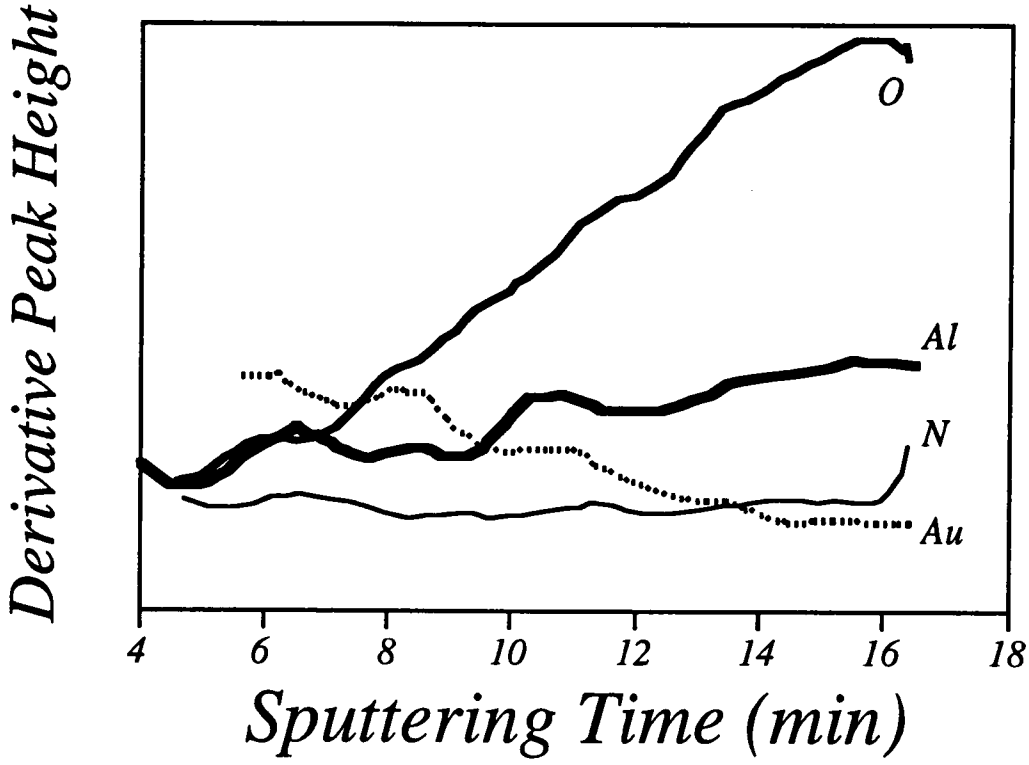

Figure. 4.50. Depth profile across the interface of Au/AlN couple. Substrate irradiated in air at $2J/cm^2$. The couple was annealed at 300°C for 1 hr. In this analysis, gold appears in contact with Al_2O_3 rather than AlN. The couple showed weak adhesion.

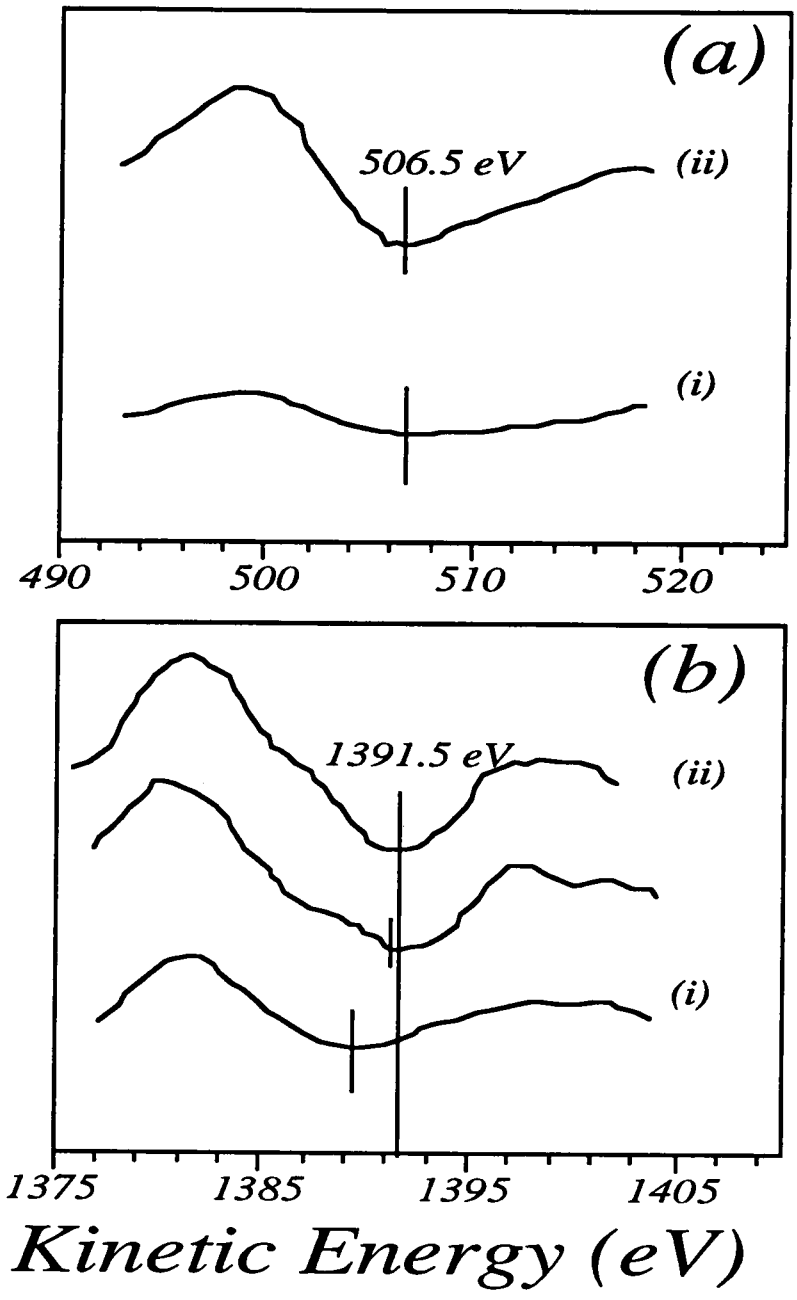

Figure 4.51. O KLL (a) and Al KLL(b) spectra at the interface of Au/AlN couple substrate irradiated in air at 2 J/cm^2. The couple was annealed at 300°C for 1 hr. Oxygen is from stoichiometric Al_2O_3 (a), but aluminum is from Al_2O_3 (Al KLL: ~ 1389) at the interface (peak i) and from substoichiometric oxygen poor alumina in the subsurface (peak ii) (b).

decomposed AlN reoxidized only on the surface layers.

Annealed at 500°C for 1 hr

Figure 4.52a shows Au LVV peak changes at the interface. As the interface is approached, this Auger peak shifts to the lower kinetic energy direction by ~ 1.5 eV. There are also peak shape changes (figure 4.52a (i) - (iii)). Al KLL peaks are somehow complex shaped in the interfacial range (figure 4.52b(i) and metallic aluminum is also detected in the subsurface (ii).

4.5.5 Interface of gold/pre-sputtered sapphire couples

In gold/Al_2O_3 couple, the strong bonding was obtained by sputtering the sapphire substrate prior to film deposition. The sputtering and deposition process were described in section 3.1.2. The interface of this couple was analyzed by the technique using Auger electron escape depth described in the section 3.3.3.2.

Au NVV peaks

In the range of 20 to 80 eV, gold NVV peak positions are ~ 43, 55, and 70 eV (main peak : 70 eV) and Al LVV kinetic energies for Al_2O_3 are approx. 35 and 54 eV (main peak : 54 eV). The low kinetic energy Au NVV spectrum of the non-sputtered film is given in figure 4.53a (spectrum i). A new peak appeared in the same kinetic energy range, when the spectrum was taken close to the edge of the sputter-made crater (Figure 4.53a, spectrum ii). This peak, located at 54 eV, corresponds to Al LVV and overlaps with one of the minor peaks of the gold spectrum. The presence of this peak indicates that either the substrate is partly exposed by ion bombardment or the escape depth of the Al LVV (4Å) is equal to or larger than the thickness of the gold film in this location. Finally, spectrum (iii) was taken even closer to the edge of the crater where the gold film is very thin and the signal of Al LVV becomes more prominent. In spectrum (ii) the gold peak is located at 70 eV, the same position as the reference peak shown in spectrum (i),

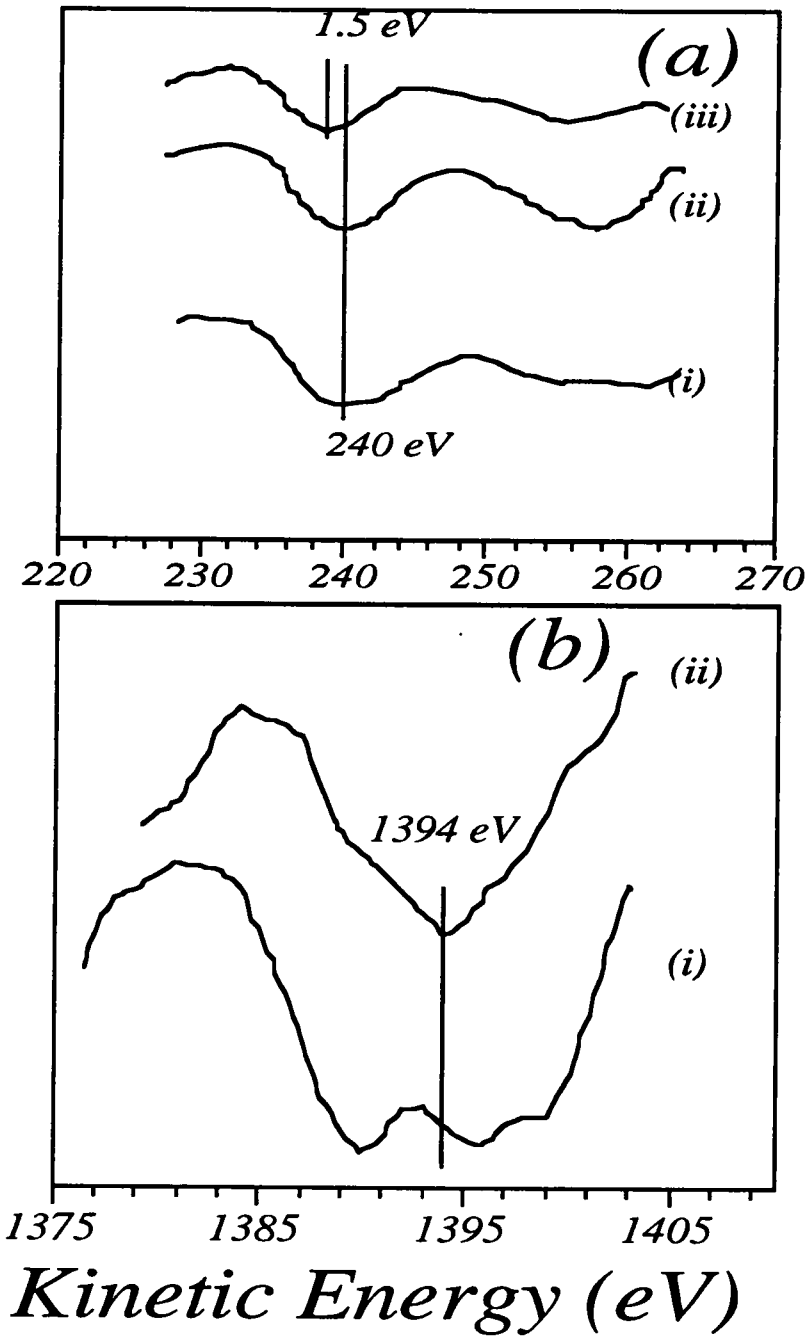

Figure 4.52. Au LVV (a) and Al KLL (b) Auger peaks at the interface of Au/AlN couple with substrate irradiated in air at 2 J/cm^2. The couple was annealed at 500°C for 1 hr. Au LVV peak shifts in the low energy direction by 1.5 eV (a) and complex change in Al KLL peak is seen along with metallic aluminum feature (b).

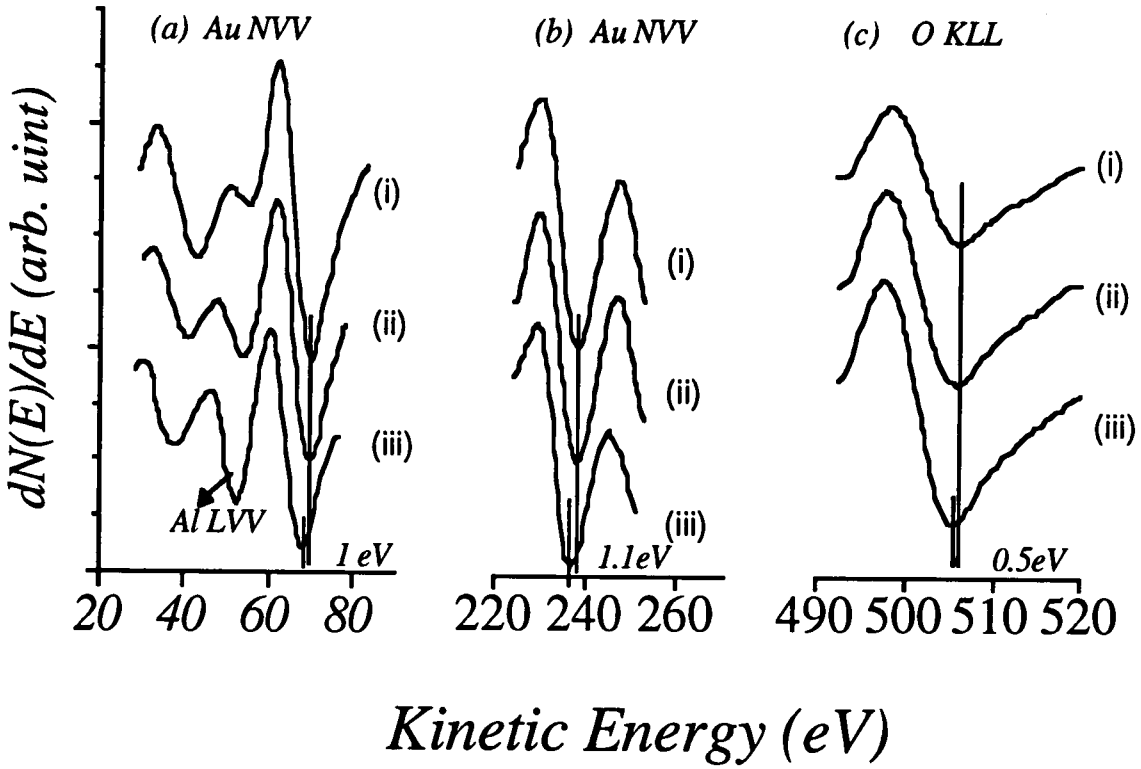

Figure 4.53. AES spectra from three different regions in the specimens. (a) Low kinetic energy region for Au NVV Auger electrons; (b) High kinetic energy region for Au NVV Auger electrons; (c) O KLL Auger electrons. In all the figures, position I is far from the film denuded crater, position III is closest to the crater, and position II is intermediate between I and III. Shifts toward lower kinetic energies in spectra taken at position III in (a) and (b) reveal an interfacial reaction involving Au. The shift toward higher kinetic energies in spectra I and II of (c) indicates presence of oxygen-deficient Al_2O_3.

but in spectrum(iii) the gold peak is shifted toward lower kinetic energies by ~ 1 eV.

Shifting of the 55 eV Au NVV peak at the position of spectrum (iii) cannot be resolved due to the presence of the main Al LVV peak. Instead of deconvolution of these peaks, another gold NVV peak in the energy range of 220 to 250 eV was also analyzed in order to check the chemical change indicated by the peak shift at 70 eV. Au NVV peak in this energy range is well separated from other Auger peaks. Another advantage of choosing this peak is that it reflects more interface since the Auger electron escape depth in this energy range is larger than that of the NVV peak in the lower energy range, but the high energy Au NVV peak has less atomic sensitivity factor. Spectrum (i) in figure 4. 53b was taken at a position farther away from the edge of the crater, while spectrum (iii) was taken at the closest distance to the edge and spectrum (ii) comes from an intermediate position (figure 4. 53b). As expected, a shift of ~ 1 eV toward lower kinetic energy is detected in spectrum (iii).

O KLL peak spectra

The O KLL spectra from three regions close to the crater edge were studied (figure 4. 53c). Following the same convention of figure 4. 53b, spectra (i) and (ii) are signals coming from the region farther away from the interface where the film is thick enough so that only the signal coming from the region near the interface is not blocked by the film. In position (iii) the gold film is too thin and a large portion of the substrate contributes to the signal making the contribution from the interface too small to be detected. Spectra (i) and (ii) show a peak shift of 0.5 eV towards higher kinetic energy values relative to the peak position in spectrum (iii) which comes from bulk Al_2O_3.

Al KLL peak spectra

In order to detect the interface with Al KLL peak (1388 eV), the electron beam was positioned where the gold film has a thickness equal to or less than the

Auger electron escape depth (approx. 15 - 20 Å) [64]. The Al KLL spectrum from metallic aluminum shown at the bottom of figure 53 is used as a reference. The spectrum above it was obtained from a region where the gold film thickness was close to the escape depth of the Auger electrons. The signal of the Al KLL spectrum is coming from the aluminum present at the gold-alumina interface and the sapphire substrate. No Auger gold signal exists in this kinetic energy region. The following third and fourth spectra were obtained by displacing the beam slightly towards the crater. As the gold film thickness decreases more Auger electrons come from the substrate lowering the proportion of signal coming from the gold-alumina interface. Finally the uppermost spectrum in figure 4. 54 is from aluminum atoms in an Al_2O_3 environment. The signal from the interface clearly shows that the ion etching performed on the substrate prior to gold deposition induced decomposition of Al_2O_3 leaving some metallic aluminum on the surface. As already mentioned, in terms of Auger signal intensity the contribution from Al_2O_3 increases as the thickness of the gold film decreases, making the relative contribution from the interface significantly smaller. This can be realized from a comparison of the third and fourth spectra. Practically, no metallic aluminum is detected in the fourth spectrum; instead, the Al peak coming from Al_2O_3 has broadened. This peak broadening suggests that sputter etching also produced non-stoichiometric Al_2O_3 layers below the metallic film. This indication of a non-stoichiometric Al_2O_3 is reinforced by the shift toward higher kinetic energy in 0.5 eV detected in the O KLL spectra (figure 4.53c). Upon careful inspection of the spectrum at the interface, comparison with the Al KLL from metallic aluminum and the Al KLL from Al_2O_3 shows that the fine structure of the Al KLL spectrum at the interface has peaks that appear neither in the sapphire substrate nor in the metallic aluminum spectra. These peaks are indicated with arrows in the second spectrum of figure 4. 54. This result suggests that aluminum may also be present in a chemical environment different from that of Al_2O_3 or metallic aluminum.

The gold NVV signals coming from the gold-Al_2O_3 interface is only detectable when the film is thin enough so that a large proportion of the gold signal is coming from the interface. On the other hand the Al signal coming from the interface is detected when the gold film is thick enough so that most of the

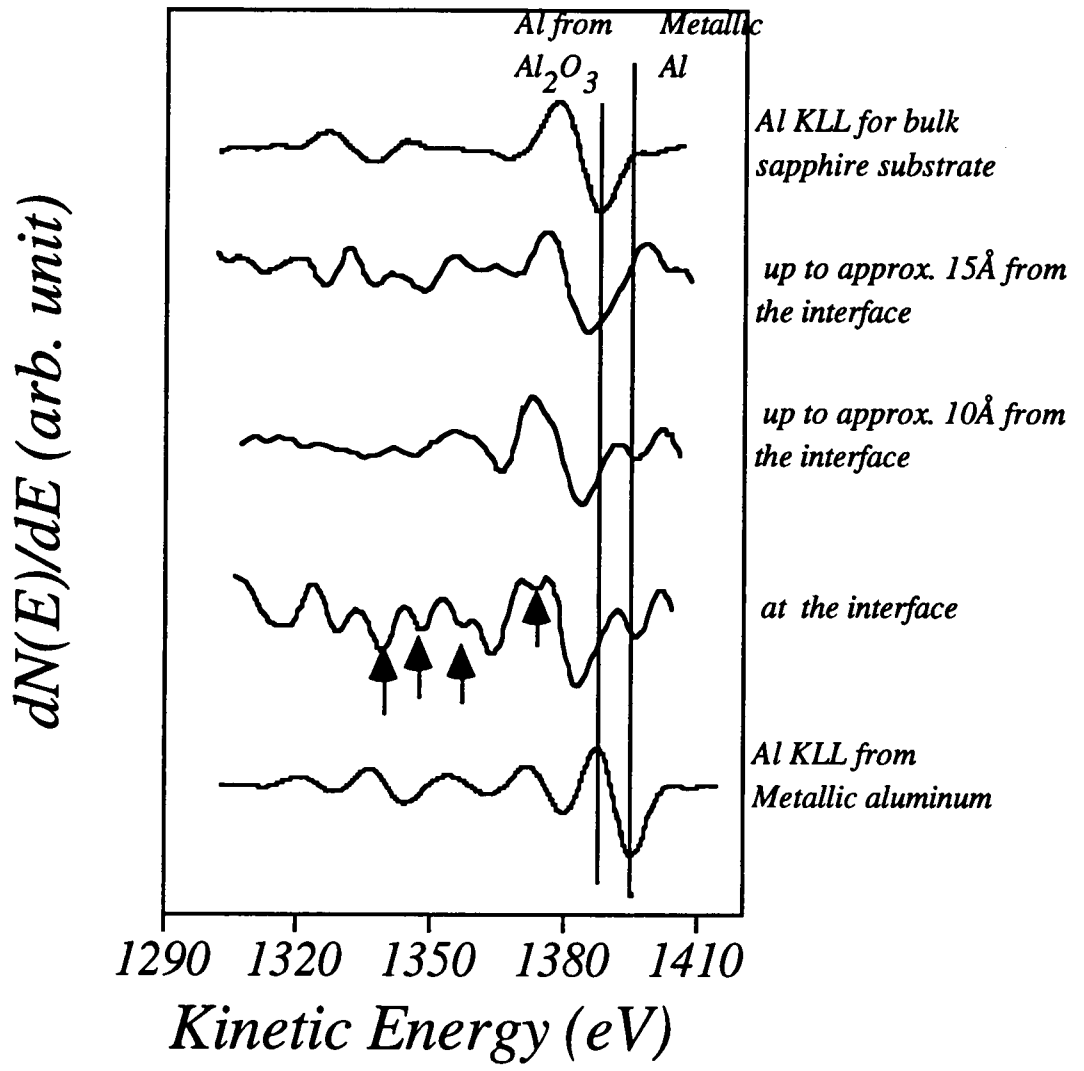

Figure 4.54. Al KLL peak spectra Metallic aluminum features with complex Auger fine structures are seen .

signal comes from only the interface and not from the substrate, as shown in figure 4. 54.

Finally, an identical study was performed on the Au-Al_2O_3 interface for films deposited on as-received sapphire. In these couples, shifts of Au or O peaks were *never* detected in the spectra taken at the Au-Al_2O_3 interface. *No metallic aluminum* was detected in this case either.

4.6 Studies on the interface and dielectric loss of SiO_2 in Cu/SiO_2 couple

Under 1 MV/cm electric field with 300°C heating for 12h, the resistivity of the copper film increased. This means that copper drifted into SiO_2 layers, resulting in dielectric loss of SiO_2. The interface of Cu/SiO_2 couple was investigated with AES and the copper concentration in the SiO_2 substrate after the dielectric loss was measured with SIMS.

Figure 4.55 is AES peak spectra of the oxygen at the surface of copper film and at the interface between the film and SiO_2 substrate. The peaks from the interface were obtained after sputtering the film. O KLL peaks at the interfacial area change from 512 eV to ~ 505 eV as encompassing the interface by sputter-etching. O KLL at 505 eV is believed to be from SiO_2 because it was concurrently acquired when Si LMM (76 eV) from silica was detected.

Figure 4.56 is SIMS depth profiling of Cu in SiO_2 in the Cu/SiO_2 couple annealed at 300°C for 12 hr under 1 MV/cm electric field application. The count rates in log scales are expressed as a function of elapsed times. The count rate abruptly increases and decreases at the interface due to the matrix effect that often produces artifacts in SIMS analysis. Then, Si, SiO, and O concentrations increase, while copper concentration decreases. However, the copper concentration increases again at around 4800 sec elapsed time (from $2x10^4$ to $5x10^4$ in the count rates) and then continuously decreases to the back ground level (10^4), forming a hump, clearly indicating the copper drift into the SiO_2. Several runs of SIMS were performed in several different areas in the same sample, but results obtained were always similar.

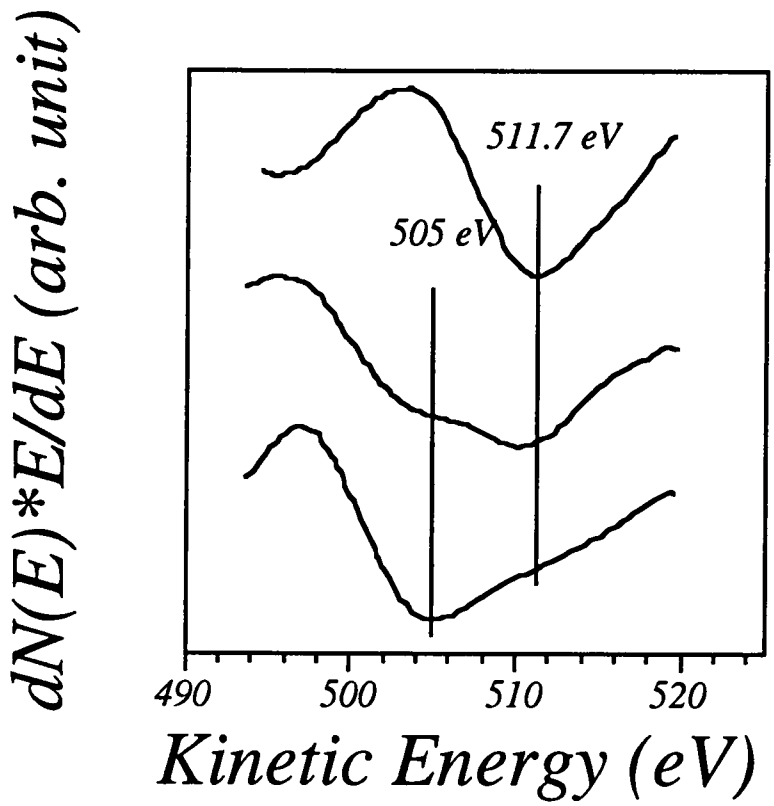

Figure 4.55. O KLL peaks across the interface of Cu/SiO_2 couple annealed at 300°C. The peak positions change from ~ 512 eV to ~ 505 eV as encompassing the interface by sputter-etching. The O KLL at 512 eV indicates that Cu_2O is formed at the interface.

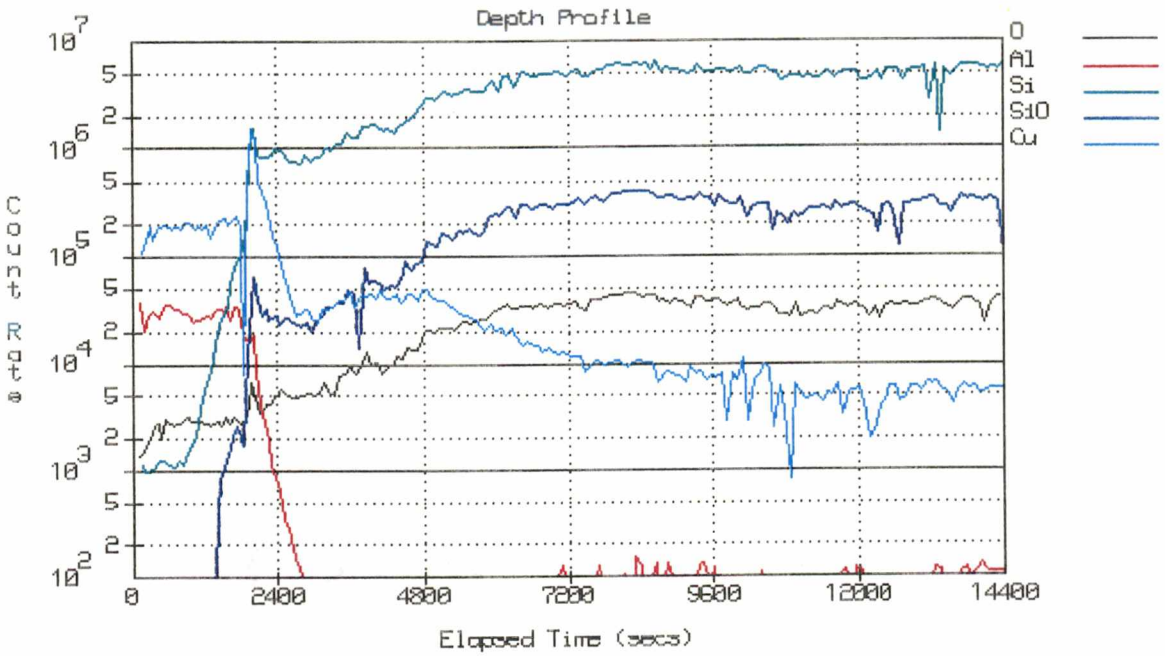

Figure 4.56. SIMS for copper drifted into the SiO_2 substrate under electric field application.

SIMS was also performed on Cu/SiO_2 couple annealed at 300°C for 12 hr under no electric field. Copper was not found in SiO_2 matrix, but AES analysis showed the formation of SiO_2 at the interface.

CHAPTER 5

DISCUSSIONS

The discussion presented in this chapter deals with 1)adhesion mechanisms of metallic films/ to laser-irradiated ceramics couples (Cu/Al_2O_3, Au/Al_2O_3, Cu/AlN, Au/AlN couples) and of gold film to pre-sputtered sapphire couple, 2) copper drift phenomena into the silicon dioxides, 3) in situ study of Al_2O_3 decomposition, and 4) AES analytical techniques.

5.1 Interface in the metallic film/surface-modified Al_2O_3 couples

When Cu/Al_2O_3 couples with substrates irradiated at $\geq$ 1 J/cm^2 in air and at 1 J/cm^2 in Ar-4%H_2 atmospheres were annealed at 300°C and 500°C for 1 hr, respectively, the magnitude of adhesion strength was the highest obtained in this work. Analysis results of laser-irradiated Al_2O_3 surface and interfacial reactions in these couples are discussed in this section.

5.1.1 Laser irradiation induced surface modification of alumina

XPS and AES analyses clearly show that metallic aluminum features are formed on the surface of both alumina and sapphire substrates when they are irradiated either in oxidizing or in reducing atmospheres (figures 4.14, 4.15, 4.20, and 4.21). However, the metallic aluminum features shown in figures 4.14 and 4.15 are not exactly those that correspond to pure metallic aluminum. Two possibilities can be considered in this respect: one is the existence of substoichiometric alumina together with metallic aluminum, and the other is a superposition of Auger peaks from metallic aluminum and alumina. The former is more likely, because the formation of substoichiometric alumina can not be avoided during the decomposition of alumina producing metallic aluminum. The

formation of substoichiometric alumina can also be evidenced by TEM observation. As revealed by a cross-sectional TEM micrograph the metallic aluminum particles are embedded in the alumina matrix (figure 4.26).

The metallic aluminum was also detected in the substrate irradiated in air with 0.4 J/cm^2. According to measurement, the temperature raise in sapphire substrates laser-irradiated at 0.4 J/cm^2 does not exceed 800°C during irradiation [106]. In fact, a laser energy density of 0.7 J/cm^2 is required to melt the substrate [9], indicating that the substrate temperature is above 2000 °C during irradiation. Therefore, a metallic aluminum on the substrate at 0.4 J/cm^2 was not produced by thermal evaporation or reduction of the liquid.

Dreyfus et al. [106] reported that various species were ejected from the surface of sapphire irradiated at an energy density of 0.4 J/cm^2. Therefore, photo-ablation will be produced during irradiation at this low energy density. The preferential ablation may have caused the compositional difference and resulted in the formation of metallic aluminum. However, the amount of aluminum produced in this way is little because most of them reoxidize as soon as the substrate is exposed to air.

The amount of metallic aluminum formed on the surface of substrates irradiated in air at laser energy densities larger than 0.7 J/cm^2 is much less than the amount obtained by irradiation in Ar-4%H_2 atmosphere. As shown in figure 4.14 and 4.15, in neither case is metallic aluminum detected on the utmost surfaces of the irradiated substrates, implying that the metallic aluminum on the surface of the irradiated alumina is reoxidized. At high temperature, a reducing atmosphere helps to reduce a larger amount of molten alumina and the amount of metallic aluminum obtained after solidification is larger. This means that the metallic aluminum and/or substoichiometric alumina are formed not only by the thermal decomposition, but also by the reducing atmosphere present during the irradiation. When the laser irradiation is conducted in the oxygen atmosphere, the oxygen formed in the alumina due to the decomposition will be relatively difficult to escape the surface, hence, the possibility of the formation of metallic aluminum layer on the surface will be decreased. More over, it is important to notice that the oxygen concentration on the alumina surface is more than the stoichiometric value. This

was evidenced by the XPS measurement which showed the excess oxygen on the alumina surface laser-irradiated in air (table 4.4).

The electronic structure on the surface of the substrates can also be changed by laser irradiation. These changes are detected by XPS valance band spectra (figure 4.22) which is indicative of the modifications in the oxidation degree of Al. Laser irradiation of alumina produces a decrease in the width of the valence spectrum. According to the calculation of the density of electronic states using a tight-binding model, the width of the valence band decreases when a lattice expansion occurs [107]. The decrease of the width of valence band spectra by the laser irradiation may be attributed to the increase in the concentration of vacancies and interstitials causing a lattice expansion.

In several instances the oxygen peak could be separated into two contributions, one from the aluminum oxide and the other one from a hydroxyl-like bonding configuration. The hydroxyl-like configuration can be attributed to either of three causes: 1) water absorption, 2) adsorbed hydroxyl groups from a reacted water molecule, or 3) adsorbed hydrogen that forms a hydroxyl-like species with the oxygen of the substrate. In any of the first two possibilities the total oxygen to aluminum ratio should be significantly larger than the stoichiometric ratio when the $O_{hydroxyl}$ /O_{total} ratio is large. The results in table 4.4 indicate that the excess oxygen in the as-received sapphires can then be attributed to either of the two first causes mentioned above.

The relative oxygen content to aluminum (O/Al in tables 4.3 and 4.4) in the near surface region is higher than the stoichiometric value in samples irradiated in an Ar-H_2 atmosphere at laser energy densities $\leq$ 1 J/cm^2. This looks like a contradiction, because oxygen depletion in Al_2O_3 should take place upon laser irradiation in a reducing atmosphere. It can be explained as follows:

i) Oxygen depletion takes place during irradiation in Ar-4%H_2 atmosphere. The amount of oxygen depletion may be proportional to the laser energy density.

ii)The metallic aluminum or substoichiometric alumina are reoxidized to the stoichiometric alumina on the surface. Therefore, oxygen concentration at the surface is higher than that in the subsurface. The relative concentration of the

oxygen on the surface increases as the laser density increases.

iii) O1s and Al2p peaks were used in this XPS quantitative analysis. Since the sampling depth of O1s is less than that of Al2p, O1s is more surface-sensitive than Al2p, therefore, the measured O/Al ratio is higher than the stoichiometric value. (The binding energy of O1s is higher than that of Al2p. That means that the photoelectron kinetic energy from O1s is less than that from Al2p.)

On the other hand, for samples irradiated at 3 and 5 J/cm^2 in an Ar-4%H_2 atmosphere the O/Al ratio is less than the stoichiometric value. In these higher energy densities, it seems that the increased amount of metallic aluminum and/or substoichiometric alumina in the subsurface reduced the ratio. It is noticeable that the ratio decreases as the laser energy increases when the irradiation conducted in Ar-4%H_2 atmosphere.

As-received substrates also have an oxygen excess on the surface, but sputtering reduces the O/Al ratio to the stoichiometric value, implying that most of them are adsorbed as a surface contaminant. Therefore, they will be easily sputtered away during the film deposition.

XPS results showed that carbon always exists on the surface of the as-received substrate and its amount varies depending on the samples and analysis areas. The carbon adsorbed on the surface can be easily eliminated by annealing the substrate at elevated temperature. Therefore, the annealing can produce a standard condition of an as-received substrate. Figure 4.19a shows much reduced carbon on the surface after annealing the substrate at 1350°C for 72 hr. After laser irradiation in Ar-4% H_2 atmosphere, the amount of the carbon increased remarkably as shown in figure 4.19b. Similar results were obtained with AES. The fact that the carbon deposit increases on the laser irradiated surface in Ar-4%H_2 can be the results of an increasing catalytic activity of the irradiated surface. In this case the reoxidation and carbon absorption can be a competing process depending on the gas contents in the processing chamber. In the substrate irradiated in oxygen atmosphere carbon content on the surface is less, because the reoxidation is more likely to occur than carbon deposit.

Another laser irradiation effect of alumina is the surface smoothening by

melts and flows. DeSilva studied extensively the effects of laser irradiation on alumina substrate in his Ph. D Thesis [93]. Surface smoothening of the substrates is not only desirable for the metallization of the conductive path in the circuit, but also may be an indication of changes in the surface chemical properties induced by heating.

5.1.2 About analytical techniques using AES

When the polycrystalline alumina is laser irradiated, melting is not uniform even across one grain; the protruded area in a grain melts and the melt flows to fill the lower region as observed by SEM. The spatial resolution of XPS is at best a few μm , thus, many grains are analyzed at the same time when polycrystalline Al_2O_3 and AlN are analyzed. Therefore, XPS is not adequate to analyze the exact irradiation effect, because of roughness of the substrates (at least 0.1μm) and the large average area measured by XPS. Thus, it may not be useful in analyzing the exact adhesion mechanism that takes place between laser irradiated alumina and deposited film. AES has a much better spatial resolution, and for this reason it is very useful tool to analyze the small area in a grain that affected more by laser irradiation. Since more disordered regions in the substrate generally tend to react more with deposited films, AES should also be used for the analysis of the interface associated with the film deposited on the laser- irradiated alumina and aluminum nitride substrates.

AES can resolve the state of aluminum well, whether metallic or in the ceramics, because the Auger electron kinetic energy of aluminum in the elemental state differs by 14 eV with that in alumina and 9 eV with that in AlN in LVV Auger transition and about ~ 8 eV for both ceramics in KLL Auger transition. On the other hand, the binding energies of the core level electrons measurable with XPS differ much less (~ 4 -5 eV).

5.1.3 Copper/alumina with the substrate laser-irradiated at 1 J/cm^2 in oxygen

This couple showed very strong bonding when the couple was annealed

at 300°C for 1 hr.

As shown by XPS study, excess oxygens form on the surface of laser-irradiated Al_2O_3. At the interface, O KLL peaks are from alumina and from a similar copper oxide detected at the surface of copper film (figure 4.31). That is, when copper is deposited on alumina irradiated in an oxygen atmosphere the film atomic layers contacting with the substrate tend to form a copper oxide. It can be questioned if the oxides at the interface is a double oxide of copper and aluminum or with two separated oxides. The following interpretations of the figure 4.31 lead to the conclusion that the formation of the compound may be the most probable mechanism of the strong bonding. As the interface is approached, the first oxygen is from the cuprous oxide (Cu_2O) and further sputtering reveals the splitted oxygen KLL peak. The new peak in the splitted O KLL is located at ~ 508 eV that differs from the O KLL from the alumina (506 eV) and from the cupric oxide (CuO at ~ 509 eV). This peak may be from the Cu-O-Al compound formed at the interface. The compound may be CuO. AlO (= CuAlO2). It is also hard to believe that two different stable ceramics such as Al_2O_3 and Cu_2O react with each other at the interface and then produce the strong bonding. Therefore, the double oxides is most probably the strong bonding mechanism rather than the two separated oxides.

A number of experiments have shown that the adhesion of metallic film to alumina can be enhanced if the metal in contact with the substrate is oxidized. O'Brien and Chaklader [108] found that the work of adhesion between liquid copper and sapphire reached a maximum at an oxygen partial pressure of 10^{-9} atm. They suggested that formation of $CuAlO_2$ at the interface caused the spreading of copper droplets in sapphire. The smaller wetting angle means the better adhesion, as explained in section 2.5. Reactions in the CuO-Cu_2O-Al_2O_3 system to give $CuAl_2O_4$ and Cu_2AlO_4 were reported by Gadalla and White [109]. The process developed by Burgress et al. [110], for direct copper-alumina bonding in hybrid electronic packages, probably produces a mixed aluminum and copper oxide that promotes strong bonding.

5.1.4 Copper/alumina with the substrate laser-irradiated in Ar-4%H_2 at 1 J/cm^2

No Auger peak shift occurred at the interface of the couple laser-irradiated in Ar-4%H_2 atmosphere after 300°C annealing. This means no chemical reaction between the deposited copper and the irradiated substrate occurred.

Metallic aluminum or substoichiometric alumina formed on the alumina substrate laser irradiated in Ar-4%H_2. Therefore, we can predict that the deposited copper may react with the alumina substrate laser-irradiated in Ar-4%H_2, since the surface of the alumina is not in stable chemical state. However, the adhesion strength in this couple was much weaker than in the couple with the substrate irradiated in air that was annealed at the same temperature [93].

It seems that the reoxidation of metallic aluminum and substoichiometric alumina on the surface that naturally takes place in the irradiated alumina in Ar-4%H_2 may have acted as reaction barrier between the copper film and the non-stoichiometric alumina in the subsurface. Therefore, the reaction at the interface may take place, provided that the reoxidized layer is broken. It seems that the reoxidized layer are stable at 300°C.

After annealing at 500°C, pull testing result showed that the adhesion was enhanced significantly. Since all other conditions were the same, the reason for enhanced adhesion was only due to enhanced interfacial reaction. After annealing at 500°C oxygen from the copper oxide was found as shown in figure 4.32(i), while no oxygen from the copper oxide was found at the interface of this couple after 300°C annealing of this couple. Assuming that the copper oxide forms by the diffusion of the oxygen dissolved in the copper film, the diffusion of oxygen may have not occurred at 300°C annealing. Also, we can expect that oxygen from a part of the irradiated alumina substrate with excess oxygen can diffuse toward the interface and then react with copper film. However, this kind of excess oxygen may easily combine with metallic aluminum and substoichiometric alumina if a proper heating is provided.

The other significant change in this sample after 500°C annealing is the broadening of the oxygen peak. The elevated temperature may have damaged the reoxidized layer, but the layer was not eliminated or mixed up with film and/or

the substrate because oxygen Auger peak (~ 507 eV) right below the copper film is close to stoichiometric Al_2O_3 (figure 4.32 ii). Further sputtering below the copper film shows broadened oxygen peaks, implying that alumina is not stoichiometric (figure 4.32. iii, iv). The peaks are slightly broadened toward high energy direction. This means that below the reoxidized layer alumina and under-stoichiometric alumina coexist. Szalkowski et al [65] reported that approx. 0.6 eV of oxygen Auger peak position shifted consistently toward high kinetic energy direction per reduced oxidation number in the case of the vanadium oxide. Although this value does not applied to Al_2O_3, it can be suggested that oxygen peak position will shift to higher kinetic energy direction as reducing the oxidation number of the oxide is reduced.

As shown in figure 4.33, direct copper LMM Auger peak shifts to lower kinetic energy direction by approx. 1.7 eV (peak ii), indicating the formation of copper oxide at the interface. Below the copper oxide layer, direct copper LMM Auger peaks are significantly changed (peak iii). The main peak position is that of the elemental copper, but it is broadened, and new fine peaks at lower kinetic energy range appear. Obviously, the reaction between the copper and substrate occurs. This may have led to the strong bonding. However, figure 4.33 indicates that not all of the copper contacting with the substrate was reacted to form any compound because the main copper peak position is still from the elemental copper. The reaction between copper and the substrate may be schematically described in figure 5.1.

Based on the above analysis, the strong bonding mechanisms for the couple laser-irradiated in Ar-4%H_2 may be summarized as follows:

i)copper oxide formation at the interface by diffusion of the oxygen probably dissolved in the bulk copper and/or excess oxygen in a part of the irradiated alumina.

ii) copper-aluminum-oxygen compound as evidenced by the oxygen KLL Auger peak broadening and the formation of the new copper Auger peaks at the lower kinetic energy direction than the elemental copper peak.

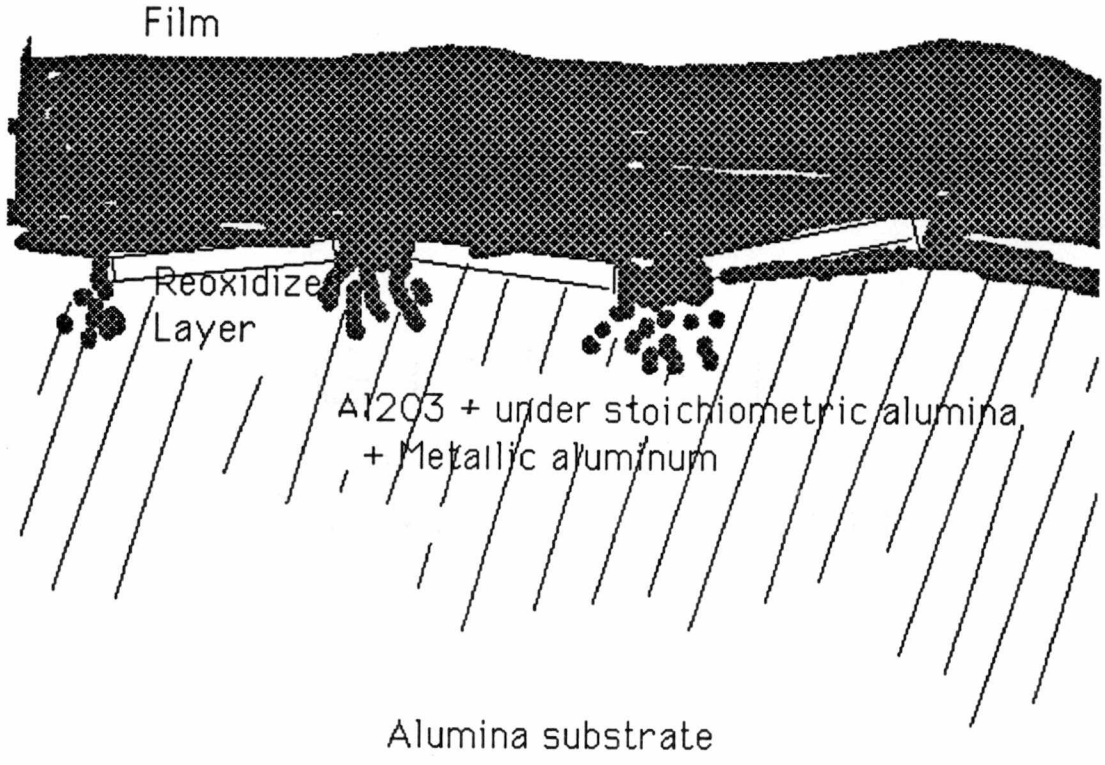

Figure 5.1 A schematic of the reaction between the copper film and the alumina laser-irradiated in Ar-4%H_2. In this model, it is assumed that the reoxidized utmost surface is partly broken by heating and then copper contacts with the non-stoichiometric alumina, resulting in the reaction.

5.1.5 Cu/as-received Al_2O_3 couple annealed at 500°C

Sometimes copper deposited on the as-received alumina showed very strong bonding after 500°C annealing. The analysis of the interface of this strongly bonded couple showed peak shifts of Al KLL peak by + 4 eV and of O KLL by + 2 eV at the interface (figure 4.31). These Auger peak shifts at the interface denote that aluminum is not from Al_2O_3 and oxygen is not from either Al_2O_3 or copper oxides. This implies that the intermediate compound between copper film and alumina developed linking these two dissimilar materials. However, this kind of linking does not always happen in this couple. It seems that the strong bonding is very much dependent upon the surface condition of the substrate before the film deposition. In most cases, the surface of the alumina is covered with a certain surface contaminants that impair the interfacial reactions, resulting in the weak bonding.

5.1.6 Cu/Al_2O_3 with the substrate irradiated in Ar-4%H_2 at 3 J/cm^2

This couple also showed very strong bonding after 500°C annealing, although it was weak upon 300°C annealing. It seems that the mechanism is very similar to the irradiation at 1 J/cm^2. However, no evidence of Cu_2O (O KLL at 512 eV) formation that is the most stable copper oxide was found at the interface and in the film, and the copper oxide layer was very thin as compared to the copper oxide developed in the couple irradiated at 1 J/cm^2. The analysis of the substrate before the film deposition showed that excess aluminum had formed on the irradiated surface. Therefore, the available oxygen for the formation of copper oxide is very small in this couple as compared to the couple with the substrate irradiated at 1 J/cm^2.

5.1.7 Gold/alumina couples irradiated in air and Ar-4%H_2 atmospheres

As evidenced by the gold Auger peak shift, a chemical reaction between gold and alumina can occur when the alumina is irradiated in an oxygen-rich

atmosphere at a laser energy density of 1 J/cm^2. This result is consistent with the adhesion strength enhancement obtained in these couples. An adhesion strength of 50 MPa for that couple measured by the pull test is much higher than the value of 1 MPa that is obtained for substrates irradiated in Ar-4%H_2 at 1 J/cm^2.

Gold is not expected to react with oxygen, or oxides, because the heat of formation of Au_2O_3 is + 39 Kcal/mol [111, 112]. However, Moore and Thornton found that a strong bond developed when gold was melted on fused silica in the presence of oxygen [113]. Their results also demonstrated a chemical reaction between molten gold and silica although the reaction of gold with oxygen is not thermodynamically possible.

The OKLL peak positions are 506.3 eV and 506.8 eV for the substrates irradiated in oxygen rich and Ar-4%H_2 atmospheres (figures 4.36 -a and -b). The Al KLL electron Auger peaks in the absence of the gold film are 1389.4 eV and 1390.8 eV for laser irradiation in oxygen and in Ar-4%H_2, respectively. The reference peak positions of the differentiated Auger peak spectra for aluminum from metallic aluminum and alumina are ~ 1388 and 1396 eV, respectively. Therefore, the two substrates contacting with gold film are not from the stoichiometric alumina. These non-stoichiometries may be due to the laser irradiation. However, the substrate irradiated in oxygen rich atmosphere reacted with gold film as evidenced by the O KLL peak shift by 1.2 eV at the interface, but the other irradiated in Ar-4%H_2 did not.

The shift of Al KLL at the interface of the Au film/alumina couple irradiated in oxygen may be associated with the excess oxygen that may have reacted with gold film at 300°C.

Al KLL at 1390.8 eV from the alumina irradiated in Ar-4%H_2 at 1 J/cm^2 indicates that metallic aluminum and substoichiometric alumina could be present in alumina irradiated in Ar-4%H_2, because the overlap of Al KLL peaks from these different chemical states could shift the total aluminum peak towards higher kinetic energies. However, the utmost surface of this substrate is easily reoxidized to the stoichiometric alumina as shown in figure 4.15. That layer may have acted as a reaction barrier. In the depth profile conducted in this work, the evidence of the reoxidation was not detected, because the reoxidized layer will be only a

mono layer and the Auger electron escape depth of Al KLL is 4 -5 monolayers. Once the reaction takes place in the couple, the thickness of the reacted layer should be more than a mono layer. Since the sputtering rate used in this work is a few Å/cycle, the reacted layers will be easily detected. Therefore, no peak shift in this depth profile indicates that there is no interfacial reaction.

The other possibility for the no detection of the reoxidized layer is ion bombardment induced damage. However, the damage induced with 500 eV energy ion bombardment is very small, as estimated by the TRIM calculation. The calculation will be shown in the later section of this chapter.

5.2 Interface in the metallic films/ surface-modified AlN couples

As briefly mentioned in the section 4.5.3, there is a strong correlation between the amount of oxygen at the interface and the adhesion strength. In this section, the surface change due to laser irradiation and the interface analysis of the couples will be discussed.

5.2.1 Laser induced surface modifications of AlN

As-received AlN substrate used in this work shows very rough surface ($\leq$ 0.4μm) and larger grains than Al_2O_3 as described in section 3.1.1. As shown in a SEM micrograph (figure 4.24), these substrates includes large cavities on the surface and exhibits sharp edges for each grain. The melting threshold energy density appears to be at about 0.7 J/cm^2 (figure 4.23b), since the irradiation with 0.5 J/cm^2 does not change the topography as compared with the as-received (figure 4.23a). As the laser energy density is increased, remarkable differences on the surface topography are observed (figures 4.23, 4.25a, and 4.25b) and the degree of surface smoothening increases.

Along with the decrease in the surface roughness of AlN substrate, remarkable changes in the surface chemistry took place after laser irradiation. Since Al_2O_3 is thermodynamically more stable than AlN [95], mechanical and thermal processing in air induces the oxidation of the AlN surface. Therefore, the

surface of as-received AlN was mostly Al_2O_3 (figure 4.16). After laser-irradiation in Ar-4%H_2 at 4 J/cm^2, the Al LVV peak position shifts to the higher kinetic energy, implying that the surface is ablated and/or the substrate is decomposed leaving metallic aluminum layers (figure 4.17). However, the surface is not the perfect AlN even after removing the surface by laser irradiation, because the surface Al LVV peak is not from AlN (peak *i* in figure 4.17). Two possibilities can be considered in this respect; i) the laser ablation cannot eliminate the surface oxide completely, or ii) complete ablation takes place, but thermally decomposed metallic aluminum from AlN is exposed to the atmosphere and then reoxidized. The latter is more likely to be the case since the surface is considerably smoothened and subsequent sputtering changes the chemical composition from a mixture of AlN and Al_2O_3 to a composite of Al and AlN (peak *iii* in figure 4.17) . These trends can also be found by oxygen and nitrogen Auger peaks (figure 4.18). The surface of as-received AlN exhibits mostly oxygen Auger peak, whereas the irradiated surface shows both nitrogen and oxygen Auger peaks. Of course, the oxygen peak is from the Al_2O_3 and the nitrogen peak is from the AlN (figure 4.18).

It may be of interest to determine sizes and distribution of the metallic aluminum clusters in the AlN matrix. Cross-sectional TEM micrograph shows that undecomposed AlN particles are embedded in the metallic aluminum patch (figure 4.28) and that approx. patch size is ~ 1 - 2 μm. Auger mapping shown in figure 4.29 agrees well with the TEM result. Here, the Auger mapping is a planar view. The electrical resistivity was measured on the surface of laser irradiated AlN and it was found that the resistivity decreased as the laser energy density was increased [114]. This indicates that the amount of metallic aluminum in AlN increases with increasing the laser energy density. This is in contrast with the result that laser irradiated alumina was electrically insulating and approx. size of the metallic aluminum embedded in the alumina laser irradiated in Ar-4%H_2 atmosphere at 3 J/cm^2 is approx. 25 nm.

5.2.2 Cu/AlN couple with the substrate laser irradiated in air at 0.3 J/cm^2 energy density

This couple was annealed at 300°C for 1 hr. Oxygen at the interface of this couple is from the copper oxide as well as aluminum oxide (figures 4.30 and 4.31). The existence of Al_2O_3 indicates that the laser irradiation did not remove the aluminum oxide layer that inherently existed on the as-received AlN substrate. Since the threshold energy density for the melting of the alumina and aluminum nitride (approx. 0.7 J/cm^2) is much higher than this energy density, it is hard to believe that any chemistry change on the ceramic surface occurred. However, various O KLL kinetic energies and peak shifts of the Cu LMM and Al KLL at the interface imply that the chemical reaction took place in this couple after 300°C annealing.

Possible changes on the substrate irradiated at 0.3 J/cm^2 are the surface cleaning and presence of excess oxygen. When the alumina was irradiated in air at 0.4 J/cm^2, excess oxygen was detected on the surface as shown in table 4.4. The excess oxygen existing in the alumina layer on the surface of AlN may have played a role in the copper oxide formation at the interface. When the strong bonding was obtained for the couple with an as-received AlN substrate after 300°C annealing, there might have been less surface contaminants by chance so that they could not impair the reaction between the film and the substrate.

5.2.3 Cu/AlN couple with the substrate irradiated in air at 3 J/cm^2 and in Ar-4%H_2 at 1.5 J/cm^2

This couple with the substrate irradiated in air at 3 J/cm^2 showed weak bonding at 300°C annealing but very strong at 500°C annealing. Although the energy densities are different, the couple irradiated in Ar-4%H_2 at 1.5 J/cm^2 also showed similar trend. Therefore, the couples with the substrates irradiated in air at 3 J/cm^2 and in Ar-4%H_2 at 1.5 J/cm^2 annealed, respectively, at 300°C (weak bonding) and 500°C (strong bonding) were analyzed.

By comparing the depth profiles acrossing the interface of these two

couples, a big difference in the gradient of oxygen concentrations can be realized. In the couple annealed at 300°C, the oxygen concentration variation at the interface is almost negligible as compared to the changes of Al and N concentrations (figures 4.42). This means that the film mostly contacts with the AlN substrate. In the other couple annealed at 500°C, on the other hand, the concentration gradient of oxygen increases steeply as the interface is approached (figure 4.44). The oxygen seems to be mostly from copper oxides because the oxygen concentration decreases with the decrease of the copper concentration as approaching to the interface. In both couples copper oxide formed at the interface, however, the kinetic energies of O KLL in the layer closer to the interface of the couple annealed at 300°C and at 500°C are, respectively, ~ 510 eV and 512 eV which are indicative of the formation of CuO and Cu_2O, respectively.

It is hard to believe that the excess oxygen exists on the surface of the AlN laser-irradiated in Ar-4%H_2 at 1.5 J/cm^2. However, the depth profiling of the couple annealed at 500°C shows that considerably thick oxide layers exist at the interface (figure 4.44). As the interface is traversed by the sputtering, the O KLL peaks change from 512 eV to 507.5 eV and the Al KLL peaks from ~ 1392 eV to 1395 eV. As previously discussed, O KLL at 507.5 eV and Al KLL at 1392 eV mean that most probably a Cu-Al-O compound formed at the interface of this couple. In this respect, the strong bonding mechanism of the copper deposited on AlN substrate is similar to the copper on alumina substrate. As indicated by the 1395 eV Al KLL, metallic aluminum is formed in both of the substrates by the laser induced decomposition of AlN. That metallic aluminum may have been reoxidized and then Cu-O-Al compound produced when the couple was annealed at higher temperature (500°C in this work).

In the couple with the substrate irradiated in air at 3 J/cm^2 and annealed at 300°C, O KLL and Al KLL showed similar behavior to the case of the irradiation in Ar-4%H_2 at 1.5 J/cm^2, but the low concentration of the oxygen may have produced poor linking between the copper film and AlN substrate, resulting in the weak bonding.

At the moment, the origin of the oxygen introduced at the interface during

annealing at 500°C is questionable. The possibilities are as follows:

(i) The dissolved oxygen in the film may have been diffused to the surfaces of the film, followed by the oxidation (the diffusivity of the oxygen increases with increasing the temperature).

(ii) The oxygen may have become encaptured in between the film and the substrate during deposition due to the rough surface characteristic of the AlN substrate (figure 4.25). The captured oxygen may have diffused out during annealing and the amount of the diffused oxygen is proportional to the annealing temperature.

(iii) The oxygen may be from the annealing furnace. The oxygen from the chamber may have diffused through the film and reacted with the film and substrate at the interface.

If case (i) is true, oxygen concentrations at both of the surfaces of the film should be the same. If case (iii) is true, the concentration of the oxygen on the film surface should be larger than that at the interface. However, in the couple annealed at 500°C the concentration at the interface is much higher than that on the surface of the film. Therefore, the oxygen may be argued to have come from the interface as explained in case (ii).

5.2.4 Cu/AlN couple with the substrate irradiated in air at 1 J/cm^2

This couple showed strong bonding when it was annealed at 500°C. At the interface the copper was in contact with two different areas, that is, Al_2O_3 and AlN enriched areas as explained in section 4.5.3.4. In both areas, copper oxides were detected (figures 4.47 and 4.48), however, oxygen from copper oxides in contact with Al_2O_3 is mainly from CuO, while the other is mainly from Cu_2O. In both cases, after removing the film O KLL peak positions are ~ 507 eV, that is not exactly from the Al_2O_3 and the Al KLL is from the non-stoichiometric alumina or aluminum nitride. Therefore, it is concluded that in both areas interfacial reactions take place whose product may be Cu-O-Al compound.

However, the amount of the reaction products will be different.

5.2.5 Gold/AlN couple with the substrate irradiated in air at 2 J/cm^2

Upon annealing at 300°C, gold film /AlN couples exhibit weak bonding as shown in figure 4.4, and, in general, the adhesion strength decreases with increasing laser energy densities. However, an increase of the annealing temperature to 500°C resulted in very strong adhesion of the couples irradiated in both air and Ar-4%H_2, regardless of the energy densities.

In the interface of the couple annealed at 300°C, oxygen is from the Al_2O_3 (~ 506 eV). That means that the metallic aluminum decomposed from AlN substrate is reoxidized and no reaction with gold film takes place. In agreement with this, the Al KLL at the interface is from the stoichiometric alumina. The metallic aluminum and/or substoichiometric Al_2O_3 and/or AlN detected after encompassing the interface for both couples implies that AlN is decomposed by the laser irradiation, followed by the reoxidation.

After 500°C annealing of this sample, gold LVV peak shifted by - 1.5 eV and Al KLL peaks exhibited complex shaped, indicating that an interfacial reactions took place. Since the gold can not react with oxygen and/or alumina, the possible interfacial reaction can be considered as following. *During the 500°C annealing the stable reoxidized aluminum oxide was broke and then the gold film contacted with the unstable metallic aluminum and substoichiometric Al_2O_3 and/or AlN. Hence, the reaction might have taken place, leading to the strong bonding.*

5.3 Gold film deposited onto ion bombarded sapphire

Pull-tests show that the adhesion of sputter-deposited gold films to annealed and pre-sputtered sapphire is over 15 times higher than that of the film deposited onto as-received sapphire. No annealing after deposition is required to achieve such a strong bonding. The causes of the increase in bonding strength has been analyzed by AES and are discussed in the next sections.

5.3.1 Ion bombardment effect on Al_2O_3 substrate

Al_2O_3 was reduced by 7 keV Ar ion bombardment, because the Auger electron kinetic energies of Al LVV from metallic aluminum (68 eV) was detected (figure 4.29). However, the metallic aluminum produced do not cover the entire bombarded surface, because the Al peak from the metal, that has a higher sensitivity factor than the corresponding peak Al from Al_2O_3, is much lower than the latter.

Kim et. al. [95] reported that oxides with formation free energy (ΔG_f°) above -60 kcal/mol were reduced by 400 eV Ar^+ ion bombardment, while oxides with ΔG_f° below -118 kcal/mol were stable to this exposure. They concluded that the ratio of reduced oxide to total sputtered amount during ion bombardment is inversely proportional to the magnitude of ΔG_f°. Evidence of the reduction of ferric oxides to FeO was reported by McIntyre et. al. [115]. The heats of formation of these oxides are -177 kcal/mole. However, Mitchell et. al. [116] found that the reduction in at % oxygen during ion bombardment at a beam energy between 1 and 4 keV for a-Fe_2O_3, Fe_3O_4 and FeO was always ~5% of each initial concentration, which is almost negligible. When they used 1 keV Xe ions, the reduced oxide decreased even further, to ~4 at. % of the initial concentrations. The formation free energy of Al_2O_3 (- 377 kcal/mol) is much lower than those of the iron oxides. From Kim's work, one could expect Al_2O_3 not to be reduced by ion bombardment but rather to undergo mostly sputtering. Our results thus suggest that there is no clear correlation between ion-induced ceramic oxide reduction and heat of formation, at least for reduction taking place at the very near-surface.

Electron irradiation during AES analysis can also cause decomposition of the ceramics [77]. The threshold electron dose for decomposition of Al_2O_3 is approx. 7.8C/cm^2 after 50 nA for 3 kV beam energy and an incubation period is usually required for the decomposition onset at any given current density. However, the peak shown in figure 4.30 was obtained immediately after acquiring the data with a current density much lower than the threshold value for decomposition onset under electron irradiation. Therefore, it is concluded that in

these experiments the reduction of Al_2O_3 is due to the ion bombardment. At an ion energy of 3 keV no reduction was detected. By contrast, Schrott et al. reported reduction of Al_2O_3 with 0.5 keV Ar^+ ion bombardment [117] using a much higher ion current than used here. Clearly, the ion energy is not the only parameter influencing the reduction behavior of Al_2O_3.

5.3.2 Effects of Sputtering on gold/Al2O3 couples

One of the advantages of performing the interface analysis with a variable coverage film is that the effects of the ion beam bombardment required for AES analysis can be reduced. The displacement, vacancies plus replacement collisions, generated by the 500 eV Ar^+ ions impinging on a 1.1 nm Au film/sapphire were calculated using the TRIM code [85] and are shown in figure 5.2. The threshold displacement energies for Au, O and Al were assumed to be 20, 40 and 18 eV, respectively. The displacement energy for oxygen is possibly a lower limit, as per data in the literature [118] . For this film thickness, the damage is almost completely confined to the film, and only 10 % of the gold atoms at the interface have been displaced from their positions. In the case of 0.1 nm film the damage at the interface increases considerably, as can be seen in figure 5.1b. The ion gun current was 2 nA and the average flux, calculated using 200x200 mm^2 sputtered area, was 3.1 x 1013 ions/(cm^2.s). The sputtering rate with 500 eV Ar^+ ions is $4.3x10^{-3}$ nm/s as obtained using the same TRIM full cascade calculation.

The damage per unit time at the interface in displacements per atom (dpa) is plotted as a function of film thickness in figure 5.3. The total damage can be calculated by integrating the damage per unit time during the sputtering interval as

$$\int_0^{t_S} S(x)dt = v_s^{-1}\int_0^{x} S(x)dx$$

where S(x) is the damage per unit time plotted in figure 5.2, t_S is the sputtering time, the variable x represents the film thickness and v_S is the sputtering rate. In this approximation, the damage generated by removing the gold film up to a thickness of 0.11 nm and 0.6 nm are, respectively, 0.25 dpa and 0.56 dpa. This

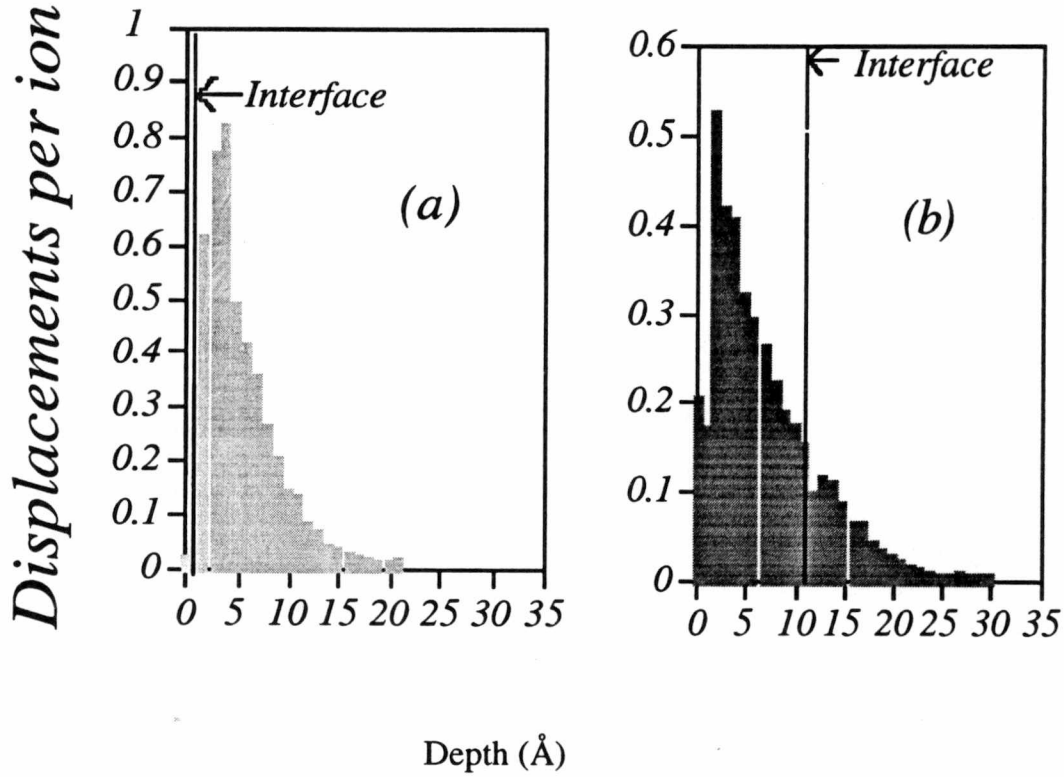

Figure 5.2. Atomic displacement profile produced by 500eV Ar^+ ion bombarded as a function of depth . (a) 1 Å-thick gold film : , (b) 11 Å-thick gold film

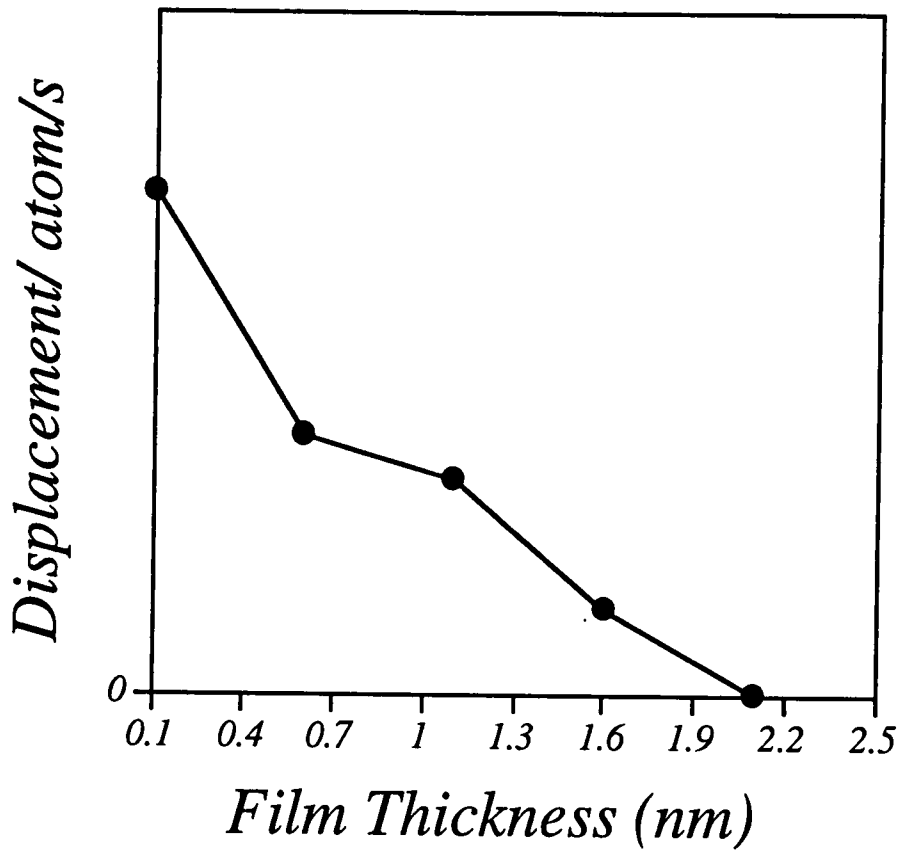

Figure 5.3. Displacements per ion at interface as a function of film thickness

damage is at most about half of the damage generated for denuding the interface (1.05 dpa). This analysis indicates that a substantial damage to the interface is avoided if a thin gold film remains in the surface during the analysis of the interface.

As already indicated in the experimental section, neither shifts in the electron Auger peaks of gold nor reduction of Al_2O_3 were detected in specimens that had not undergo 7 keV pre-sputtering. The analyses for these specimens were performed using the same technique, demonstrating that the damage produced at the interface did not introduce artifacts in any of the results presented here.

5.3.3 Gold film/sapphire substrate interface

We have shown that strong adhesion of gold films is obtained when the Al_2O_3 substrates are bombarded before deposition with 7 keV Ar ions. Post-deposition annealing is not required to enhance bonding. There is also a definite effect of annealing preceding substrate sputtering prior to deposition, as shown in Table 4.1. Annealing removes contaminants such as carbon, hydrocarbon and hydroxyl [12, 119, 120]. Surface contaminants on the substrate may act as a barrier impeding the occurrence of bonding [19].

It was shown that the interface region and its immediate neighborhood can be probed taking advantage of the electron escape depth and the shallow wedge in the film. For instance, when the gold film deposited on the substrate is ~ 1.5 nm the chemical state of Al at the interface can be analyzed using the Al KLL Auger electrons that have an electron escape depth of ~ 2 nm. As the electron beam is moved toward the center of the sputtered region, the film becomes thinner and larger portions of the substrate are probed.

The increased kinetic energy of the oxygen KLL Auger electrons at the interface (figure 4.52c) reveals that oxygen at the interface is in sub-stoichiometric alumina because the kinetic energy of the oxygen Auger peak tends to decrease with increasing oxidation number [65]. As revealed by the oxygen positive peak shift, metallic aluminum features appear in the Al KLL

Auger peak spectrum (figure 4.53). Metallic aluminum features are more prominent at the near surface than in the subsurface, as shown in the series of Auger peak spectra in figure 4.53. Increasing the analysis volume from the substrate surface, the Al KLL Auger peak becomes more characteristic of Al_2O_3. The Al KLL peak spectrum from the substrate near-surface (approx. 5Å depth), figure 4.53, shows a complex fine structure containing peaks which are neither from metallic aluminum nor from Al_2O_3 peaks. These peaks may stand for the reaction of pre-sputtered sapphire with gold film. The reduced kinetic energy of the Au NVV Auger electron at the interface (figures 4.52 -a, and -b) indicates that gold has reacted at the interface. This result is in agreement with the conclusion from the O KLL Auger peak that a metastable interfacial compound is formed at the interface. This metastable compound seems to be favored by the highly metastable reduced alumina generated during presputtering and the relatively high kinetic energy of the incoming gold atoms.

5.4 Copper drift into SiO_2 matrix under an applied electric field application

In studying copper penetration into SiO_2, it is of interest to know how the elemental copper is changed to the copper ion prior to the drift. One possibility is that copper is firstly oxidized at the interface by annealing and copper ions are then generated from the oxide under electric field application, followed by the drift into the matrix.

Figure 4.54 clearly shows that copper oxide is formed at the interface of Cu/SiO_2. In the same couple, copper is detected in the SiO_2 substrate as shown in the SIMS profile of figure 4.55. It was also reported that electric field enhanced copper penetration was achieved at temperature as low as 250°C [121, 122]. No copper drift was found when the electric field is applied in the vacuum atmosphere [89]. Therefore, the formation of oxide at the interface may be very important for the copper drift. It may be a source of copper ions under an applied electric field.

It is not clearly understood why the concentration decreases at the Cu/SiO_2 interface and increases deeper inside. Also, no change in the

concentration was detected at the interface of SiO_2/Si.

Figure 5.4 is a schematic of the electric field driven diffusion path of Cu into SiO_2. Further study will be required to investigate the mechanism.

5.5 Electron irradiation induced decomposition of Al_2O_3 substrate

Decomposition of Al_2O_3 has also been achieved by ion beam bombardment and laser irradiation. As already shown these methods can be used for a wide range of applications such as surface modification, thin film metallization, enhancing adhesion of metallic films to various surface modified substrates, etc.. Electron beam induced decomposition of ceramics might also be open for these applications but requires further studies. Electron bombardment can induce physical or chemical desorption of ionic, neutral and molecular species from the surface and can also promote decomposition of insulating materials.

The decomposition of the subsurface layers is much slower than that of the surface layer. Probably, the reason for this delay is that the oxygen formed by decomposition in the inner layers must be transported to the surface for desorption.

A dose of ~ 4.9×10^{19} electrons/cm^2 (7.8 C/cm^2) at 3 kV is required to initiate the electron-induced decomposition of alumina. This dose is independent of all but the lowest instantaneous electron flux used in this paper. The decomposition rate of alumina first increases with dose from the onset, but it decreases at larger doses, e.g., higher than 8×10^{20} electrons/cm^2 for the case shown in figure 4.8. The dose required for the decomposition onset is however strongly dependent upon the state of the surface. All the reported dose threshold values were obtained after the specimen surface was sputter-cleaned with 1 keV Ar^+ ions until the carbon Auger peak disappeared.

The decomposition onset can be drastically delayed by carbon surface contaminants that apparently act as a barrier for the desorption of oxygen evolving from decomposition. When a significant carbon layer is present on the surface of sapphire the threshold dose for decomposition more than doubles relative to the sputter-cleaned substrates. Therefore, maximum decomposition

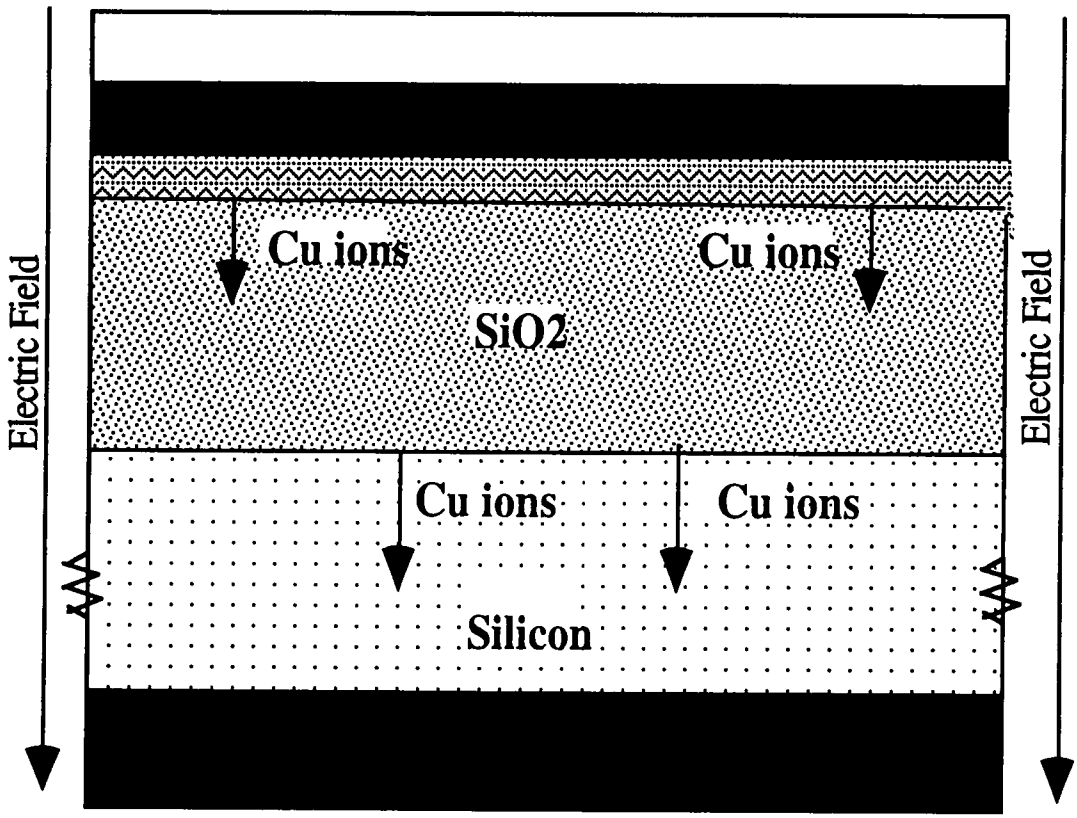

Figure 5.4. Schematic of copper diffusion into silica under an electric field.

rate can be obtained when no surface contaminants are present. A very low current (≤ 20 nA) and a low voltage (3 kV) are required to eliminate oxide decomposition during analysis. A large rastering area significantly reduces the electron flux and thus increases the time required for the decomposition onset (see Table 4.2).

It has been reported that the heating produced by electron bombardment of insulating materials can change the near-surface chemical composition [123]. However, since the threshold dose required for the onset of decomposition is, within experimental error, independent of the flux for an electron beam current greater than 53 nA, heating due to electron bombardment does not affect the decomposition behavior significantly.

The kinetic results shown in figure 4.8 correspond to the decomposition that takes place only in approximately the first surface monolayer. This independence of the decomposition onset flux implies that each electronic process inducing decomposition is independent. Besides the electron induced decomposition of the oxide, reoxidation can take place by oxygen molecules present in the chamber atmosphere that impinge on the sapphire surface. However the electron fluence required for the decomposition onset is nearly independent of the rastering area (less than 6% difference, as can be seen in table 1). There is almost no re-oxidation. Then, neglecting re-oxidation, the decomposition kinetics can be expressed by the equation

$$\frac{N}{N_o} = 1 - \exp(-J\sigma t) \qquad (5.1)$$

The data in figure 4.8 was fitted using equation (5.1) with the cross sections as an adjustable parameter. The value of σ was found to be 3×10^{-24} cm^2. The magnitude of the cross section is significantly smaller than values reported for ESD (~ 10^{-20} cm^2) [124, 125].

The effect of the residual gas in the chamber on electron irradiation-induced decomposition was studied for SiO_2 by Thomas [75]. In his study, the saturation value of N/N_O decreases as the partial pressure of oxygen increases (see figure 4 in ref. 75).

We have observed that when the spot-size beam is used Al_2O_3 decomposition starts almost immediately for a flux of $2.9x10^{20}$ electrons/cm^2.s. As shown in figure 4.7e, after 30 s of irradiation a significant portion of the first monolayer has been decomposed, but further decomposition seems to proceed very slowly. In fact, the peak of aluminum from alumina after 300 s indicates that a very significant portion of alumina at the surface has not been decomposed yet (figure 4.7e). On the other hand, in scanning mode it is seen that only a small part of the monolayer has been decomposed after 27 s, but almost complete decomposition took place after 270 s (figure 4.7d). If each electron produces an independent event of excitation/decomposition we should expect that at a higher flux the onset time should be shorter, as observed, and also that the decomposition should end earlier. An earlier end, however, appears to be inconsistent with the previously described results. The cause of this apparent contradiction is the contribution of the Auger electrons excited by back scattered electrons in the near surface region that is close to but not within the irradiated region. The area that is outside the surface of incidence of the primary beam is not decomposed, in principle, and contributes always a certain amount to the intensity of the aluminum peak from undecomposed alumina. Figures 5.5 -a and -b are schematics of the relation between the irradiated area and the region where the back scattered electrons produce excitation and emission of Auger electrons for the cases of spot beam and scanning mode. Clearly the ratio of area irradiated by the primary beam to area irradiated by the back scattered electrons is much larger for the scanning beam than for the spot beam. Ishimura and Shimishu [126] calculated the backscattering corrections for Auger analysis. They computed the backscattering factor, $R= 1 + I_b/I_p$, where I_b and I_p are the Auger intensities excited by back scattered and primary electrons, respectively. In the case of aluminum, for an energy of the primary beam of 3 keV and a binding energy of the Auger electron of 100 eV the R factor is 1.67 [126]. This indicates that 67% of the signal is contributed by the excitations induced by the back scattered electrons from both inside and outside the zone irradiated by the primary beam.

The Auger signal of aluminum from sapphire does not disappear even if all the region irradiated by the primary beam has been decomposed because the

back scattered electrons excite Auger electrons also outside the irradiated region. The ratio of the aluminum peak from metallic aluminum (68 eV) to the aluminum peak from alumina (54 eV) when the area irradiated by the primary beam is fully decomposed is,

$$R_d = C\frac{A_p}{A_b - A_p} = \frac{Cl}{4\tau(1+\frac{\tau}{l})} \qquad (5.2)$$

where C is a constant accounting for the sensitivity factors of the aluminum peaks, A_p is the area irradiated by the primary beam and A_b is the area irradiated by the back scattered electrons. The area irradiated by the primary beam has been assumed to be a square of side l and τ is a characteristic length related to the range of the back scattered electrons outside the zone irradiated by the primary beam (figure 5.5). As the scanning area is increased l becomes much larger than τ and the ratio τ/l may be neglected in eq. 5.2, which reduces to

$$R_d \cong \frac{C}{4}\frac{l}{\tau} \qquad (5.3)$$

The ratio R_d increases as the length of the rastering area increases as can be seen in figure 4.9.

5.6 Studies on the sample charging during AES analysis

In the analysis of the metal/ceramic interface, the sample charging due to the electron accumulation in insulating materials can be avoided by taking advantage of the conductive film at the sputter crater edge. However, a bare ceramic insulator often produces the charging during AES analysis that results in an artificial peak shift. A new way to surmount this problem was devised in thiswork and successfully applied to the analysis. In this section the principle to deal with the charging of the insulator is discussed.

Figure 5.6 is a schematic of the dependence of the secondary electron emissions induced by the incident electron for typical insulating materials as a

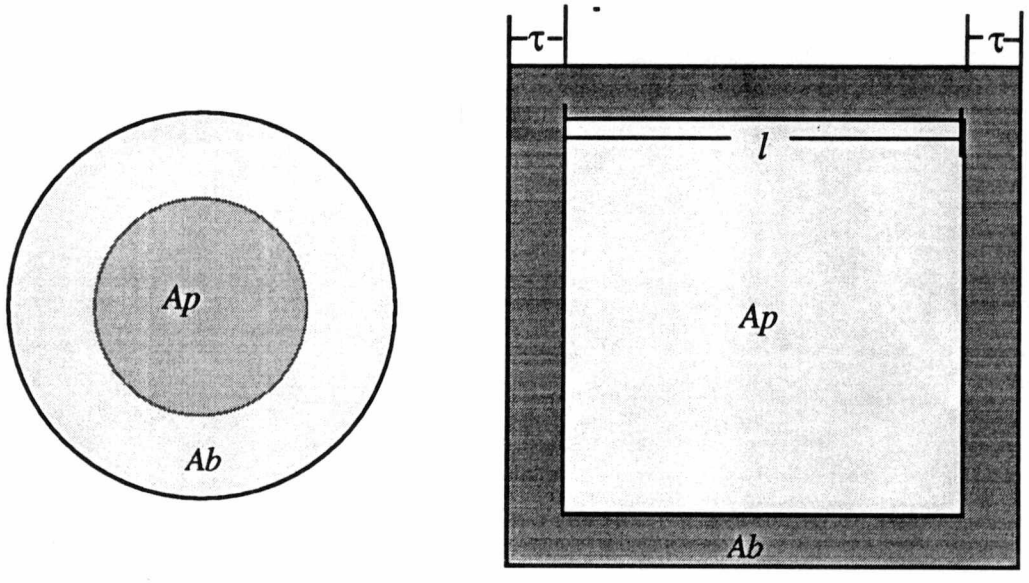

(a) (b)

Figure 5.5. Schematics of the relation between the irradiated area (Ap) and the region (A_b) where the back scattered electrons produce excitation and emission of Auger electrons for spot beam (a) and scanning mode (b).

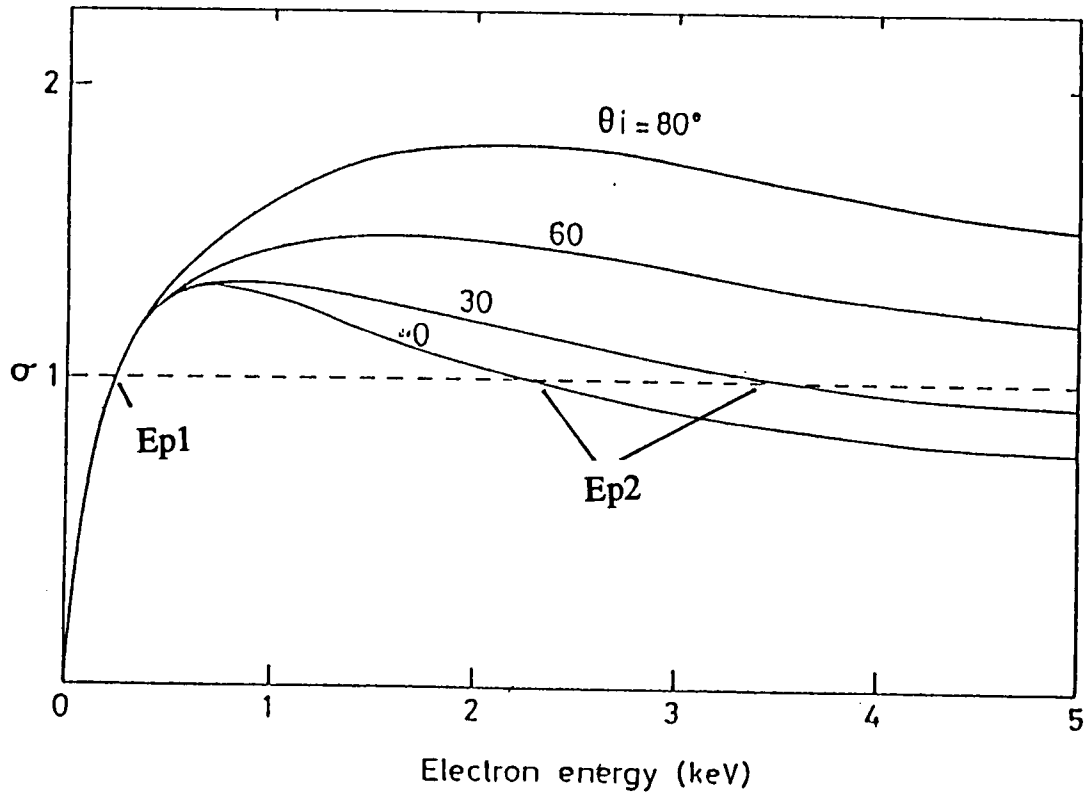

Figure 5.6. A schematic of the secondary electron emission coefficient as a function of the incident electron beam angle and energy.

function of the incident angles. δ , the secondary electron yield, is the number of the secondary electron per incident electron. When $\delta = 1$ (at the two cross over points in the figure 5.6), no charging occurs. When $\delta < 1$, the sample is negatively charged and the kinetic energy of the emitted Auger electrons will be reduced, causing to a peak shift to lower energies in the peak spectra. When increasing the incident beam angles, a cross over point in the higher incident beam energy region (E_{p2}) shifts toward higher electron energies (figure 5.6). Therefore, the increased incident beam angles allow one to use higher incident electron energies without the sample charging. However, figure 5.6 is only applicable to a flat sample. If the surface of the ceramic has a certain roughness like alumina and polycrystalline AlN, the curve in figure 5.6 is no longer applicable.

Electron trajectories at each electron impinging area should be considered to predict the charging during AES analysis of the ceramic with a certain roughness. At given incident electron beams, electron trajectories generated byincident electron beams are various depending on the impinging areas on the surface of the polycrystalline ceramics. Electron beams impinging on the grain boundaries or in the cavities will have longer trajectories than those impinging on the protruded areas, resulting in more sample charging. A conceptual schematic for this is shown in figure 5.7. In this case, the sample charging is dependent on $\Sigma\delta_i$ that is varied upon the analysis areas. The area dependence of the sample charging is well shown in figures 4.13 -a and -b. The charging varies from positive to negative even within a grain.

Conventional methods such as a reduction of accelerating voltages and current densities, using conducting masks, heating, etc. can be employed in the specific cases as already explained in section 2.6.3.3. Recently, a more general method using an electron flooding gun when $\delta > 1$ and/or a positive ion gun when $\delta < 1$ was suggested to control the charging during AES by Ishimura et. al. [127]. They could analyze an insulator without any charging with this way. Sputtering problem when using an ion gun was also solved by using the low energy helium ions rather than the usual argon ion [127]. This method has also a problem since the static charging on the surface is only temporarily frozen. Therefore, the sample charging of the insulating materials still remains as a challenging problem in the

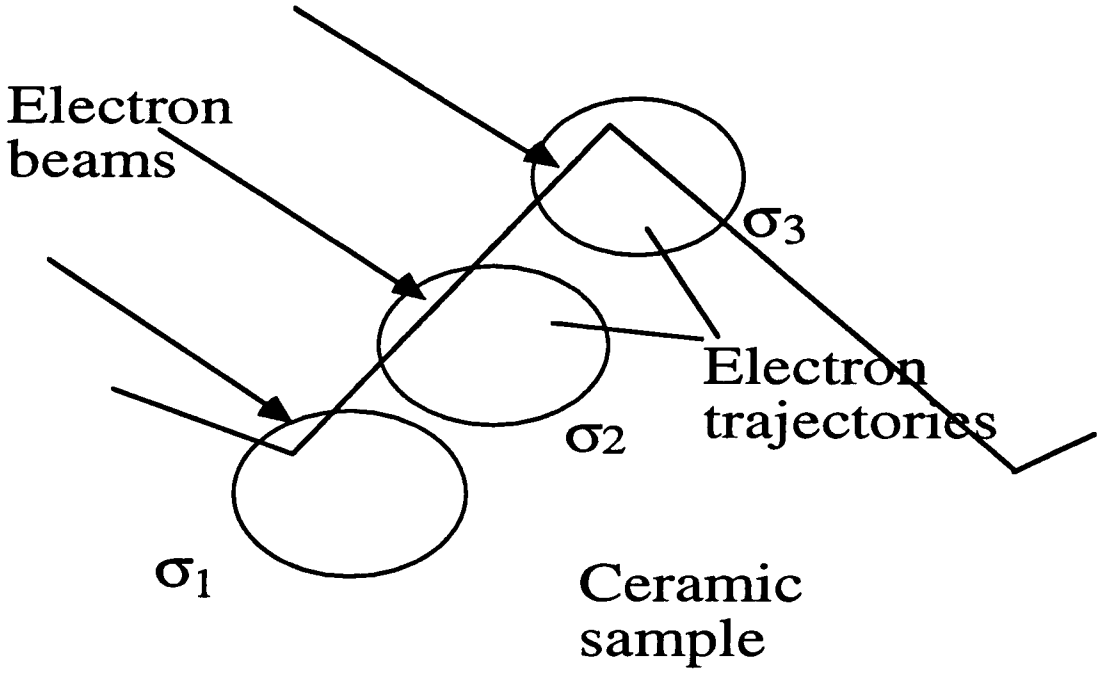

Figure 5.7. A conceptual schematic of the two dimensional electron trajectories possibly produced in a particle or grain as a function of the surface topography and the electron impinging position. When the AES analysis area includes more than a grain or a particle, if $\Sigma\sigma_i > 1$, $= 1$, and <1, positive charging, charge neutrality, and negative charging are obtained respectively.

AES analysis.

In this work, the charging was solved by a new technique using the surface topography. The secondary electron image was enlarged and the analysis area was selected within a grain. The charging could be controlled by selecting the analysis area (both position and area) on the top of a grain or a particle. It was aimed at adjusting the electron trajectories as described in figure 5.7. When $\Sigma\delta_i \approx 1$, the charging can be minimized.

CHAPTER 6

SUMMARY AND CONCLUSIONS

Metallic film/Laser surface modified ceramic couples

- *Cu/Al_2O_3 couple*

1) Excess oxygen is found on the surface of Al_2O_3 laser-irradiated in the oxidizing (e.g., air), whereas metallic aluminum is detected if the irradiation atmosphere is reducing (e.g., Ar-4%H_2). However, in *both* cases metallic aluminum ~ 20 nm in diameter is formed in the subsurface of the substrate.

2) Excess oxygen introduced in the Al_2O_3 substrate gives rise to the formation of copper oxide in the copper film closer to the interface of Cu/Al_2O_3 couple after low temperature (300°C) annealing. Along with the formation of the copper oxide, a Cu-Al-O compound develops at the interface of this couple.

3) The adhesion of this couple with the substrate irradiated in Ar-4%H_2 atmosphere of ≥ 1 J/cm^2 can be enhanced by annealing at 500°C. The interfacial reaction between the copper, metallic aluminum, and substoichiometric Al_2O_3 defines the adhesion mechanism.

- *Au/Al2O3 couple*

1) Strong bonding of these couples takes place when the substrate is irradiated in air, while couples involving substrates irradiated in Ar-4%H_2 exhibit weak bonding.

2) The formation of an Au-O-Al compound at the interface, which occurs when the substrate is irradiated in air, is responsible for strong bonding in this couple.

• *Copper/ AlN couples*

1) As received AlN substrate is covered with aluminum oxide on the surface. Laser irradiation eliminates the oxide layer by ablation.

2) Significant surface smoothening and decomposition take place in laser irradiated AlN. However, decomposed metallic aluminum formed from the decomposition is reoxidized upon exposure to air. Thus, aluminum oxides form in the utmost surface layers, leaving buried metallic aluminum.

3) Al_2O_3 and AlN coexist on the laser irradiated AlN surface. It seems that the adhesion strength can be importantly affected by the relative amount of these compounds at the surface, where the metallic film is deposited.

4) When the couple contains a substrate irradiated at low energy densities ($\leq \sim 1.5$ J/cm^2), a relatively low temperature (300°C) is required to enhance the adhesion. By contrast, when the substrate has been irradiated at a higher energy density ($\geq$ 1.5 J/cm2), also higher annealing temperature (500°C) produce comparable adhesion improvement.

5) The mechanism leading to strong bonding of the Cu/AlN couple is the formation of a Cu-Al-O compound at the interface of the couple similar to that formed in the case of the Al_2O_3 substrate. Hence more aluminum oxides at the surface produces higher adhesion strength.

6) When the substrate has been irradiated at lower laser energy densities within a given range, a lower annealing temperature produces a high adhesion strength. This result may be related to the observation that aluminum oxide on the surface of as-received AlN substrate is less ablated during the laser irradiation.

• Au/AlN couple

1) When the couple with the substrate irradiated in air at 2 J/cm^2 is annealed at 300°C and 500°C, the adhesion was weak and strong, respectively.

2) 500°C annealing induced the interfacial reaction of this couple, as evidenced by the gold Auger peak shift and a complex fine structure of Al KLL peaks at the interface.

Gold film/presputtered sapphire couple

1) Pull-tests show that the adhesion of sputter-deposited gold films to annealed and pre-sputtered sapphire is over 15 times higher than that of the film deposited onto as-received sapphire. No annealing *after* deposition is required to achieve such a strong bonding.

2) Formation of metallic Al together with oxygen-depleted alumina is detected on the surface of Al_2O_3 bombarded with 7 keV Ar^+ ions.

3) This interfacial metastable compound seems to be the cause of the strong bonding between gold and sputter-etched Al_2O_3. The formation of the compound is favored by the reaction between the reduced alumina generated during presputtering and the relatively high kinetic energy of the incoming gold atoms.

Analytical techniques

1) Sample charging during AES analysis of polycrystalline ceramic materials can be reduced or eliminated by focusing the analysis area in a grain and selecting the top part of the grain.

2) Decomposition of the Al_2O_3 by electron beam bombardment can be

eliminated by reducing the current density below ~ 7.8 C/cm^2 at an accelerating voltage of 3 KV. Similar value for the decomposition was obtained for AlN.

3) The interfacial reactions taking place in the metal/ceramic couples can be detected by analyzing on the film using higher Auger electron kinetic energies. This method can eliminate above mentioned sample charging and decomposition problems without any efforts, and is especially very useful when the thickness of the interface is very thin, viz., less than a few monolayers.

4) When the thickness of the interface is relatively thick, conventional sputter depth profiling method can also be successfully used for the interface analysis. In this case analysis area should be the sputter crater edge. Then, the sample charging can be eliminated until the sputter etching exposes the substrate after removing the interface, because the interface in the analysis area is continuously connected to the metallic film.

Decomposition kinetics

1) Surface contaminants act as a barrier for the decomposition.

2) As evidenced by Al KLL Auger peak, decomposition can take place in the subsurface at least 3 - 4 monolayers.

3) The reason why the decomposition does not take place completely, as seen in the Auger spectra, is due to the back scattered electrons.

REFERENCES

REFERENCES

1. Jian Li, Tom E. Seidel, and Jim W. Mayer, MRS Bulletin, Vol. XIX, No. 8 (1994) 16
2. Amanda H. Kumar and Rao R. Tummala, The Journal of Minerals, Metals, and Materials Society, July (1990)76
3. A. D. Westwood and M. R. Notis, the Journal of the Minerals, Metals, and Materials Society, June (1991) 10-15
4. J. M. Liu, H. Kurz, and N. Bloembergen: laser-solid interaction and Transient Thermal Processing of Materials, MRS Symp. Proc. , J. Narayan, W. L. Brown, and R. A. Lemons, eds., North Holland, New York, NY, vol. 13 (1983) 3-12
5. W. L. Wolfe: Handbook of Military Infrared Technology, U.S. Government Printing office, Washington DC (1965).
6. N. Von Allmen: in Laser and Electron Beam Processing of Materials, C. W. White and P. S. Peercy, eds., Academic Press, New York, NY (1980) 6-19
7. M. F. Von Allmen, " Physical Processes in Laser-Materials Interactions", edited by M. Bertolotti, Plenum Press, New York (1983) 57
8. W. L, Brown: in Laser and Electron Beam Processing of Materials, C. W. White and P. S. Peercy, eds., Academic Press, New York, NY (1980) 20-36
9. D. H. Lowndes, M. Desilva, M. J. Godbole, A. J. Pedraza, and D. B. Geohegan, MRS proceedings, Vol 285 (1992) 191
10. M. A. Schildbach and A. V. Hamza, Phys. Rev. B45, (1992) 6197
11. A. J. Pedraza, J. W. Park, M. J. Desilva, D. H. Lowndes, D. N. Braski, and H. M. Meyer, Amer. Inst. Phys. Conf. Proc. 288(1993) 329
12. A. J. Pedraza, J. W. Park, H. M. Meyer, and D. N. Braski, J. Mater. Res. Vol.9, No. 9 (1994) 2251
13. H. Esrom, Mat. Res. Soc. Proc., Vol. 204, (1991) 457
14. Aluminum Properties and Physical Metallurgy, ed. by J. E. Hatch, American Society for metals, Metals Park, OH (1984)
15. A. J. Pedraza, J-Y Zhang, and H. Esrom, Mat. Res. Soc. Proc., Vol. 285 (1993) 209
16. J. E. Griffith, Y. Qui, and T. A. Tombrello, Nucl. Instrum. Methods Phys. Res.

vol. 198 (1982) 27

17. L. E. Seiberling, J. E. Griffith, and T. A. Tombrello, Radiat. Eff. Vol 52 (1980) 201
18. J. E. E. Baglin, G. J. Clark, and J. Bottiger, in Thin Films and Interface II, Mater. Res. Soc. Symp. Proceedings, (1984) 179
19. J.E.E. Baglin, Mat. Res. Soc. Symp. proc. Vol. 47 (1985) 3
20. W.M. Skinner, *J. Appl. Phys.* 74(3), 1 August 1993, American Institute of Physics
21. A. E. Berkowitz, R. E. Benenson, R. L. Fleischer, L. Wielunski, and W. A. Lanford, Nuclear Instruments and Methods in Physics Research B7/8 (1985) 877-880.
22. J.E.E Baglin, A.G. Schrott, R.D. Thompson, K.N. Tu and A. Segmueller, *Nuclear Instrument and Methods in Physics Research* B19/20 (1987) 782-786, North Holland, Amsterdam
23. Z. L. Liau, J. W. Mayer, W. K. Brown and J. M. Poate, J. Appl. Phys. Vol 49 (1978) 5295.
24. O. F. Goktepe and M. L. Roush, Nuclear Instruments and Methods in Physics Research B7/8(1985) 803-807
25. T. Hioki, A. itoh, S. Doi, J. Kawamoto, and O. Kamigato, Nuclear Instruments and Methods in Physics Research B7/8(1985) 521-525
26 Jian Li, Tom E. Seidel, and Jim W. Mayer, MRS Bulletin, Vol. XIX, No. 8 (1994) 16
27. R. F. Bunshah and C. V. Dechpandey, J. Vac. Sci. Technol. A3(3) (1985) 553-559
28. Thin Film Processes, (J. L. Vossen and W. Kern, eds.). Academic Press, New York, 1978
29. R. F. Bunshah, " Deposition Technologies for Films and Coatings." Noyes, New Jersey, 1982
30. R. F. Bunshah, "Deposition Technologies for Films and Coatings." Noyes, New Jersey, 1982
31. T. Takagi, J. Vac. Sci. Technol., A2(2) (1984) 382-388
32. D. M. Mattox, J. Vac. Sci. Technol. A7 (1989) 1105-1114

33. T. Takagi, Thin Solid Films Col 92 (1982) 1-17
34. " Thin Film processes", J. L. Vossen and W. Kern, eds., Academic Press, New York, 1978
35. "Sputtering by Particle Bombardment" R. Behrish, ed., Topics in Applied Physics. Vol. 47. Springer, Berlin, 1981
36.W. D. Westwood, MRS Bulletin Vol. XIII, No. 12 (1988) 46
37. S. P. Murarka and M. C. Peckarar, " Electronic Materials : Science and Technology, Academic Press, Inc. (1989)
38.T. M. Besmann, D. P. Stinton, and R. A. Lowden, MRS Bulletin Vol. XIII(1988) 45 -49
39. Cecilia Y. Mak, MRS Bulletin, Vol. XIX (1994) 55 -62
40. A. J. Pedraza, M. J. Godbole, M. J. Desilva, and D. H. Lowndes, Mater. Res. Soc. Symp. Proc. Vol. 285 (1993) p.203
41. M. J. Desilva and A. J. Pedraza, D. H. Lowndes, J. Mater. Res., Vol. 9, No.4, (1994) 1019
42. A. Y. Cho and J. R. Arthur, Prog. Solid State Chem. Vol. 10(1975) 157
43. Theodore G. Moustakas, MRS Bulletin, Vol. XIII (1988) 29
44. Molecular Beam Epitaxy 1986, edited by C. T. Foxon and J. J. Harris, North Holland Amsterdam, (1987)
45. H. M. Manasevit, Appl. Phys. Lett. Vol. 12 (1968) 158
46. H. M. Manasevit and W. I. Simpson, J. Eletrochem. Soc. Vol. 116(1969) 1725
47. Sorab K. Ghandhi and Ishwara B. Bhat, MRS Bulletin, Vol. VIII (1988) 37
48. E. D. Hondros: in 'Precipitation processes in solids', 1; 1978, Warrendale, PA, The Metallurgical Society of AIME.
49. M. G. Nicholas: mater. Sci. Forum, Vol. 29 (1988) 127
50. D. Briggs, M.P. Seah, " Practical surface analysis", 2nd ed., vol.1(John Wiley and Sons, (1990) 15.
51. J. E. McNutt and G. M. Andes, J. Chem. Phys. Vol. 30 (1959) 1300
52. R. F. Reilman, A. Msezane and S. T. Manson, J. Electron Spectrosc., Vol 8 (1976) 389
53. I. M. Band, Yu, I. Kharitonov and M. B. Trzhaskovskaya, Atomic data and Nuclear data Tables, Vol. 23, (1979) 443

54. J. J. Yeh and I. Lindau, Atomic data and Nuclear Data Tables, Vol. 32 (1985) 1
57. W. P Dianis and J. E. Lester, Anal. Chem., 45 (1973) 169
58. J. J. Oglivie and A. Wolberg, Appl. Spectrosc., 3(1972) 401
59. M. F. Ebel and H. Ebel, J. Electron Spectrosc., 3(1974) 169
61. M. F. Chung and L. H. Jenkins, Surface Sci., 22 (1970) 479
62. W. A. Coghlan and R. E. Clausing, Atom. Data, 5,(1973) 317
63. D. A. Shirley, Phys. Rev. A, 7 (1973) 1520
64. P. W. Palmberg, Anal. Chem., Vol. 45 (1973) 549A
65. F. J. Szalkowski and G. A. Somorjai, J. Chem. Phys. Vol. 56 (1972) 6097
66. H. W. Werner and N. Warmoltz, J. Vac Sci. Technol. A2 (1984) 726
67. G. Bartu, R. Linder and C. Bryson, Surf. Interface Anal. Vol. 11, (1988) 307
68. W. Wei, J. Vac. Sci. Technol. A6 (1988) 2576
70. H. E. Bishop, B. Chronik, C. Le Gressus, A. Le Moel, Surf. Interface. anal. Vol.6 (1984)
71. J. C. Reviera, Surf, Sci., Vol. 161 (1985) 521
72. E. Kny, J. Vac. Sci. Technol., Vol. 17(1980) 658
73. J. Kleefeld and L. L. Levenson, Thin Solid Flms, Vol. 64 (1979) 389
74. H. Aksela and S. Aksela, J. Phys. B: Atom. Mol. Phys., Vol. 7 (1974) 1262
75. S. Thomas, Journal of Applied Physics, Vol. 45 (1974) 161- 166
76. J. S. Johannessen, W. E. Spicer and Y. E. Strausser, J. Appl. Phys., Vol. 47 (1976) 3028
77. T. Inoue, Jap. J. Appl. Phys., Vol. 16 (1977) 851
78. G. Queirolo and G. U. Pignatel, J. Electrochem. Soc., Vol. 127 (1980) 2438
79. R. F. K. Herzog, W. P. Poschenrieder and F. G. Satkiewicz, NASA Contract No. NAS5-9254, Final Report, GCA-TR-67-3N, 1967
80. J. A. Mchugh, Methods of Surface Analysis, (1975) 229
81. M. F. Ebel, J. Electron Spectr. Rel. Phen. Vol. 14, (1978) 287
82. S. Hofmann and J. Erlewein, Mikrochim. Acta, Vol. I (1979) 65
83 J. H. Thomas III and S. Hofmann, J. vac. Sci. Technol., Vol. A3 (1985) 1921
84. J. Biersack and L. Haggmark, Nucl. Inst. and Meth., Vol. 174(1980) 257
85. " The Stopping and Range of Ions in Solids", by J. F. Ziegler, J. P. Biersack and U. Littmark, Oergamon Press, New York, 1985 (ISBN 0-08 021603-X)
86. J. F. Ziegler and J. M. Manoyan, Nucl. Inst. and Meth., Vol. B35 (1989) 215-

87. R. Z. Bachrach, S. B. M. Hagstrom, and S. A. Flodstroem, Physical Review B, Vol. 10, 6, (1979) 2837

88. J. W. Park, A. J. Pedraza, D. H. Lowndes, and W. R. Allen, unpublished

89. J. D. Mcbrayer, "Diffusion of Metals in Silicon Dioxide", Ph. D. Thesis, Stanford University, (1984)

90. Y. Shacham-Diamand, A. Dedhia, D. Hoffstetter, and W. G. Oldham, J. Electrochem. Soc. Vol. 140, No.8 (1993) 2427 -2432

91. J. D. MacBrayer, R. M. Swanson, and T. W. Sigmon, J. Electrochem. Soc. Vol. 133, No. 6 (1986) 1424

92. M. Paulus and F. Reverchon, J. Phys. Rad. Phys. Appl., 22 Suppl. Vol. 6, (1961) 103.

93. M. DeSilva, Ph. D. Thesis "Excimer laser induced surface activation of ceramics for electroless deposition and enhanced metal adhesion", The University of Tenn., Knoxville (1994)

94. R. Kumar, MS Thesis " Adhesion enhancement of metallic films deposited onto excimer laser treated ceramic substrates ", The Univ. of Tenn., Knoxville (1994)

95. K. S. Kim, W. E. Baitinger, J. W. Amy, and N. Winograd, J. Electron Spectroscopy and related phenomenon, Vol. 5(1974) 351-367

96. S. Ishimura and R. Shimishu, Surface Science, Vol. 112 (1981) 386 - 408

97. S. Ishimura and R. Shimishu, Surface Science, Vol. 115 (1982) 259 - 269

98. D. Briggs and M. P. Seah, " Practical Surface Analysis", 2nd ed., Vol. 1 (John Wiley ans Sons) (1990) 109

99. F.S Ohuchi, R. H. French, and R. V. Kasowsky, J. Appl. Phys. Vol. 62 (6) (1987) 2286.

100. F. S. Ohuchi and M. Kohyama, J. Am. Ceram. Soc. Vol. 74(6) (1991) 1163.

101. P. S. Ho. and J. E. Lewis, Surf. Interface.Anal., Vol. 12 (1988) 329

102. S Hofmann and J. M. Sanz, in *Proceedings of 8th International Vacuum Congress*, Cannes 1980, Vol. I, Thin films, Vol. 90, Paris (1980)

103. J. P. Tobin, W. Hirschwald and J. Cunningham, Appl. Surf. Sci., Vol. 16 (1983) 441

104. C. D. Wagner, L. H. Gale, and R. H. Raymond, Anal. Cham., Vol. 51 (1979) 466

105. A. J. Pedraza, R. A. Kumar, and D. H. Lowndes, Appl. Phys. Lett., Vol. 66(9) (1995) 1065-1067

106. R.W. Dreyfus, R. Kelly, and R.E. Walkup, Appl Phys. Lett. Vol. 49, (21) (1986) 1478.

107. R. H. French, R. L. Coble, R. V. Kasowsky and F. S. Ohuchi, Physica B, Vol. 150 (1988) 47.

108. T. E. O'Brien and A. C. D. Chaklader, J. of the Amer. Cera. Soc., Vol.58(1974) 329

109. A. M. M. Gadalla and J. White, Trans. Brit. Ceram. Soc., Vol 63 (1964) 39

110. J. F. Burgess, C.A. Neugebauer, G. Flanagan and R.E. Moore, Solid State Technol.,(1975) 42

111. J. E. McDonald and J. G. Eberhart, Trans. Met. Soc. AIME, Vol. 233 (1965) 512

112.W. A. Weyl, p. 36 in Adhesion and Adhesives-Fundamentals and Practice, ed. by J. E. Rutzler and R. L. Savage, John Wiley & Sons, New York, 1953.

113. K. D. C. Moore and H. R. Thornton, J. Res. Natl. Bur., Std., Vol. 62(1959) 127

114. H. Esrom, J-Y Zhang and A. J. Pedraza, Mat. Res. Soc. Symp. Proc. Vol. 236, (1992) 383-388

115. N. S. McIntyre and D. G. Zetaruk, Analytical Chemistry, vol. 49, No. 11, Sep. (1977) 1521 - 1529

116. D. F. Mitchell, G. I. Sproule, and M. J. Graham, J. Vac. Sci. Technol., Vol. 18(3), (1981) 690 - 694

117. A, G, Schrott, R. D. Thompson and K. N. Tu, Mat. Res. Soc. Symp. Proc. Vol. 60 (1986)

118. Z. F. Ziegler, J. P. biersack, and U. Littmark, " The stopping and range of Ions in Solid", vol.1, Pergamon Press, New York (1985) 115-124

119. Y. Ota, J. Appl. Phys. 51 (1980) 1102

120. G.E. Becker and J.C. Bean, *J* . Appl. Phys. 48(1977) 3395

121. Y. Shacham-Diamand, in Proceedings of the TECHON conference, San Jose, CA, Oct. 1990

122. Y. Shacham-Diamand, A. Dedhia, D. Hofstetter, and W. G. Oldham, in Proceedings of VMIC, San Jose, CA, June 11-12, 1991
123. L. Pittaway, Brit. J. App. Phys. 15 (1964) 967
124. D. Menzel and R. Gomer, J. Chemical Physics, Vol. 41 (1964) 3311-3328
125. P. A. Redhead, Canadian Journal of Physics, Vol. 42 (1964) 886-905
126. S. Ishimura and R. Shimishu, Surface Science, Vol. 112 (1981) 386 - 408
127. S. Ishimura, H. E. Bauer, J. Seiler and S. Hofmann, Sur. Interface Anal., Vol. 14, (1989) 250

VITA

Jaewon Park was born in Heunghae, Korea on Oct. 14,1957. He was educated in Heunghae elementary and middle schools, and Daeryun Senior high school at Deagu city. He entered KooK-Min University at Seoul and received Bachelor's degree from the Department of Metallurgical Engineering in February 1985. He received a gold medal at the commencement ceremony for the academic excellence and also served in the military for approximately 3 years while in his undergraduate study.

Upon graduating from the Kook-Min University, the author was employed by the Korea Nuclear Fuel Company (KNFC) and worked there for 5 years as a materials engineer until he joined The University of Tennessee, Knoxville, in May 1990. The author received M.S degree in August 1992 and Ph. D degree on December 1995 from the Department of Materials Science and Engineering.

The author is a member of the ASM International, The Metallurgical Society, and Materials Research Society .